Optical and core-level X-ray spectroscopy of correlated two-dimensional materials

by

Connor Alexander Occhialini

B.S. Physics and Mathematics, University of Connecticut, 2018

Submitted to the Department of Physics
in partial fulfillment of the requirements for the degree of

DOCTOR OF PHILOSOPHY

at the

MASSACHUSETTS INSTITUTE OF TECHNOLOGY

September 2024

Authored by: Connor Alexander Occhialini
Department of Physics
June 7, 2024

Certified by: Riccardo Comin
Professor of Physics, Thesis Supervisor

Accepted by: Lindley Winslow
Associate Department Head of Physics

Optical and core-level X-ray spectroscopy of correlated two-dimensional materials

by

Connor Alexander Occhialini

Submitted to the Department of Physics
on June 7, 2024 in partial fulfillment of the requirements for the degree of

DOCTOR OF PHILOSOPHY

ABSTRACT

The intersection of low-dimensionality and strongly correlated electrons in van der Waals (vdW) materials offers a rich landscape of ordered phases and associated excitations for potential applications in nanoelectronics. The coupling between distinct degrees of freedom in correlated materials provide routes to realize novel functional properties, which can be further manipulated by the high tunability intrinsic to vdW materials through, e.g., heterostructures and doping. However, identifying the mechanism of correlated phases poses a fundamental challenge due to coexistent and competing orders. This requires detailed knowledge of the microscopic interactions/excitation spectra, methods to disentangle the individual roles of coexistent orders, and selective probes of symmetry-breaking within different coupled degrees of freedom. In this thesis, we demonstrate the utility and complementarity of resonant X-ray spectroscopy and symmetry-selective optical probes in combination with appropriate external tuning parameters (e.g. strain, pressure, ligand substitution, layer number) for revealing the origin of correlated phases in low-dimensional vdW materials.

We first investigate the triangular lattice antiferromagnet NiI_2. Frustrated exchange interactions result in a helimagnetic ground state and spin-induced ferroelectric order, making bulk NiI_2 a type-II multiferroic. Using a combination of optical spectroscopic probes, including Raman, magneto-optics, and second harmonic generation, we demonstrate the persistence of multiferroic order to the single-layer limit. We then aim to resolve the microscopic magnetic interactions and their interplay with the lattice symmetry to identify the origin of the magnetic ground state. Towards this goal, we investigate the magnetic ground state and transition temperature versus hydrostatic pressure and layer number, and directly probe the evolution of magnetic/structural orders with resonant magnetic X-ray scattering/structural diffraction, respectively. From these results, we demonstrate the central role of interlayer exchange interactions and their coupling to the structural symmetry in driving the magnetic ground state of NiI_2.

We next investigate the broader class of triangular lattice nickel dihalides, NiX_2 (X = Cl, Br, I), to identify the origin of sharp optical excitations, i.e. excitons, in nickel-based vdW magnets. We employ Ni-L_3 edge resonant inelastic X-ray scattering (RIXS) to access a

q-resolved and site-specific view into the excitation spectra. We identify the sharp excitons with spin-forbidden intra-configurational multiplets of octahedrally-coordinated Ni^{2+}, which become renormalized by Ni-X charge transfer. We also observe a finite dispersion of these excitations, demonstrating a multiplet delocalization that is controlled by the ligand-tuned charge transfer gap in a process analogous to ground state superexchange. These results establish the microscopic origin of these excitons and provide a mechanism to explain their possible coupling to the magnetic order/excitations.

Finally, we study the iron-based superconductor FeSe, which displays a rotational symmetry breaking electronic nematic phase in proximity to unconventional superconductivity without magnetic order. To understand the origin of nematicity, we investigate the ordering of the orbital degrees of freedom using X-ray linear dichroism with in-situ uniaxial strain tuning, electronic transport measurements and structural diffraction. We observe a lattice-independent orbital polarization acting as the primary nematic order parameter. This resolves the orbital origin of nematicity in FeSe and suggests that anisotropic spin fluctuations are the mechanism of unconventional superconductivity.

Thesis supervisor: Riccardo Comin
Title: Professor of Physics

Acknowledgments

The work performed throughout my Ph.D. and presented in this thesis would not have been possible without the continued support and collaborative efforts from many individuals.

First, I want to thank my Ph.D. advisor Riccardo Comin for always being supportive, encouraging and letting me follow my scientific curiosity. The freedom to pursue exciting research under your guidance has been an immensely rewarding experience.

Thanks to Jonathan Pelliciari for his scientific mentorship, friendship, and for introducing me to the field of RIXS. We have had many productive and enjoyable times both on and off the beamline. I will always be appreciative of your guidance.

A particular thanks to my close collaborator and friend Luiz Martins for always giving good advice and making experiments constantly enjoyable. I am proud of the work we have been able to accomplish together at MIT and will always appreciate the good times in the lab, at beamtime, and hanging out after work.

Thanks to Qian Song for introducing me to the nickel dihalides and van der Waals magnets and being an endless resource of knowledge and assistance in the lab. Much of the work here would not be possible without your dedication and help throughout the years.

Thanks to Yi Tseng for being my close collaborator and friend the past few years. I appreciate your scientific advice and am proud of the work we have been able to achieve together in our overlapping time at MIT.

Thanks to Shua Sanchez and the team at Argonne National Laboratory, Phil Ryan, Gilberto Fabbris, Yongseong Choi and Jong-Woo Kim for introducing me to uniaxial strain experiments and for your dedication to our shared projects on FeSe. This work would not have been possible without each of your commitment and hard work. I look forward to more successful collaborations.

To my more recent close collaborators in the lab Ahmet Demir and Luca Nessi, it has been an absolute pleasure working with you and I appreciate our friendship. I hope we can continue working with each other in the coming years. An additional thanks to Ahmet for a critical reading of this dissertation and his valuable comments.

I want to acknowledge all the excellent people in the Comin lab with whom I've had the opportunity to work with throughout the years, including Zhihai Zhu, Jonathan Pelliciari, Min Gu Kang, Jiarui Li, Abraham Levitan, Qian Song, Luiz Martins, David Rower, Kahraman Keskinbora, Younghun Lee, Jiaruo Li, Shua Sanchez, Ahmet Demir, Dongjin Oh, Luca Nessi, Lukas Powalla, Meg Shankar and Sahaj Patel. I will always be appreciative of the

welcoming and friendly environment we have maintained in the group throughout my years at MIT.

Thanks as well to all my collaborators both at MIT and elsewhere, including Emre Ergeçen, Batyr Ilyas, Nuh Gedik, Qishuo Tan, Xi Ling, Bryan Fichera, Ang-Yu Lu, Daniel Rodan Legrain, Clement Collignon, Valentina Bisogni, Shiyu Fan, Claudio Mazzoli, Christie Nelson, Ronny Sutarto, Jesse Smith, Jesse Kapeghain, Antia Botana, Danila Amoroso, Paolo Barone, Silvia Picozzi, Betrand Dupé, Matthieu Verstraete, Hebatalla Elnaggar and Frank de Groot. It has been a pleasure working with all of you and the work in this thesis would not be possible without your valuable contributions.

I would also like to extend gratitude to my undergraduate research mentor Jason Hancock at the University of Connecticut for introducing me to experimental condensed matter physics and X-ray science. The opportunities you have provided me over the years have been invaluable.

I also thank Monica Wolf, Gerry Miller, Lars Llorente, Cathy Modica and Sydney Miller for their continued assistance navigating administrative matters and for always being a friendly presence in Building 13 and Building 6 for a hallway chat.

Thanks to Prof. Long Ju and Prof. Leonid Levitov for serving on my thesis committee and their valuable input on this dissertation.

Thanks to Prof. Nuh Gedik for being a supportive academic advisor (and collaborator) throughout my time at MIT.

I would also like to thank my family for their constant love and support. To my parents, Tom and Beth, as well as Bill, Diane and Kevin, I would not be here without your sacrifices and encouragement. I am deeply indebted to you for giving me the opportunities that led me to where I am today.

Finally, I would like to extend my deepest gratitude to my wife, Victoria. I could not have finished this journey without you by my side. I appreciate all that you have done (and put up with) over my time at MIT. I will always cherish this time of our life for the many adventures we have been able to take together. Thank you for everything.

Contents

List of Figures

List of Tables

Chapter 1

Introduction

Van der Waals (vdW) materials are a subset of crystalline solids which have quasi-two-dimensional (2D) crystal structure, typically defined by 2D (single- or few-atom thick) planar sheets which are stacked to form a 3D crystal structure. The gap between individual 2D sheets is large and bonded only by (weak) vdW forces, which allows them to be mechanically exfoliated and isolated to individual 2D layers. On one hand, this highly anisotropic structure endows these materials with correspondingly anisotropic transport, optical and magnetic properties, even in the bulk. On the other hand, the isolation of pure 2D layers of these materials allows new degrees of freedom for engineering their properties. This includes the use of interfacial effects induced through composite structures of two vdW materials, termed heterostructures, or the variation of physical properties through moiré supercells which are formed between two (or more) layers in proximity along with a lattice mismatch or relative twist angle between their respective crystallographic axes.

From this perspective, the study of vdW materials has recently become a major focus of contemporary condensed matter physics. The reasons for the increased interest can be summarized by four unique opportunities: (a) the discovery of new physical properties/ground states without counterparts in bulk materials; (b) fundamental studies of ground states and dynamics of low-dimensional systems; (c) high tunability and control of physical properties through electrostatic doping/heterostructure engineering; and (d) prospects for higher efficiency electronics architectures through reduced sample volumes in single- and few-layer nanometric devices. Significant scientific discoveries have been recently achieved, including the discovery of superconductivity in twisted bilayer graphene [1], correlated insulating states in moiré heterostructures of graphene [2] and transition-metal dichalcogenides (TMDs) [3–5], long-range magnetic order in the monolayer limit [6, 7], emergent magnetism in moiré systems [8–10], and the first observation of the fractional quantum anomalous hall effect [11]. Thus, vdW materials offer many exciting opportunities for realizing new physical phenomena in quantum materials.

1.1 2D Magnetism

A major focus of current 2D materials research regards low-dimensional magnetism. The magnetic and electronic ground states observed in vdW materials are diverse, ranging from highly insulating to metallic conductivities, and ground states ranging from ferromagnetic, antiferromagnetic, and non-collinear states [12]. This wide range of physical properties makes this class of vdW materials attractive candidates for applications in magnetic devices [13, 14]. While the essential physics regarding the origin of magnetism and the magnetic properties of quasi-2D magnetic materials has been established in the bulk when these materials were originally grown and characterized, significant opportunities remain for studying these materials in the true 2D limit. What is of particular interest regards, primarily, two questions: (a) do the magnetic properties persist down to the single-layer limit? and, (b) can their magnetic ground states or functional properties (e.g. magneto-electric coupling) be tuned in a way that is unique to their reduced dimensionality?

These can be exemplified by the first example of 2D magnetic order reported in a single layer vdW material in the insulating ferromagnet CrI_3 [6] [Figure 1.1(a-c)]. In the bulk form, the chromium trihalides (CrX_3, X = Br, I) were interesting materials as being among the first known examples of electrically insulating ferromagnets, which are generally rare since the magnetic exchange pathways of insulators are typically antiferromagnetic [15]. The ferromagnetic order persists to the single-layer limit, along with a layer-dependent magnetic ground state that alternates between antiferromagnetic (AFM) and ferromagnetic (FM) order for even/odd layers, respectively [Figure 1.1(c)]. This results from AFM interlayer coupling between FM vdW layers, in combination with integer layer number (N) thickness which forbids magnetic compensation for N odd. The survival of magnetic order to the single-layer limit showed that vdW magnets were viable, overcoming the Mermin-Wagner theorem which states that long-range magnetic order is absent in the 2D isotropic Heisenberg model [16]. The reason this theorem does not hold for real materials is due to the presence of magnetic anisotropy [12].

One also notes that the magnetic state of few-layer CrI_3 possesses properties which are not present in the bulk. First, the interlayer AFM coupling observed in the few-layer samples is at odds with the bulk FM ground state [18]. This was attributed to the absence of a high temperature structural transition between rhombohedral and monoclinic crystal structures in few-layer flakes, which changes the sign of the interlayer exchange [19]. Thus, the interlayer exchange coupling was known early on to be closely related the stacking symmetry of the vdW layers, which may be anticipated from the microscopic mechanisms of magnetic exchange processes in insulators (e.g. Goodenough-Kanamori rules [15]). This change in magnetic ground state makes few-layer CrI_3 highly tunable. For example, a perfectly compensated AFM bilayer can undergo a metamagnetic transition to the FM state with a modest magnetic field of 0.6-0.9 T at low temperature [6] [Figure 1.1(c)/(d)]. Additionally, it is experimentally observed that the magnetic ground state is highly susceptible to external parameters, such

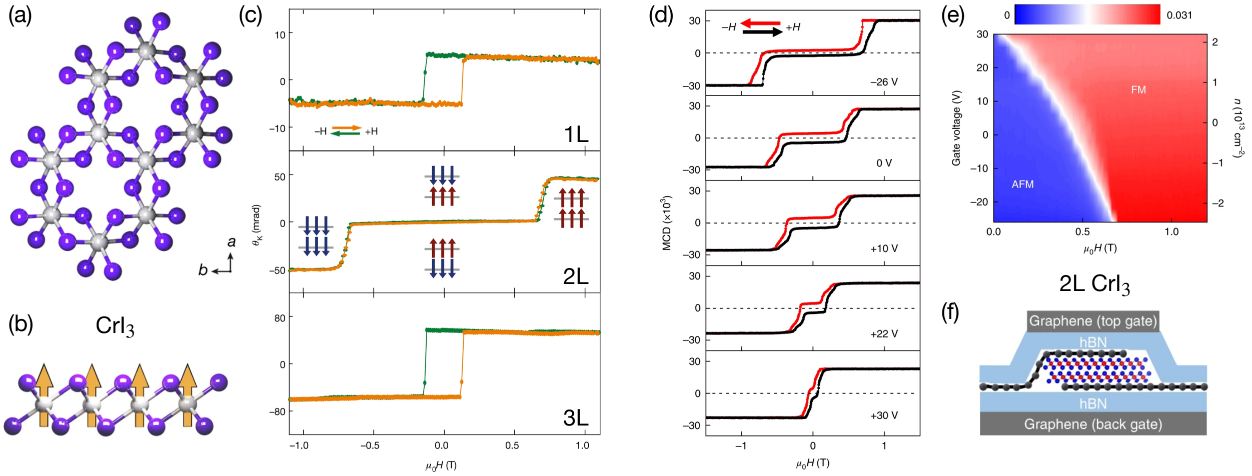

Figure 1.1: Magnetic properties of atomically-thin CrI_3. (a)/(b) Crystal and magnetic structure of single layer CrI_3 with Ising-type ferromagnetic order and local moments parallel to the c-axis. (c) Layer-dependent Kerr rotation measurements versus magnetic field, showing FM in the single- and three-layer samples, while bilayer CrI_3 is AFM. (d)/(e) Tuning of the magnetic state through electrostatic doping in 2L CrI_3. (f) Double gate device geometry for the doping dependence in (d)/(e). Panels (a)-(c) are reproduced from Ref. [6]. Panels (d)-(f) are reproduced from Ref. [17].

as hydrostatic pressure [20] and electrostatic doping [17, 21] [Figure 1.1(d-f)]. Furthermore, the intrinsically low-symmetry configuration of the AFM bilayer CrI_3 leads to an emergent linear magnetoelectric coupling, related to a breaking of inversion (P) and time-reversal (T) symmetry of the AFM configuration [22].

These initial studies highlight the main interests of 2D magnets and particularly their unique emergent properties and high degree of tunability compared to bulk-like samples [13]. These studies were performed in parallel with reports of other 2D ferromagnetic semiconductors such as $CrGeTe_3$ [7] and metals Fe_3GeTe_2 [23], as well as the first reports of antiferromagnetic few-layer materials belonging to the class of transition metal thiophosphates MPX_3 (M = Mn, Fe, Co, Ni; X = S, Se) [24, 25]. Together, these materials formed the basis for the renewed field of 2D magnetism in the context of vdW materials.

1.2 Magnetoelectric coupling and multiferroic order

Among the main goals in 2D magnets is establishing the control and readout of magnetic states through electrical manipulation, which constitutes a major route towards the goals of antiferromagnetic spintronics [26]. Broadly, these goals may be summarized by non-volatile reading/writing of antiferromagnetic states, high-frequency operation speeds and insensitivity to stray magnetic fields, overcoming technical limitations of current (ferro)magnetic based memory (MRAM), for example. Electric-field tunable antiferromagnetic states in the context of both ultrathin films and vdW materials may be a viable path to realize these properties, particularly for devices based on tunneling magnetoresistance (TMR) [13].

Favorable towards these goals is the observation of very large TMR in many vdW magnetic layers, including CrX_3 materials down to the few-layer limit [27–29]. However, in these examples, switching the TMR states requires relatively large magnetic fields. Therefore, electric control of magnetic states, and the realization of important functional properties such as exchange bias, have been pursued using heterostructure engineering of 2D magnets. While progress has been made, including the observation of exchange bias in heterostructures [30], moiré engineering of long-range magnetic order [31, 32] and heterostructure based artificial multiferroics, these approaches involve significant complexity to achieve the desired properties at the level of device fabrication. An alternative route is to stabilize intrinsic multiferroic states in 2D materials, thus realizing direct magnetoelectric coupling within a single 2D layer without relying on interfacial or proximity effects.

Multiferroics refer to materials possessing two (or more) simultaneous orders within different degrees of freedom, including ferroelectric, ferro/antiferromagnetic, ferroelastic and/or ferrotoroidal orders [15]. The overarching principle is that materials in which such orders coexist will possess an intrinsic, microscopic coupling among the different ferroic orders, allowing mutual control through their distinct conjugate fields (e.g. applied magnetic field, electric field, or stress). For this work, we focus on the subset of multiferroics characterized by coexistent ferroelectricity and magnetic order [33], also known as magnetoelectric multiferroics [34].

Such magnetoelectric multiferroics appear in two main types, called type-I and type-II [15]. For the case of type-I, the ferroelectric and magnetic order occur through different mechanisms and with different transition temperatures. For example, the archetypal type-I multiferroic is $BiFeO_3$ where the ferroelectricity ($T_c \simeq 1100$ K) is driven by the classic 'lone pair' ferroelectric mechanism on the Bi ions and the antiferromagnetic order on the magnetic Fe ions occurs independently at the lower temperature $T_N \simeq 643$ K [34, 35]. Even though the ferroelectric and magnetic orders are independent, it is found that below T_N, the magnetism and the ferroelectricity are mutually coupled leading to pronounced magnetoelectric effects [35].

In contrast, type-II multiferroics are characterized by a spin order that directly induces ferroelectric polarization. In these materials, the coupling between the two orders is microscopically direct, leading to stronger magnetoelectric effects compared to type-I multiferroics [33]. The standard examples are the manganites such as $TbMnO_3$, where a spin spiral order leads to a concomitant spin-induced ferroelectric order below $T_N \simeq 27$ K which is highly tunable by external magnetic field [36] [Figure 1.2(a)]. Spin-induced ferroelectricity requires a non-collinear magnetic order that breaks inversion symmetry and arises as an effect of spin-orbit coupling at either the transition metal or the ligand site, as formalized in the generalized Katsura-Nagaosa-Balatsky (gKNB) or spin-current model [39, 40]. Such magnetic states are typically incommensurate and can be stabilized by frustrated magnetic exchange interactions [41] (see Chapter 3).

Thus, accessing this route towards magnetoelectricity in 2D materials requires the identi-

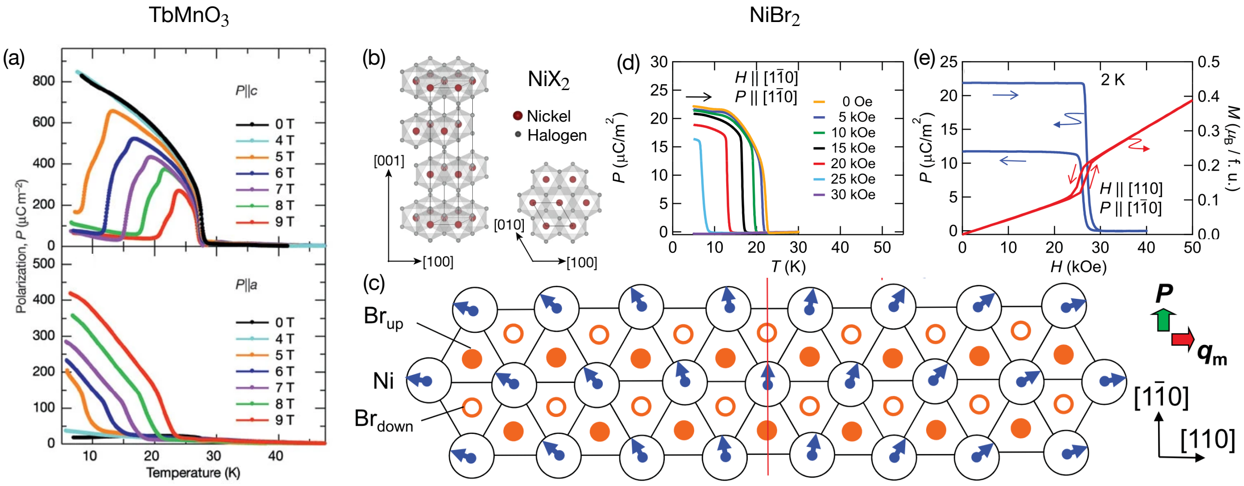

Figure 1.2: Type-II multiferroicity in $TbMnO_3$ and $NiBr_2$. (a) A spin-induced ferroelectric polarization appears within the incommensurate spin-cycloidal phase of $TbMnO_3$ below $T_N \simeq 27$ K which is strongly tunable by external magnetic fields. (b) $R\bar{3}m$ structure of the nickel dihalides (NiX_2), possessing weakly vdW bonded triangular lattice sheets of magnetic Ni^{2+} ions. (c) Incommensurate spin-cycloidal phase of $NiBr_2$ appearing below $T_{N,2} \simeq 22$ K, with magnetic moments shown as blue arrows. (d)/(e) A magnetic-field tunable ferroelectric polarization appears in the spin cycloidal phase. Panel (a) is reproduced from Ref. [36]. Panel (b) is reproduced from Ref. [37]. Panels (c)-(e) are reproduced from Ref. [38].

fication of candidate 2D materials with non-collinear magnetic structures, and demonstrating that these non-trivial magnetic states can persist to the single layer limit. This contrasts with the initial reports of 2D magnetism discussed above, which consist of relatively simple forms of long-range magnetic order, including Ising-type ferromagnetism (along with interlayer FM or AFM stacking) and Néel/zig-zag type antiferromagnetic states within the vdW plane [6, 24, 25]. Each of these states are collinear, meaning that the local spin on each site lies along a unique crystallographic axis in either a parallel (FM) or antiparallel (AFM) configuration. While such states are certainly of interest, simple collinear magnetic order is usually of high symmetry, which forbids magnetoelectric effects and spin-induced ferroelectricity.

In this vein, it is known that many examples of type-II multiferroics belong to the class of triangular lattice antiferromagnets [Figure 1.2(b)]. The triangular lattice geometry naturally leads to geometrically frustrated magnetic exchange interactions, and non-collinear/incommensurate magnetic states are commonly observed as noted already in original investigations of their magnetic structures by neutron scattering (e.g. [41–43]). The simplest examples are the transition-metal dihalides, MX_2, where M = Mn, Fe, Co, Ni and X is a halogen (X = Cl, Br, I). These materials all possess a similar layered crystal structure, consisting of weakly-bonded 2D triangular lattice layers of edge-sharing, octahedrally coordinated magnetic transition metal sites [Figure 1.2(b)]. Type-II multiferroicity has been observed in the bulk form of many of these materials [38, 44, 45], as first demonstrated in the spin cycloidal phase of $NiBr_2$ below $T_N \simeq 22$ K [38] [Figure 1.2(c-e)]. Additionally, these materials are exfoliable and can be isolated to a single triangular-lattice layer. However, the properties of these materials to the few-layer limit had yet to be studied at the start of the work presented here.

Therefore, these materials are identified as promising candidates to realize the strong magnetoelectric coupling inherent to type-II multiferroics in the single layer limit for use in vdW devices, as highlighted by recent theoretical work showing that this class could be viable from first-principles calculations [46, 47]. In the first part of this thesis, we thus focus on the transition-metal dihalide NiI_2 and provide the first evidence that the non-collinear magnetism [42] and the associated type-II multiferroic order [45] can persist to the single-layer limit (Chapter 5). We then study in detail the magnetic exchange interactions to understand the microscopic origin of the non-collinear magnetic state, the role of reduced dimensionality, and their relationship to the multiferroic order (Chapters 6 and 7).

1.3 Excitons and the optical detection/control of magnetism

A related goal to the electric control of magnetic order is the detection and manipulation of magnetic states through optical methods. The optical response of 2D materials carries particular significance to the field due to the general lack of suitable probes. Given the small sample volume in the single-layer limit, traditional probes of magnetic order such as magnetometry and neutron diffraction are not feasible. Thus, most of the evidence for magnetic order in 2D materials comes from magneto-optical methods, such as the magneto-optical Kerr effect (MOKE) [6, 7] or magnetic circular/linear dichroism (MCD/MLD), polarized photoluminescence (PL) [48], Raman spectroscopy [24, 25] and second harmonic generation (SHG). This is because a majority of 2D magnets are correlated insulators with large transport gaps [18], and thus electrical transport measurements of, e.g., the anomalous hall effect [23], are not possible. More generally, detecting antiferromagnetic states with optical probes is even more critical, as one cannot rely on directly switching the magnetic state with an external magnetic field as in ferromagnets.

The insulating/semiconducting nature of most 2D magnets does, however, lead to a rich optical response in the visible/near infrared range (photon energy $\sim$ 1-4 eV). Besides standard interband transitions which typically appear as broad, featureless absorption bands, one also commonly observes various types of excitonic responses near and below the band edge. Excitons are collective excitations where photoexcited electrons in the conduction band minimum (CBM) are bound to the photoexcited holes in the valence band maximum (VBM) through their mutual Coulomb interaction. The resulting attractive e-h interaction leads to an energetic stability of this bound state, which appears at energies below the band gap (energy E_g) by an energy equal to the binding energy (E_b). We note that compared to 3D materials, the 2D nature of vdW materials likely increases the exciton binding energy due to the reduced dielectric screening [49]. The above description of excitons is appropriate for the situation where the relevant lowest-energy electronic states are best represented as highly dispersive, itinerant bands. These types of excitons are termed interband Wannier excitons [50, 51] and appear as strong peaks in absorption and PL spectra of direct band gap semiconductors, where the CBM and VBM occur at the same point in momentum space [Figure 1.3(b)].

These types of excitons are those which dominate the optical response of monolayer TMDs [51–54] [Figure 1.3(a-b)], which have been utilized in many contexts ranging from characterization of the electronic structure, the discovery of interlayer and moiré excitons [55], optically induced ferromagnetism [9] and the first indirect optical evidence of the fractional quantum anomalous hall effect [11]. Distinct from most 2D magnets, however, the TMDs are highly covalent systems, and the band description is the most appropriate one for the electronic structure and the optical response. In strongly correlated systems, such as many 2D magnets, the picture is more complicated due to the highly localized d orbitals from which the local magnetic moments originate.

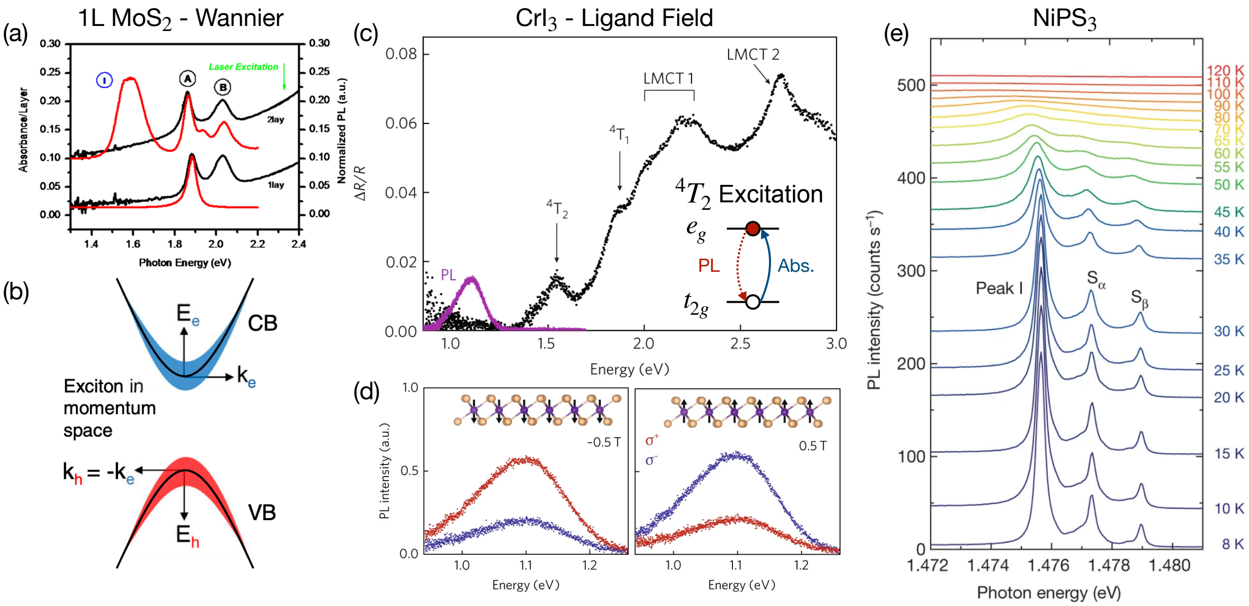

Figure 1.3: Excitons in two-dimensional semiconductors and insulators. (a) Emerging photoluminescence from a direct band gap Wannier-type exciton in thin layers of the transition-metal dichalcogenide (TMD) MoS_2. (b) Schematic of the conduction band (CB) and valence band (VB) extrema at the K point in TMDs forming excitons through electron-hole pairs near the direct band gap. (c) Differential reflectance and photoluminescence of monolayer CrI_3. The lowest energy peak is a dd transition of Cr^{3+} ($^4T_2$) corresponding to an inter-orbital crystal field excitation (inset). (d) Circular polarization in the $^4T_2$ emission is sensitive to the magnetization of monolayer CrI_3. (e) Sharp excitons appearing below the magnetic phase transition of the vdW AFM $NiPS_3$ ($T_N \simeq 155$ K) as measured by PL. Panel (a) is reproduced from Ref. [53]. Panel (b) is reproduced from Ref. [51]. Panels (c)/(d) are adapted from Ref. [48]. Panel (e) is reproduced from Ref. [56].

The crossover in the description of the electronic structure can be separated based on the energy and degree of localization for the excitation. In general, lower energy features are more localized, while for higher energy excitations near or above the bandgap, a band description may be more appropriate. For instance, while the chromium trihalides are relatively localized *d*-electron systems, it is argued that the giant equilibrium magneto-optical responses in an intermediate energy range (in the visible region just below the band gap $\sim$ 2-3 eV) are dominated by interband Wannier type excitons which couple strongly to the spin split band structure resulting from the ferromagnetic order [57]. The same mechanism is suggested in the optical response of the more recently reported vdW antiferromagnet CrSBr [58]. It has also been demonstrated that circularly polarized optical excitation resonant to the interband excitons of $\mathrm{CrI_3}$ with large MCD contrast can deterministically flip the overall magnetization [59]. Thus, excitons in the context of magneto-optics possess a dual importance. On one hand, understanding the coupling of the photoexcited exciton state to the spin degrees of freedom is an important route to study for the all-optical control of magnetism in vdW materials. Secondly, these excitons provide large magneto-optical effects for the non-destructive readout of the underlying magnetism.

In systems with localized *d*-orbitals, other types of excitations with a distinct microscopic interpretation can arise which are related to highly localized transitions between different spin orbital configurations of the *d*-orbitals. Such transitions are termed ligand-field or *d*-*d* transitions and are essentially transitions localized to a single transition metal site [60]. The characteristic spectra depend on the electronic filling (valence), the multielectronic ground state (high spin/low spin), the crystal field splitting, and the electronic interactions (e.g. Hund's coupling), and are well-known in the context of molecular systems in the chemistry community for transition metal complexes [61, 62]. Ligand-field or *d*-*d* transitions are sometimes termed Frenkel excitons. However, it is important to note some key distinctions with Wannier excitons. In the latter, the energy of the excitation is defined in terms of a binding energy with respect to the band gap. Ligand-field or Frenkel excitons are rather uncorrelated (or only weakly related to) the band gap, but instead have an absolute energy related to a well-defined transition between two localized energy states, thus allowing one to directly extract key energetic parameters of the system.

Ligand-field transitions are typically weak in condensed matter systems, because of optical dipole selection rules which restrict their intensity [60]. However, they are the most common lowest-energy excitations appearing below the band gap in correlated materials with characteristic energies of 1-3 eV, which describes the common situation for correlated vdW magnetic insulators. This has been highlighted in the case of $\mathrm{CrX_3}$ in the older optical literature [63] as well as in more recent studies [48], where the lowest energy optical absorption and photoluminescence is interpreted as the primary crystal field transition characteristic of $\mathrm{Cr^{3+}}$ ions [Figure 1.3(c)]. The polarized PL response of these excitations have been crucial for identifying the long-range magnetic order in the single layer of both $\mathrm{CrBr_3}$ [64] and $\mathrm{CrI_3}$ [48] [Figure 1.3(d)].

From this perspective, recent work has reported surprisingly sharp optical excitations appearing below the band gap of other correlated magnets, such as $NiPS_3$ and NiI_2 [56, 65] [Figure 1.3(e)]. There is ongoing discussion in the community regarding the origin of these transitions, but they have nonetheless become an important tool for the characterization of the magnetic ground state in Ni^{2+} based vdW magnets [66–69] due to their hypothesized connection to/activation by long-range magnetic order. It is also observed that these peaks are linearly polarized in absorption and emission, related to the direction of the local spin moment on the nickel sites as determined from neutron scattering [66, 70]. Furthermore, ultrafast optical experiments show that resonant optical excitation can efficiently modulate the antiferromagnetic order [71, 72]. Thus, understanding the microscopic origin of these sharp optical excitations, their relationship to the local spin degree of freedom and how they couple to the long-range magnetic order remain critical open questions. Finally, one needs to identify routes to tune these excitations and how they may be generalized beyond the case of Ni^{2+} systems.

In Chapter 8, we resolve these questions using resonant inelastic X-ray scattering (RIXS) to study the local electronic structure of the Ni^{2+} atoms in the vdW magnetic nickel dihalides (NiX_2, X = Cl, Br, I). We establish the microscopic origin of these excitonic states, show how they may be energetically-tuned by the ligand environment, and use the momentum resolved character of RIXS to reveal their delocalized nature. These results show how these excitons may be generalized to other systems, how they may couple to the long-range magnetic order, and provides a new technique for studying the properties of delocalized excitons in condensed matter systems. This understanding is critical to engineer the exciton properties for the detection and manipulation of magnetic order through optical excitation.

1.4 Magnetism, electronic nematicity, and unconventional superconductivity

Magnetic interactions in correlated (quasi)-2D materials also play an important role in the mechanisms of high-T_c unconventional superconductivity. Common to many strongly-correlated electronic phases, the presence of unconventional superconductivity is typically accompanied by various competing electronic orders, which can be either antagonistic to or assist superconductivity. The most studied examples are the copper oxide high-T_c superconductors (‘cuprates’), where the parent phase (e.g. La_2CuO_4) is an AFM insulator. When one dopes either holes or electrons to the system, the AFM insulator state is suppressed and superconductivity emerges near the point where the AFM state is quenched [73]. In addition to superconductivity, other electronic orderings - such as charge-density waves [74] - may also emerge, which are typically accompanied by anomalous electronic transport [73]. A central theme emerging from this thread of research is that understanding the interactions determining these competing orders (e.g. CDW or magnetic order) and their correlation, or lack of correlation, with superconductivity are critical towards understanding the unconventional pairing mechanism.

From this perspective, the discovery of the iron-based superconductors (IBSCs) provided a new platform for studying unconventional superconductivity [75, 76]. In contrast to cuprates, the parent phase of many IBSCs are (bad) metals. The common structural motif is a square lattice of Fe-atoms, tetrahedrally-coordinated by either a chalcogen (S, Se, Te) or pnictogen (P, As) [77, 78] [Figure 1.4(a,b,e)]. The lattice and electronic structures are quasi-2D, with some materials being exfoliable [79]. The prototypical parent compound is $BaFe_2As_2$, with FeAs 2D sheets [75] [Figure 1.4(a)]. Undoped samples show a stripe type spin-density wave (SDW) ground state ($\mathbf{Q} = (\pi, 0)$) [Figure 1.4(c,e)], which can be traced to a Fermi surface instability, although electronic correlations and local moment physics are also important [78]. The confluence of correlated, localized electrons with well-defined local moments alongside metallicity and a well defined Fermi surface has led to ongoing debates regarding which perspective is appropriate for describing these systems [80]. Upon electron (e.g. Co) or hole (K) doping, the SDW phase is suppressed and superconductivity emerges near a quantum critical point (QCP) of the SDW order [81] [Figure 1.4(c)]. These observations demonstrated early on the key interplay between magnetic order and superconductivity in IBSCs, similar to cuprates.

Distinct from cuprates, the magnetic order observed in many IBSCs (e.g. $BaFe_2As_2$) breaks C_{4z} rotational symmetry in the square Fe-lattice. The magnetic wavevector is stripe-like, with magnetic moments oriented along a unique Fe-Fe bond direction, with two-fold (C_{2z}) rotational symmetry [Figure 1.4(e)]. On one hand, this rotational-symmetry-breaking magnetic order induces a tetragonal-to-orthorhombic structural phase transition in the planar square lattice [81]. Additionally, this transition is accompanied by an exceptionally large resistivity anisotropy, where the resistance along the two orthorhombic directions can differ by over a factor of 2 below the magnetic transition temperature T_N [82]. This resistance anisotropy is also present above T_N under applied uniaxial stress, and shows a divergent susceptibility with respect to the uniaxial stress as T_N is approached from above [83]. This strain-susceptibility follows a Curie-Weiss type divergence, similar to the behavior of the magnetic susceptibility of an Ising-type ferromagnet. The large anisotropy in comparison the magnitude of the structural distortion (order of 0.1%), in conjunction with its divergent behavior, provides strong evidence for an electronic origin. This strongly anisotropic state is referred to as *electronic nematicity*.

For the case of $BaFe_2As_2$, it is believed that the nematic phase is driven directly by the magnetic degrees of freedom and the stripe-type SDW phase, called the *spin-nematic* model [84]. This is supported by the proximity between the SDW and orthorhombic structural phases throughout the phase diagram [Figure 1.4(c)]. Importantly, the large nematic susceptibility remains strong near the SDW QCP [83]. Upon suppression of the long-range magnetic order, optimal superconductivity is observed, although strong anisotropic spin fluctuations persist in the paramagnetic state down to low temperature. The strength of these low-energy spin fluctuations decrease below superconducting T_c, along with the nematicity induced structural orthorhombicity [85, 86]. From these observations, it is thought that these anisotropic spin fluctuations are the key ingredient for unconventional superconduc-

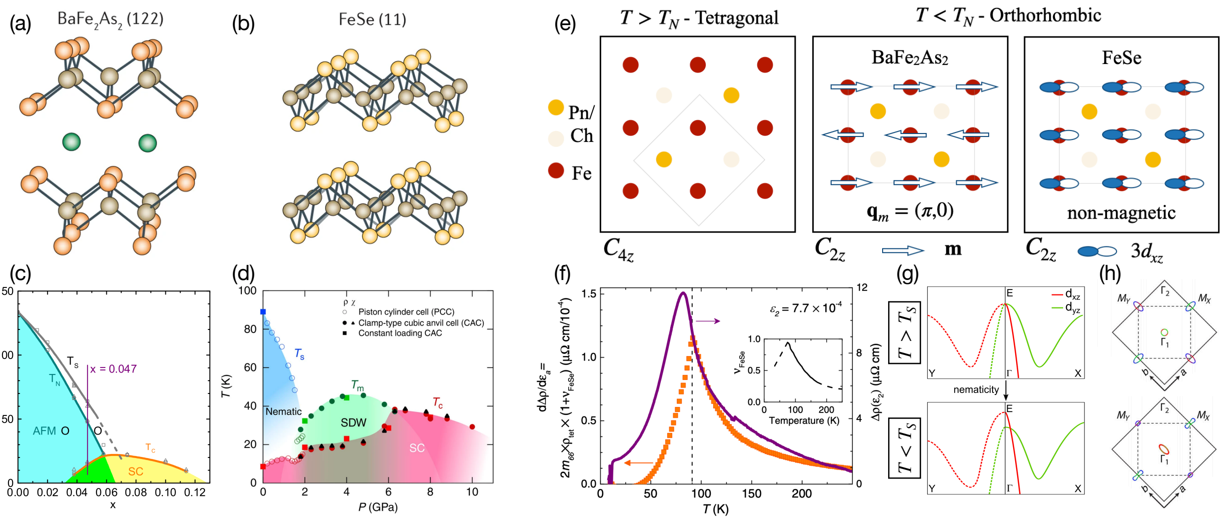

Figure 1.4: Iron-based superconductivity and electronic nematicity in $BaFe_2As_2$ and FeSe. Crystal structures of (a) $BaFe_2As_2$ ('122' compound) and (b) FeSe ('11' compound). (c) Electron doping phase diagram of $Ba(Fe_{1-x}Co_x)_2As_2$. (d) Phase diagram of stoichiometric FeSe under hydrostatic pressure. (e) Structural and magnetic phases in the nematic state: (left) high temperature tetragonal (C_{4z} symmetric) square FePn/FeCh lattice (Pn - pnictogen, Ch - chalcogen) common to $BaFe_2As_2$ and FeSe; (center) Orthorhombic phase $BaFe_2As_2$ with stripe-type magnetic order with $\mathbf{q}_m = (\pi, 0)$ rlu and C_{2z} symmetry; (right) Non-magnetic orthorhombic phase of FeSe displaying orbital order with preferential $n(3d_{xz}) > n(3d_{yz})$ orbital occupation. The orthorhombic distortion is exaggerated for clarity. (f) Divergent elastoresistance versus temperature in FeSe signaling the electronic nematic phase at $T_S \sim 90$ K. (g) Schematic of the momentum-dependent nematic band shift of the $3d_{xz}/3d_{yz}$ bands and (h) the corresponding Fermi surface reconstruction in the nematic phase of FeSe. Panels (a)/(b) are reproduced from Ref. [78]. Panel (c) is reproduced from [86]. Panel (d) is reproduced from Ref. [327]. Panel (f) is reproduced from Ref. [93]. Panel (g) is reproduced from Ref. [106]. Panel (h) is reproduced from Ref. [104].

tivity. Importantly, this shows a close association between the physics of the spin-nematic state and the appearance of superconductivity in the iron-pnictides.

Due to this close association, much of the research has focused on the origin of nematicity in IBSCs. A key ingredient lies in identifying the primary order leading to the nematic state. This is fundamentally challenged by several factors. First, the rotational symmetry breaking is reflected in *all* degrees of freedom in the ordered phase. In particular, a corresponding structural transition is observed, and the nematic order appears as anisotropy in the structural, orbital, spin and charge degrees of freedom. These may be measured by diffraction, optical spectroscopy [87], electronic Raman scattering [88], angle-resolved photoemission (ARPES) [89], inelastic neutron scattering (INS)/RIXS [80, 90], nuclear magnetic resonance (NMR) [91], and electronic transport [83]. Therefore, identifying the leading interaction based only on the anisotropy in the nematic state with a given probe is not sufficient due to a microscopic coupling between all degrees of freedom in the ordered phase.

Furthermore, C_{4z} rotational symmetry breaking leads to the formation of orthorhombic twin domains in single crystals [82, 92, 93] [Figure 1.4(e)]. Thus, in the absence of a poling field (applied stress) to detwin these domains, bulk probes will average out the corresponding anisotropy, restoring a macroscopic C_{4z} rotational symmetry. This requires measurements with a detwinning stress applied, or sub-micron beam spot sizes to measure the intrinsic anisotropy from a single-domain. However, applying finite stress to system poses yet another experimental difficulty by inducing a finite anisotropy above T_N, i.e. a finite nematic order is induced by applied strain due to the divergent nematic susceptibility [83]. This means that measurements of an order parameter will display a broad cross over across T_N with finite applied stress, rather than a direct measurement of the intrinsic nematic order parameter. Thus, separating the true nematic order parameter from secondary effects induced by the highly anisotropic electron state is far from a trivial task, but holds particular importance for identifying the mechanism of superconductivity in IBSCs.

Challenging the spin-nematic phenomenology of nematicity in IBSCs is the related compound FeSe [78, 94] [Figure 1.4(b)]. In the undoped parent compound, an orthorhombic structural transition is observed at $T_S \simeq 90$ K without the presence of long-range magnetic order [95] [Figure 1.4(d,e)]. Significant spin-fluctuations are nonetheless observed by multiple techniques including RIXS [96], inelastic neutron scattering (INS) [97, 98], and nuclear magnetic resonance (NMR) [99]. Particularly, strong fluctuations at both $\mathbf{Q} = (\pi, 0)$ and $\mathbf{Q} = (\pi, \pi)$ wavevectors as observed, with $\mathbf{Q} = (\pi, 0)$ becoming favored below T_S [97], suggesting possible magnetic frustration that becomes partially lifted in the nematic state. The large resistivity anisotropy characteristic of electronic nematicity is also reported, approaching 10% along the Fe-Fe directions near T_S [93] along with the expected Curie-Weiss divergence at T_S, providing strong evidence for an electronic-origin nematic state [Figure 1.4(f)]. Alongside a well-developed nematic phase, coexistent bulk superconductivity in undoped samples is observed at $T_c \simeq 9$ K [100], which is seemingly unusual in comparison to Co-doped $BaFe_2As_2$. In further contrast to the latter, NMR and INS measurements show a suppression of spin fluctuations below T_c [19, 99], while the orthorhombic structural distortion is unaffected [101]. Finally, optimal superconductivity is not observed when the nematic transition is quenched by doping (e.g. isovalent doping with S) [102] or under hydrostatic pressure [103] [Figure 1.4(d)]. All of these observations indicate that while spin fluctuations may be important for superconductivity, a distinct nematic state is formed in FeSe compared to the iron pnictides.

Consistent with this proposal, it has been suggested that orbital order, rather than a stripe-type SDW, is the leading nematic instability in FeSe [99] [Figure 1.4(e)]. This scenario was first evidenced by NMR [99] and angle-resolved photoemission spectroscopy (ARPES) [95]. NMR shows a substantial splitting of the Knight shift which was attributed to a ferro-orbital ordered state, with a distinct evolution of the spin-fluctuations determined from the spin-relaxation time which are significantly activated only below T_S [99]. In ARPES, the band structure near E_F is spanned by the t_{2g} set of d orbitals, $3d_{xz}/3d_{yz}$ and $3d_{xy}$, with the former two being degenerate above T_S [95, 104, 105] [Figure 1.4(g)]. The bands form circular hole-like pockets at the Γ point and elliptical electron-like pockets at the X/Y points ($\mathbf{Q} = (\pi, 0)$) [Figure 1.4(h)]. Electronic correlations are observed to be strong on the d_{xy} orbitals, but weaker for the d_{xz}/d_{yz} states. Large band reconstructions are observed below T_S, including a momentum dependent splitting of the d_{xz}/d_{yz} orbitals with a sign change between the Γ and zone-boundary [104, 106] [Figure 1.4(g,h)]. From this behavior, it was hypothesized that orbital-dependent spin fluctuations can explain the momentum-dependent band shifts and the corresponding distortions of the Fermi surface, which are then the primary degree of freedom driving nematicity despite the lack of long-range magnetic order [107]. Notably, a momentum-dependent band shift does not correspond to a trivial orbital ordering of the d_{xz}/d_{yz} states, which would instead correspond to a momentum-independent (uniform) shift of the d_{xz} and d_{yz} bands.

While the spin and orbital degrees of freedom are certainly closely intertwined, the above picture is evidenced from the itinerant electronic states and Fermi surface anisotropy far below T_S. Additional ARPES measurements on S-doped FeSe reveal that the strain-induced nematic order above T_S may possess a distinct band anisotropy [108]. This suggests that the Fermi surface anisotropy measured below T_S may not reflect the true nematic order parameter. These measurements may instead be complicated by feedback effects between the Fermi surface reconstruction and the development of anisotropic $(\pi, 0)$ spin-fluctuations below T_S [97]. Thus, strong evidence exists to support a nematicity driven by both orbital and spin degrees of freedom in FeSe, although a consensus has yet to be reached. The above complicating factors require a more direct measurement of the local orbital degrees of freedom.

To address this problem, we have developed a new technique to identify the origin of nematicity in FeSe. This is achieved through measuring the local $3d_{xz}/3d_{yz}$ orbital anisotropy with Fe K-edge X-ray linear dichroism (XLD) spectroscopy as a function of in-situ tunable uniaxial strain (Chapter 9). This goes beyond the ARPES results, which are sensitive to the band structure and itinerant states. X-ray spectroscopic measurements instead directly measure a quantity proportional to the locally-projected orbital polarization. A key advance is the use of in-situ, tunable strain while simultaneously monitoring the local orbital occupations (XLD), the anisotropy of the itinerant states (resistance anisotropy/elastoresistance), and the strain-state/structural anisotropy (X-ray diffraction). From these results, we can disentangle the anisotropy in each degree of freedom as a function of both strain and temperature across the nematic transition temperature. We conclude that orbital polarization is the primary order of the nematic phase in FeSe.

1.5 Outline of thesis

This thesis is organized as follows. First, we give an overview of correlated electron systems, including the origin of electron correlations, crystal field splitting and band gaps of correlated insulators in Chapter 2. Next, we discuss the origin of inter-atomic magnetic exchange interactions in insulators, magnetic ground states on the triangular lattice, and mechanisms of spin-induced ferroelectricity in Chapter 3. In Chapter 4, we discuss the techniques used in this thesis, including X-ray absorption spectroscopy (XAS), resonant elastic and inelastic X-ray scattering (REXS/RIXS), and optical techniques including Raman spectroscopy and magneto-optical spectroscopy. Chapters 5-7 are focused on the magnetic ground state properties of NiI_2, including the optical investigation of NiI_2 to the single layer limit (Chapter 5), high-pressure tuning of the ground state in bulk and few-layer NiI_2 probed with optical spectroscopy and structural diffraction (Chapter 6) and finally the direct measurement of the magnetic order in bulk and mesoscale thickness flakes in NiI_2 using REXS in Chapter 7. In Chapter 8, we report RIXS measurements on the nickel dihalides, establishing the origin of excitons and identifying their ligand mediated delocalization. Finally, we study the origin of nematicity in the IBSC FeSe in Chapter 9 using X-ray Linear Dichroism (XLD), X-ray diffraction and transport anisotropy as a function of uniaxial strain. We conclude and provide a future outlook in Chapter 10.

Chapter 2

Electronic Structure of Strongly Correlated Systems

Each material of focus in this thesis may be considered a correlated electron system. Electronic correlations arise from the localized d-orbitals in transition-metal compounds. On one hand, strong electronic interactions are crucial to explain the nature of the band gaps and emergence of local magnetic moments in these systems. Furthermore, the relevant physics determines the interatomic magnetic exchange interactions leading to long-range magnetic order. Finally, multielectronic correlations and crystal field interactions are essential to describe the excited states of these systems which may be observed in optical measurements. The goal of this section is to give an overview of the main interactions for correlated d electron systems, including intra-atomic electronic correlations, crystal field, spin orbit coupling, and the nature of correlated band gaps.

The theory of atomic/molecular physics reviewed here plays a dual role for the content of this thesis. On one hand, atomic physics is the foundation of core-level X-ray spectroscopy, a fundamental experimental technique we utilize in the following chapters. Secondly, the electronic ground states and localized excitations of correlated insulators, e.g. Frenkel-type excitons, are best described from a local cluster perspective including the full Coulomb interactions and multielectronic configurations at the transition metal site, for which the starting point is essentially atomic physics. Several of the examples of this chapter are tailored toward deriving the multiplet excitations of Ni^{2+} compounds discussed in following chapters.

This section is drawn from Ref. [109] for the electronic structure of atoms, Refs. [15, 60, 110] for crystal field and spin-orbit coupling effects, and the treatment in Refs. [15, 111] for the electronic structure of Mott-Hubbard and charge-transfer insulators.

2.1 Electron-electron interactions in free atoms

The origin of electronic interactions in free atoms is closely related to the indistinguishability of electrons and the Pauli exclusion principle. We consider the Hamiltonian of a free atom neglecting spin orbit coupling,

$$H = -\frac{\hbar^2}{2m}\sum_i \nabla_i^2 - \sum_i \frac{e^2 Z}{r_i} + e^2 \sum_{i>j} \frac{1}{r_{ij}} := H_0 + V + H_{ee} \tag{2.1}$$

For atomic number Z, electron charge $|e|$, $r_i = |\mathbf{r}_i|$ and $r_{ij} = |\mathbf{r}_i - \mathbf{r}_j|$. We consider the one-electron problem with $H_{ee} = 0$ solved, with hydrogenic single-particle spin-orbital wavefunction solutions

$$|n, l, m_l, s, m_s\rangle = R_{n,l}(r)\ Y_l^{m_l}(\vartheta, \varphi)\ \sigma_{m_s}$$

where $R_{n,l}$ are the radial wavefunctions and $Y_l^{m_l}$ are the spherical harmonics. A basis for multielectron atoms are the product wavefunctions, such as,

$$\Psi = \prod_i \psi_i(r_i)$$

where i represents a given set of full quantum numbers $|n, l, m_l, m_s\rangle$. However, by Pauli's exclusion principle, the overall wavefunction must be antisymmetric with respect to interchange of any two electrons. This can be achieved by recasting the product wavefunctions into Slater determinants, which for two electrons in orthonormalized form is,

$$\Psi = (2!)^{-1/2} \begin{vmatrix} \psi_1(r_1) & \psi_1(r_2) \\ \psi_2(r_1) & \psi_2(r_2) \end{vmatrix} = \frac{1}{\sqrt{2}} \left(\psi_1(r_1)\psi_2(r_2) - \psi_1(r_2)\psi_2(r_1)\right) \tag{2.2}$$

Thus, if the spin-orbitals ψ_1/ψ_2 are the same, then the overall wavefunction is zero. An important consequence of Pauli's exclusion principle is a partial positional correlation of electrons with the same spin. Electrons of the same spin on average must occupy different orbitals and therefore, on average, are positionally anticorrelated compared to electrons of opposite spin. When accounting for this effect with the electron-electron interaction H_{ee}, this describes the stability of spin triplet vs. singlet multielectronic configurations (multiplets).

In practice, the spin-orbital wavefunctions are not of the form $|n, l, m_l, m_s\rangle$ for multielectronic systems, but rather one recouples the angular momentum into a total angular momentum basis before constructing an antisymmetric wavefunction. This gives multielectronic states of definite total $\mathbf{J}$ or, in the absence of spin orbit coupling, total $\mathbf{J}/\mathbf{L}/\mathbf{S}$ separately which diagonalize H with H_{ee} included. In the latter situation, called LS or Russell-Saunders coupling, the recoupled states are labeled by term symbols ${}^{2S+1}L_J$. As an example, for a simple configuration of inequivalent electrons $1s^1 2s^1$, one may consider the multielectronic spin singlet and triplet terms ${}^1S$ and ${}^3S$, respectively.

We first consider the matrix elements with the Coulomb interaction for the ${}^1S$ and ${}^3S$

states of the $1s^1 2s^1$ configuration, $\langle {}^{1/3}S|H_{ee}|{}^{1/3}S\rangle$. It can be shown that,

$$\langle {}^1S|H_{ee}|{}^1S\rangle = \langle(1s)(2s)|H_{ee}|(1s)(2s)\rangle + \langle(1s)(2s)|H_{ee}|(2s)(1s)\rangle := F^0(1s,2s) + G^0(1s,2s)$$
$$\langle {}^3S|H_{ee}|{}^3S\rangle = \langle(1s)(2s)|H_{ee}|(1s)(2s)\rangle - \langle(1s)(2s)|H_{ee}|(2s)(1s)\rangle := F^0(1s,2s) - G^0(1s,2s)$$

where $|ij\rangle = |\phi(r_1)\phi(r_2)\rangle$ are ordered for the spatial variables of the two electrons, as shorthand. The angular integrals in this case are trivial, while in the general case the radial integrals require numerical calculation. Namely, the triplet term is relatively stabilized by $-2G^0(1s,2s)$ which is the (spherically symmetric) Coulomb exchange integral and corresponds to an exchange of the two electrons within the two orbital states $1s/2s$. Meanwhile, $F^0(1s,2s)$ is the (spherically symmetric) direct integral. For higher momentum states, there are additional multipolar terms for the exchange interaction termed the direct and exchange Slater integrals, which are defined from the radial integrals,

$$F^k(i,j) = \int_0^\infty \int_0^\infty \frac{2r_<^k}{r_>^{k+1}} \big|R_i(r_1)\big|^2 \big|R_j(r_2)\big|^2 dr_1 dr_2 \tag{2.3}$$

$$G^k(i,j) = \int_0^\infty \int_0^\infty \frac{2r_<^k}{r_>^{k+1}} R_i^*(r_1) R_j^*(r_2) R_j(r_1) R_i(r_2) dr_1 dr_2 \tag{2.4}$$

where indices i include quantum numbers n_i and l_i for the appropriate radial functions, and $r_>$ ($r_<$) refers to the greater (lesser) of r_1/r_2. For equivalent electrons $F^k(i,j) = G^k(i,j)$ by definition. The radial functions and values of the Slater integrals need to be evaluated numerically, typically with Hartree-Fock methods, but are useful to parameterize the energy of different multiplets. The maximum order for the Slater integrals for angular momenta l_i/l_j is $k = 0, 2, ..., 2 \times \min(l_i, l_j)$ for F^k and $k = |l_i - l_j|, |l_i - l_j| + 2, ..., l_i + l_j$ for G^k, which are restricted by the angular integrals of the corresponding matrix elements with H_{ee}.

Here, we are primarily concerned with equivalent electrons in partially filled shells d^N for $1 \le N \le 9$. We take as a working example the case of d^8 which is the most relevant for the case of Ni^{2+} ions considered in this thesis (Chapter 8). In the atomic limit, the possible multielectronic terms range from $L = 0, 1, 2, 3, 4$ and $S = 0, 1$, yielding ${}^1S$, ${}^3S$, ${}^1P$, ${}^3P$, ${}^1D$, ${}^3D$, ${}^1F$, ${}^3F$, ${}^1G$, ${}^3G$. However, not all of these terms are consistent with Pauli principle and the requirement for an antisymmetrized wavefunction forbids states with $L + S = 2n$ for $n \in \mathbf{Z}$. Thus, the allowed LS terms for d^8 are,

$${}^1S,\ {}^3P,\ {}^1D,\ {}^3F,\ {}^1G$$

Wavefunctions for these terms may be derived by construction using Clebsch-Gordon summations over the two-electron product wavefunctions to transform to a basis $|L, S, J, M_J\rangle$, which we do not elaborate here. Importantly, the energies of the d^8 multiplet terms can be easily calculated by the following relation,

$$\langle \psi_{L,S}^{J,M_J} | H_{ee} | \psi_{L,S}^{J,M_J} \rangle = \sum_k \left[f_k F^k(i,j) + g_k G^k(i,j) \right] \tag{2.5}$$

valid for two-electron wavefunctions in LS coupling $\psi_{L,S}^{J,M_J}$, where the coefficients f_k/g_k are given by,

$$f_k = (-1)^L (2l_i+1)(2l_j+1) \begin{pmatrix} l_i & k & l_i \\ 0 & 0 & 0 \end{pmatrix} \begin{pmatrix} l_j & k & l_j \\ 0 & 0 & 0 \end{pmatrix} \begin{Bmatrix} l_i & l_j & L \\ l_j & l_i & k \end{Bmatrix}$$
$$g_k = (-1)^S (2l_i+1)(2l_j+1) \begin{pmatrix} l_i & k & l_j \\ 0 & 0 & 0 \end{pmatrix}^2 \begin{Bmatrix} l_i & l_j & L \\ l_i & l_j & k \end{Bmatrix}$$

where $(...)/\{...\}$ are the Wigner 3-j/6-j symbols. Substituting $l_i = l_j = 0$ and $S = 0/1$ for the example of ${}^1S/{}^3S$ splitting reproduces the results from above. For the d^8 configuration, the ground and first excited state configurations and their energies in terms of F^k are,

$$E({}^3F) = F^0(dd) - \frac{8}{49}F^2(dd) - \frac{1}{49}F^4(dd)$$
$$E({}^1D) = F^0(dd) - \frac{3}{49}F^2(dd) + \frac{1}{441}F^4(dd)$$

Note that the ground state ${}^3F$ term is the one predicted from the empirical Hund's rules. That is, the ground state is the term of highest spin ($S = 1$) and among those (${}^3P/{}^3F$), the one with the highest L is the ground state.

Towards the present discussion, it is also useful to calculate the configuration-average energy of the d levels, which can be calculated by summing Eq. 2.5 over all possible terms,

$$E_{\text{ave}}(dd) = F^0(dd) - \frac{2}{63}F^2(dd) - \frac{2}{63}F^4(dd) \tag{2.6}$$

We note that this is a general relation for d shells (not just d^8), and the $F^k(dd)$ parameters will depend on n. Other important configurations are of the type $2p^5 3d^{N+1}$, which are the intermediate states of $2p \rightarrow 3d$ core hole excitation by resonant X-rays (Chapter 4). Therefore, we also report the configuration average energy,

$$E_{\text{ave}}(pd) = F^0(pd) - \frac{1}{15}G^1(pd) - \frac{1}{70}G^3(pd) \tag{2.7}$$

These are important quantities, as they define the central energy of the different respective configurations, which serve as the definitions for the on-site Coulomb energies $U_{dd} = E_{\text{ave}}(dd)$ and $U_{pd} = E_{\text{ave}}(pd)$. These quantities enter into matrices for configuration interactions, as well as estimates of on-site U values in the ground states.

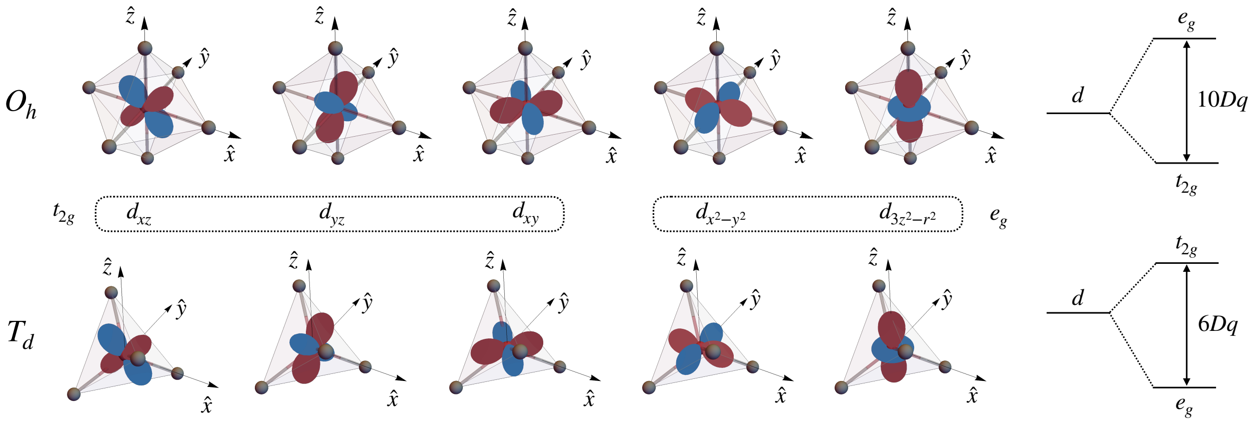

Figure 2.1: Real projections of the d orbitals of t_{2g} and e_g symmetry for O_h (top) and T_d (bottom) coordinations, with single-particle energy diagrams for each configuration.

2.2 Crystal field

Having discussed the origin of multielectronic interactions and multiplet splitting in the atomic limit, we now discuss how interactions with other atoms of the crystal effect the electronic structure.

For this discussion, we will consider a common situation involving a $3d$ transition metal forming a crystal with surrounding ligands (e.g. chalcogen, halogen, pnictogen, etc.) which bond to the $3d$ states through valence p-orbitals. For the d-orbital set with angular momentum $l = 2$, there are total of 5 orbital states. In the free atom, the angular part of the electronic wavefunctions are typically represented by the spherical harmonics, consistent with the spherical symmetry of the atomic site, or as $Y_l^m(\vartheta, \varphi)$. When atoms form crystals, the symmetry of the local electric environment is reduced.

The symmetry of the electrostatic environment of the transition metal ion depends on the local arrangement of atoms to which it is bonded, which is determined by the coordination number and the point group symmetry of the crystal. The high symmetry configurations typically encountered are octahedral (point group O_h) and tetrahedral (point group T_d), with ligand coordinations of 6 and 4, respectively, shown in Fig. 2.1. These are the situations for $\mathrm{NiI_2}$ and FeSe, respectively, as discussed in subsequent chapters. The important effect of these interactions with the ligands is a breaking of degeneracy of the d orbital levels, which correspondingly changes the many-body ground state.

In O_h and T_d symmetry, the d-orbitals are split into two sets named t_{2g} and e_g. These labels refer to rotational symmetry properties in the O_h/T_d point groups, as can be looked up in character tables [112]. They have degeneracy of 3 and 2, respectively. Most commonly, the e_g and t_{2g} orbitals are expressed in terms of cubic harmonics, which are real projections of the spherical harmonics with the correct rotational symmetry properties for O_h/T_d symmetry.

They are, respectively:

$$|3d_{3z^2-r^2}\rangle = Y_2^0 \tag{2.8}$$

$$|3d_{x^2-y^2}\rangle = \frac{1}{\sqrt{2}}\left(Y_2^2 + Y_2^{-2}\right) \tag{2.9}$$

$$|3d_{xy}\rangle = \frac{-i}{\sqrt{2}}\left(Y_2^2 - Y_2^{-2}\right) \tag{2.10}$$

$$|3d_{xz}\rangle = \frac{-1}{\sqrt{2}}\left(Y_2^1 - Y_2^{-1}\right) \tag{2.11}$$

$$|3d_{yz}\rangle = \frac{i}{\sqrt{2}}\left(Y_2^1 + Y_2^{-1}\right) \tag{2.12}$$

Within this cubic harmonic representation, the splitting of the single-particle $3d$ orbitals in O_h symmetry is intuitive. The e_g doublet $\{|3d_{3z^2-r^2}\rangle, |3d_{x^2-y^2}\rangle\}$ has lobes that point towards the surrounding ligands, while the t_{2g} triplet $\{|3d_{xy}\rangle, |3d_{xz}\rangle, |3d_{yz}\rangle\}$ has lobes that point towards the interstitial regions between the ligands (Fig. 2.1). Thus, the latter experience less direct ionic repulsion and are lower in energy. In O_h symmetry, the energetic splitting is defined as $E(e_g) - E(t_{2g}) := 10Dq > 0$, with e_g orbitals at higher energy[1]. $10Dq$ is typically around 1-2 eV, depending on the transition-metal and the ligand states. For tetrahedral coordination, the energetic sequence is reversed with $E(t_{2g}) > E(e_g)$, with a splitting of $6Dq$.

Mathematically, these functions diagonalize the crystal field Hamiltonian, H_{CF}. For more complex symmetry, it is useful to express the crystal field as a potential expanded in spherical tensors, e.g. functions with the same angular momentum transformation properties of the spherical harmonics. The orbital wavefunctions in reduced symmetry diagonalizing H_{CF} are far less intuitive compared to O_h symmetry, and must be determined numerically. One may expand

$$H_{\mathrm{CF}} = \sum_{k,q} A_k^q C_k^q \tag{2.13}$$

where A_k^q are coefficients and $C_k^q = \sqrt{\frac{4\pi}{2k+1}} Y_k^q$ are renormalized spherical harmonics. The tensor acts on the orbital part of the wavefunction, and considering a basis of d orbitals ($l = 2$), the maximal order is $k = 4$ for C_k^q. Restrictions on the expansion coefficients are determined by applying the symmetry elements of the point group $\mathcal{P}$, such that $g \circ H_{\mathrm{CF}} = H_{\mathrm{CF}}$ for all $g \in \mathcal{P}$. The result for O_h symmetry is

$$H_{\mathrm{CF}}(O_h) = \alpha \left[C_4^0 + \sqrt{\frac{5}{14}}\left(C_4^4 + C_4^{-4}\right) \right] \tag{2.14}$$

In general, α should be a function of the radial coordinate, but in practice this is ignored

---

[1] This terminology is mainly for historical reasons, based on formulae from early point charge models. In real materials, point charge models are rarely accurate estimations even for relatively simple materials.

and α may be treated as an empirical parameter. We can connect this to the energy splitting ($10Dq$) of the e_g/t_{2g} states by checking the matrix elements, e.g.:

$$\langle d_{x^2-y^2}|H_{\mathrm{CF}}(O_h)|d_{x^2-y^2}\rangle = \frac{11\alpha}{42} \tag{2.15}$$

$$\langle d_{xy}|H_{\mathrm{CF}}(O_h)|d_{xy}\rangle = \frac{-3\alpha}{14} \tag{2.16}$$

which are easily calculated from the Wigner-Eckart theorem and from which we may deduce $\alpha = \frac{21}{10} * 10Dq$. The result for D_{3d} symmetry on a basis of d orbitals, relevant for trigonally-distorted octahedral coordinations is,

$$H_{\mathrm{CF}}(D_{3d}) = \alpha C_2^0 + \beta\left(C_3^3 - C_3^{-3}\right) + \gamma C_4^0 + \delta\left(C_4^3 + C_4^{-3}\right) \tag{2.17}$$

valid for a quantization axis along the (111) direction with 3-fold rotational symmetry of the local octahedron, with $\alpha, \beta, \gamma, \delta$ being independent parameters. This crystal field potential is relevant for the $R\bar{3}m$ lattice symmetry of $\mathrm{NiI_2}$, which we consider in Chapter 8. Such trigonal crystal field distortions are important for magnetic anisotropy (Chapter 3). Parameterizations in terms of orbital energy levels and splittings can be easily built as desired by considering the analogs to matrix elements for O_h symmetry above, keeping in mind the definition of the quantization axis used to derive the symmetrized potential (typically, the axis of highest rotational symmetry).

The successful part of crystal field theory is in modeling the local symmetry of the potential properly. The crystal field potential has a symmetry that aligns with the site symmetry point group of the atom of interest. This must be a subgroup of the point group of the material. It is common to discuss the local atomic structure in terms of "approximate" octahedral or tetrahedral symmetry as a first-order approximation, however lower-symmetry distortions are expected if predicted by the site group symmetry, which can be determined by crystallography. The energy range of these lower-symmetry crystal field contributions can be on the same order (or larger) than perturbation from spin-orbit coupling in $3d$ transition metal compounds.

Many efforts to justify different quantitative interpretations of the coefficients A_k^q and microscopic origin of the potential H_{CF} have been put forward, including purely electrostatic and covalency models, but none are fully quantitative. Good estimations for the combination of these effects can be derived from maximally-localized Wannier functions in DFT, which capture well the bond covalency [113]. In effect, the expansion coefficients are to be understood as symmetry-restricted parameters that are fit to experimental data. Through the systematic study of many transition-metal and rare-earth complexes, empirical trends in the values of these parameters have been established, referred to as the spectrochemical series [60].

The most critical part is that adding the crystal field Hamiltonian to the multielectron Hamiltonian considered in the previous section changes the wavefunction of the many-body

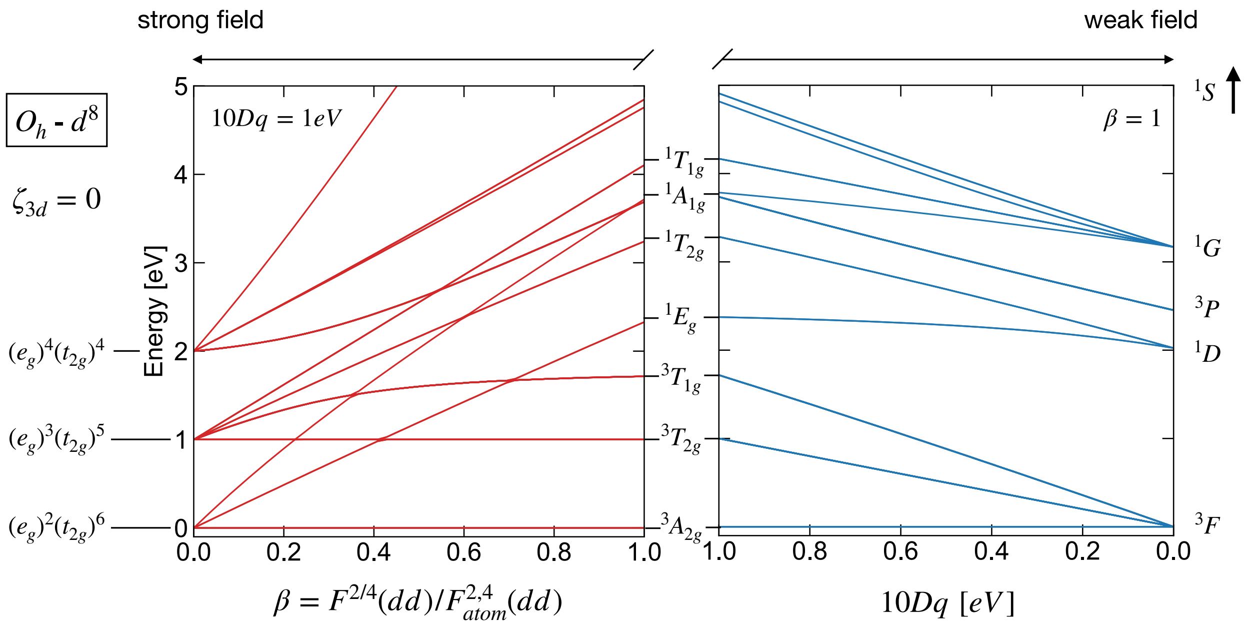

Figure 2.2: Multiplet splitting in the strong and weak field limit for the d^8 configuration in O_h symmetry crystal field.

ground state. We will consider our working example of d^8 configurations and restrict to O_h symmetry. The symmetry of the orbital wavefunction changes to reflect rotational symmetry properties of the crystal field. To understand how, one can determine the character of the angular momentum state in the $SO(3)$ group for the free atom and decompose it into the irreducible representations of the site-symmetry group of the transition metal in the crystal. Looking at the ground state term ^3F for d^8, one finds that the F angular momentum term splits to T_2, T_1, A_2 irreps. of O_h. Thus, provided that the underlying single-electron momenta $l = 2$ have even parity, we will have a splitting of the ground state into three triplets, $^3A_{2g}/^3T_{2g}/^3T_{1g}$.

Depending on the strength of the crystal field relative to the multiplet (electron interaction) effects, the wavefunctions will interpolate between (i) the weak field limit where LS coupling holds and crystal fields are a perturbation and (ii) the strong field limit, where the wavefunctions are better approximated in a basis of orbital occupations (e.g. $(t_{2g})^n(e_g)^m$). In practice, one works in an intermediate case and the orbital occupations are non-integral due to multiplet or spin-orbit coupling effects, which mix different terms. Here we consider the strong field limit to discuss some key interactions.

The ground and first excited state of a d^8 ion in an octahedral crystal field are the $^3A_{2g}$ and the $^3T_{2g}$ terms, respectively. As we saw, in the weak field limit, these states are derived from the same ^3F ground state term, while in the strong field limit, they are respectively stabilized from the $(t_{2g})^6(e_g)^2$ and $(t_{2g})^5(e_g)^3$ orbital configurations (Fig. 2.2). Thus, intuitively, the $^3A_{2g}$ term is the ground state because it minimizes the crystal field energy by filling the lower energy t_{2g} state completely, resulting in a half filled e_g state. One component of the respective wavefunctions written in the orbital basis are,

$$\Psi(^3A_{2g}) = |(x^2-y^2)^+(3z^2-r^2)^+|, \quad \Psi(^3T_{2g}) = |(xy)^+(3z^2-r^2)^+| \tag{2.18}$$

where superscripts label $m_s \in \{+,-\}$ and $|\cdots|$ is shorthand for antisymmetrization in Eq. 2.2. These wavefunctions are checked based on their transformation properties under O_h symmetry operations and comparison to character tables. The contribution of the crystal field energy to these terms with respect to the center of the configuration is $-12Dq/{-2Dq}$ (each e_g hole has energy of $-6Dq$ and each t_{2g} hole has energy of $+4Dq$). Meanwhile, it can be shown that the interaction energy for both terms is the same,

$$\langle\Psi|H_{ee}|\Psi\rangle = F^0(dd) - 8F^2(dd) - 9F^4(dd)$$

Thus, the energy difference of the two terms is only determined by the octahedral energy splitting, $10Dq$. Excitations of the form $^3A_{2g} \to {}^3T_{2g}$ can be locally excited and measured by photon probes. Such an excitation is referred to as a (spin-allowed) $d \to d$, or ligand/crystal field, transition. The energies of these excitations determine the optical absorption properties of transition metal complexes and also appear as low-energy excitations of insulating solid state materials with large band gaps. In our case, we will also refer to this special case of transition as an *inter-configurational multiplet*, referring to a transition (either spin allowed or spin forbidden) between the $t_{2g}^6 e_g^2$ and $t_{2g}^5 e_g^3$ configurations.

Additional important multiplets considered here are the *intra-configurational multiplets* which preserve the $t_{2g}^6 e_g^2$ ground state filling. To figure out which terms are allowed, we can consider the decomposition of two e_g holes into irreps. of O_h,

$$E_g \times E_g \to A_{2g} + A_{1g} + E_g$$

While the A_{2g} is a triplet term (the ground state), the E_g/A_{1g} are singlet terms which derive from the $^1D/^1G$ LS coupled terms in the weak field limit, respectively. We may write down their wavefunctions using the strong field basis as,

$$\Psi(^1A_{1g}) = \frac{1}{\sqrt{2}}\left(|(3z^2-r^2)^+(3z^2-r^2)^-| + |(x^2-y^2)^+(x^2-y^2)^-|\right) \tag{2.19}$$

$$\Psi(^1E_g) = \frac{1}{\sqrt{2}}\left(|(3z^2-r^2)^+(3z^2-r^2)^-| - |(x^2-y^2)^+(x^2-y^2)^-|\right) \tag{2.20}$$

and compute their energies with the Coulomb interaction Hamiltonian, parameterized by Slater integrals,

$$\begin{aligned} \langle\Psi(^1A_{1g})|H_{ee}|\Psi(^1A_{1g})\rangle &= F^0(dd) + \frac{8}{49}F^2(dd) + \frac{51}{441}F^4(dd) \\ \langle\Psi(^1E_g)|H_{ee}|\Psi(^1E_g)\rangle &= F^0(dd) + \frac{21}{441}F^4(dd) \end{aligned}$$

Critically, since the electron filling is the same, the $^3A_{2g}/^1A_{1g}/^1E_g$ multiplets have the same contribution from the crystal field and are stabilized by a common factor of $-12Dq$, and the difference in the energy within this set is given purely by the multiplet effects. Excitations of the type $^3A_{2g} \rightarrow {}^1E_g/^1A_{1g}$ can also occur optically, but they are further reduced in cross section because they are spin-forbidden (triplet to singlet excitations). We discuss optical selection rules in Chapter 3 and provide an extended overview of the manifestation of these spin-forbidden excitations in experiments in Chapter 8.

2.3 Spin-orbit coupling

Spin-orbit coupling (SOC) is critical for rare-earth systems, but is typically a perturbation for the spectra of light transition metal compounds, which we consider here. This marks the distinction between LS, or Russell-Saunders, coupling and jj coupling. In the former, many-body states may be labeled with L,S as good quantum numbers, whereas only total J remains after including SOC. In the jj coupling scheme, it is more convenient to first couple each electron in a basis of total j for each electron, then couple the single-electron j into a multielectron total J state.

The spin-orbit coupling Hamiltonian is,

$$H_{\mathrm{SO}} = \sum_i \zeta_i \mathbf{l}_i \cdot \mathbf{s}_i \tag{2.21}$$

which describes a coupling between single electron orbital ($\mathbf{l}_i$) and spin ($\mathbf{s}_i$) moments, where ζ_i is the SOC magnitude. SOC originates as a relativistic effect and it is well known that the magnitude of SOC scales with atomic number Z (approximately Z^4 for a hydrogenic model). For $3d$ transition metals, ζ_i is $\mathcal{O}(10\text{ meV})$, and may safely be treated as a perturbation to LS or crystal-field coupled states. This contribution will split LS terms into substructure based on total J (e.g. $^3P \rightarrow {}^3P_0/^3P_1/^3P_2$), and can mix components from different LS terms with the same J. The effect of weak SOC is most important for solids with partially filled t_{2g} shells and Jahn-Teller active ions, where SOC on this order can compete with lower symmetry crystal fields and impact the ground state. Higher energy multiplets will acquire a fine-structure, which impacts the level structure as measured in optical absorption.

One situation of relevance for this thesis where SOC cannot be ignored is the core levels which form the initial states for resonant X-ray spectroscopy (Chapter 4). These states are at very large binding energy and experience much larger spin-orbit coupling than the valence shell, since core-levels experience a higher unscreened effective nuclear charge, have higher kinetic energy and thus are more relativistic. For specific relevance here, we consider excitations of the type $2p^63d^n \rightarrow 2p^53d^{n+1}$, which define the principle $L_{2,3}$ edges. Starting with $n = 9$, the final state has a closed d shell and we may consider only a single hole in the $2p$ levels. This can be treated very simply by coupling the $2p$ levels into a total J basis. Only $J = \frac{1}{2}, \frac{3}{2}$ are possible, leading to a basis $2p^{m_J}_{1/2}$ and $2p^{m_J}_{3/2}$. Looking to the matrix elements with H_{SO}, we have[2]

$$\langle 2p_{1/2}|H_{\mathrm{SO}}|2p_{1/2}\rangle = -\zeta_{2p}, \quad \langle 2p_{3/2}|H_{\mathrm{SO}}|2p_{3/2}\rangle = \frac{\zeta_{2p}}{2} \tag{2.22}$$

For 3d transition metals, the value of the core level SOC ζ_{2p} is $\mathcal{O}(10\text{ eV})$, which defines the $L_{2/3}$ edge splitting, discussed more below.

For the example of $n = 9$, the states can be effectively treated on a single particle basis. However, in a more general case, the intermediate state $2p^5 3d^{n+1}$ state will not have a closed d shell. To describe the structure of $L_{2/3}$ edges, it is critical to include multiplet coupling between the $2p$ hole with the valence $3d$ shell, parametrized by the Slater exchange integrals $G^1(pd)/G^3(pd)$. The intermediate state multiplet splitting in the $3d$ transtion metals is lower than the core-hole spin orbit coupling, but can be on the same order of magnitude. This multiplet coupling of the $2p$ core hole and the valence $3d$ shell dominates the absorption structure, leading to a major failure of single-electron descriptions for $L_{2,3}$-edge absorption spectra [110].

Finally, we note that SOC is critical for the magnetic anisotropy (single-ion and two-site anisotropy) and theory of spin-induced ferroelectricity, discussed in Chapter 3, and is thus critical for the multiferroic properties of $\mathrm{NiI_2}$. While SOC of the transition metal site is an important mechanism for t_{2g} systems (early transition metals), e_g orbital systems do no have a first order effect of SOC. This is because the isolated t_{2g} shell can be mapped to the properties of an effective $\tilde{l} = 1$ orbital angular momentum, and the splitting of the d orbital follows exactly the case of an $l = 1$ (p shell) as derived above, occurring at first order in ζ. Meanwhile, the effect of ζ of the e_g space occurs only at second order. However, significant SOC effects can also be introduced through the ligand states, which bond primarily with p orbitals. In the case of $\mathrm{NiI_2}$ and other transition-metal halides, the SOC of the heavy ligand sites (e.g. Br, I) are the primary origin of SOC-induced phenomena.

2.4 Electronic structure of correlated insulators

We now consider how the effect of correlated d orbitals can be integrated into the description of the electronic structure of solid state materials. For describing band structure of relatively localized systems, one typically starts with a tight binding model, considering a local atomic basis where electrons can hop between different sites $i \to j$, which can be written as,

$$H_{\mathrm{tb}} = -\sum_{i\neq j,\sigma} t_{ij} c^\dagger_{j,\sigma} c_{i,\sigma} \tag{2.23}$$

where t_{ij} is the hopping parameter between sites i, j, $c^\dagger_i/c_i$ are the creation/annihilation operators at site i and σ is the spin index. The hopping parameter is usually defined by the

---

[2] Wavefunctions can be easily constructed with a Clebsch-Gordon summation on a basis of $l = 1$, $s = 1/2$.

distance (e.g. first/second neighbors characteristic of different index pairs $\langle i, j \rangle$) and is in general orbital dependent.

It is well known that for an odd number of electrons per site within the tight binding model, the system is always metallic since there will be a band that is not fully occupied. For an even number of electrons, uncorrelated materials can be insulators, which are referred to as *band insulators*. However, many strongly-correlated materials, regardless of electron filling, are observed to be insulators. What is missing in the description of the bare tight-binding model is the tendency of electrons to become localized due to the energetic cost of electron addition to an occupied site of correlated electronic levels. That is, the processes of electron transfer between two sites, $d_i^n d_j^n \rightarrow d_i^{n-1} d_j^{n+1}$ will carry an energetic cost, which is defined as $U (= U_{dd})$. This can be incorporated by including an additional term proportional to the site occupations,

$$H = H_{\mathrm{tb}} + U \sum_i n_{i,\uparrow} n_{i,\downarrow} \tag{2.24}$$

where n are number operators. This Hamiltonian represents the Hubbard model. For a half-filled band, there will be a cross-over from metallic to insulating behavior, determined by the ratio U/t. For $U/t \gg 1$, the electrons will be effectively localized to a single site and double occupancy will be quenched. In the opposite limit, the bandwidth provided by sufficiently large t is sufficient to overcome this energetic cost and metallicity is restored in the limit $U/t \ll 1$. This is the simplest model to describe *Mott insulators*, which are defined by insulating conductivity gap directly due to the presence of correlated electrons. The Mott insulating ground state is characterized by strong antiferromagnetic spin exchange between neighboring sites, which will be discussed in the next chapter.

Charge delocalization does not only occur by hopping directly between d levels in the process described above. There also exist ligand atoms, which hybridize with the d levels, allowing another mechanism for delocalization. The typical situation is (a) correlated, small bandwidth d levels, (b) itinerant bands of ligand p states and (c) ligand-p to metal-d charge transfer/hybridization processes. The nature of the lowest energy charge excitations depends on the relative energy of direct hopping processes of the type $d^n d^n \rightarrow d^{n-1} d^{n+1}$, set by a Hubbard-like U term, and those of the type $d^n p^6 \rightarrow d^{n+1} p^5$, which is set by the charge-transfer energy Δ. Charge transfer between metal and ligand sites are critical to give a proper account of the effects of covalency, and the lowest energy charge excitations determine the magnitude and mechanism of the leading-order magnetic exchange interactions, the crystal field magnitude, and also the energy scale of multiplet effects in the solid state as we discuss extensively in Chapter 8.

We first detail the definition of the energy gap and the parameters Δ and U_{dd}. For U_{dd} one can take average correlation energy between d electrons, which is given by the configuration average Coulomb energy on the d-shell derived above $(F^0 - 2/63(F^2 + F^4))$. Note that the Slater integrals are heavily screened in the solid state compared to bare atomic values, with the reduction being strongest for the lowest order multipoles (e.g. F^0) and much weaker for higher multipoles (F^2, F^4) [110, 113]. The average correlation energy for a d^n configuration

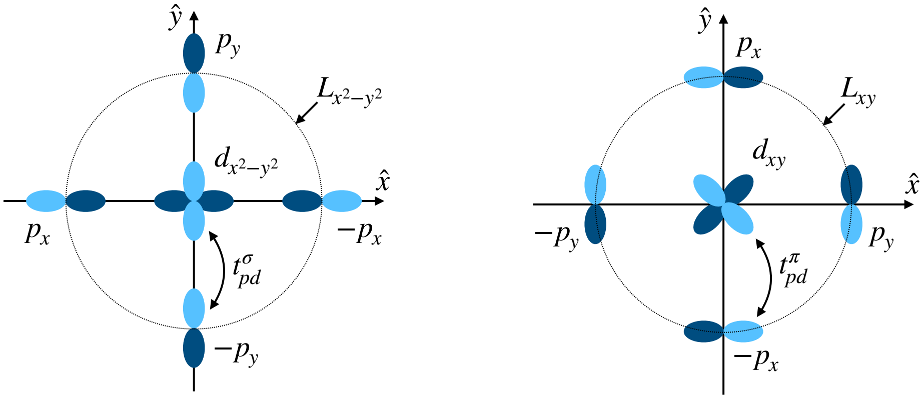

Figure 2.3: Molecular orbitals in O_h symmetry for $d_{x^2-y^2}$ (left) and d_{xy} (right) orbitals. Indicated are the hopping integrals t^{σ}_{pd} and t^{π}_{pd}. Linear combinations of the four $p_{x/y}$ orbitals constitute the symmetrized ligand orbitals $L_{x^2-y^2}$ and L_{xy}, respectively.

is $(U_{dd}/2)(n)(n-1)$. Further, one defines the average single particle energy levels of the d electrons ϵ_d and of the ligand states ϵ_p. In the single particle limit, the charge transfer gap is exactly what one expects, $\Delta = \epsilon_d - \epsilon_p$. However, in the general case one has to include the correlation effects. The interplay of d-shell correlations, charge transfer energy and on-site (single-particle) energies are defined by the energy between different configurations, denoted $d^n\underline{L}^m$ where $\underline{L}$ refers to a ligand hole states. By convention, the energy difference $d^n\underline{L}^0 \to d^{n+1}\underline{L}^1$ is Δ, and the next configuration $d^{n+2}\underline{L}^2$ has an additional excitation energy of $\Delta + U_{dd}$. In this case, one can derive that $\Delta(d^n) = \epsilon_d - \epsilon_p + nU_{dd}$. Note that it is important to include full multiplet coupling and configuration interactions within and among the configurations $d^n/d^n\underline{L}^1/d^n\underline{L}^2$/etc. The current treatment ignores the possible effects of correlations on the ligand p orbitals (e.g. $F^k(Lp, Lp)$), instead treating them as essentially fully covalent single particle bands, as well as the Coulomb interactions between the metal d and ligand p states (e.g. $F^k(Lp, 3d)/G^k(Lp, 3d)$)

The relative energy of U_{dd} and Δ sets the dominant low-energy delocalization processes. For simplicity we consider the case where the hopping is small $t \ll U_{dd}, \Delta$. In the case that $\Delta \gg U_{dd}$, the energy gap is determined in terms of the $d \to d$ hopping, through parameters t_{dd} and U_{dd} as in the Hubbard model and ligand-to-metal charge transfer is quenched. In the opposite limit, one may still observe a finite band gap, which is instead proportional to Δ with hopping amplitude given by t_{pd}. The former is called Mott-Hubbard insulator, while the latter is termed a charge transfer insulator. The general classification was first developed by Zaanen, Sawatsky and Allen and is known as the ZSA scheme [111]. As a general trend, early transition metal compounds in the common ionic valences are closer to the Mott-Hubbard regime (Ti^{3+}, V^{3+}, Cr^{3+}) and late transition metal compounds are closer to charge transfer insulators (Ni^{2+}, Cu^{2+}). The charge transfer gap also depends strongly on the covalency/electronegativity of the ligands and generally decreases as one goes down the periodic table.

Finally, we discuss the magnitude of the hopping terms in charge transfer insulators. There are two high-symmetry configurations where the two-site overlap integral between metal d and ligand p orbitals are non-zero. These are depicted in Fig. 2.3 for the case of the $d_{x^2-y^2}$ and d_{xy} orbitals in the xy plane. In the first case, the $d_{x^2-y^2}$ will have non-zero overlap with p_x/p_y orbitals on surrounding ligand sites with lobes that point toward each other, oriented along the nearest neighbor M-L bond (M metal, L, ligand). This type of d-p overlap is called σ-bonding and is given a hopping integral t^{σ}_{pd}. In the other case, the relevant ligand orbitals with non-zero overlap with the d_{xy} state instead have lobes perpendicular to the M-L bond, called π-bonding and with transfer integral t^{π}_{pd}. For a fixed M-L distance, $t^{\sigma}_{pd} > t^{\pi}_{pd}$ (with a typical ratio $t^{\sigma}_{pd}/t^{\pi}_{pd} \sim$ 1.5-2.0). These hopping integrals can be parametrized by the Slater-Koster parameters.

The e_g/t_{2g} orbitals in O_h symmetry are precisely those which hybridize with the ligand p states through σ/π bonding, respectively. From this, the total basis of surrounding $3\times 6 = 18$ ligand p orbitals derived from the 6 ligand sites constituting the ML_6 octahedral clusters can be restricted only to those linear combinations which match the symmetry of the d orbital states. Thus, for each d orbital (e.g. x^2-y^2) there will be a corresponding linear combination of surrounding p orbitals transforming by the same symmetry (denoted $L_{x^2-y^2}$), along with a well defined transfer integral between them (t^{σ}_{pd}). These linear combinations are known as molecular orbitals, and are useful for local cluster calculations with full Coulomb interactions, with the inclusion of configuration interactions of different occupation configurations of metal d and ligand p orbitals. Such a model is known as charge transfer multiplet theory [110, 113], which is used extensively in Chapter 8 to describe the excitation spectra of the nickel dihalide charge transfer insulators. This simplification is crucial because exact diagonalization of the fully interacting cluster becomes computationally unfeasible for large basis sets.

Chapter 3

Magnetic Order and Spin-Induced Ferroelectricity in Triangular-Lattice Systems

In this chapter, we review the origin of interatomic spin exchange interactions and the resulting magnetic ground states for the case of charge-transfer insulators, with a specific focus to triangular lattice systems. We also review the mechanisms of spin-induced ferroelectricity for spin-spiral systems.

3.1 Inter-atomic spin exchange

For correlated insulators, the interaction-driven localization of the d electrons leads to the presence of local atomic-like orbital states with a spin-orbital ground state determined by the multiplet coupling for the respective electronic configuration. This is determined by the intra-atomic Hund's exchange J_H, which can be regarded as an effective (ferromagnetic) spin-spin interaction for electrons on the same atomic site. Thus, electrons on the same atomic site with the same spin will have a lower average correlation energy (spherically averaged $U_{dd} - J_H$) compared to electrons of opposite spin (U_{dd}) [114, 115]. Ground states with maximal total spin are relatively stabilized by the Hund's coupling. Note that this terminology is only an approximation, and the full multiplet coupling with antisymmetrized wavefunctions needs to be taken into account [109].

In the case of Ni^{2+} ions in O_h crystal field, we found that the ground state is the ${}^3A_{2g}$ term, with $S = 1$ and no orbital moment. Thus, there is a local spin degree of freedom, but in the free atom in the absence of external spin interactions or an external magnetic field, the different spin projections $S_z \in \{-1, 0, 1\}$ remain degenerate. In solids, the degeneracy is broken by long-range spin exchange interactions with other atoms in the crystal, which we refer to as inter-atomic spin exchange J. This is typically written in terms of the Heisenberg

Hamiltonian,

$$H = -\sum_{i,j} J_{ij}\mathbf{S}_i \cdot \mathbf{S}_j \tag{3.1}$$

where here i, j refer to different transition metal sites with interacting pairs of local moments $\mathbf{S}_i/\mathbf{S}_j$, respectively. With this sign convention, $J_{ij} < 0$ corresponds to antiferromagnetic exchange.

The actual origin of inter-atomic and intra-atomic exchange in solid state materials are quite different. For the latter, it is directly related to Pauli exclusion and the wavefunction antisymmetrization, which stabilizes triplet pairing since there is a partial positional anti-correlation for the required antisymmetric orbital state. This interaction does not directly involve the spin degree of freedom, but results from the effect that symmetric/antisymmetric spin coupling has on the associated orbital state, and the interactions themselves are directly parameterized in the orbital degrees of freedom. In correlated insulators, the origin of inter-atomic spin exchange is instead due to orbital overlap and spin-dependent, Pauli-restricted hopping processes connecting the two sites and the spin degree of freedom is involved more explicitly. In contrast to a Hund's like exchange interaction, the sign of inter-atomic exchange of this type can be either ferromagnetic (FM) or anti-ferromagnetic (AFM), depending on details of the ground state electronic structure and the lattice geometry.

To solve to problem properly, one has to consider antisymmetrized wavefunctions on the basis of two or three-sites, but general arguments can be made using perturbation theory [15]. We first consider a situation of direct hopping between two half-filled d orbitals on neighboring atoms. The transfer integral is given by t_{dd} and in the insulating limit ($U_{dd} \gg t_{dd}$) the ground state corresponds to a single electron on each site. We can represent the minimal basis of ground state wavefunctions as $|\uparrow, \downarrow\rangle/|\uparrow, \uparrow\rangle$ referring to a single-electron spin on each site, representing AFM and FM coupling, respectively. We consider these excitations in the absence of hopping ($t = 0$) to have equal energies of E_0 while the double occupied states $|\uparrow\downarrow, 0\rangle/|0, \uparrow\downarrow\rangle$ have equal energies E_0+U_{dd}. Notably, hopping between the two sites are permitted for the AFM configuration, but Pauli forbidden for the FM configuration. When turning on finite coupling between the different sites, the energy of the AFM configuration is stabilized by a factor of $-2t_{dd}^2/U_{dd}$, as given from a second order perturbation.

This is the origin of an effective AFM exchange of $J = -2t_{dd}^2/U_{dd}$ as is the well known result for the single-orbital Hubbard model. This involves a direct kinetic exchange between two d orbitals. However, even for Mott-Hubbard insulators, where the lowest energy hopping processes are of direct dd type, the hopping processes are typically mediated by intermediate ligand states in a process known as superexchange due to long inter-metal distances [116, 117].[1] We highlight some of the main examples of superexchange relevant for the present cases below, which closely follows the treatment of Ref. [15].

---

[1] In $3d$ transition metals, direct dd exchange is more common for partially filled t_{2g} systems, e.g. early transition metals or high-spin states of Mn, Fe and Co. For e_g systems (late transition metals), these are closer to the charge-transfer insulator limit and magnetic interactions are almost solely due to superexchange [15].

We first consider the most simple case of a single-half filled $x^2 - y^2$ orbital at neighboring sites, which share common σ bonds with an intermediate ligand p orbital forming a linear (180 deg.) bond (Fig. 3.1). In this case, there are two different types of hopping processes resulting in the interchange of spins, both of which are only allowed with AFM alignment on the two d orbitals. The first involves a process that transfers the spin of TM-site 1 to the second TM-site from a two-step process through the common ligand p orbital. This intermediate state has an energy of U_{dd}, with the ligand interchange processes involving an energy scale of Δ and a hopping integral t_{pd}. This leads to the first effective AFM exchange term, $J \propto -2t_{pd}^4/(\Delta^2 U_{dd})$. A second process is possible where the spin exchange is mediated by an intermediate state involving one ligand electron being transferred to each TM-site, thus having an intermediate state with two-charge transfer processes and a double occupancy of ligand-holes. This state has energy $2\Delta + U_{pp}$ (where U_{pp} is isotropic correlation energy for the ligand p states). The overall exchange process through this intermediate state leads to an effective $J \propto -4t_{pd}^4/(\Delta^2(2\Delta + U_{pp}))$. Note that both processes are only allowed for AFM aligned TM sites. Thus, the perturbative estimate gives an overall AFM superexchange interaction for two transition metal sites of,

$$J(180^\circ) \simeq -\frac{2t_{pd}^4}{\Delta^2}\left(\frac{1}{U_{dd}} + \frac{2}{2\Delta + U_{pp}}\right)$$

which is a similar results to the one considering direct dd overlap in the single-orbital Hubbard model, although the processes mediating this exchange will depend on different energy scales (e.g. metal-ligand hopping t_{pd} and the charge-transfer energy Δ).

The superexchange model is also useful in describing the interactions for bond angles different than 180°. In particular, we show the expected FM exchange for 90° M-L-M bonds. We consider the same situation of two half-filled e_g orbitals at the TM sites, which form σ bonds with separate (orthogonal) p orbitals at the same ligand site [Fig. 3.1]. If the spins at the TM sites are AFM coupled, then a virtual hopping process can occur with an intermediate state where both p orbitals are half-filled and with anti-parallel spins, corresponding to an energy of $2\Delta + U_{pp}$, as above. This gives a second-order correction of $\Delta E(AFM) \sim -t_{pd}^4/(\Delta^2(2\Delta + U_{pp}))$ for the relative AFM alignment of d orbital spins. If the TM spins are instead FM ordered, the same virtual hopping process occurs but the intermediate state will have two parallel spins on the same ligand site, which are relatively stabilized by the (ligand) Hund's exchange J_H^p. Thus, the intermediate state has energy $2\Delta + U_{pp} - J_H^p$, and the energetic corrections for the FM state is $\Delta E(FM) \sim -t_{pd}^4/(\Delta^2(2\Delta + U_{pp} - J_H^p))$. Thus, the FM state is more stable in this 90° geometry, with an effective total exchange interaction (expanded for small J_H^p),

$$J(90^\circ) \simeq \frac{t_{pd}^4}{\Delta^2}\frac{J_H^p}{(2\Delta + U_{pp})^2}$$

The strength of this FM interaction, being mediated by an additional energy scale of J_H^p, is typically weaker in magnitude compared to the direct AFM exchange in the linear M-L-M

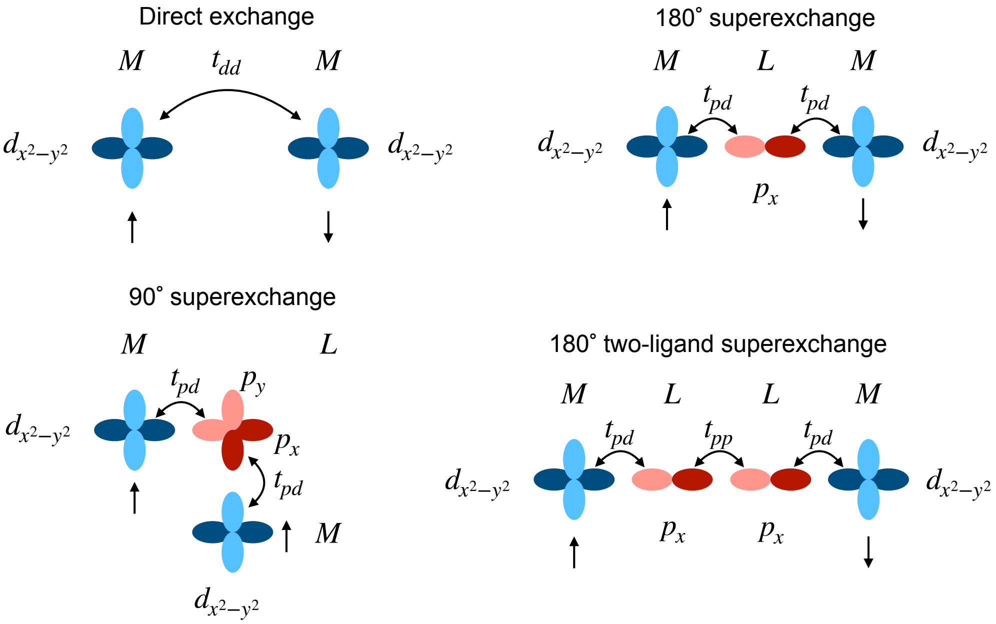

Figure 3.1: Common kinetic processes for interatomic spin exchange for a single half-filled e_g orbital.

geometry.

These results for $J(180°)$ and $J(90°)$ are two examples of the Goodenough-Kanamori rules [118, 119], which are a set of semi-empirical rules for determining the sign and approximate (relative) magnitude of the interatomic spin exchange determined from details of the electron filling, dominant orbital hopping pathways, and the local bonding geometry. The cases we have described here are specifically tailored towards the case of the half-filled e_g orbitals of octahedrally coordinated Ni^{2+} ions ($3d^8$), which are used to discuss the exchange interactions on the triangular lattice in the next section.

Before this, we discuss longer-range interactions involving two intermediate ligand states. Such processes are critical for both vdW materials and for long-range exchange interactions in frustrated magnets, such as the triangular lattice systems [41, 46, 120]. This is particularly true for interlayer exchange interactions (across the vdW gap) in vdW magnets, as such processes almost always involve two ligand orbitals. Such processes will be weak unless there is significant hopping integrals t_{pd} and/or small charge transfer gaps Δ, which is one reason why the interlayer interactions in highly ionic vdW magnets are weak (beyond the trivial reason of large interlayer separation). Solving the exchange on the full basis of TM and ligand states explicitly, while possible, does not lead to simple closed form expressions since they involve many different potential perturbative corrections at higher order. Instead, one can note that in charge transfer insulators with small Δ, the electronic states have contributions from ligand-hole configurations as discussed in Chapter 2. For a given ground state wavefunction Ψ of an electronic configuration $3d^n$, one can then write the general wavefunction as $\Psi = \alpha\ 3d^n(\Psi) + \beta\ 3d^{n+1}\underline{L}(\Psi)$, where the ligand-hole configuration states

$3d^{n+1}\underline{L}$ are formed from the corresponding ligand-molecular orbitals.

With this representation, one can then express the superexchange directly from virtual hopping processes between overlapping ligand orbitals based on the ligand-projected component of the wavefunction, e.g. $\beta 3d^{n+1}\underline{L}(\Psi)$. For a simple linear overlap between the neighboring ligand orbitals, such as the M-L-L-M linear bond in Fig. 3.1, the resulting exchange would be the expected AFM with a similar form to the single-orbital Hubbard model,

$$J \simeq -\beta^2 t_{pp}^2/U_{pp}$$

where the new relevant hopping and correlation scales are t_{pp} and U_{pp} for the ligand-ligand hopping integral and ligand on-site Coulomb repulsion, respectively. Note that the parameters t_{pd}, Δ and U_{dd} are accounted for implicitly in the configuration mixing calculation required to determine the coefficient β. As β increases, i.e. the proportion of self-doped ligand holes $\underline{L}$ increases, the exchange interaction increases for exchange processes involving two ligands.

Besides the ground state superexchange interactions, the energy scales and hopping processes described here are also relevant for describing the propagation/dispersion of excited electronic states [121–123]. For instance, if instead of the same ground state (multielectronic) configuration at each site, photoexcitation could create a local orbital and/or spin excitation Ψ_e which then interacts with the background of TM sites in the ground state Ψ_i. One can then discuss not only an exchange of spins (related to interchange between sites $i \leftrightarrow j$ of the spin projection m_s), but also the exchange of the spin-orbital multielectronic configuration. We discuss such a process leading to the momentum dependence of multiplet excitations in charge transfer insulators, with a particular emphasis on the role of the ligand states and the ligand-hole electronic configuration in Chapter 8.

3.2 Magnetic ground states of triangular-lattices

We now apply the above exchange interaction rules to the triangular-lattice geometry which is relevant for many TM dihalide compounds [46]. The TM dihalides usual adopt either the $\mathrm{CdCl_2}$ or $\mathrm{CdI_2}$ lattices with $R\bar{3}m$ or $P\bar{3}m1$ space groups, respectively [2]. Each structure consists of the same triangular lattice of octahedrally coordinated, edge-sharing transition metal sites with a different interlayer stacking symmetry. Here, we focus on the $R\bar{3}m$ structure relevant for the nickel dihalides ($\mathrm{NiX_2}$).

We begin by discussing the isotropic Heisenberg-type interactions within the triangular lattice layer, so-called *intralayer* exchange interactions. These are depicted in Fig. 3.2. The first nearest neighbors (NN) ($J_1^{\parallel}$) correspond to M-L-M bonds of 90° due to the edge-sharing geometry. Thus, e_g-e_g exchange interactions are dominant FM and $J_1^{\parallel} > 0$ in the sign convention of Eq. 3.1. The half-filled e_g orbitals do not have significant direct *dd* overlap,

---

[2] Note that the fluorides of many of these compounds, e.g. (Mn, Fe, Co, Ni)$\mathrm{F_2}$, instead stabilize in the three-dimensional rutile structures, while $\mathrm{CuBr_2}$ is layered but with a distinct quasi-1D monoclinic structure.

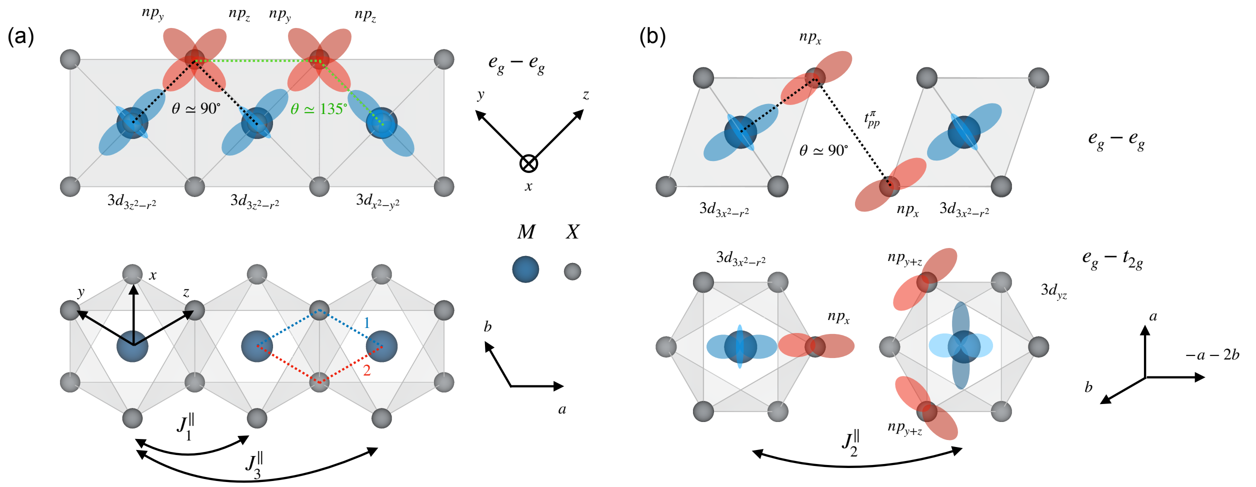

Figure 3.2: Intralayer superexchange processes on the triangular lattice.

and this contribution is expected to be weak although direct t_{2g}-t_{2g} overlap in early TM dihalides is expected to be important [15].

These first-NN interactions are the only ones involving a single-ligand state in the presently considered lattice geometry, while all others proceed by at least two intermediate ligands. Thus, for ionic systems, the FM intralayer exchange dominates, stabilizing FM order within the layer. This is the case for $\mathrm{NiCl_2}$ [124], where further neighbor interactions are negligibly weak [47]. The third-NN process involves M-L-L-M superexchange with an M-L-L angle of approximately 135°. Thus, σ-bonded np orbitals with the e_g states have a strong t_{pp}^{σ} overlap. This leads to a relatively strong AFM exchange, but is scaled significantly by the metal-ligand covalency and thus becomes significant compared to the single-ligand processes only for large ligands (e.g. I, Br). Thus, $J_3^{\|} < 0$ and is strongly dependent on ligand [125].

To conclude the discussion of the interactions within the triangular lattice layers, we discuss the second-NN interactions. Initial studies of these materials implicitly considered that since these interactions have shorter inter-metallic distances compared to the third-NN that they would be larger and thus more important to describe the ground states [41, 42]. However, many studies find that for d^8 nickel compounds, these interactions are rather weak [47, 125, 126]. This is likely due to competition between two exchange processes of opposite sign and small magnitude, related to e_g-e_g (AFM) and t_{2g}-e_g (FM) exchange. The former is small because the intermediate ligands are oriented perpendicular to their bond, thus involving weaker π-type ligand-ligand overlap. The latter is small due to two effects. First, the exchange from filled t_{2g} orbitals to half-filled e_g orbitals is FM and weak, as it is an intermediate-state effect mediated by J_H on the metal site [15]. Secondly, while the two-ligand overlap involves significant σ-type overlap, the t_{2g} covalency is smaller than the e_g states ($t_{pd}^{\pi} < t_{pd}^{\sigma}$), thus suppressing further the superexchange magnitude. These competing contributions leads to a net weakly FM interaction, $J_2^{\|} > 0$, and with $|J_2^{\|}| \ll |J_1^{\|}|, |J_3^{\|}|$ for all ligands (and at elevated pressures [126]).

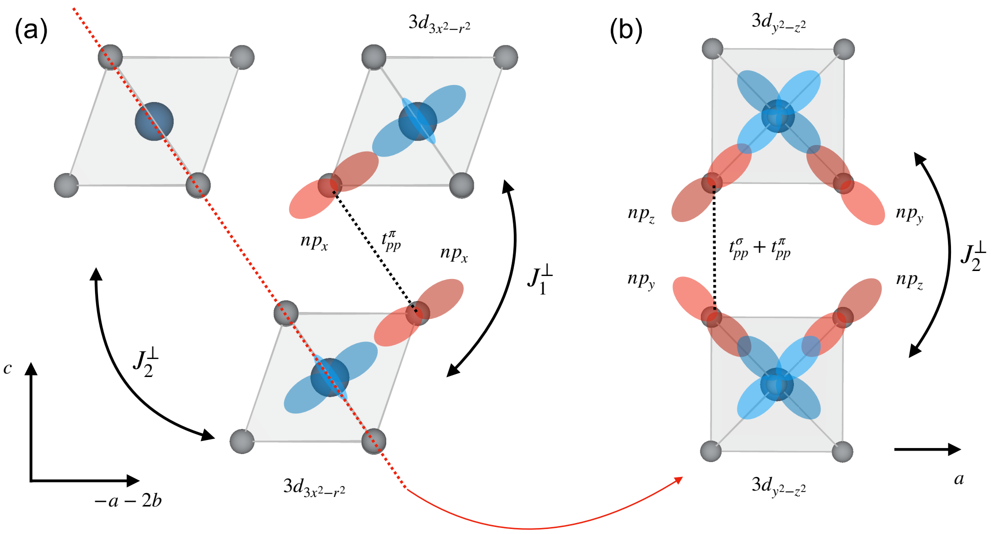

Figure 3.3: Interlayer superexchange processes in the $R\bar{3}m$ phase of transition-metal dihalides.

Finally, we briefly discuss the interlayer exchange interactions. We consider the case of $R\bar{3}m$ symmetry. The dominant exchange processes are the interlayer first- and second-NN exchanges $J_1^{\perp}$ and $J_2^{\perp}$, respectively. These are depicted in Fig. 3.3, where we have isolated a single neighbor of each type and suppressed others for visual clarity. In the high symmetry structure, the c/a ratio makes the inter-metal distances approximately the same as the $J_2^{\|}$ and $J_3^{\|}$ interaction. Thus, if long-range intralayer exchanges are important, one expects interlayer interactions to be on the same order of magnitude based on distance arguments alone. Similar to these long-range intralayer interactions, these interlayer interactions are both mediated by two-ligand superexchange processes.

Indeed, the processes determining $J_1^{\perp}$ and $J_2^{\perp}$ are nearly identical to those determining $J_2^{\|}$ and $J_3^{\|}$, respectively, as can be seen by comparing Figs. 3.2 and 3.3. Therefore, $J_1^{\perp}$ is nearly negligible and weakly FM, while $J_2^{\perp}$ is the dominant interlayer contribution and is strongly AFM. One notable difference is the absence of intermediate metal atoms in the interlayer case. This means that under perturbations like hydrostatic pressure, the c axis distance is more easily reduced (higher compressibility) compared to the compression of the triangular lattice layer. Thus, interlayer interactions are more susceptible to modification by pressure [126] (see Chapter 6). Further, the relative alignment of the intermediate ligands will be modified differently by local distortions such as a trigonal distortions of the ML_6 octahedra.

We now discuss the ground states that are stabilized by these exchange interactions. We consider only the intralayer exchange, while the effects of interlayer exchange are considered more explicitly in Chapter 7. The problem has been analyzed in detail in Ref. [41] and was commonly employed in the initial neutron scattering investigations of triangular lattice systems [43, 127, 128]. The presence of multiple magnetic exchange interactions with different signs results in magnetic frustration, in particular for $J_1^{\|}$ and $J_3^{\|}$. These interactions act along

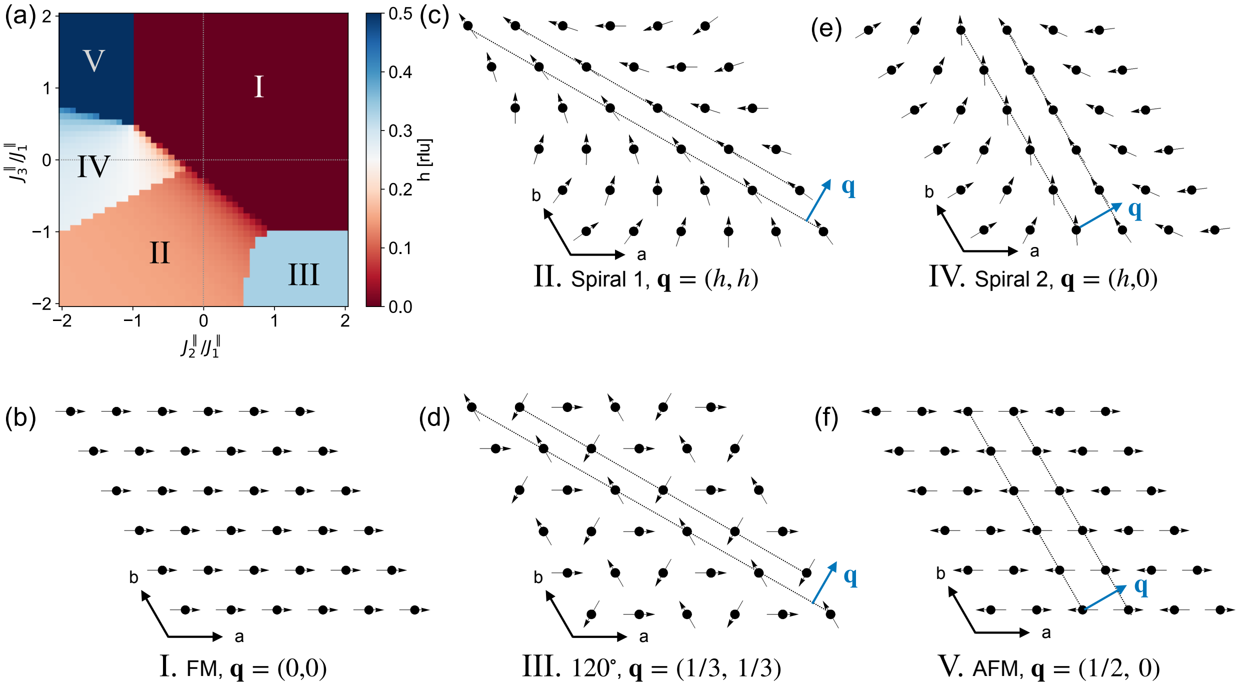

II. Spiral 1, **q** = (h, h)

IV. Spiral 2, **q** = (h,0)

I. FM, **q** = (0,0)

III. 120°, **q** = (1/3, 1/3)

V. AFM, **q** = (1/2, 0)

Figure 3.4: Ground states of the triangular lattice with intralayer exchange.

the same real space direction, with opposite signs and the same order of magnitude. Thus, for sufficiently large $J_3^\parallel/J_1^\parallel$, simple AFM and FM ground states within the plane are no longer favored, and instead incommensurate magnetic ground states are stabilized to balance the exchange energy.

The classical magnetic ground state for isotropic Heisenberg exchange can be determined by writing the exchange energy versus the magnetic wavevector $\mathbf{q}$ [41], that is

$$J_n(\mathbf{q}) = \sum_{\langle i,j\rangle_n} J_n e^{-i\mathbf{q}\cdot\mathbf{r}_{ij}}$$

where $\langle i,j\rangle_n$ correspond to spin pairs separated by $\mathbf{r}_{ij}$ and interacting through exchange interaction J_n (explicit forms forms for the main exchanges $J_n^\parallel(\mathbf{q})$ and $J_n^\perp(\mathbf{q})$ can be found in Chapter 7). The wavevector $\mathbf{q}$ can then be determined by minimizing $E(\mathbf{q}) = -\sum_n J_n(\mathbf{q})S^2$ and solving the system of equations $\partial E(\mathbf{q})/\partial q_i = 0$.

We plot the ground states considering $J_1^\parallel$-$J_2^\parallel$-$J_3^\parallel$ in Fig. 3.4, where we set a ferromagnetic $J_1^\parallel > 0$ (relevant for the nickel dihalides). FM is the ground state when $J_1^\parallel$ is the dominant exchange interaction (Fig. 3.4(b)). First looking at the limit of $J_3^\parallel = 0$, we find a transition into an incommensurate spiral state for a critical value $J_2^\parallel/J_1^\parallel = -0.33$ with wavevector $\mathbf{q} = (h, 0)$ (IV: Spiral 2) in reciprocal lattice units (rlu) (Fig. 3.4(e)). This is the ground state observed in NiI$_2$ [42, 45], however since $J_2^\parallel \simeq 0$ in the nickel dihalides, a different mechanism is required to justify this phase as we explore in Chapters 6 and 7. The magnitude of the incommensurate wavevector for the Spiral 2 state can be solved analytically and is given by

$$\text{Spiral 2:}\quad h = \frac{1}{2} - \frac{1}{2\pi}\cos^{-1}\left(\frac{1}{2}\frac{J_1^{\parallel} + J_2^{\parallel}}{J_2^{\parallel} + 2J_3^{\parallel}}\right)$$

In the other limit for $J_2^{\parallel} = 0$, a transition to a distinct spiral state (II: Spiral 1) is stabilized with $\mathbf{q} = (h, h)$ for $J_3^{\parallel}/J_1^{\parallel} < -0.25$. This is the spiral state realized in $\mathrm{NiBr_2}$ [38, 128]. One can also extract an analytical expression for the wavevector,

$$\text{Spiral 1:}\quad h = \frac{1}{2\pi}\cos^{-1}\left(\frac{1}{4}\left[1 + \sqrt{1 - 2J_1^{\parallel}/J_3^{\parallel}}\right]\right)$$

where we suppress the dependence on $J_2^{\parallel}$ for clarity [41, 42]. Finally, at larger values of $|J_2^{\parallel}|$ and $|J_3^{\parallel}|$, two commensurate states are possible. This includes a 120° state (III, Fig. 3.4 (d)) and a stripe-type antiferromagnetic state (V, Fig. 3.4(f)). Each of these ground states have been observed experimentally for different transition metals, although experimentally, incommensurate spin spiral phases appear to be the most common (see Refs. [129] and [46], and references therein).

The magnetic states in Fig. 3.4 are shown with moments within the triangular lattice plane. The isotropic Heisenberg model chooses a specific wavevector $\mathbf{q}$, but does not provide details on the specific spin texture, e.g. amplitude modulation vs possible spin spiral states as we show above. The specific rotation plane/spin axis for different materials is determined by the magnetic anisotropy. This has two primary forms, the single-ion anisotropy and the two-ion anisotropy. These can be expressed through more general forms of the exchange interactions, specifically:

$$H = \sum_{i,j} \mathbf{S}_i \cdot \mathbf{J}_{ij} \cdot \mathbf{S}_j + \sum_i A_i S_i^2$$

where $\mathbf{J}_{ij}$ is the general exchange tensor and A_i are components of the single-ion anisotropy.

The single ion anisotropy tends to stabilize magnetic order along unique directions of the local site environment, which is determined by the crystal field and spin-orbit coupling at the transition-metal site. This defines either a well-defined direction or plane in which the spins lie. In Fig. 3.4, the displayed spin texture is consistent with XY anisotropy, as observed in $\mathrm{NiBr_2}$, where spins pointing along the trigonal C_{3z} axis are relatively destabilized due to slight trigonal distortions.

On the other hand, there are 3 primary components to $\mathbf{J}_{ij}$: (i) the isotropic component (given by the trace) which is equivalent to the isotropic Heisenberg exchange contributions analyzed above, (ii) the antisymmetric off diagonal components, and (iii) the anisotropic symmetric components. Antisymmetric exchange is one mechanism to stabilize non-collinear magnetic states in absence of exchange frustration, known as the Dzyaloshinskii-Moriya interactions [15]. However, in order for these terms to be allowed, one requires the lack of crystallographic inversion symmetry on the bond between the two interacting spins. This is not the case of the transition metal dihalides, and thus we ignore these terms. The anisotropic symmetric exchange terms are allowed. These terms stabilize relative orientations of neighboring spins, also referred to as bond-directional anisotropy. The well-known Kitaev model is a particular parameterization of anisotropic symmetric exchange [130].

In the end, these terms will energetically favor a local anisotropy axis which depends on the orientation of the bonds connecting the two sites. Thus, the anisotropy axes will be different for distinct spin pairs, even if the local crystal field environments (and hence, single-ion anisotropy axes) are identical. Such Kitaev-like terms naturally emerge from an edge-sharing geometry [130]. The latter leads to a partial destructive interference between the symmetric exchange paths, labelled as 1 (blue) and 2 (red) in Fig. 3.2(a), with the result of a Kitaev-like term creating an anisotropy axis along the local x direction for the depicted NN spin pair [125]. These terms are crucial to describe the emergence of distinct spin rotation planes in the nickel dihalides, and may even energetically favor different magnetic propagation vectors [131]. These interactions are induced by SOC, in this case provided by the ligands mediating the superexchange interactions[3]. Thus, these anisotropy terms are anticipated to be strongest in the heavier ligands (e.g. I [47]).

3.3 Mechanisms of spin-induced ferroelectricity

With an appropriate magnetic anisotropy and exchange frustration, the triangular lattice systems can thus stabilize incommensurate spin spiral states. A consequence of this type of magnetic order is a breaking of inversion symmetry, which in turn can induce ferroelectric order. This leads to type-II multiferroic ground states as discussed in Chapter 1. Indeed, many triangular lattice systems with such magnetic ground states are found to be multiferroic [33, 38, 44, 45].

Incommensurate magnetic states without a net magnetization come in three principal types, spin-density wave (SDW), cycloidal and proper-screw/helical ground states. The first represents a sinusoidally amplitude-modulated phase, e.g. $\mathbf{S}_i = \cos(\mathbf{q}\cdot\mathbf{r}_i)\ \hat{x}$ for $\mathbf{q} \parallel \hat{z}$ without loss of generality and where i labels a particular magnetic site. This phase does not break inversion symmetry. A cycloidal phase refers to a spin spiral phase where the spins rotate in a plane containing the magnetic wavevector $\mathbf{q}$, e.g. $\mathbf{S}_i = (\cos(\mathbf{q}\cdot\mathbf{r}_i), 0, \sin(\mathbf{q}\cdot\mathbf{r}_i))$. This magnetic texture breaks inversion symmetry but is achiral (preserves the mirror plane perpendicular to $\mathbf{q}$). Finally, a proper-screw state has a spin rotation plane perpendicular to $\mathbf{q}$, e.g., $\mathbf{S}_i = (\cos(\mathbf{q}\cdot\mathbf{r}_i), \sin(\mathbf{q}\cdot\mathbf{r}_i), 0)$. The proper-screw state also breaks inversion symmetry, in addition to all mirror planes and is thus chiral. Each of these states in a simplified 1D model are shown in Fig. 3.5. The breaking of inversion symmetry is closely related to the presence of a finite spin helicity for the cycloidal and helical states, defined as

---

[3] SOC of the transition-metal site can contribute as well, however this likely requires t_{2g} orbital systems (e.g. early transition metals) where SOC has a direct effect on the $3d$ states. SOC-effect is quenched at first-order for e_g orbital systems.

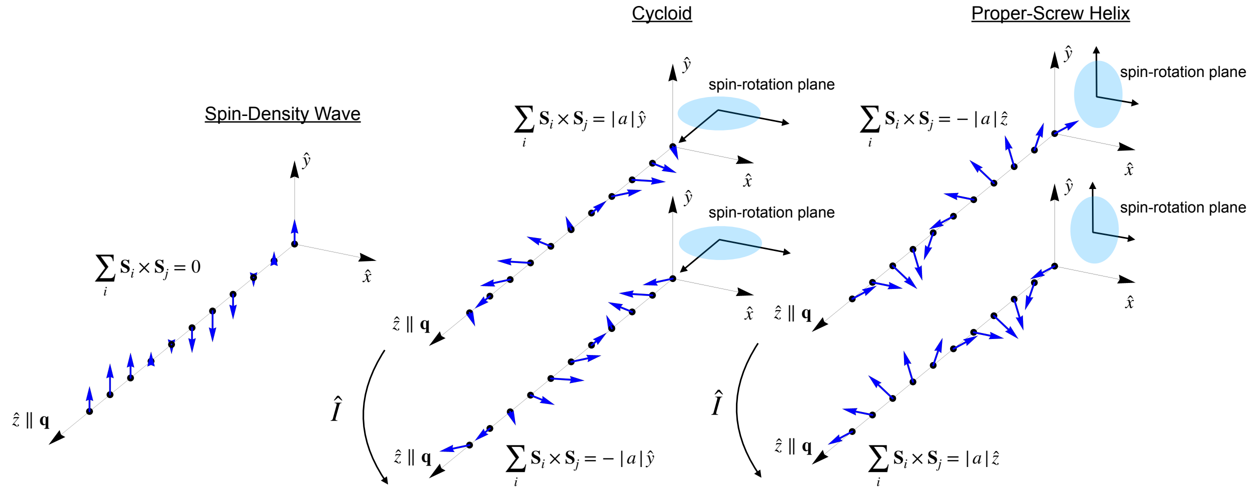

Figure 3.5: Types of incommensurate magnetic states.

$h = \sum_i \mathbf{S}_i \times \mathbf{S}_{i+1}$. The former has finite spin helicity $h \perp \mathbf{q}$ while the latter has $h \parallel \mathbf{q}$, both of which reverse sign under the application of inversion ($\hat{I}$).

The theory of spin-induced ferroelectricity was first developed in the context of cycloidal systems [33]. The model which explains the appearance of finite electric polarization in cycloidal systems is the inverse-Dzyaloshinskii-Moriya (inverse-DM), or spin-current/Katsura-Nagaosa-Balatsky (KNB) model [39, 132]. This predicts a ferroelectric polarization ($\mathbf{P}$) defined by,

$$\mathbf{P} = \sum_{ij} \vec{e}_{ij} \times \mathbf{S}_i \times \mathbf{S}_j$$

where $\vec{e}_{ij}$ is the unit vector connecting spin pairs. In the example of a perfect cycloid (Fig. 3.5), the contribution to spin helicity for each spin pair $\langle i, j \rangle$ is equal and oriented within the spin rotation plane and perpendicular to $\mathbf{q}$. Thus, each site generates a local $\mathbf{P}_i$ oriented perpendicular to $\mathbf{q}$. Microscopically, one can view this effect from the same mechanism of the DM interaction. In the direct DM interaction, an inversion-breaking bond induces a net spin canting given by an anti-symmetric exchange, $H_{DM} = \mathbf{D}_{ij} \cdot \mathbf{S}_i \times \mathbf{S}_j$ where $\mathbf{D}_{ij}$ is perpendicular to the plane defined by the M-L-M bond (antisymmetric contribution to the $\mathbf{J}_{ij}$ tensor discussed in the previous section). In the inverse DM interaction, a non-collinear spin structure in an otherwise centrosymmetric lattice leads to a distortion of the bonding environment that generates a $\mathbf{D}_{ij}$ vector in agreement with the observed spin canting [133]. Given a well-defined spin chirality across the entire helix, this leads to a polar distortion of the lattice, generating a net $\mathbf{P}$ [33]. The origin of this polarization is SOC.

The sign of $\mathbf{P}$ is directly related to the helicity of the spin structure, and thus switching $\mathbf{P}$ by an electric field induces a change in the cycloid helicity as has been experimentally verified [134]. We note that distortions from the perfect cycloid (e.g. ellipticity of the spiral) can additionally lead to finite-momentum (modulated) components of $\mathbf{P}$ at multiples of $\mathbf{q}$. Due to the coupling between the local dipole and the lattice, small polar displacements of either the transition-metal or the ligands from their high-symmetry positions lead to a structural superlattice at finite $\mathbf{q}$, which has been detected with diffraction methods [135].

The KNB model is successful in predicting the direction of spin-induced $\mathbf{P}$ for most cycloidal systems [33]. However, it fails to account for the observation of finite $\mathbf{P}$ in proper-screw systems [136]. Indeed, in a proper-screw helix, one has $\mathbf{S}_i \times \mathbf{S}_j \parallel \vec{e}_{ij} \parallel \mathbf{q}$ for all spin pairs, and thus the KNB model gives precisely $\mathbf{P} = 0$. However, finite polarization is observed and, more generally, the KNB model does not predict the correct direction of $\mathbf{P}$ for some low symmetry systems that are not perfectly cycloidal or helical [40]. The canonical example is $CuFeO_2$ which is a triangular lattice of Fe atoms [136].

To explain this discrepancy, an alternative model was proposed termed the spin-dependent *pd* hybridization [33, 136, 137]. In effect, this model predicts a spin-induced $\mathbf{P}$ that is induced on the metal-ligand bond, due to a spin-dependent covalency between the metal d and ligand p states resulting from SOC. Importantly, this model induces a bond-polarization that may involve both ligand- and transition-metal SOC. Unlike the KNB/inverse-DM model, this term involves a single spin site, while the former is an intersite contribution generated by non-collinearity of two neighboring spins. The metal-ligand bond polarization is given by $\mathbf{P}_i^{(j)} = (\mathbf{S}_i \cdot \vec{r}_{ij})\vec{r}_{ij}$ where $\mathbf{r}_{ij}$ is a vector along a given M-L bond. This mechanism is thought to be the leading contribution to the polarization in triangular lattice systems, including MnI_2 [44], $NiBr_2$ [45] and $CuFeO_2$ [136], and in particular predicts $\mathbf{P} \perp \mathbf{q}$ for proper-helix systems.

The metal-ligand hybridization term being non-zero requires a combination of both specific magnetic and lattice symmetries, the latter defined by the metal-ligand bonding environment. This is a general property of spin-induced $\mathbf{P}$ is spin-helix systems [138], where magnetic order alone is insufficient to yield a unique polar axis. Unlike cycloidal systems which preserve only a single m' mirror plane perpendicular to $\mathbf{q}$, thus allowing spin induced $\mathbf{P} \perp \mathbf{q}$ regardless of the lattice structure, helical systems preserve $2'$ axes both parallel and perpendicular to $\mathbf{q}$. Polar space groups must have at most a single 2-fold rotational axis (the polar axis), and thus the combination of both magnetic and lattice symmetries are required to allow a spin-induced $\mathbf{P}$ in helical systems. This is precisely what occurs in the transition-metal dihalides [38, 45].

The two above models are the main ones used to justify the spin-induced $\mathbf{P}$ in type-II multiferroics. They give simple rules and microscopic interpretations for relatively high-symmetry spin structures. However, they do not encompass all possibilities. In particular, it is observed in MnI_2 that there is magnetic field induced rotation of $\mathbf{q}$ from a proper-screw state along $(h, 0)$ (Spiral 2) to (h, h) (Spiral 1) with $\mathbf{P} \perp \mathbf{q}/\mathbf{P} \parallel \mathbf{q}$ in each state, respectively [44]. This situation is not described by either the inverse-DM or the spin-dependent *pd* hybridization models. To overcome this, a more generalized model was proposed known as the generalized KNB (gKNB) model. In this model, one accounts for both the intrasite polarization $\mathbf{P}_i(S_i) = P_i^{\alpha\beta} S_{i,\alpha} S_{i,\beta}$ and the intersite $\mathbf{P}_{ij}(S_i, S_j) = P_{12}^{\alpha\beta} S_{i,\alpha} S_{j,\beta}$ contributions, where spin-dependent *pd* hybridization belongs to the former and the inverse-DM to the latter [40, 138]. By symmetry, one can show that the intersite polarization term is antisymmetric with respect to the spin components, and thus couples as $\mathbf{P}^{\alpha}_{12} = \mathbf{M}_{\alpha\beta}(\mathbf{S}_i \times \mathbf{S}_j)_{\beta}$, where $\alpha, \beta \in \{x, y, z\}$. This generalized $\mathbf{M}$ tensor formalism can be calculated from first principles and accounts for a more complete description of spin-induced ferroelectric order caused by canted spin pairs [40, 138]. Therefore, in the general case, a full accounting of all symmetry-allowed components are required to describe the spin-induced ferroelectric order. This approach is used to describe multiferroic state of NiI_2 in the Chapter 5.

As a final note, it is worth emphasizing that many microscopic models are based on simplified metal-ligand bonding geometries, most particular a linear M-L-M bond [39, 137, 139], and further considering particular electronic configurations of the metal and ligand ions, e.g. a partially-filled t_{2g} shell overlapping with a light ligand atom with weak SOC, such as oxygen. Thus, many of the analytical results have been derived for high-symmetry lattice geometries or specific electronic configurations which are not generally applicable. Analytical results found commonly in the literature must therefore be used with caution. Furthermore, the canted-spin-pair mechanisms, including the the symmetry-based approaches of [40, 138], consider only the basis of the transition-metal ions without explicit consideration of the ligand sites beyond their effects on the symmetry. This is problematic because, depending on the geometry and the details of the ions at each site, the microscopic local electric dipoles leading to a macroscopic ferroelectric polarization can be either at the transition metal or the ligand sites.

The location of the charge dipole is closely related to which atomic species contributes the largest SOC. For instance in oxides, the ligand SOC is weak and ferroelectricity is observed to be mainly contributed by the SOC of the TM site, such as in CuFeO_2 [140] or manganites [33]. Electronically, these compounds have partially filled t_{2g} shells, and thus SOC effects of the TM ions can enter at first order. However, for the case of the nickel dihalides discussed here, the TM ions have fully filled t_{2g} shells and do not contribute significant SOC, which is instead introduced by heavy ligands (e.g. Br and I).

Therefore, in the nickel dihalides, the local charge dipoles likely reside on the ligand sites as supported by recent numerical calculations in NiI_2 [141] and NiBr_2 [142]. The bonding geometry of the triangular lattice with 90° M-L-M bonds from the edge-sharing octahedra cannot be described by the linear cluster models [39, 137, 139], which do not account for the correct bonding symmetry, while the phenomenological approaches accounting for the proper symmetry do not account for the ligand states explicitly. Thus, significant work remains to gain a full microscopic description of the ferroelectric polarization induced by different spin spiral structures in low-symmetry lattice environments where SOC is dominated by the ligand. The microscopic description answering the question: "where is the ferroelectric polarization?" in these systems remains obscured outside of numerical calculations.

This is particularly important to describe the modulated components of the ferroelectric order and spin-lattice coupling effects leading to incommensurate structural distortions. Such locally oscillating charge dipoles directly contribute to the ferroelectric order at $\mathbf{q} = 0$ and encode critical information regarding the microscopic mechanisms of the spin-induced ferroelectricity [33, 135]. Resolving these issues is of particular importance towards evidence of multiferroic order in the 2D limit from atomic-resolution scanning probe measurements. For instance, recent STM [143] measurements in NiI_2 have resolved an oscillating charge at a harmonic of the predicted helimagnetic wavevector. This observation was interpreted in terms of a continuum model of Ref. [132] whose predictions for the $\mathbf{q} = 0$ ferroelectric order are not immediately reconcilable with the spatially uniform component predicted by the generalized KNB model [40]. Thus, reaching a full understanding of this problem will be critical to gain a full description of the phenomenon of spin-induced ferroelectricity outside of the canonical examples in transition-metal oxides, and holds particular importance for building solid evidence of spin-induced ferroelectricity in ultrathin vdW materials.

Chapter 4

Photon probes of spin/orbital order and excitations

In this chapter, we review the main techniques used in this thesis to probe spin-orbital ground states, electronic anisotropy, and collective excitations (magnons, phonons, excitons). Each technique utilizes photon spectroscopy and scattering, ranging from the optical regime (Raman scattering and magneto-optical spectroscopy) to the X-ray regime (X-ray absorption spectroscopy, X-ray linear dichroism, and Resonant elastic/inelastic X-ray scattering).

4.1 Light Matter Interaction

We first describe the fundamental interaction between electromagnetic fields and the electrons in the sample. The treatment here follows similar derivations in Refs. [109, 144–146]. We write the Hamiltonian of the electronic system in terms of the single electron momentum $\mathbf{p}$, position $\mathbf{r}$, and mass m as,

$$H_0 = \frac{\mathbf{p}^2}{2m} + V(\mathbf{r})$$

Meanwhile, each mode $\mathbf{k}$ of the electromagnetic field with energy $\hbar\omega_{\mathbf{k}}$ is described as a harmonic oscillator in second quantized notation as,

$$H_{ph} = \sum_{\mathbf{k}} \hbar\omega_{\mathbf{k}} \left(a_{\mathbf{k}}^{\dagger} a_{\mathbf{k}} + \frac{1}{2} \right)$$

where $a_{\mathbf{k}}/a_{\mathbf{k}}^{\dagger}$ are annihilation/creation operators for a photon of wavevector $\mathbf{k}$, respectively. In the quantization of the electromagnetic field, one can express the vector potential $\mathbf{A}(\mathbf{r}, t)$ as,

$$\mathbf{A}(\mathbf{r}, t) = \sum_{\mathbf{k}} a_{\mathbf{k}} \vec{\epsilon}_{\mathbf{k}} e^{i(\mathbf{k}\cdot\mathbf{r} - \omega_{\mathbf{k}} t)} + a_{\mathbf{k}}^{\dagger} \vec{\epsilon}_{\mathbf{k}}^{*} e^{-i(\mathbf{k}\cdot\mathbf{r} - \omega_{\mathbf{k}} t)}$$

where $\vec{\epsilon}$ represents the photon polarization vector[1].

To describe the interaction between the electron and electromagnetic field, in the simplest approximation, one can perform a gauge shift to the single electron Hamiltonian H_0 by replacing $\mathbf{p} \rightarrow \mathbf{p} - e\mathbf{A}$, with electron charge $-|e|$, and adding a term describing the interaction between the spin degree of freedom (described by a Pauli vector $\vec{\sigma}$) with the magnetic field component of the electromagnetic wave $\propto \vec{\sigma} \cdot \mathbf{B} = \vec{\sigma} \cdot \nabla \times \mathbf{A}$.[2] After performing these substitutions and utilizing the Coulomb gauge $\nabla \cdot \mathbf{A} = 0$, one arrives at the following form of the interaction Hamiltonian H_{int},

$$H_{int} = -\frac{e}{m}\mathbf{p} \cdot \mathbf{A} + \frac{e^2}{2m}\mathbf{A} \cdot \mathbf{A} - \frac{e}{m}\vec{\sigma} \cdot (\nabla \times \mathbf{A})$$

with the overall Hamiltonian for the light-matter system becoming $H = H_0 + H_{ph} + H_{int}$.

Terms within H_{int} that are linear in the vector potential $\mathbf{A}$ correspond to the absorption *or* emission of a photon, along with a corresponding transition of the electronic state. Scattering processes involve absorption plus subsequent emission, and thus the linear in $\mathbf{A}$ terms only lead to scattering at second-order. Meanwhile the term quadratic in $\mathbf{A}$ (second term in H_{int}) describes direct scattering processes, e.g. absorption plus emission of photons. This last term describes normal Thompson scattering. In the context of X-rays, this term describes the usual (isotropic charge) diffraction and (non-resonant) inelastic X-ray scattering.

What is important for the cross-section of scattering events are the matrix elements of the light matter interaction Hamiltonian with electronic states in the material. For instance, for an initial/final electronic state ψ_i/ψ_f, one needs to consider matrix elements of the form $M_{fi} = \langle \psi_f | H_{int} | \psi_i \rangle$. The form of the transitions can be determined by multipole expansion of H_{int} into powers of r. The standard approach is to expand the plane-wave term of the vector potential about $\mathbf{k} \cdot \mathbf{r} \ll 1$,

$$e^{-i\mathbf{k}\cdot\mathbf{r}} = 1 - i\mathbf{k} \cdot \mathbf{r} - 1/2(\mathbf{k} \cdot \mathbf{r})^2 + \cdots$$

The approximation is a good one, since $\mathbf{k}$ is set by the photon wavelength ($|\mathbf{k}| = 2\pi/\lambda$) and $\mathbf{r}$ is the average radius of the electron (order of Bohr's radius, ~ 0.05nm). Thus, the approximation to leading order is a good one for energy below the hard X-rays $E < 5$ keV. If we then take the lowest order term in H_{int} (ignoring the contribution of the $\mathbf{A}^2$ term) we get

$$M_{fi}(E1) = -\frac{e}{m}\langle \psi_f | \mathbf{p} \cdot \mathbf{A} | \psi_i \rangle = -\frac{e}{m}\langle \psi_f | \mathbf{p} \cdot \vec{\epsilon}_{\mathbf{k}} | \psi_i \rangle = \frac{e}{i\hbar}(E_f - E_i)\langle \psi_f | \vec{\epsilon}_{\mathbf{k}} \cdot \mathbf{r} | \psi_i \rangle$$

where we used the relation $\mathbf{p} = -\frac{m}{i\hbar}[H_0, \mathbf{r}]$. This lowest order term describes a dipole (E1)

---

[1] Throughout, we will use $\vec{\epsilon}$ to denote photon polarization, a vector quantity, and ε or $\varepsilon_{\alpha\beta}$ to denote the dielectric tensor.

[2] This simplified version of the light-matter interaction ignores important relativistic corrections terms which are required to describe non-resonant magnetic scattering and higher order multipoles of the light-matter interaction tensor [145].

transition. Since $\mathbf{r}$ is odd under parity, such a transition only connects states with opposite parity. Another important term, derived from the next order $\mathbf{k} \cdot \mathbf{r}$ term in the plane wave expansion is

$$M_{fi}(E2) \propto \langle \psi_f | (\vec{\epsilon}_{\mathbf{k}} \cdot \mathbf{r})(\mathbf{k} \cdot \mathbf{r}) | \psi_i \rangle$$

and is known as an (electric) quadrupole (E2) transition. With two factors of $\mathbf{r}$, the E2 transition can have finite amplitude between two states of the same parity ($\vec{\epsilon}_{\mathbf{k}}$ and $\mathbf{k}$ are properties of the photon). Finally, we consider the magnetic dipole (M1) transition, which can be expressed as

$$M_{fi}(M1) \propto \langle \psi_f | (\mathbf{k} \times \vec{\epsilon}_{\mathbf{k}}) \cdot (\mathbf{L} + 2\mathbf{S}) | \psi_i \rangle$$

which is derived from a combination of the second plane-wave expansion term with the $\mathbf{p} \cdot \mathbf{A}$ term of H_{int} and the lowest-order contribution of the $\vec{\sigma} \cdot \mathbf{B}$ term in H_{int}. Similar collections of terms can be derived for higher order multipoles of the light-matter interaction [145].

Each of these transitions are characterized by particular selection rules, or relative values of the quantum numbers of ψ_i/ψ_f so that the transition $i \to j$ is non-zero [109]. In the E1 approximation, one can consider the photon as carrying a single unit of angular momentum $\ell = 1$. The dipole transition operator can be re-expressed as a spherical tensor of rank 1, $T_k^{(q)}$, with $T_1^{(\pm 1)}$ corresponding to left/right circular polarizations $\sigma_{+/-}$. Thus, the E1 transition operator is of odd-parity and connects electronic states of opposite parity. By combination of the parity and the effective angular momentum properties of the photon, dipole transitions (in the absence of spin-orbit coupling (SOC)) only connect transitions related by $\Delta L = \pm 1$, e.g. $s \leftrightarrow p$, $p \leftrightarrow d$, etc. Importantly, the transition operator for E1 involves matrix elements involving only the position operator of the electronic state, from which the spin component can be factored in the absence of SOC. In general, this implies that the total spin for a transition between single or multielectronic states is preserved during dipolar transitions, i.e. $\Delta S = 0$. Together, the dipole selection rules $\Delta L = \pm 1$ and $\Delta S = 0$ describe the leading order selection rules for optical processes, known as the Laporte and spin-selection rules, respectively [60].

Similar selection rules can be provided for M1 and E2 processes. In the case of M1, one is directly operating on the spin space through the corresponding light-matter interaction and spin flip processes are allowed $\Delta S = \pm 1$, with the key distinction that the M1 operator is of even parity. For E2 processes, the angular momentum model for the photon states does not hold in a trivial way. The intrinsic angular momentum states of the photons involved in the transition still possess a single unit of angular momentum with $\pm \hbar$, and the transitions are single photon events, however one can visualize the spatial dispersion of the electromagnetic field interacting with the electrons leading to an additional orbital angular momentum in the light matter interaction (hence, the dependence of E2 transitions on $\mathbf{k}$). Thus, one has to think not of higher order processes in the photon transitions for additional angular momentum (e.g. *not* multi-photon transitions), but one must resort to the full multipolar expression of the light-matter interaction [145]. The E2 transition operator also has even parity, satisfies the same $\Delta S = 0$ spin selection rule as E1 processes, but from combined angular momentum and parity rules can allow transitions of the type $s \leftrightarrow d$, $p \leftrightarrow f$, etc with $\Delta L = 0, \pm 2$, in the absence of SOC. In the general case, all first order (E1, M1) processes allow all transitions of total J permitted by the angular momentum addition rules $\Delta J = 0, \pm 1$ and for second-order (E2) processes, all transitions $\Delta J = 0, \pm 1, \pm 2$ are allowed [109]. These are best represented from the angular-momentum properties of the transition operators in a spherical tensor formalism, whereby selection rules can be easily derived from angular-momentum addition rules and Racah-Wigner algebra (e.g. Chapter 2).

What we are principally interested in here is the measurement of magnetism with photons, but photons in the dominant dipole-allowed processes do not directly address the spin degree of freedom. One way is through M1 transitions allowing $\Delta S \neq 0$, however these are typically very weak. The remaining possibilities may be summarized as relativistic effects. This includes the presence of SOC in the initial state (ψ_i) and/or the final state (ψ_f) in the electronic Hamiltonian. The reason for this is that $\mathbf{L}$ and $\mathbf{S}$ are no longer good quantum numbers and thus transfer of orbital angular momentum from the photon can become sensitive to the spins, thus relaxing the selection rules. Alternatively, one can consider relativistic corrections to the light-matter interaction Hamiltonian, such as those describing non-resonant magnetic scattering [145], but again the cross section of such processes is small. Generally, it may be noted that unless it is explicitly forbidden by symmetry, if a transition can become dipole-allowed by a symmetry-breaking (e.g. inversion symmetry) or by the inclusion of SOC, the dipole-allowed process will almost always be the dominant process observed.

4.2 Core-level X-ray spectroscopy

In core-level X-ray spectroscopy, incident photons are tuned in resonance to the binding energy of a core-level electron of one of the constituent atoms in the material of interest [110, 146]. The binding energies of these core-levels are specific to the atomic species, leading to characteristic spectra that provide an energy-dependent selectivity in the cross-section of scattering/absorption processes to particular atoms in the crystal. This is the first major advantage of core-level spectroscopy, i.e. elemental sensitivity in the transition matrix elements.

While the interesting physics of materials occurs in the weakly bound, partly-filled valence orbitals near the Fermi level, the core electrons are blind to much of the details of the solid state and form fully filled shells which may be treated as almost pure atomic-like electronic states [109]. Furthermore, their high binding energies lead to a much larger spin-orbit coupling (SOC) interaction than the valence electrons. As we mentioned in Chapter 2, this results in a large SOC splitting of the core shells with $\mathbf{L} \neq 0$. This forms the second major advantage of such measurements, which is that the core levels are relatively simple atomic-like states with well-defined and energetically-separated $\mathbf{J}$ manifolds. Thus, well defined selection rules governing the core-to-valence transitions (selected by the edge resonance, i.e. incident photon energy) allow one to determine useful (unknown) properties of the spin and orbital degrees of freedom of the valence states, utilizing the precise knowledge of the initial core levels. From this perspective, one can view resonantly tuned X-rays as providing a local spin-, orbital-, and element-resolved projection of the valence electronic states.

The characteristic resonances are called absorption edges, which are defined by the initial core state [110]. These edges are defined as K, L_{1-3}, M_{1-5}, etc, which are labels for different core level manifolds. The letter refers to the shell number n in increasing order ($K \rightarrow 1$, $L \rightarrow 2$ and $M \rightarrow 3$) and subscripts refer to the different sublevels defined by angular momentum $\mathbf{L}/\mathbf{J}$. K edges are transitions with $1s$ initial states, the most tightly bound and thus the highest energy edge of the atom. K-edges of the $3d$ transition metals (Ti - Cu) lie in the hard X-ray range ($\sim 5 - 10$ keV, $\lambda \sim 1 - 3$Å). The L_1 edge is the $2s$ initial state and the $L_{2,3}$ edges are the $2p$ initial state which has SOC splitting into the $2p_{1/2}$ (L_2) and $2p_{3/2}$ (L_3) edges, at higher and lower energy, respectively. The $L_{2,3}$ edges of $3d$ transition metals are in the soft X-rays ($\sim 500 - 1000$ keV, $\lambda \sim 1 - 3$ nm), with L_2/L_3 edge splitting between (10-50 eV).

4.2.1 X-ray absorption spectroscopy and dichroism

One of the fundamental forms of core-level spectroscopy is X-ray absorption spectroscopy (XAS), where the fine structure (versus incident energy) of the absorption near a particular core-level resonance is monitored. The absorption ($\alpha(\omega)$) is defined in a transmission measurement $I(\omega) = I_0(\omega)e^{-\alpha(\omega)*\ell}$ where ℓ is the thickness of the sample and I_0 is the incident intensity. However, in practice, one usually monitors secondary processes related to absorption through the decay mechanisms of the excited photoelectron. Specifically, one can monitor photoemitted electrons (known as total electron yield (TEY)) or the total emission of photons emitted on the core-valence recombination (known as total fluorescence yield (TFY)). TEY measurements are surface sensitive due the limited escape depth of electrons (known from photoemission spectroscopy), while TFY measurements are more bulk sensitive but can be heavily distorted by re-absorption of the emitted photons. Defining a transition operator $\vec{T}$ (e.g. E1/E2), and the XAS cross section can be determined by the transition rate determined through Fermi's golden rule,

$$\alpha(\omega) \propto \left|\langle\psi_f|\vec{T}|\psi_i\rangle\right|^2 \delta((E_f - E_i) - \hbar\omega)$$

The nature of the initial states and final states depend on the core-level, the transition type (E1/E2), and incident energy across the edge.

$3d$ transition-metal K edges consist of transitions of the type $1s \rightarrow 4p$, with the $4p$ states being the lowest energy shell that is accessible by dipole transitions. These levels are at higher energy than the $3d$ orbitals and are unfilled. Nonetheless, significant information about the lattice and local coordination symmetry can be gleaned from the $4p$ orbitals, which are highly sensitive to covalency effects and the coordination environment [110, 147–149].

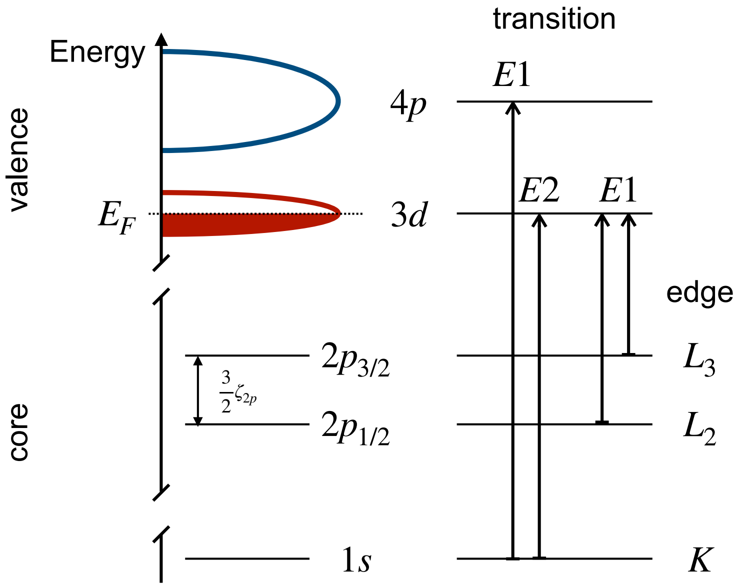

Figure 4.1: Definition of the K and $L_{2,3}$ core-level resonances. The typical electronic structure near the Fermi level for ($3d$) transition metal compounds with a partially filled $3d$ shell and unfilled metal $4p$ states at higher energy. The K edges result principally from $1s \to 4p$ transitions through an E1 transition, while weaker E2 transitions of the type $1s \to 3d$ are generally measurable, appearing as weaker absorption features at the pre-edge. The $L_{2,3}$ edges are transitions from the SOC-split $2p$ manifold, with dominant E1 transitions of the type $2p_{1/2} \to 3d$ (L_2) and $2p_{3/2} \to 3d$ (L_3). E2 transitions are too weak to be observed at the $3d$ transition metal L edges due to the lower photon energy (smaller $\mathbf{k}$, $E \sim$ 500-1000 eV) compared to the K edges ($E \sim$ 5-10 keV).

The spherically symmetric initial states ($1s$) result in relatively simple dipole selection rules, and the full polarization dependence is easily interpretable. For instance, the angular matrix elements $\langle 2p|\vec{T}(E1)|1s\rangle$ are proportional to $\vec{\epsilon} \cdot \vec{p} \propto \cos(\theta)$ (for linear polarization) where $\vec{p}$ is a unit vector defining the principle axis of the p orbital and θ is the angle between $\vec{\epsilon}$ and $\vec{p}$. The description of the near edge structure for the K edges can be interpreted in first approximation in terms of the single-particle density of states $\rho(\omega)$ (without considering the core-hole potential) with $\alpha(\omega) \sim |M_{ij}|^2\rho(\omega)$. This is because multiplet coupling with the $1s$ core hole is low and the final states are highly delocalized.

For TM compounds, of more interest are the $3d$ orbitals. These states lie energetically below the $4p$ states, and their contribution to K edge spectra appears as weaker "pre-edge" features before the main $1s \to 4p$ edge [110, 150]. Transitions of the type $1s \to 3d$ are dipole forbidden in centrosymmetric crystals, but quadrupole transitions are allowed ($\Delta l = 2$). Thus, for centrosymmetric site symmetry the pre-edge will be weak with an intensity on the order of 10^{-4} compared to the dipole-allowed main edge [145].

Of interest to us is in local coordination symmetries which break inversion symmetry in the site-symmetry group of the transition metal atom. In this case, a local mixing of a dipole contribution to the $3d$ orbitals is allowed, which is related to hybridization effects with the surrounding ligands. Thus, the metal-centered, antibonding molecular orbitals will have a local mixing between the $3d$ and $4p$ states, e.g. $|\Psi\rangle = \alpha|3d\rangle + \beta|4p\rangle$. The interaction mixing terms with different parity is necessarily odd under inversion, and thus such mixing is forbidden for centrosymmetric *site* symmetry (e.g. O_h). Note that inversion symmetry only needs to be broken locally and this process does not imply that inversion is broken at the level of the crystallographic point group (which is a sufficient, but not a necessary condition). In this case, dipole transitions are activated into the projected $4p$ component of the electronic states near the $3d$ pre-edge. The resulting dipole transitions quickly dominate over the weaker, direct $1s \rightarrow 3d$ transitions, leading to much larger intensity (e.g. $10^{-2} - 10^{-1}$ relative to $1s \rightarrow 4p$) even for relatively weak $3d$-$4p$ hybridization [150]. This gives strong, dipole-allowed access to the $3d$ orbitals in the hard X-rays with simple polarization selection rules, which we exploit to study the $3d$ orbital occupancy mismatch in FeSe in Chapter 9.

Specifically, we utilize the technique of X-ray linear dichroism (XLD). XLD refers to the difference of the absorption coefficient for different linear polarization states of the incoming light. In isotropic samples, or crystals with at least 3-fold rotational symmetry around the incident wavevector $\mathbf{k}$, the absorption coefficient for dipole transitions is also isotropic, e.g. independent of the incoming linear polarization [151]. A difference in absorption is driven by a breaking of this rotational symmetry of the local-site environment. For example, with wavevector $\mathbf{k} \parallel \hat{z}$ axis, transitions of the type $\langle 4p_x|T_x|1s\rangle$ and $\langle 4p_y|T_y|4s\rangle$ can become inequivalent, where T_x an T_y are the dipole transition operators for $\vec{x}$ and $\vec{y}$ polarized light. Such absorption coefficients can become inequivalent through either a difference in occupation of the final state orbitals $n(p_x) \neq n(p_y)$ or, relatedly, a difference in their energies $E(p_x) \neq E(p_y)$. Thus, finite XLD with proper choice of incident energy can probe the energy splitting and orbital occupation mismatch of the valence orbitals.

In contrast to the K edges, the TM $L_{2,3}$ edges are more directly sensitive to the d-orbitals with direct dipole-allowed transitions of the type $2p_{1/2}/2p_{3/2} \rightarrow 3d$. The large SOC of the $2p$ shell means that such transitions are directly sensitive to the spin and orbital moments of magnetic order, which can be separated by sum rules in circular dichroism (CD) [152, 153]. This has lead to the technique of X-ray magnetic circular dichroism (XMCD) [110], which has been critical for the characterization of magnetism in e.g., ultrathin films, multi-sublattice systems, and ferrmimagnets. The sum rules of XMCD elegantly highlight the advantages of well-defined, energetically-separated $\mathbf{J}$ manifolds forming the initial states of core-level spectroscopy.

Furthermore, the shallower $2p$ core-level displays much stronger interactions with the valence electrons. The initial state is of the type $2p^6 3d^n$ and the final state of the absorption process is $2p^5 3d^{n+1}$ and one must consider matrix elements of the form $\langle 2p^5 3d^{n+1}|\vec{T}|2p^6 3d^n\rangle$ for calculating the XAS spectrum. Uniquely, the strong $2p$-$3d$ multiplet coupling means that the XAS spectral shape at the $L_{2,3}$ edges is not at all related to the single-particle density of states of the valence shell. Instead, one must consider the multielectronic configurations (Chapter 2) of the $2p^6 3d^n \equiv 3d^n$ and $2p^5 3d^{n+1}$ configurations, with the latter determining the XAS spectral shape [110]. Thus, through TM $L_{2,3}$ edge XAS, one can extract electronic correlation parameters on the d shell (e.g. Slater parameters F^k), in addition to other local parameters such as the crystal field splitting and the ground state SOC in the d shell. In addition, one can also measure satellite structures in the XAS profiles related to charge transfer configurations of the type $3d^{n+m}\underline{L}^m$, which along with X-ray photoemission spectroscopy (XPS) allow the characterization of the charge transfer gap Δ and the metal-ligand hopping parameters t_{pd} which are critical for understanding the electronic structure [110, 111, 154, 155]. We utilize these properties of TM $L_{2,3}$ XAS to probe the electronic structure of the charge-transfer insulator series NiX_2 in Chapter 8. As a final note, such experiments infer ground state properties through the excited state configurations and their spectral weight. More direct information on the ground state can be inferred from resolving the inelastically scattered photons through resonant inelastic X-ray scattering (RIXS), discussed below.

4.2.2 Resonant X-ray scattering: elastic and inelastic

While significant information can be gleaned from spectroscopic measurements (e.g. XAS), the energy range of the core-level transitions in the X-rays means that the incident photons have sufficient momentum to address the characteristic length scales of condensed matter systems up to and exceeding a single Brillouin zone. In particular, one can perform diffraction in resonant conditions, allowing the measurement of long-range order in the spin, orbital and charge degrees of freedom and providing a unique window into the finite momentum ground states of correlated systems (Resonant elastic X-ray scattering - REXS). In addition, one can perform inelastic scattering measurements, allowing the identification of the associated collective excitations and ground state electronic structure (Resonant inelastic X-ray scattering - RIXS).

These processes are fundamentally related to XAS by the same type of core-level transitions discussed in the previous section. REXS and RIXS are both photon in-photon out spectroscopies. Incident photons with energy $\hbar\omega_i$ and wavevector $\mathbf{k}_i$ tuned to a core-level resonance are incident on the sample in the ground state configuration $|i\rangle$. A dipole matrix element leads to a core-to-valence transition and the creation of an intermediate state with a core-hole ($\underline{c}$) present, $|n\rangle$, with an intermediate state lifetime of Γ_n. This first photon absorption step is identical to the single-step XAS process. Subsequently, a photon with $\hbar\omega_f$ and wavevector $\mathbf{k}_f$ is emitted, transitioning the intermediate state to the final state $|f\rangle$ through a valence-to-core transition.

In the dipole approximation with transition operator $\vec{T} = \vec{\epsilon}_i \cdot \mathbf{r}$, the scattering amplitude describing such processes depends on both the incoming and outgoing wavevector ($\mathbf{k}_{i/f}$), energy ($\hbar\omega_{i/f}$) and polarization ($\vec{\epsilon}_{i/f}$) and is given in terms of a second-order perturbation as [145, 146, 156],

$$I \propto \sum_f \left| \sum_n \frac{\langle f|(\vec{T}')^\dagger|n\rangle\langle n|\vec{T}|i\rangle}{\hbar\omega_i - (E_f - E_i) + i\Gamma_n} \right|^2 \delta(\hbar\omega_i - (E_f - E_i)) \tag{4.1}$$

where $(\vec{T}')^\dagger = (\vec{\epsilon}_f)^* \cdot \mathbf{r}^*$ corresponds to the outgoing photon variables. This expression is the Kramers-Heisenberg formula, relevant for resonant processes when the denominator $(\hbar\omega_i - (E_f - E_i) + i\Gamma_n)$ becomes small.

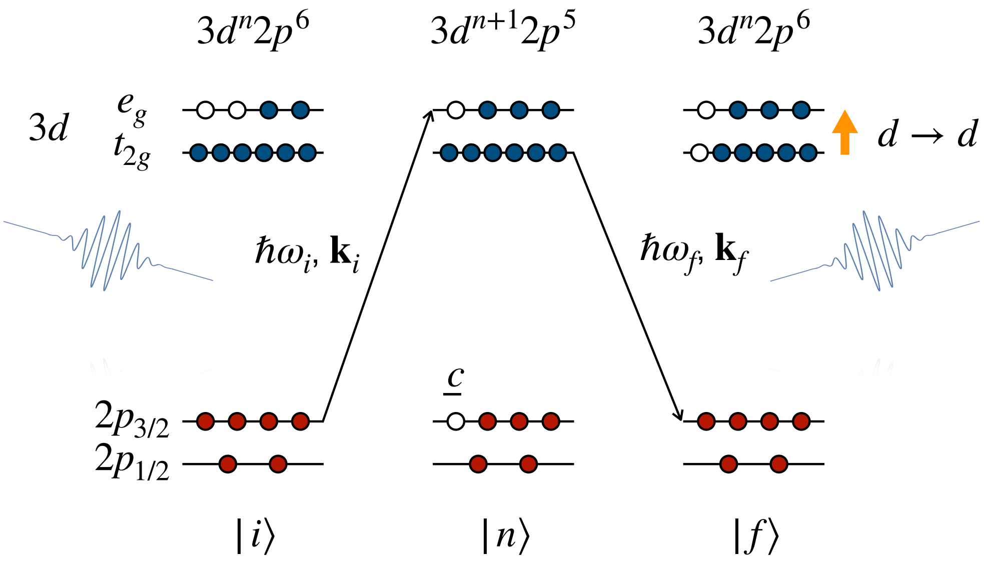

Figure 4.2: Schematic of a $d \to d$ excitation process through L_3 edge resonant scattering. The initial state $|i\rangle$ consists of a $3d^n 2p^6$ configuration. A photon of energy $\hbar\omega_i$ resonant to the $2p_{3/2} \to 3d$ transition is incident on the sample, causing a transition to the $3d^{n+1}2p^5$ configuration in the intermediate state $|n\rangle$ with a $2p$ core hole $\underline{c}$ present. The core-hole is recombined through the emission of a photon with energy $\hbar\omega_f$ and a transition to the final state $|f\rangle$ in the $3d^n 2p^6$ configuration. The final state of the $3d$ shell can be different than the initial state, corresponding to a $d \to d$ excitation - or, more generally, any collective excitation involving the d orbitals - which is dipole allowed in the two-dipole transition process. The energy of this excitation is reflected in the energy loss of the emitted photon $\Delta\omega = \omega_f - \omega_i$ which can be monitored as a function of momentum transfer $\mathbf{q} = \mathbf{k}_f - \mathbf{k}_i$.

For REXS, the scattering process is elastic with $\omega_i = \omega_f$, with $|f\rangle = |g\rangle$ and with the momentum transfer $\mathbf{k}_f - \mathbf{k}_i \equiv \mathbf{q}$ matched to a characteristic periodicity of the system (e.g. structural/magnetic Bragg peak, or a periodic modulation of charge, magnetic or orbital order). The term inside the modulus of Eq. 4.1 corresponds to the resonant scattering amplitude of a single atom f'. Diffraction from infinite crystals at zero temperature is given by the structure factor with $\mathbf{q} \in \mathbf{G}$ where $\mathbf{G}$ is the reciprocal lattice,

$$I(\mathbf{q}) = \left| \sum_n f_n e^{i\mathbf{q}\cdot\mathbf{r}_n} \right|^2$$

where $\mathbf{r}_n$ are atomic positions within a unit cell of the lattice. In standard (non-resonant) X-ray diffraction, the atomic form factor $f_n \equiv f_{n,0}$ is a (spherically symmetric) scalar quantity, related to the total electronic charge of the scattering atom, which is independent of the photon polarization. On resonance, the scattering amplitudes given by Eq. 4.1 may be seen as resonant corrections to the atomic form factor. Thus, the atomic form factor becomes selective to particular atoms in the unit cell, particular valence orbitals of those atoms defined by the transition operator and the core level to which the incident photons are resonant, and also to the spin/orbital degrees of freedom as opposed to just the overall electronic charge. At the TM $L_{2,3}$ edges, diffraction from charge [74], orbital [157] and magnetic [158] orders within the correlated d orbitals have been demonstrated with this technique [159].

A useful practice for describing the resonant contribution to the scattering amplitude is to separate the terms depending on the electronic states from the photon polarization/wavevector dependence [145]. This leads to the scattering tensor $f_{\alpha\beta}$, which in the dipole approximation can be related to the scattering amplitude by $f_n(\epsilon', \epsilon) = (\epsilon')^*_\beta \, f_{\alpha\beta}\epsilon_\alpha$ where,

$$f_{\alpha\beta} = \sum_n \frac{\langle f|r_\alpha|n\rangle\langle n|r_\beta|i\rangle}{\hbar\omega_i - (E_f - E_i) + i\Gamma_n}$$

One can then describe different contributions to the scattering and their coupling the incoming and outgoing polarization dependence through symmetry restrictions to the matter-only form factor $f_{\alpha\beta}$. For example, the isotropic (spherically symmetric) charge contribution to $f_{\alpha\beta}$ corresponds to the trace component of the tensor $\sum_\alpha f_{\alpha\alpha}$, which has a polarization dependence as $\epsilon' \cdot \epsilon$, i.e. the same as expected for Thompson scattering. Of particular interest to us is the scattering tensor for local magnetic moments. These are described by the antisymmetric traceless components of $f_{\alpha\beta}$, and by time-reversal symmetry are complex. For a local magnetic moment with components $\vec{m} = (m_x, m_y, m_z)$, the scattering tensor takes the form,

$$f_{\alpha\beta} \propto \begin{pmatrix} 0 & -im_z & im_y \\ im_z & 0 & -im_x \\ -im_y & im_x & 0 \end{pmatrix}$$

where the sensitivity to the local magnetic moments is provided directly by the breaking of local time-reversal symmetry in the valence states and the large SOC of the core-levels at the L-edges, thus allowing sensitivity to the spin moment even in the dipole approximation. The polarization dependence of resonant magnetic scattering in the dipole approximation is given by the cross product $\epsilon' \times \epsilon$ [160], and thus magnetic scattering leads to scattering in the cross-polarized channel. This polarization dependence described through the scattering tensor allows one to disentangle the microscopic symmetry of the underlying order through a full polarization dependence of the scattering intensity in experiments. The magnetic contrast of REXS at the TM $L_{2,3}$ edges is used to characterize the magnetic order of bulk and thin layers of $\mathrm{NiI_2}$ in Chapter 7.

In contrast to REXS, RIXS describes the process of inelastic scattering with $\omega_i \neq \omega_f$. RIXS is two-dimensional spectroscopy, where one tunes both the incident energy across a core-level resonance ω_i and the corresponding energy-loss of the scattered photons ω_f are monitored [110, 156]. According to Eq. 4.1, the incident energy axis is closely related to XAS.

At the TM L-edges, the intermediate states $|n\rangle$ are given by different terms of the $2p^5 3d^{n+1}$ configuration, and different fine structure components can lead to different scattering cross section between the initial $|i\rangle$ and final $|f\rangle$ states of the ground state $3d^n$ configuration. Thus, the control of the intermediate electronic states through tuning of the incident energy across the XAS spectrum can correspondingly tune the cross section of different energy loss features, providing rich information on the nature of the both the excitations and the ground state electronic structure.

The energy transfer $\Delta\omega$ in RIXS corresponds to the energy of excited states of the system. In the same manner as REXS and XAS, these excitations are sensitive to the spin, orbital, charge and lattice degrees of freedom for the targeted valence orbitals. The technique is also momentum resolved, with momentum transfer $\mathbf{q}$ approaching the first Brillouin zone boundary of solid state materials in the soft X-ray range. Thus, one can measure the collective excitations of the material and monitor their dispersion relations $\omega(\mathbf{q})$. The energy resolution for soft X-ray RIXS (TM L-edges) is currently on the order of 10's meV for state of the art instrumentation [161] and is therefore within the appropriate energy-momentum constraints for studying the collective excitations of solid state systems [156].

In the low-energy regime, RIXS has been demonstrated to measure many forms of bosonic excitations [156], including phonons, magnons, bi-magnons, charge excitations, plasmons and excitons. At higher energies, one can measure the local multiplet transitions (e.g. dd transitions) of the absorbing ion, as discussed in Chap. 2, and charge-transfer transitions [110]. While these types of excitations can also be observed in optical absorption [60], RIXS has the advantage of a direct dipole-allowed sensitivity to dd excitations due to the two-step dipole transition process described by Eq. 4.1. This is depicted in Fig. 4.2 for the case of a simple a crystal-field (inter-orbital $t_{2g} \rightarrow e_g$) transition in a single-particle picture for a $3d^8$ configuration. Additionally, one can also measure spin-state and $\Delta S \neq 0$ transitions due to the core-hole SOC, in addition to their finite momentum properties with the $\mathbf{q}$-resolved probe of RIXS. This has been used to provide evidence for fractionalized excitations (e.g. orbitons) in low-dimensional spin chains [123] and collective spin state transitions to explain mechanism of excitonic magnetism in cobaltates [121].

Thus, RIXS allows a full characterization of the multiplet spectra of TM ions, characterizing all of the key parameters of the ground state configuration, as well as revealing potentially new collective properties to which optical spectroscopy is largely insensitive. For the former, this provides more direct information on the ground state electronic Hamiltonian of the TM ion compared to XAS, since energy loss features reflect multiplets of the $3d^n$ configuration while XAS measures the multiplet spectra of the $3d^{n+1}2p^5$ configuration. The latter has significant modifications in the intermediate state due to the core-valence multiplet coupling and the different electronic filling of the d shell. Also XAS is limited by the lifetime broadening (Γ_n), which can be on the order eV, while the inelastically scattered photons in RIXS are limited by the instrumental resolution and intrinsic broadening [110]. We utilize both the direct dipole-sensitivity of RIXS to $\Delta S \neq 0$ multiplet excitations and their $\mathbf{q}$-dependence to study the nature of excitons in the nickel dihalides in Chapter 8.

4.3 Optical spectroscopy

4.3.1 Optical dichroism and birefringence

The modifications in the polarization of light transmitted through or reflected by materials gives substantial information about the symmetry of the underlying crystal. All such processes are related to the dielectric tensor, $\varepsilon_{\alpha\beta}$, which in turn determine the refraction index and the reflectivity $r_{\alpha\beta}$. There are two primary effects which are typically probed: dichroism and birefringence. As mentioned in the case of X-ray absorption above, dichroism refers to the difference of absorption between two orthogonal polarization states, i.e. linear dichroism (LD) and circular dichroism (CD). Birefringence is instead a difference of the phase between two orthogonal light polarizations. Dichroism and birefringence are thus related to difference in the imaginary (Δk) and real (Δn) parts of the complex refractive index $\tilde{n} = n + ik$, respectively, which are related through Kramers-Kronig relations.

These effects can be measured either by directly probing the difference in the reflectance or transmittance for the two polarization states, or by their effect on incident linear polarized beams. In general, an incident linear polarized beam will become elliptically polarized with a rotation of the principle axis upon reflection, referred to as the ellipticity (η) and rotation (θ), respectively. The ability to perform extremely precise polarimetry measurements of these quantities in the optical range (down to the nano- to micro-radian level [162, 163]) makes possible the detection of subtle optical manifestations of symmetry-lowering transitions in solid state materials.

The presence of finite dichroic/birefringent responses can signal either broken rotational or time-reversal symmetries, where the former can be either crystallographic or magnetic in origin. For time-reversal symmetric media, the dielectric tensor is symmetric $\varepsilon_{\alpha\beta} = \varepsilon_{\beta\alpha}$. For an incident wavevector $\mathbf{k}_i$ along a principle axis (e.g. a high-symmetry axis), then the dielectric tensor for the transverse polarized light is isotropic,

$$\varepsilon = \begin{pmatrix} \varepsilon_{xx} & 0 \\ 0 & \varepsilon_{xx} \end{pmatrix}$$

The system then possesses no dichroism, and incident linear polarization is preserved on reflection or transmission.

A reduction of rotational symmetry in the plane perpendicular to $\mathbf{k}$ results in a difference of the diagonal components of the dielectric tensor, thus allowing finite linear birefringence or dichroism. In the principle basis, the dielectric tensor is then

$$\varepsilon = \begin{pmatrix} \varepsilon_{xx} & 0 \\ 0 & \varepsilon_{xy} \end{pmatrix}$$

In this case, the reflectivity along the principle axes is given by $R_{x,y} = \left|\frac{\sqrt{\varepsilon_{xx,yy}}-1}{\sqrt{\varepsilon_{xx,yy}}+1}\right|^2$. Incident linear polarization along the principle axes is preserved, but will become elliptical or rotated for other directions. Thus, linear dichroism/birefringence leads to finite η/θ which goes to zero for $\vec{\epsilon}$ parallel to either of principle axes, allowing one to experimentally identify this effect.

The origin of $\varepsilon_{xx} \neq \varepsilon_{yy}$ does not need to be structural in origin. Instead, purely magnetic origins of LD exist, referred to as magnetic linear dichroism/birefringence (MLD/MLB) or the Voigt effect [164]. These effects are due to contributions to the dielectric tensor resulting from the interaction between the light polarization and the local spin degree of freedom. Thus, if the crystal possess a global unique spin axis, a quadratic interaction of the form $\varepsilon_{\alpha\beta} \propto S_\alpha S_\beta$ contributes to the dielectric tensor, leading to linear dichroism [164]. This was previous observed in the collinear rutile antiferromagnets. More recently, giant LD in collinear vdW antiferromagnets has been observed [69, 70, 165]. As opposed to the standard MLD which is directly related to the spin direction, these effects were instead attributed to a magnetically-induced anisotropy in the electronic structure due to the rotational symmetry breaking magnetic wavevector. $\varepsilon(\omega)$ is a strong function of frequency, particularly in semiconductors/insulators across the band gap, and thus the origin of the dichroism can change depending on the probing wavelength. In particular, strong dichroic responses are observed on excitonic resonances of either Wannier [57] or Frenkel [69, 70] character, such as those investigated in Chapter 8.

Finally, although not utilized in this thesis, we mention the detection of magnetic moments through optical circular dichroism. A global magnetization $\mathbf{M} \parallel \hat{z}$ leads to an anti-symmetric contribution to $\varepsilon_{\alpha\beta}$. For an otherwise rotationally symmetric lattice, this leads to a dielectric tensor for the plane perpendicular to $\mathbf{k}_i \parallel \mathbf{M}$,

$$\varepsilon(\omega) = \begin{pmatrix} \varepsilon_{xx}(\omega) & i\epsilon_{xy}(\omega) \\ -i\epsilon_{xy}(\omega) & \epsilon_{xx}(\omega) \end{pmatrix}$$

where $\epsilon_{xy}(\omega)$ is a (frequency-dependent) quantity proportional to $\mathbf{M}$. This leads to circular dichroism/birefringence, related to imaginary and real parts of $\epsilon_{xy}(\omega)$. It is important to note that although $\epsilon_{xy}(\omega) \propto \mathbf{M}$, this is also a strong function of frequency and can be heavily rescaled if the magnetization couples non-trivially to the electronic structure effecting the absorption properties near the probing wavelength. Thus, a trivial proportionality between magneto-optical phenomena and the overall magnetization $\mathbf{M}$ must be treated with caution, particularly across metamagnetic transitions when an external magnetic field changes the ground state. Practically, circular dichroism leads to ellipticity upon reflection of incident linear polarized light (Kerr ellipticity, η_k), while circular birefringence leads to the rotation of the linear polarization angle (Kerr rotation, θ_k). The key distinction is that these effects reverse sign under magnetization reversal, and are equal for any incident polarization angle (in qualitative distinction with MLD/MLB). Optical linear dichroism and its characteristic angular dependence is used to detect the rotational symmetry breaking of the magnetic ground state in $\mathrm{NiI_2}$ in Chapters 5-8.

4.3.2 Raman spectroscopy

Raman spectroscopy is an inelastic scattering of photons, typically referring to photon energies in the optical range (e.g. 1 - 4 eV). The Raman process corresponds to an absorption and subsequent emission of a photon, usually through dipole transitions, along with the creation/destruction of an excitation of the system (e.g. phonon). The dominant contribution to the Raman scattering cross-section is given by the third-order perturbation [166, 167], with

$$I \propto \sum_{n.m} \left| \frac{\langle i|(\vec{T}')^{\dagger}|m\rangle\langle m|H_{e-ph}|n\rangle\langle n|\vec{T}|i\rangle}{(\hbar\omega_i - (E_n - E_i))(\hbar\omega_i - (E_m - Ei) - \hbar\omega_{ph})} \right|^2 \delta(\omega_i - \omega_s - \omega_{ph})$$

where $\vec{T}$ are dipole transition operators, H_{e-ph} is the electron-lattice interaction, $|i\rangle$ and $|n\rangle/|m\rangle$ are the initial and (virtual) intermediate electronic states, $\hbar\omega_i/\hbar\omega_o$ is the incident/scattered photon energy and $\hbar\omega_{ph}$ is the energy of the created phonon. This term corresponds to a Stokes Raman processes where a phonon excitation is created, corresponding to an energy loss of the scattered photons by which the δ-function enforces energy conservation. This equation is the dominant process on resonance conditions, but is also the leading term in off-resonance conditions, describing a process where electron-lattice interactions lead to the creation of a phonon through intermediate virtually-excited electronic transitions. Raman is typically performed in off-resonance conditions, although resonance effects are important in heavily studied graphene and TMDs [166, 167].

Raman is principally used to measure optical phonons with $\mathbf{q} \simeq 0$, where the latter is restricted by the small photon momentum in the optical range. The types of phonons that can be measured by this technique are restricted by symmetry to be inversion-symmetric lattice vibrations (in centrosymmetric crystals). These are Γ-point optical phonons whose lattice displacements $\vec{Q}_i$ belong to parity-even irreducible representations (e.g. A_g, B_g, E_g). The symmetry of the phonons measured by Raman can be determined through the corresponding Raman tensor, which reflect the underlying point group of the crystal. Similar to the factorization of the polarization dependence and the matrix elements of the matter states in the case of resonant X-ray scattering, the form of the Raman tensor is,

$$I(\epsilon', \epsilon) \propto \left| (\epsilon')^*_{\mu} R_{\mu\nu} \epsilon_{\nu} \right|^2$$

where $R_{\mu\nu}$ is the (3x3) Raman tensor, depending only on the material, and ϵ'/ϵ are scattered/incident polarization vectors. Symmetry restricted Raman tensors for different irreps are extensively tabulated and can be determined from group theoretical arguments [167, 168]. For non-resonance Raman scattering from phonons, the Raman tensor is symmetric and real, in accordance with the symmetry properties of the electronic polarizability [167]. The full polarization dependence of the Raman-active phonons is a useful tool for the characterization of the point group symmetry of the material.

As an example, we can consider the two Raman active modes observed in backscattering geometry in the $CdCl_2$ structure with $R\bar{3}m$ space group, relevant for the high-temperature phase of the nickel dihalides [42]. The two Raman active phonons are of A_g and E_g symmetry, with corresponding Raman tensors,

$$R(A_g) = \begin{pmatrix} a & 0 & 0 \\ 0 & a & 0 \\ 0 & 0 & b \end{pmatrix}, \quad R(E_g) = \begin{pmatrix} a & 0 & 0 \\ 0 & -a & b \\ 0 & b & 0 \end{pmatrix}$$

where a,b are two real constants and the z axis of the tensor is along the C_{3z} axis. One can measure the Raman tensor by monitoring the scattering intensity with linear polarized excitation with a variable angle θ with respect to the crystallographic axes. One further resolves the scattered light with an analyzing polarizer to measure the scattered light either parallel ('XX') or perpendicular ('XY') to the incident light. In backscattering geometry, these scattering configurations are referred to as the $z(xx)\bar{z}$ and $z(xy)\bar{z}$ channels, respectively, where the notation $\mathbf{k}_i(\epsilon_i\epsilon_o)\mathbf{k}_o$ labels the incident wavevector, incident polarization, scattered polarization and scattered wavevector. In this case, one has incident polarization $\epsilon = (\cos(\theta), \sin(\theta), 0)$ and scattered polarizations $\epsilon' = \epsilon$ (XX) and $\epsilon' = (-\sin(\theta), \cos(\theta), 0)$ (XY), respectively. In this configuration, one finds that the intensity for the A_g phonon $I_{XX}(A_g) = |a|^2$ and $I_{XY}(A_g) = 0$, and for the E_g phonon $I_{XX}(E_g) = |a|^2\cos^2(2\theta)$ and $I_{XY}(E_g) = |a|^2\sin^2(2\theta)$. Thus, the intensity of A_g phonons in $R\bar{3}m$ symmetry are angle-independent in XX and extinct in XY, while E_g phonons are four-fold in both XX and XY with an out-of-phase angle-dependence.

The use of circular polarization also provides well defined selection rules in Raman. Circular polarizations propagating along the z axis are given by $\sigma_{+/-} = (1/\sqrt{2}, \pm i/\sqrt{2}, 0)$. Continuing the above example, one finds $I_{\sigma'_+\sigma_+}(A_g) = |a|^2$ and $I_{\sigma'_-\sigma_+}(A_g) = 0$, while $I_{\sigma'_+\sigma_+}(E_g) = 0$ and $I_{\sigma'_-\sigma_+}(E_g) = |a|^2$. Thus, in the $R\bar{3}m$ phase, the A_g phonons only appear in the co-rotating channels $(\sigma'_+\sigma_+)$, $(\sigma'_-\sigma_-)$ and E_g phonons appear only in the counter-rotating channels $(\sigma'_+\sigma_-)$,$(\sigma'_-\sigma_+)$. Relaxation of these selection rules can be a sensitive detection of reduced point group symmetry. Finally, we note that for symmetric Raman tensors off of resonance conditions and in the absence of time-reversal symmetry breaking, phonons have the same intensity for incident σ_+/σ_- and further obey $I_{\sigma'_+\sigma_+} = I_{\sigma'_-\sigma_-}$ and $I_{\sigma'_-\sigma_+} = I_{\sigma'_+\sigma_-}$; that is, excitations do not show circular dichroism.

Of more interest for us is the measurement of magnetic excitations with Raman. Early studies showed that in rutile antiferromagnets (e.g. MnF_2, CoF_2 and NiF_2), single- and two-magnon excitations could be observed [169], confirmed by direct comparison to neutron scattering measurements. More recently, the measurement of magnetic excitations, including spin wave gaps, quasi-elastic magnetic scattering, and two-magnon scattering have been crucial characterization tools for magnetic order in vdW magnets, including e.g., CrI_3 [170], VI_3[171], and $NiPS_3$ [25, 68].

In the original works, the inelastic scattering by magnons was considered by two mechanisms involving either direct M1 transitions or E1 transitions coupled through virtual intermediate electronic states with finite $\mathbf{L}$ and non-zero SOC [169], with the latter capturing the correct observed polarization selection rules. Thus, the observation of magnetic excitations is likely related to SOC-assisted dipole transitions. This is similar to RIXS, except the involved electronic states at the two energies (X-ray vs optical) are quite distinct, with optical measurements providing weaker overall SOC within the valence shell in contrast to the strong core-level SOC in $L_{2,3}$-edge RIXS.

The Raman tensor for $\mathbf{q} = 0$ magnons through the E1 mechanism is antisymmetric (for orbital singlet ground state configurations) and couples to the cross product $\epsilon' \times \epsilon$ [169]. The specific Raman tensors can be predicted with knowledge of the *magnetic* point group symmetry and the irrep of the magnon excitation at the Γ point. For the simplest case of a purely anti-symmetric Raman tensor in the backscattering configuration,

$$R(M) = \begin{pmatrix} 0 & ia \\ -ia & 0 \end{pmatrix}$$

the expectation is $I_{XX}(M) = 0$, $I_{XY}(M) = |a|^2$ for linear polarized light, and $I_{\sigma'_+\sigma_+}(M) = I_{\sigma'_-\sigma_-}(M) = |a|^2$, $I_{\sigma'_-\sigma_+}(M) = I_{\sigma'_+\sigma_-}(M) = 0$. Thus, simple magnon excitations of purely antisymmetric form are extinct in parallel polarization, have an angular independent intensity in cross-polarization, and appear in the co-rotating channel with circular polarization. The specific form of the Raman tensor for a magnon requires full consideration of the magnetic point group symmetry, and are not generally antisymmetric [170, 172].

Further, antisymmetry of the Raman tensor alone is not sufficient to confirm a magnetic origin of the correspondent excitation, as such tensors are also allowed from time-reversal even processes on resonance. The time-reversal asymmetric processes (magnetic) can be confirmed through comparison of Stokes (St, creation) and anti-Stokes (ASt, destruction) scattering [173]. The complex coefficients of magnetic Raman tensors reflect the fact that these terms reverse sign under a time-reversal operation. For the ground state, applying time-reversal corresponds to reversing the local spin moment, $|S, m_s = S\rangle \rightarrow |S, m_s = -S\rangle$. Meanwhile, the magnons can be expressed in terms of the raising/lowering operators at a given magnetic site i, $S_i^{+/-}$ corresponding to $\Delta m_s = \pm 1$, respectively. From the expression of the Raman tensor in terms of these effective spin operators, one can observe a close correspondence between time-reversed states and St/ASt processes. Besides the usual thermal factor from Bose-Einstein occupation [173], ASt scattering is equivalent to applying time-reversal in regular St scattering [173]. For real, symmetric Raman tensors (e.g. phonons) the tensors are the same and the expected St/ASt intensity ratio is given only by the usual Bose factor. For magnetic excitations, anomalous St/ASt ratios can be observed [174], related to finite circular dichroism which may become allowed if time-reversal symmetry is broken. Specifically, one expects opposite dichroic contrast in St/ASt if the dichroism is of magnetic origin [170]. Raman spectroscopy of the phonons and magnetic excitations is used in Chapters 5 and 6 to study the magnetic phase of NiI_2 down to the few-layer limit and at high-pressures, respectively.

Chapter 5

Evidence for a single-layer van der Waals multiferroic

This chapter is adapted from the corresponding paper published in *Nature* (Ref. [37]) with modifications, corrections, and additional discussion.

This paper is a co-first author work between Qian Song, Emre Ergeçen, Batyr Ilyas and the present author (C.A.O.). Q.S. initiated the project, grew the crystals and fabricated the BPE devices. Q.S. and C.A.O. performed the Raman spectroscopy, LD, and photocurrent measurements, supervised by Riccardo Comin. E.E. and B.I. performed the SHG measurements and corresponding analysis, supervised by Nuh Gedik. The first principles calculations were performed by Jesse Kapeghian, Danila Amoroso and Antia Botana. D.A., Paolo Barone and Silvia Picozzi performed the Monte Carlo calculations. Takashi Taniguchi and Kenji Watanabe provided and characterized the hBN crystals.

5.1 Introduction

Multiferroic materials have garnered wide interest for their exceptional static [33, 45, 175] and dynamical [176–178] magnetoelectric properties. In particular, type-II multiferroics exhibit an inversion-symmetry-breaking magnetic order which directly induces a ferroelectric polarization through various mechanisms, such as the spin-current or the inverse Dzyaloshinskii-Moriya effect [33, 179] (Chapter 3). This intrinsic coupling between the magnetic and dipolar order parameters results in record-strength magnetoelectric effects [33, 180]. Two-dimensional materials possessing such intrinsic multiferroic properties have been long sought for harnessing magnetoelectric coupling in nanoelectronic devices [17, 21, 175]. In this chapter, we report type-II multiferroic order in a single atomic layer of the transition metal-based van der Waals material NiI_2. The multiferroic state of NiI_2 is characterized by a proper-screw spin helix with given handedness, which couples to the charge degrees of freedom to produce a chirality-controlled electrical polarization. We use circular dichroic Raman measurements to directly probe the chiral magnetic ground state and its electromagnon modes originating from dynamic magnetoelectric coupling. Using optical linear birefringence and second-harmonic generation measurements, we detect an anisotropic ground state breaking three-fold rotational and inversion symmetry, supporting polar order. The evolution of the optical signatures as a function of temperature and layer number reveals an ordered, magnetic, polar state that persists down to the ultrathin limit of monolayer NiI_2. These observations establish NiI_2 and transition metal dihalides as a new platform for studying emergent multiferroic phenomena, chiral magnetic textures and ferroelectricity in the two-dimensional limit.

The recent discovery of intrinsic magnetic order in atomically-thin van der Waals (vdW) materials [6, 7] has created new opportunities for the study of collective spin phenomena in free-standing two-dimensional (2D) systems and nanoscale devices [13, 14]. In past years, significant efforts have been made to achieve direct electrical control and manipulation of magnetic properties in 2D [17, 21], but the mechanisms remain elusive. A more promising avenue towards realizing electrical control of 2D magnetism may be found in vdW materials with intrinsic type-II multiferroicity. In type-II multiferroics, the direct coupling between the magnetic and ferroelectric order parameters is enabled by the presence of a spin configuration lacking inversion symmetry [181–183], resulting in a large and robust magnetoelectric response [33, 36, 180].

Among possible multiferroic vdW materials, several families have been identified [12, 13, 184], most prominently the transition metal dihalides (MH_2, M = transition metal, H = halogen). Of particular promise is the magnetic semiconductor NiI_2 [12, 46, 47, 185, 186], which is host to a rich phase diagram including a type-II multiferroic ground state [45, 187]. NiI_2 crystallizes in the rhombohedral $R\bar{3}m$ structure at room temperature, forming a triangular lattice of Ni^{2+} ions ($3d^8$, $S = 1$) which are stacked along the c-axis and held together by weak interlayer bonding [Fig. 5.1(a)]. The 2D triangular lattice geometrically frustrates the intralayer magnetic exchange interactions that govern the long-range ordering of the local Ni spins [46, 47, 188]. This leads to a sequence of magnetic phase transitions in NiI_2, first to an antiferromagnetic (AFM) state at $T_{N,1} \simeq 75$ K[1], and then to a proper-screw helimagnetic ground state below $T_{N,2} \simeq 59.5$ K. The latter exhibits long wavelength helical magnetic structure with propagation vector $\mathbf{Q} = (0.138, 0, 1.457)$ reciprocal lattice units (r.l.u.) [42] [Fig. 5.1(b)]. The helimagnetic transition is concomitant with the appearance of an in-plane electrical polarization perpendicular to the ordering vector [45] as well as crystal symmetry lowering from rhombohedral to monoclinic [42].

In this study, we investigate the multiferroic states in bulk and few-layer NiI_2 crystals [189]. Due to the complexity of the ground state, which simultaneously breaks mirror, rotational, and inversion symmetries, we employ a suite of complementary optical techniques to track the multiple signatures of the polar and magneto-chiral orders, as a function of temperature and layer number. Optical birefringence is found to originate from a lowering of

---

[1] The nature of this antiferromagnetic state between 60 and 75 K has not been elaborated in detail, although ferroelectric polarization along any axis has not been observed [45]. This intermediate state has important implications for the leading magnetic interactions in NiI_2 and is explored in Chapter 7.

the lattice symmetry at both the $T_{N,1}$ and $T_{N,2}$ transitions, and is consistent with a breaking of **c**-axis three-fold rotational symmetry (C_{3z}) and a reduction to a single in-plane two-fold symmetry operation (C_2) [190] (Chapter 4). We further use second harmonic generation (SHG) as a probe of inversion-symmetry breaking, which, together with lowering of rotational symmetry to C_2, enables us to track the presence of polar order down to the single-layer limit. To confirm the presence of magnetochiral order in the helimagnetic phase of NiI_2, we perform Raman spectroscopy with circularly polarized light to resolve a coupled spin-lattice electromagnon excitation with strong optical activity as a signature of spin chirality. These experimental findings are supported by first-principles and Monte Carlo simulations, together providing robust evidence for the persistence of type-II multiferroic order down to single-layer NiI_2.

5.2 Results

5.2.1 Optical Characterization of Multiferroic Order in Bulk NiI_2

We first performed high-resolution, single-domain linear dichroism measurements on bulk NiI_2 – representing the difference in reflectivity ΔR between two perpendicular, linear polarization states – across the two transitions at $T_{N,1}$ and $T_{N,2}$ [Fig. 5.1(c)]. The appearance of optical birefringence indicates the breaking of the three-fold (C_{3z}) rotational symmetry in the parent $\bar{3}m$ point group (see Fig. 5.10). The temperature dependence of ΔR bears a striking resemblance to the magnetic susceptibility (χ_{mag}, Fig. 5.1(c)), with a kink at $T_{N,1}$ and a sharp jump at $T_{N,2}$. Therefore, the reduction in the lattice rotational symmetry is a direct proxy for the change in the magnetic ground state. We further record the dependence of the linear dichroism signal on the angle of linear incident polarization with respect to the crystallographic axes, $\Delta R(\theta)$. These results (inset of Fig. 5.1(c) and Fig. 5.10) display a maximum dichroism of positive sign (blue lobes) for polarization parallel to the crystallographic **a**-axis and display the expected two-fold rotational symmetry, confirming that the low-temperature phase is characterized by a local, unique C_2 axis.

To confirm the polar nature of the low-temperature symmetry group, we measured SHG in bulk NiI_2 from a mono-domain region identified through SHG imaging (Fig. 5.1(d) and Fig. 5.8). Electric-dipole SHG (E1 SHG) is used as a direct probe of inversion-symmetry breaking [191]. Here, the E1 transition mechanism is ensured by tuning the energy of the fundamental beam to a wavelength $\lambda = 991$ nm that is below the optical band-gap and *dd* transitions [190] (for more details, see Chapter 8). This is verified with rotational anisotropy SHG (RA-SHG) measurements, which agree well with the E1 SHG tensor elements predicted for the C_2 monoclinic point group in the helimagnetic phase (inset of Fig. 5.1(c) and Fig. 5.8 below). For wavelengths in the vicinity of the *d*-*d* transitions ($\lambda = 780$ and 826 nm), M1-transition SHG originating purely from spin order, which does not necessitate inversion symmetry breaking, is also present (see Fig. 5.8). The combined observation of E1 SHG (lattice inversion-symmetry breaking) and optical birefringence (rotational-symmetry breaking) directly confirms the presence of a polar phase in NiI_2 and an underlying single-$\mathbf{Q}$, helical magnetic ground state. The resulting electrical polarization induces a bulk photovoltaic effect which was detected in photocurrent measurements on a thin NiI_2 flake (see Fig. 5.4).

To underscore the connection between the optical signatures of polar order and the underlying magnetic state, we have performed Raman measurements ($\lambda = 532$ nm) on bulk NiI_2. Above $T_{N,1}$, the cross-polarized (XY) Raman spectrum of NiI_2 displays a single phonon at 80.2 cm^{-1} of E_g symmetry [189]. Our measurements reveal a major change in the Raman response in the magnetically-ordered phase, including the appearance of two new high-energy modes around 120.8, and 168.8 cm^{-1} [Fig. 5.1(e)] which exhibit polarization selection rules corresponding to single magnon excitations [170, 192] [see Fig. 5.5, 5.6] (Chapter 4). At low-energy transfer, a pronounced quasi-elastic signal (QES) develops on approaching $T_{N,1}$[189] [Fig. 5.1(e)]. Below $T_{N,2}$, this broad excitation hardens into two sharp and distinct modes [Fig. 5.1(e)/(f)], which display a complex set of polarization selection rules compared to the higher energy magnon and phonon excitations [see Fig. 5.5, 5.6] suggesting that they may be electromagnons [33, 176–179]. In support of this interpretation, circular polarized excitation reveals a large Raman optical activity (ROA) for the electromagnon peaks [Fig. 5.1(f)] that is absent for all other phonon and magnon excitations [Fig. 5.5]. The presence of large ROA for the electromagnon underscores it as a direct signature of magneto-chiral order. The reversal of the ROA between Stokes and anti-Stokes scattering [Fig. 5.1(f)] is in agreement with the optical selection rules observed for Raman-active magnetic excitations in previous studies [170].

5.2.2 Layer-Dependence of the Multiferroic Transitions

The presenteed optical characterization of bulk samples serves as a blueprint for the exploration of the multiferroic state in few-layer NiI_2 samples. Figure 5.2(a) shows an optical image of 1- and 2-layer NiI_2 crystals grown by physical vapor deposition on hBN. The optical anisotropy of NiI_2 is directly captured using cross-polarized microscopy, signaling the presence of birefringent domains on both the 1- and 2-layer regions at $T = 5$ K [Fig. 5.2(b)]. As temperature is increased, the birefringent domains vanish from the 1-layer region between T = 15-25 K, and from the 2-layer region between T = 25-35 K [Fig. 5.2(b)]. Crucially, a reduction of rotational symmetry from three-fold to two-fold is also observed in single-layer samples, as confirmed by angular dependent linear dichroism ($\Delta R(\theta)$) measurements [Fig. 5.2(c)]. Angle dependent linear dichroism traces collected in different domains, determined from the cross-polarized images, show the presence of unique two-fold (C_2) axes (highlighted by dashed lines in Fig. 5.2(c)). The detailed layer dependence of the rotational symmetry breaking transition is obtained through birefringence-induced polarization rotation measurements ($\theta(T)$) in Fig. 5.2(d), which reveals a monotonic evolution of the transition temperatures from 1- to 4-layer samples. As discussed in Chapter 4 and below, birefringence-induced polarization rotation captures the same optical signature, namely ro-

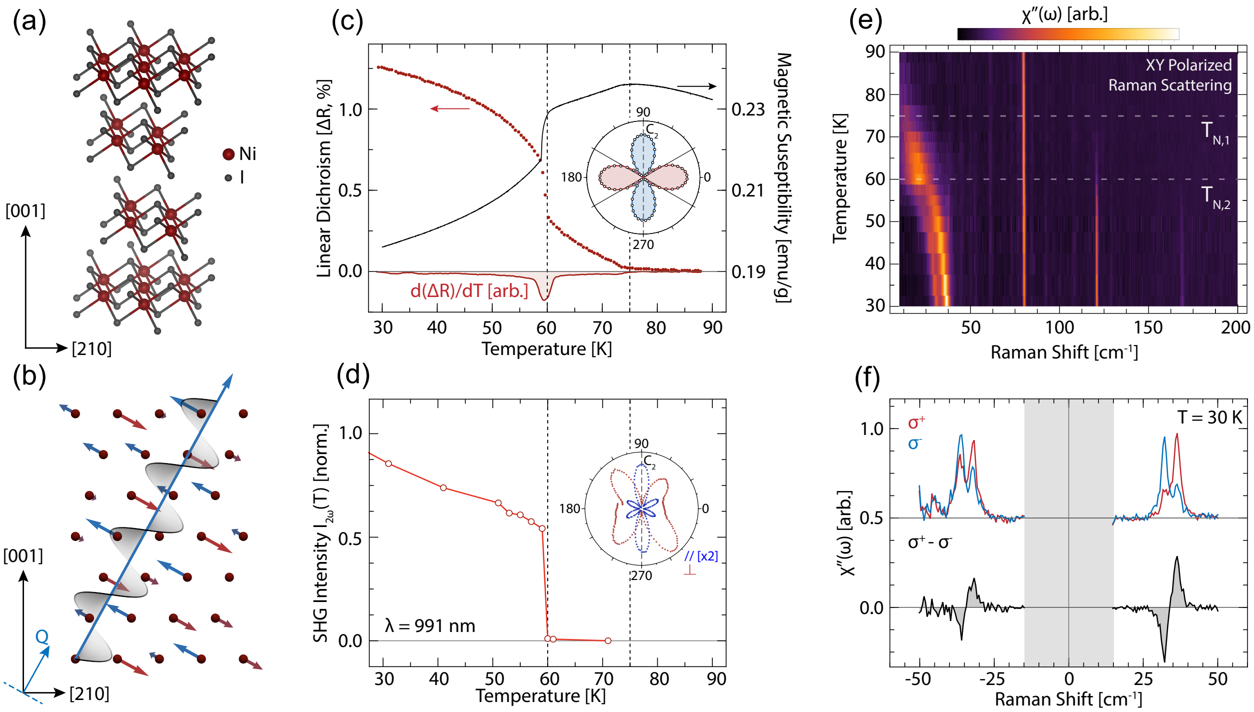

Figure 5.1: (a), The high-temperature $R\bar{3}m$ structure of NiI$_2$. (b), The helical magnetic structure of bulk NiI$_2$ below $T_{N,2} = 59.5$ K (see text). (c), Temperature-dependent linear dichroism ($\Delta R(T)$) measurements on a mono-domain region of bulk NiI$_2$, overlaid on the magnetic susceptibility χ_{mag}. The inset shows the angular-dependence of ΔR at $T = 30$ K – radial lines indicate the crystallographic **a** axes and the dashed line corresponds to the local C_2 axis. (d), Below band gap ($\lambda = 991$ nm) temperature-dependent SHG in bulk NiI$_2$. The inset shows rotational anisotropy SHG patterns for a mono-domain region in the $\parallel$ and $\perp$ polarization channels with the dashed line corresponding to the C_2 axis orientation. Vertical dashed lines in (c),(d) indicate the $T_{N,1}$ and $T_{N,2}$ transitions. (e), Temperature-dependent Raman spectra in the XY polarization channel. (f), Circular-polarized Stokes and Anti-Stokes Raman spectra of the soft mode excitations for σ^+/σ^- incident polarization (top) and the net circular dichroism ($\sigma^+ - \sigma^-$) (bottom).

tational symmetry breaking, as optical linear dichroism measurements. From these data, we define the transition temperatures as the values of maximum slope of the polarization rotation signal (where $d\theta/dT$ is minimum), yielding 21 K for single-layer, 30 K for 2-layer, 39 K for 3-layer and 41 K for 4-layer flakes.

Temperature-dependent E1 SHG ($\lambda = 991$ nm) measurements from 4-, to 1-layer NiI$_2$ samples [Fig. 5.2(e)] provide complementary information on the breaking of inversion symmetry down to the single layer limit. For all samples, the SHG intensity displays a clear drop near the transition temperatures observed independently from the birefringence data. The SHG signal from single-layer samples is genuine as demonstrated by temperature-dependent SHG imaging of multiple monolayer regions (see Fig. 5.9 below). For these SHG spatial maps, we note a temperature-independent residual SHG contrast from single-layer NiI$_2$ samples which likely originates at the NiI_2/hBN interface due to surface inversion symmetry breaking. The breaking of inversion symmetry demonstrated through SHG and the 3-fold rotational symmetry breaking observed in birefringence measurements [Fig. 5.2(b)] establish the persistence of a polar ground state in few- and single-layer samples. Concurrently, Raman measurements reveal the persistence of the magnetic soft modes down to the two-layer limit (see below Fig. 5.7 for PVD samples and Fig. 5.11 for exfoliated chemical vapor transport grown samples). The quantitative agreement of the transition temperatures from these independent measurements, as well as the smooth trend of these optical signatures as layer number is reduced from bulk to the monolayer, thus offer strong evidence for the survival of the polar, helimagnetic phase down to the monolayer limit in NiI_2.

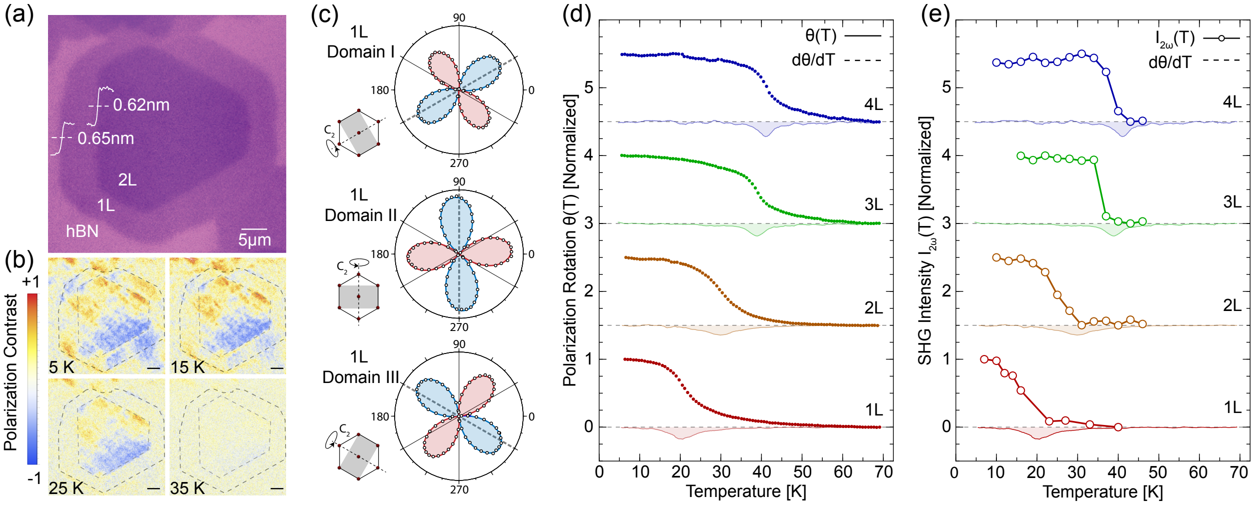

Figure 5.2: (a), Optical image of 1- and 2-layer NiI_2 samples grown on hBN with atomic step height profiles measured by AFM (scale bar: 5 μm). (b), Temperature-dependent polarized microscopy images on the same region in (a). Dashed lines demarcate the 1- and 2-layer regions (scale bars: 5 μm). (c), Angular-dependent linear dichroism $\Delta R(\theta)$ measurements in monolayer NiI_2 on three monodomain regions determined from polarized microscopy, as in (c). Radial lines indicate the crystallographic **a**-axes and the dashed lines indicates the orientation of the local C_2 axis, as shown in the schematics at the left. (d), Temperature-dependent, birefringence-induced polarization rotation $\theta(T)$ measurements acquired in mono-domain regions of 1- to 4-layer NiI_2 samples. (e), Temperature dependent electric-dipole SHG ($\lambda = 991$ nm) intensity for 1- to 4-layer samples. Error bars in the SHG data are smaller than the size of the data points. Dashed curves in (d) and (e) represent $d\theta/dT$ calculated from layer-dependent $\theta(T)$ data in (d). Data are normalized to the value at 5 K and offset vertically for clarity.

5.2.3 Theoretical Basis for the Multiferroic phase of few-layer NiI_2

The observed reduction of the transition temperature as layer number is decreased is strongly indicative of the relevant role played by the interlayer exchange interaction, as also reported for other 2D magnets [6, 192–196], while the finite transition temperature detected in the monolayer sample points to a non-negligible magnetic anisotropy.

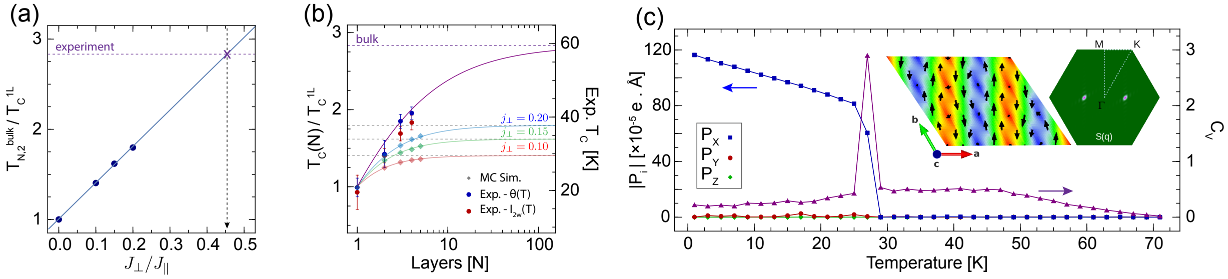

Figure 5.3: (a), Evolution of the reduced temperature t as a function of the interlayer exchange $J_\perp/J_\parallel$, where $t = T_{N,2}/T_c^{1-layer}$ is the ratio of bulk and 1-layer transition temperatures. Circles denote Monte Carlo estimates, the solid line linearly extrapolates t to larger $J_\perp$. Horizontal dashed line indicates the experimental reduced temperature, $t =\simeq 2.8$, while the vertical one points to the estimated $J_\perp \simeq 0.45 J_\parallel$. (b), Evolution of the critical temperature as a function of the number of layers (N). Full symbols (open diamonds) denote the Monte Carlo (experimental) estimates and full lines correspond to the empirical relation provided in Methods. Dotted horizontal lines represent the bulk transition temperature corresponding to the effective interlayer interaction. (c), Electrical polarization components in units of $10^{-5} e$Å (absolute value, closed square) and specific heat (stars) as a function of temperature, relative to the proper-screw spiral order represented in the insets (spin texture – black arrows represent in-plane components of spins, colormap indicates the out-of-plane spin component, s_z=+(-)1 red(blue)- and $S(\mathbf{Q})$, respectively), as obtained via Monte Carlo simulations.

We performed Monte Carlo (MC) simulations to further investigate the role of the interlayer exchange interaction in the helimagnetic transition temperature. Our starting model is the classical 2D anisotropic Heisenberg model recently introduced for NiI_2 monolayer [47], supplemented by a nearest-neighbor antiferromagnetic interlayer exchange $J_\perp$ in order to describe the bulk phase. The presence of anisotropic interactions guarantees a finite-temperature transition to a long-range ordered magnetic phase even in the monolayer [Fig. 5.3(c)]. On the other hand, the transition temperature of the bulk system is found to increase proportionally to $J_\perp$ [Fig. 5.3(a)]. Experimentally, the helimagnetic transition temperature of the 1-layer sample is strongly reduced from its bulk value, being $T_{N,2}/T_c^{1-layer} \simeq 2.8$. A linear extrapolation of the MC estimates for transition temperatures as a function of $J_\perp$ allows to estimate a quite large interlayer exchange, $J_\perp \sim 0.45\ J_\parallel$, where $J_\parallel$ is the dominant ferromagnetic intralayer interaction. Using $J_\parallel \simeq 7$ meV [47], the estimated interlayer exchange is $J_\perp = 3.15$ meV; this is in quite good agreement with the value we directly calculated by means of Density Functional Theory (DFT) calculations for 2-layer NiI_2, that is $J_\perp^{(DFT)} \sim 3$ meV. The evolution of transition temperatures as a function of the sample thickness has also been estimated with MC simulations for different number of layers N (ranging from 1 to 5) and at fixed $J_\perp$. Remarkably, all MC estimates and the experimental data are well described by a simple empirical formula that depends only on the ratio of bulk and 1-layer transition temperatures with no fitting parameters, as shown in Fig. 5.3(b).

The possible onset of a magnetically induced electric polarization in 1-layer NiI_2 has been further investigated in the framework of the generalized spin-current (or Katsura-Nagaosa-Balatsky, gKNB) model [40], where an electric dipole may be induced by spin pairs according to the general expression $\mathbf{P}_{ij} = \mathbf{M} \cdot \mathbf{S}_i \times \mathbf{S}_j$ (Chapter 3). The 3×3 $\mathbf{M}$ tensor has been evaluated from first-principles and used to estimate the polarization of NiI_2 monolayer from MC simulations. As shown in Fig. 5.3(c), a proper-screw spiral propagating along the $\boldsymbol{a}$ lattice vector stabilizes below $T_c \sim 27$ K, in reasonable agreement with the experimental value of 21 K. The corresponding magnetic point group is the polar $21'$ group, with the twofold rotational axis and the electric polarization coinciding with the spiral propagation vector and hence with the **a** axis, in agreement with the optical measurements. Within the gKNB model, the handedness of the spin spiral uniquely determines if the electric polarization is parallel or antiparallel to the polar axis. We further notice that when the magnetic helix is slanted from the basal plane with a propagation vector $\mathbf{Q} = (0.138,0,1.457)$, as it occurs in bulk samples, the purely spin-induced polarization as evaluated from our estimated $\mathbf{M}$-tensor is always parallel to the crystallographic **a** axis.

5.3 Discussion

NiI_2, down to the 2D limit, is therefore an example of a material with improper electronic ferroelectricity, where the electric polarization is driven by the emergence of an inversion-symmetry breaking magnetic order (such as the proper-screw spin helix) in an otherwise centrosymmetric lattice. The propensity for such spin-spiral ordering in the single-layer limit can be associated to the significant frustration of the intralayer exchange interactions on the underlying triangular lattice, along with crucial magnetic anisotropy effects [47]. Furthermore, NiI_2 shows superexchange mediated by the extended $5p$ states of the iodine ligands, the latter also introducing a significant spin-orbit coupling (SOC). As a result, non-negligible spin interactions beyond nearest neighbor Ni sites play a relevant role in the stabilization of the resulting proper-screw spin-helix, the latter giving rise to SOC-induced electric polarization, as described by the generalized KNB model [40]. In this framework, the observation of SHG and birefringence in monolayer NiI_2 is consistent with the proposed theoretical picture, providing a direct indication of a non-centrosymmetric polar magnetic texture that develops below the identified Curie temperature of 21 K. The observed suppression of the multiferroic transition temperature with reducing layer number further allowed us to clarify the role of the interlayer exchange interactions, which are known to contribute to the orientation of the spin-rotation plane and magnetic ordering vector in the bulk [42, 188].

Our results point to the crucial role of SOC and orbital extension of the ligands in modulating both the long-range magnetic interactions and the exchange anisotropy, ultimately determining the magnetic ground state among closely lying, competing phases [47]. This suggests that changing the ligand could be a powerful tuning knob to realize new exotic magnetic ground states in 2D, including helices, cycloids and skyrmions with unique topological and multiferroic properties [46, 47, 197]. In addition, our observations of a complex magnetic ground state in an atomically-thin vdW crystal introduces new avenues for exploring multiferroicity which are inherently unique to 2D systems. These include the robust and direct electrical control of magnetism through electrostatic doping or external fields and currents, or the realization of new interfacial multiferroic properties in artificial vdW heterostructures. Moreover, 2D materials with gate-tunable magnetoelectric coupling might offer a new platform for continuous tuning of multiferroic systems toward quantum critical behavior [198]. While our optical measurements establish the persistence of multiferroicity in NiI_2 to the monolayer limit, further characterization through piezo-response force microscopy or high-sensitivity pyroelectric current measurements will be of great importance to confirm the electrical manifestations of multiferroicity and assess its potential for these future device applications.

5.4 Methods

Growth and Characterization of Few-Layer NiI_2 Crystals Bulk-like NiI_2 crystals were grown on 300 nm SiO_2/Si and few-layer crystals were grown on hexagonal boron nitride (hBN) substrates via physical vapor deposition (PVD) in a horizontal single-zone furnace equipped with a 0.5 in. diameter quartz tube at ambient pressure. hBN was mechanically exfoliated and transferred onto 300 nm SiO_2/Si substrates, then annealed in vacuum at 700 °C for 1 h prior to the growth. In a typical synthesis, 0.1 g of NiI_2 powder (99.5%, anhydrous, Alfa Aesar) was positioned at the center of the furnace as the source material and the SiO_2/Si substrate was placed downstream at the maximum temperature gradient point. The furnace was purged by pumping the quartz tube below 0.1 Torr and then refilled with 99.99% Ar gas three times. When growing bulk-like NiI_2 crystals, the furnace was heated to $450°C$ in 15 minutes and held at that temperature for 10 minutes. For few-layer NiI_2 samples, the furnace was heated to $380\text{-}420°C$ in 15 minutes and then the SiO_2/Si substrate was taken out immediately and stored inside a nitrogen-filled glove box ($O_2 < 0.5$ ppm, $H_2O < 0.5$ ppm). The sample thickness was determined by atomic force microscopy (AFMWorkshop HR), which was performed inside a separate nitrogen-filled glovebox ($O_2 < 100$ ppm, $H_2O < 1$ ppm), using a silicon probe in tapping mode.

Growth and Characterization of Single Crystal NiI_2 Single crystal NiI_2 was grown by chemical vapor transport (CVT), from elemental precursors with molar ratio Ni:I=1:2, at a temperature gradient 700°C to 500°C. The magnetic susceptibility was measured during field cooling at 0.9 T applied out of plane, using a Magnetic Property Measurement System (MPMS-3, Quantum Design Inc.). X-ray diffraction of CVT grown crystals was performed in Bragg geometry using Cu K_α radiation (PANalytical), and the refined unit cell at room temperature is $a = 3.91$ Å, $c = 19.93$ Å.

Device fabrication for bulk photovoltaic effect measurements. The photocurrent device was fabricated by depositing two Ti(5nm)/Au(50 nm) electrodes on a sapphire substrate using a 20 μm wide wire mask. A PVD-grown bulk-like NiI_2 flake was then picked up and dropped down across the gap using a polymer-based dry transfer technique. To minimize the exposure to moisture, the polymer was dissolved in anhydrous chloroform inside the glovebox. To ensure a good and uniform electric contact, a carbon copy of the metal pads was created using the same dry transfer technique and stacked on top of the sample to provide a vertically symmetric contact. We used a 0.3 mW linearly-polarized 532 nm laser for the photocurrent measurement. The current was measured using a Keithley 2401 current meter, and the magnetic field was applied perpendicular to the electric field in plane using a 1 T electromagnet from Montana Instruments. The photocurrent measurements are shown in Fig. 5.4.

Raman Spectroscopy Measurements Polarized Raman experiments were performed in a back-scattering geometry using a confocal microscope spectrometer (Horiba LabRAM HR Evolution) with a 50x objective lens and 532 nm laser excitation at a power of 300μW (40μW) for bulk (few-layer) samples, respectively. Scattered light was dispersed by a 1800 lines/mm grating and detected with a liquid nitrogen cooled charge-coupled device (CCD) camera. The spectrometer integration time was 30/60 minutes for bulk/few-layer samples, and each scan was taken twice and then averaged before analysis. Polarized Raman spectra were recorded with a linearly polarized incident beam. For angle-resolved polarized Raman spectroscopy (ARPRS) measurements, an achromatic half-wave plate was placed just before the objective and rotated in steps of 7.5° from 0° to 180°. An analyzer was placed in front of the spectrometer entrance and kept vertical/horizontal for parallel (XX)/perpendicular (XY) configurations, respectively. For circularly polarized measurements, an achromatic quarter-wave plate was placed in front of the objective with fast axis oriented at +/- 45 degrees with respect to the incident linear polarization for σ^+/σ^- circular incident polarization, respectively. For the reported circularly polarized spectra, no analyzing polarizer is used unless otherwise specified. Temperature-dependent measurements in the range $5 - 300\,\mathrm{K}$ were performed using a Montana Instruments S50 closed-cycle optical cryostat.

Birefringence Measurements A supercontinuum light source (NKT Photonics, Fianium) monochromatized to $\lambda = 532$ nm/550 nm and a bandwidth of approximately 1 nm was used as excitation for angular-dependent linear dichroism and birefringence-induced polarization rotation measurements, respectively. All measurements were performed at normal incidence in a Montana Instruments closed-cycle optical cryostat. Linear dichroism measurements were performed with a photo-elastic modulator (PEM-100, Hinds Instruments) on the incident path of the optical setup. The beam incident on the PEM is prepared in linear polarization making an angle of 45° with the respect to the PEM fast axis and amplitude modulated with a mechanical chopper. The PEM retardance was set to 0.5λ to modulate the incident polarization between ±45° linear polarization states. The light is then focused onto the sample using a 50x objective lens. The backscattered light is measured by an amplified pho-

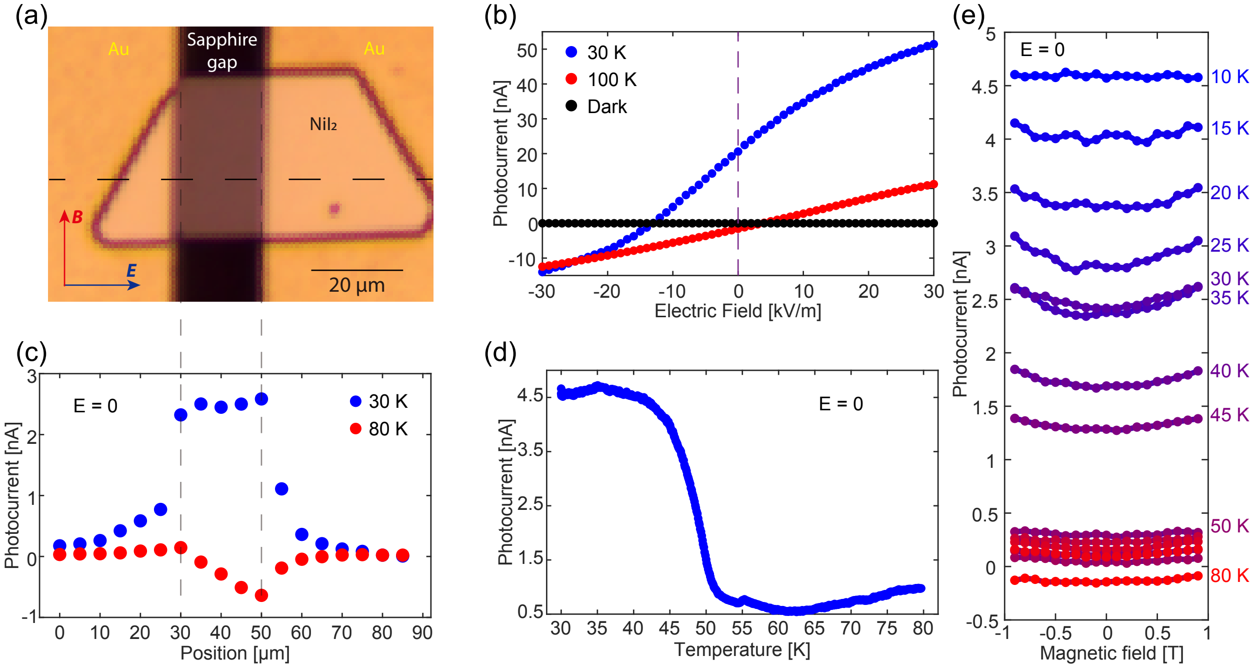

Figure 5.4: (a), Optical image of the BPE device. A PVD grown bulk-like NiI_2 flake transferred across a sapphire gap, bridging two gold pads as electrodes. Electric field is applied between the electrodes and in a direction nearly parallel to the crystallographic **a**-axis, while the magnetic field is applied perpendicular to the electric field in plane. (b), The electric field dependence of the photocurrent at 30 K, in the multiferroic phase and at 100 K (the paramagnetic phase), reveals the presence of a polarization-induced internal electric field in the multiferroic phase. (c), The position dependence of the photocurrent along the dashed line in (a), under zero bias shows a uniform, bulk contribution to the photocurrent from the NiI_2 between the electrodes. (d), The temperature dependence of the zero-bias photocurrent, showing a strong enhancement in the multiferroic phase. (e), The external magnetic field increased the zero-bias photocurrent by 10-15%, which we ascribe to an increase of the electric polarization from magnetoelectric coupling. Linearly polarized 532 nm light (0.3 mW power) was used in the BPE measurement.

todiode (ThorLabs PDA100A2), whose output is connected to a lock-in amplifier (Stanford Instruments SR865A) referenced to the second harmonic of the fundamental PEM frequency $f = 50$ kHz. The total reflectance of the sample, used as a normalization, is monitored by a second lock-in amplifier referenced to the chopping frequency $f = 557$ Hz.

To perform angular-dependent linear dichroism measurements, the angle of the perpendicular linear polarization states created by the PEM is varied across the crystal using a zero-order half-wave plate placed just before the objective. In order to ensure the angular-dependence is recorded from a uniform, mono-domain region of the sample, polarized microscopy images were first recorded at the base temperature $T = 5$ K. The sample was held at this temperature for the duration of the angular-dependent measurements in order to maintain the same distribution of birefringent domains. Birefringence-induced polarization rotation measurements on the few- and single-layer samples were performed with the PEM on the detection path of the optical setup with a retardance amplitude of 0.486λ, using a lock-in amplifier at the second harmonic of the fundamental PEM frequency for signal collection. The unrotated incident beam is kept parallel to the PEM fast-axis and analyzed by a polarizer at 45 deg. before being measured by the photodiode. This setup provided a sensitivity down to 10 μrad. For higher resolution measurements in the few-layer samples (Fig. 5.2), the reflected beam polarization was analyzed using a PEM (0.5 λ retardance) on the detection path, followed by a Wollaston prism at 45° and a balanced photodiode. This setup provided higher sensitivity down to < 1 μrad.

Polarized microscopy was performed with a broadband visible LED light source, a standard CMOS-based monochrome camera and Glan-Thompson polarizers on both the input and output light paths in reflection geometry. A detuning of 0.5 (2.0) degrees from a cross-polarized configuration was used to maximize the contrast from birefringent domains and a 5 (2) second integration time was used for the images of few-layer (bulk) samples. Cross-polarized contrast images were obtained as a function of temperature by auto-correlating the images for different temperatures to overlap with a high-temperature ($T > T_{N,1}$) reference, and subtracting the low and high temperature images.

Layer-Dependent Second Harmonic Generation Microscopy. In second harmonic generation (SHG) microscopy, an objective lens (Olympus LMPlanFL-N 50x) focuses an ultrashort laser beam onto the sample located in a cryostat (Janis ST-500). For wavelength dependent SHG experiments, we used an optical parametric amplifier (ORPHEUS, Light Conversion) seeded with a regenerative amplifier (PHAROS SP-10-600-PP, Light Conversion). These allowed us to tune the output wavelength in a wide spectral range. The estimated spot size on the sample is $\sim 2\mu m$. The laser fluence incident on the sample was set to 1 mJ/cm^2. No sample damage or degradation was observed during the measurements. Upon reflection, the second harmonic component of the beam radiated from sample was selected by a dichroic mirror and a monochromator with 2 nm spectral resolution. The second harmonic photons were detected and counted using a photomultiplier tube (Hamamatsu PMT) and a dual-channel gated photon-counter (Stanford Research SR400). To decrease the background and dark counts, the photon counter was synchronized and gated with laser pulses. To perform SHG imaging (Fig. 5.9), we keep the sample location fixed and rotate a motorized mirror to scan the laser across the sample. The polarization angle of the pulses were controlled using a wire-grid polarizer and a half-waveplate respectively to obtain the polarization resolved second harmonic traces.

Spin model and Monte Carlo simulations. To describe the magnetic properties of the system we adopted the 2D anisotropic Heisenberg model derived for NiI_2 monolayer [47] supplemented by a nearest-neighbour antiferromagnetic interlayer interaction accounting for the exchange between rhombohedral-stacked layers:

$$H = \frac{1}{2}\sum_{ij}\left(\mathbf{S}_i^{(e)}\cdot\mathbf{J}_{ij}\cdot\mathbf{S}_j^{(e)} + \mathbf{S}_i^{(o)}\cdot\mathbf{J}_{ij}\cdot\mathbf{S}_j^{(o)}\right) + \sum_i \mathbf{S}_i\cdot\mathbf{A}_{ii}\cdot\mathbf{S}_i + J_\perp \sum_{<ij>}\mathbf{S}_i^{(e)}\cdot\mathbf{S}_j^{(o)} \tag{5.1}$$

Here e and o label respectively even and odd layers perpendicular to the **c** axis, the first sum extends to third nearest neighbour within each plane while the last sum is restricted to nearest-neighbors belonging to different layers. We used the interlayer exchange $\mathbf{J}_{ij}$ and single-site anisotropy $\mathbf{A}_{ij}$ tensors evaluated from first principles for NiI_2 monolayer [47]; the non-negligible anisotropic terms guarantee a finite-temperature long-range magnetic order, with a triple-**Q** topological phase competing with single-**Q** spiral configuration. The anisotropic part of the exchange tensor has been accordingly rescaled to 60% of the ab initio estimate, thus favouring the spin-spiral solution, in agreement with the breaking of the three-fold rotational symmetry experimentally detected. We set the energy scale as $J_\parallel = -J^{1iso}$, the ferromagnetic nearest-neighbour interlayer interaction.

We performed Monte Carlo simulations using a standard Metropolis algorithm on rhombohedral stacked triangular lattices (rhombohedral supercells in hexagonal setting) in slab geometry to simulate multilayer (bulk) NiI_2. We used 10^5 MC steps for thermalization and 5×10^5 MC steps for statistical averaging at each simulated temperature. Simulations have been performed on 24×24 lattices in slab geometry comprising up to 5 layers of triangular NiI_2 (and up to 2880 spins) with two-dimensional periodic boundary conditions (PBC), and on 8×8×8 hexagonal supercells (comprising 1536 spins) with three-dimensional PBC for bulk rhombohedral system. The transition temperature is identified by the peak in the specific heat of the spin model. All MC results for multilayer slabs at different values of interlayer exchange $J_\perp$ are well described by a simple empirical function:

$$T_c(N) = T_c^{1-layer}\tanh\left(b\ln N + \frac{1}{2}\ln\frac{t+1}{t-1}\right), \tag{5.2}$$

where $t = T_{N,2}/T_c^{1-layer}$ is the reduced temperature, N is the number of layers and the coefficient $b = 1.05$ has been obtained by fitting only the $J_\perp = 0.1\ J_\parallel$ data points.

Generalised spin-current model for magnetically induced polarization. Within the generalised spin-current model gKNB [40], the total polarization is given by (Chapter 3):

$$\mathbf{P} = \frac{1}{2N}\sum_{ij}\mathbf{M}_{ij}\cdot\mathbf{S}_i\times\mathbf{S}_j, \tag{5.3}$$

where N is the number of magnetic sites, and we restricted the sum to interlayer nearest-neighbors. The M-tensor has been evaluated from first principles for a spin pair parallel to the **a** axis using the four-state method [40] (the tensor of equivalent bonds is readily obtained by enforcing crystalline symmetries). The dominant tensor components found are $M_{22} = 348\times10^{-5}$ eÅ and $M_{23} = -520\times10^{-5}$ eÅ, the other components being zero or smaller than $\sim$ 30 eÅ. Assuming a proper-screw spiral with positive/negative handedness $\tau = \pm 1$ propagating along the $\mathbf{a}$ (x) axis with pitch 2δ, the gKNB model predicts $P_x \equiv P_\parallel = 3\,M_{22}\sin(\tau\delta)/2$, in agreement with numerical MC calculations. For the proper-screw spiral propagating along the $\mathbf{Q} = (0.138,0,1.457)$ direction, with the spins rotating in a plane making an angle $\theta = 55°$ as observed in bulk $\mathrm{NiI_2}$ [42], the electric polarization predicted by the gKNB model lies in the ab plane and is perpendicular to the in-plane projection of $\mathbf{Q}$, $P_\perp = \sqrt{3}[M_{22}\cos\theta - 2M_{23}\sin\theta]\sin(\tau 0.138)/2$. In both cases, handedness τ determines the sign of $\mathbf{P}$, that is always parallel to the crystallographic axis $\mathbf{a}$.

First-principles calculations. We used Density Functional Theory (DFT) to estimate the interlayer exchange interaction and the $\mathbf{M}$-tensor of the gKNB model. The interlayer coupling $J_\perp$ has been estimated from the energy difference between a ferromagnetic (FM) and antiferromagnetic (AFM) stacking of ferromagnetically ordered $\mathrm{NiI_2}$ layers, ($\Delta\mathrm{E} = \mathrm{E}_{FM}$-$\mathrm{E}_{AFM}$). A rhombohedral-stacked bilayer has been constructed starting from the optimised $\mathrm{NiI_2}$ monolayer, with lattice parameter $a \sim 3.96$ Å and an interlayer distance of about 6.54 Å, in agreement with the previously reported bulk value [12]. A vacuum distance of about 18.45 Å was introduced between periodic copies of the free-standing bilayer along the $\mathbf{c}$ axis. To check the consistency of our results, we performed DFT calculations using both the projector-augmented wave (PAW) method as implemented in the VASP code [199, 200] and the all-electron, full potential code WIEN2k [201], based on the augmented plane wave plus local orbital (APW+lo) basis set. Ni $3p$, $3d$ and $4s$, and I $5s$ and $5p$ have been treated as valence states in VASP calculations, with a plane-wave cutoff of 500 eV and a $18 \times 18 \times 2$ k-points mesh for Brillouin-zone (BZ) integration. In the WIEN2k calculations, a muffin-tin radius of 2.5 Å was used for both Ni and I atoms, as well as an RK_{max} of 7.0. A k-mesh of $20 \times 20 \times 2$ was used for the BZ sampling. For consistency with previous monolayer calculations [47], we used the Perdew-Burke-Erzenhof (PBE) version of the generalized gradient approximation as the exchange-correlation functional [202] and further performed PBE+U calculations [203] employing $U = 1.8$ eV and $J = 0.8$ eV on the localized Ni-$3d$ orbitals within the Liechtenstein approach [114]. The interlayer exchange defined as $J_\perp = \frac{\Delta E}{6S^{(1)}S^{(2)}}$ is $\simeq +3.1$ meV within VASP and $\simeq +2.8$ meV within WIEN2k. Similar results were also obtained by introducing the spin-orbit coupling (SOC) and by employing PBEsol [204] and optB86 [205] exchange-correlation functionals, that proves robustness of our results. A similar procedure applied to $\mathrm{NiBr_2}$ bilayer yields a much smaller interlayer AFM coupling of about $\simeq +1.2$ meV, suggesting a non-trivial role of extended I-$5p$ orbital states in mediating spin exchange across layers of $\mathrm{NiI_2}$.

The $\mathbf{M}$-tensor has been evaluated following the no-substitution four-state method [40] performing DFT+U+SOC calculations with VASP on a $5 \times 4 \times 1$ supercell of $\mathrm{NiI_2}$ monolayer. We selected a pair of spins ($\mathbf{S}_1$ and $\mathbf{S}_2$) along the x-axis (parallel to the $\boldsymbol{a}$ lattice vector) and calculated the Berry-phase polarization arising from different sets of four noncollinear spin configurations, defining the **M**-tensor, in units of 10^{-5} eÅ, as

$$\mathbf{M} = \begin{bmatrix} (\boldsymbol{P}_{12}^{yz})_x & (\boldsymbol{P}_{12}^{zx})_x & (\boldsymbol{P}_{12}^{xy})_x \\ (\boldsymbol{P}_{12}^{yz})_y & (\boldsymbol{P}_{12}^{zx})_y & (\boldsymbol{P}_{12}^{xy})_y \\ (\boldsymbol{P}_{12}^{yz})_z & (\boldsymbol{P}_{12}^{zx})_z & (\boldsymbol{P}_{12}^{xy})_z \end{bmatrix} = \begin{pmatrix} 20 & 0 & 32 \\ 0 & 348 & -520 \\ 0 & 25 & 0 \end{pmatrix} \tag{5.4}$$

The accuracy of polarization values has been checked by repeating calculations with a larger vacuum of about 32 Å and including dipole corrections.

5.5 Additional Data and Discussion

Symmetry analysis of Raman tensors

NiI_2 crystallizes in the $R\bar{3}m$ structure at room temperature [189], with the irreducible representations of the Raman active phonons being A_g and E_g, with corresponding Raman tensors shown in Chapter 4. At low temperature, NiI_2 transitions into a monoclinic structure (see Chapter 6 and 7 for details). The Raman tensors of A_g phonon modes and M magnon modes have the following form:

A_g	M
$\begin{pmatrix} a & d & 0 \\ d & b & 0 \\ 0 & 0 & c \end{pmatrix}$	$\begin{pmatrix} 0 & ie & 0 \\ -ie & 0 & if \\ 0 & -if & 0 \end{pmatrix}$

Fig. 5.6 shows the ARPRS of bulk NiI_2 at 30 K in monoclinic phase. The ARPRS pattern of a phonon mode is expected to display a polar plot with four lobes and four nodes (zero intensity) while the ARPRS of a magnon mode should be a constant. The 79.9 cm^{-1} and 80.2 cm^{-1} modes are two closely spaced phonon modes (corresponding to E_g modes at room temperature) that are out of phase, which is similar to what observed in the ARPRS plots of CrI_3 and $CrCl_3$ in the monoclinic phase [206, 207]. The 120.8 cm^{-1} and 168.8 cm^{-1} are magnon modes, and the 120.8 cm^{-1} mode onsets at $T_{N,1}$, which indicates that it is an antiferromagnetic magnon. The 31 cm^{-1} and 37.5 cm^{-1} modes appear only in the multiferroic phase and are not consistent with either pure phonon or pure magnon excitations from the ARPRS analysis.

The dichroic contrast of the Raman intensity in different circularly polarized channels supports the previous assignment of each Raman mode via selection rules [Fig. 5.5(c)], as discussed in Chapter 4. The expected circular selection rules discussed there agree well with the 79.9 cm^{-1}, 80.2 cm^{-1}, and 128 cm^{-1} phonon modes [Fig. 5.6(a,b)]. This consideration, in conjunction with the angular independent ARPRS patterns, also confirms the magnetic origin of the 120.8 cm^{-1} and 168.8 cm^{-1} excitations. The 31 cm^{-1} and 37.5 cm^{-1} modes are more complex. Both excitations appear in σ_+/σ_- channels with different intensities and appear only in the multiferroic phase which suggests that they may be phonon/magnon

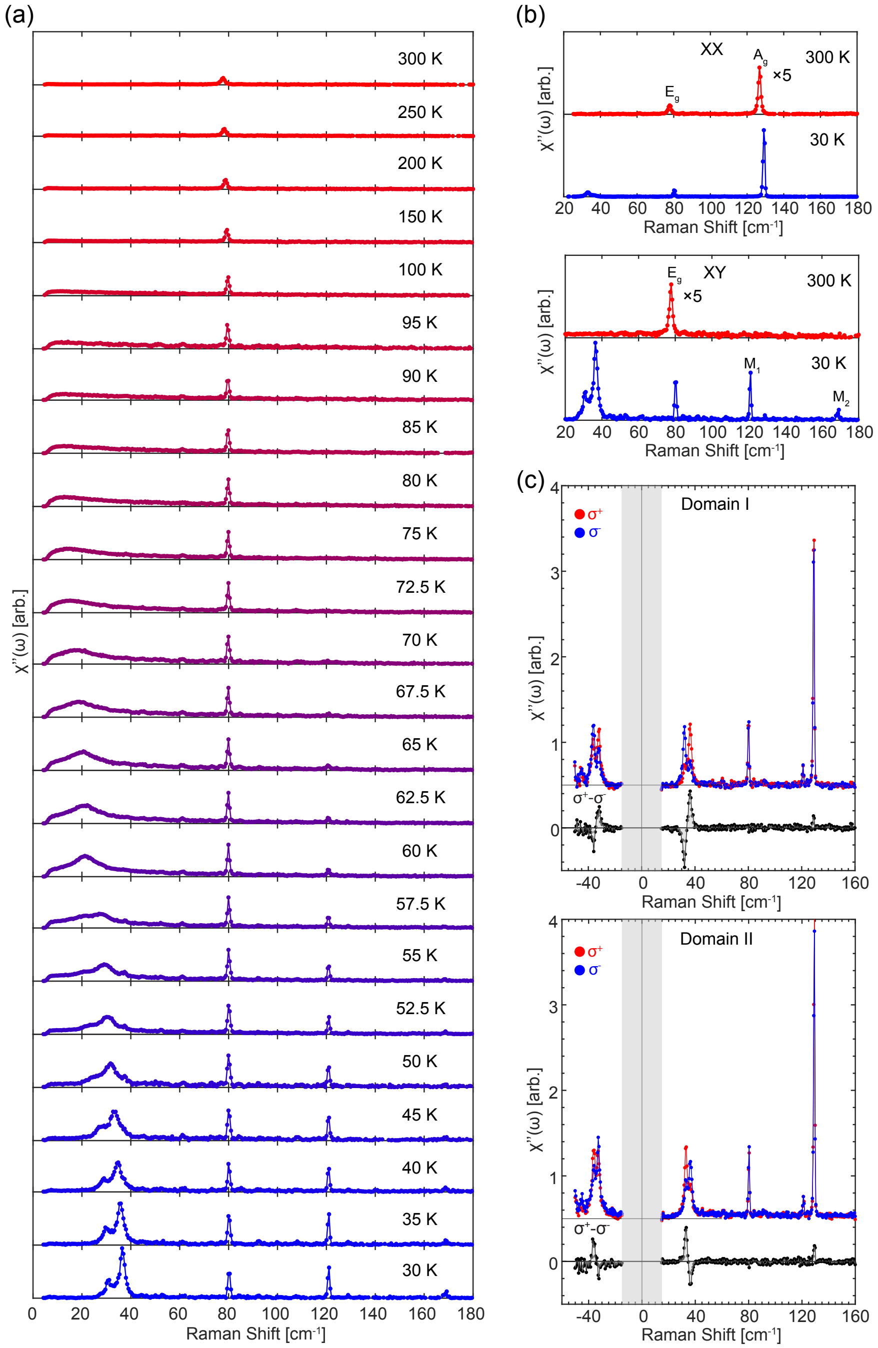

Figure 5.5: (a), Raman data in the cross-polarized XY channel from 30 K to 300 K. (b), Comparison of the cross-polarized (XY) and parallel-polarized (XX) channels at high and low temperature. (c), Circularly polarized Raman spectra at 30 K on domain I and domain II regions for σ^+/σ^- incident polarization (top) and the net circular dichroism $(\sigma^+ - \sigma^-)$ (bottom).

hybrids, or electromagnons modes [208]. The reversal of their circular dichroism between Stokes and Antistokes processes are consistent with a component breaking time-reversal

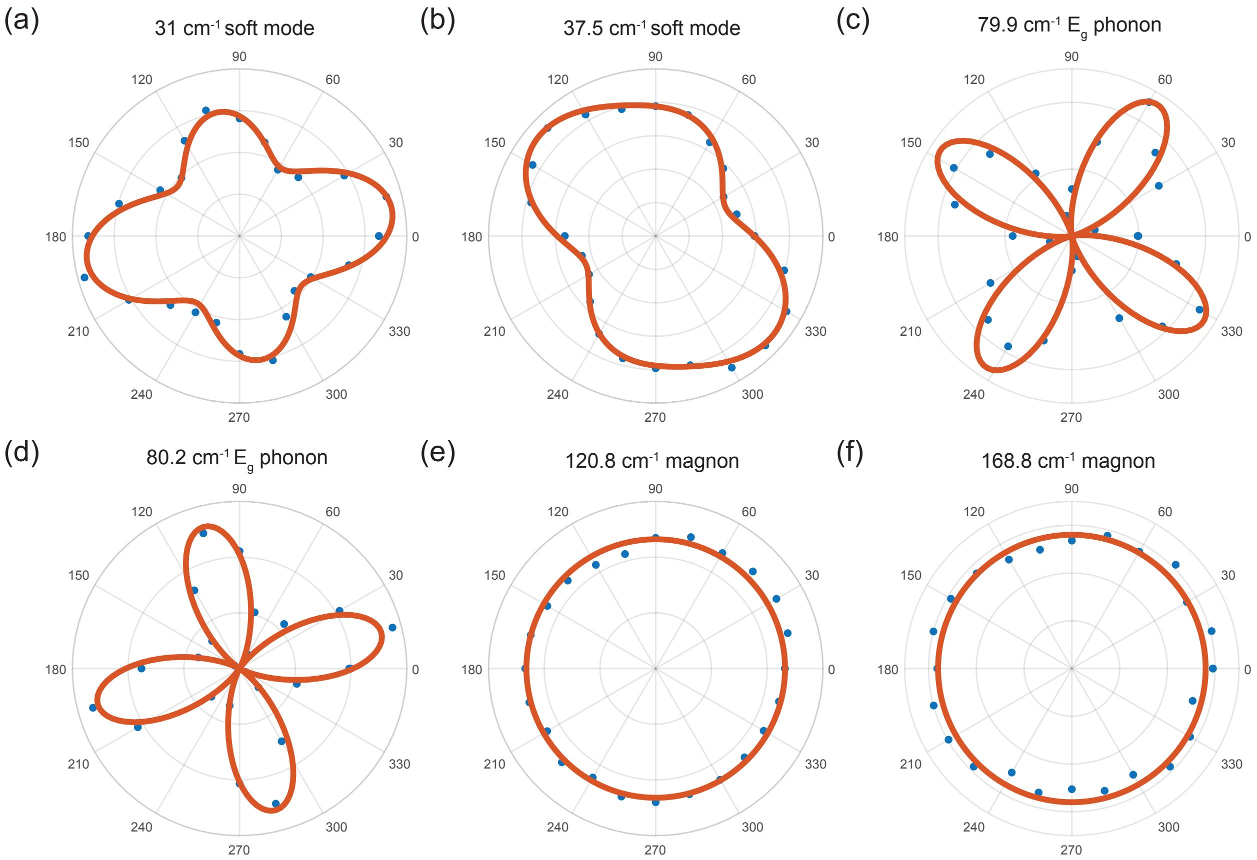

Figure 5.6: (a,b), The ARPRS polar plots of the 31 cm^{-1} and 37 cm^{-1} modes appearing in the multiferroic phase. (c,d), The 80 cm^{-1} peak is composed of two phonons below $T_{N,2}$, one at 79.9 cm^{-1} and the other at 80.2 cm^{-1}. These closely-spaced phonon modes display out-of-phase modulation with respect to the incident linear polarization and both display an E_g symmetry with respect to the high-temperature $R\bar{3}m$ phase. (e,f), The 120.8 cm^{-1} and 168.8 cm^{-1} are magnon modes. Red lines: ARPRS fits to the Raman tensors for different mode symmetries.

symmetry [173].

Fitting procedure for polarization dependent second harmonic generation

For NiI_2, the second harmonic radiated from the sample can be written as:

$$S(2\omega) = \mu_0 \frac{\partial^2 P}{\partial t^2} + \mu_0 \nabla \times \frac{\partial M}{\partial t}$$

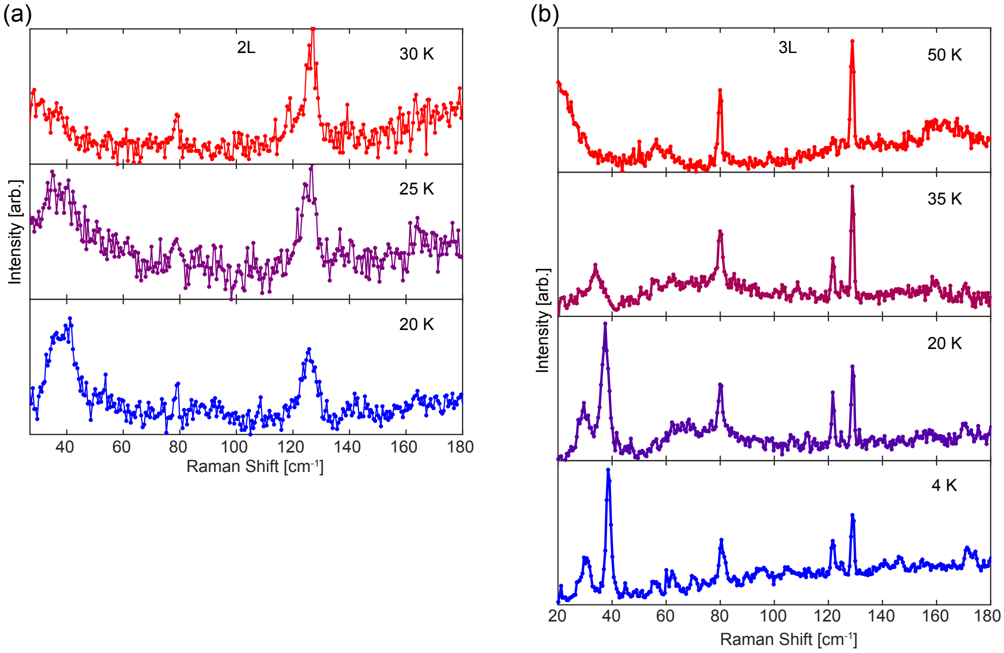

Figure 5.7: Temperature dependent Raman Spectroscopy of two- and three-layer NiI_2 in cross-polarized (XY) configuration. The low-energy excitations at around 38 cm^{-1} in (a), 2-layer and (b), 3-layer NiI_2 samples grown by PVD on hBN substrates, appearing below 25 K and 35 K, respectively. These temperatures are consistent with the transition temperatures measured from polarization rotation and SHG.

In the frequency and momentum domain, this expression takes the following form:

$$S(2\omega) = -4\omega^2\mu_0 P(2\omega) + 4\omega\mu_0 k \times M(2\omega)$$

where k represents the wavevector along the propagation direction. For normal incidence, k is along z-axis. The first term in this equation represents the electric dipole (E1) contribution to SHG, which is only present for non-centrosymmetric systems. On the other hand, the second term corresponds to magnetic dipole (M1) contribution to SHG, which can be present in magnetic systems, such as antiferromagnets, even without inversion symmetry breaking. These two contributions can be decomposed with polarization analysis of SHG signal.

For the M1 contribution, the magnetization at the second harmonic can be written as:

$$M_i(2\omega) = \chi^{(2)}_{ijk,mag} E_j(\omega) E_k(\omega)$$

where $\chi^{(2)}_{ijk,mag}$ corresponds to the magnetic SHG tensor. For the E1 contribution, the polarization at the second harmonic can be written as:

$$P_i(2\omega) = \chi^{(2)}_{ijk,elec} E_j(\omega) E_k(\omega)$$

The non-zero elements of $\chi^{(2)}_{ijk,elec}$ and $\chi^{(2)}_{ijk,mag}$ are determined by crystal symmetries. For the

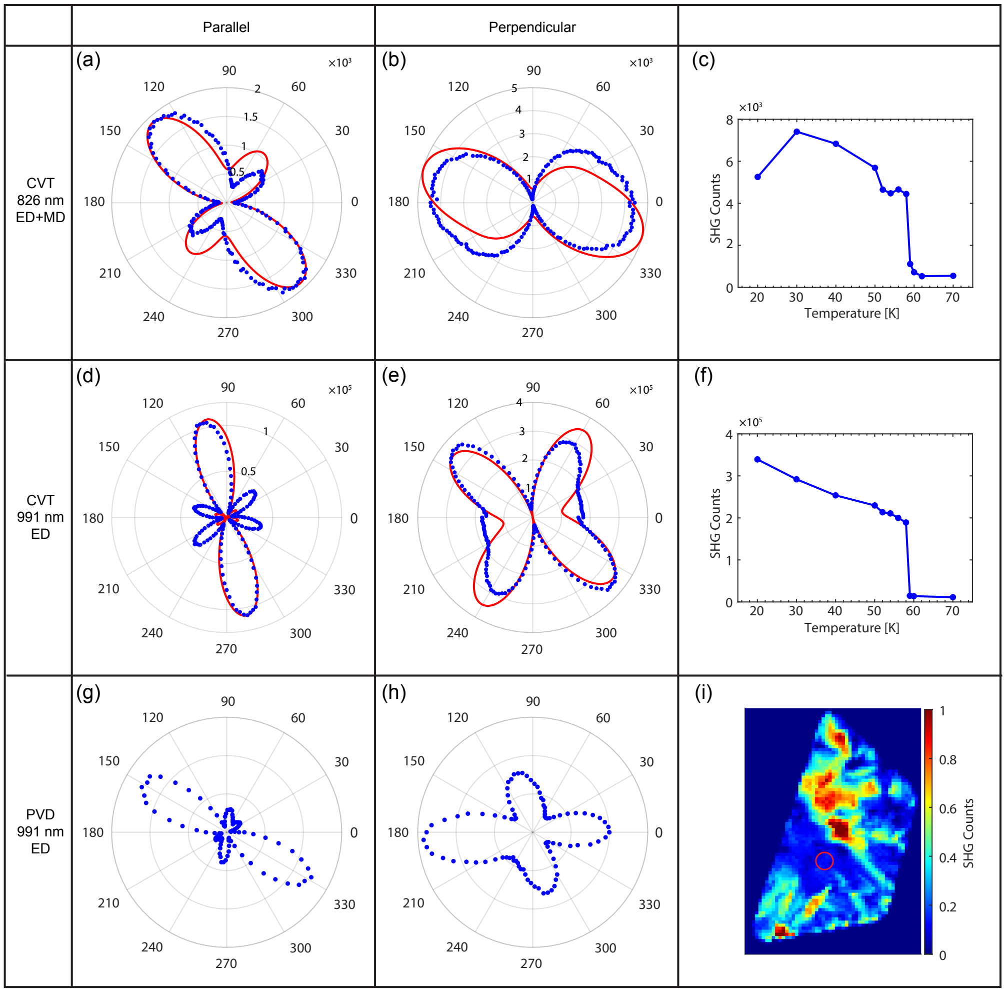

Figure 5.8: Wavelength-dependent Second Harmonic Generation of NiI_2. Rotational anisotropy SHG (RA-SHG) fits to nonlinear tensor elements and their temperature dependence on a single domain CVT grown bulk NiI_2 using (a-c), 826 nm excitation, and (d-f), 991 nm excitation. The RA-SHG traces obtained with 826 nm can only be fit with a combination of electric dipole (E1) and magnetic dipole (M1) transition contributions, whereas the RA-SHG traces obtained with 991 nm only exhibit an E1 component. (g,h), RA-SHG on PVD grown bulk NiI_2 samples shows the same signatures as the CVT grown samples. (i) SHG imaging of the PVD sample at 15 K. The red circle shows the single domain region where the RA-SHG was taken.

monoclinic C_2 symmetry, the non-zero elements of both $\chi^{(2)}_{ijk,elec}$ and $\chi^{(2)}_{ijk,mag}$ relevant for a fundamental field propagating along z-axis are: $\chi^{(2)}_{xxy}$, $\chi^{(2)}_{xyx}$, $\chi^{(2)}_{yxx}$, $\chi^{(2)}_{yyy}$ where y denotes the normal vector direction perpendicular to the mirror plane.

To extract the E1 and M1 contributions from the SHG signal, we fit our SHG polarization dependent traces in order to obtain the tensor elements both for electric and magnetic dipole SHG tensors. The polarization dependent SHG signal is collected as a function of incident electric field angle rotated along propagation axis (z-axis) and two scattered polarization

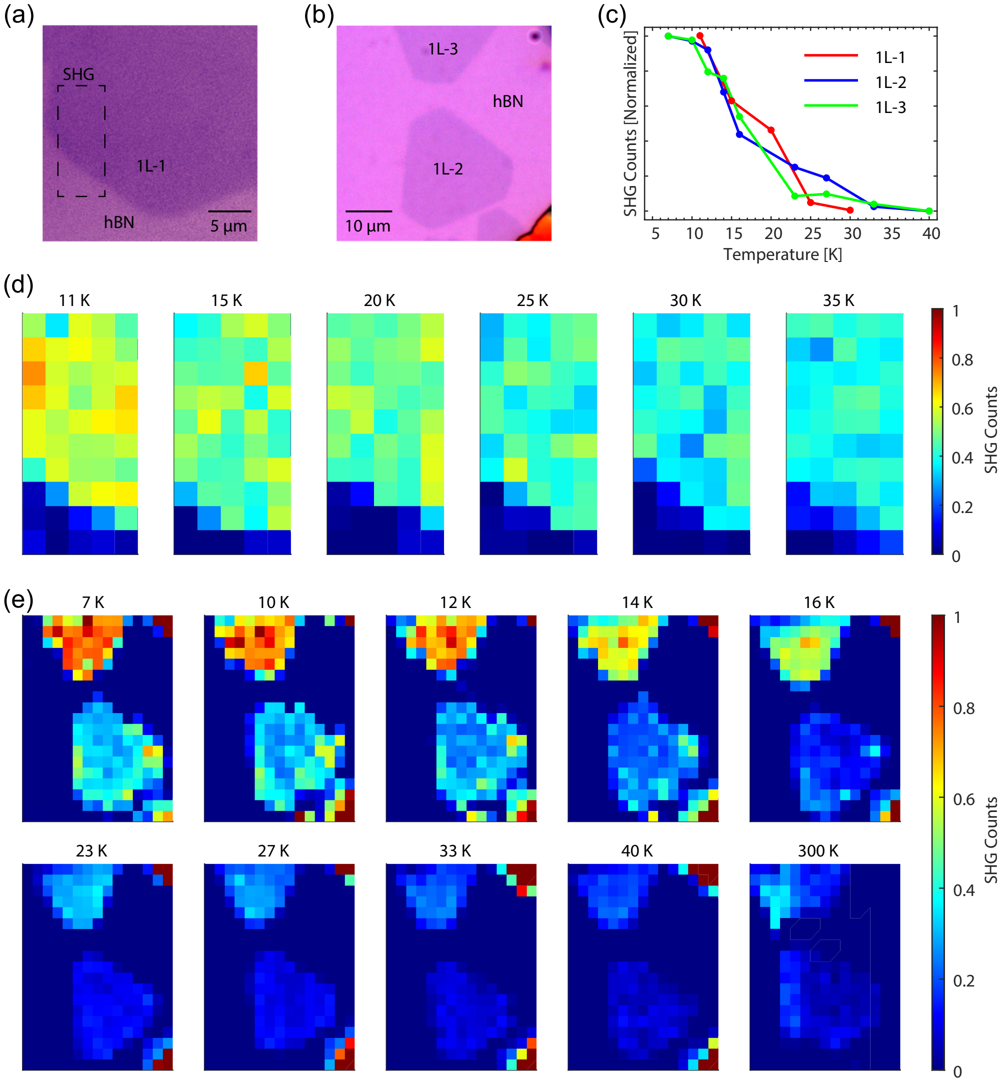

Figure 5.9: (a,b), Optical images of the region where the SHG imaging was performed. (c), Integrated SHG counts on three single-layer NiI_2 crystals show a transition around 20 K, consistent with LD measurements. (d), Temperature dependent SHG imaging of the region denoted in (a) using 780 nm excitation. (e), Temperature dependent SHG imaging of the region in (b) using 991 nm laser. Colorbar: SHG counts.

channels, parallel and perpendicular. The overall emitted second harmonic field can be represented as $S(2\omega, \theta)$ where the incident electric field is equal to $E_{inc} = E_0(\cos(\theta)x + \sin(\theta)y)$. The SHG intensity in the parallel channel is equal to $|(\cos(\theta)x+\sin(\theta)y)S(2\omega,\theta)|^2$, whereas the SHG intensity in the parallel channel is equal to $|(-\sin(\theta)x+\cos(\theta)y)S(2\omega,\theta)|^2$.

The fit results for different fundamental wavelengths (991 and 826 nm) are given in Fig. 5.8. NiI_2 is transparent for 991 nm (~ 1.25 eV), whereas 826 nm (~ 1.5 eV) overlaps with a $d-d$ transition [190] (Chapter 8). In addition to the changes in values of nonlinear tensor elements as a function of excitation wavelength, the E1 and M1 contributions can change as a function of excitation wavelength. In magnetic systems, the M1 contribution is enhanced in the vicinity of localized $d-d$ transitions. As shown in the fits for SHG traces obtained with 826 nm fundamental, both M1 and E1 contributions are required to fit the polarization dependent SHG data. On the other hand, the SHG traces obtained with 991 nm fundamental can easily be fit with only the E1 contribution, implying that it is only sensitive to the inversion symmetry breaking ferroelectric order parameter.

Angular-dependent linear dichroism and relation to induced polarization rotation

Angular dependent linear dichroism measurements were performed in backscattering geometry. A photoelastic modulator (PEM) set to half-wave retardance amplitude for the incident 532 nm wavelength was used to modulate the incident polarization between two linear, perpendicular states $\epsilon_{\|}$ and $\epsilon_{\perp}$ at the second harmonic of the PEM modulation frequency, $f \sim 100$ kHz. To control the projection of these polarization states onto the crystallographic axes, a zero-order half-wave plate was placed just before the objective lens.

In the angular dependent linear dichroism plots shown in Fig. 5.1(c), Fig. 5.2(c) and Fig. 5.10, the reported angle corresponds to the angle of the primary polarization $\epsilon_{\|}(\theta)$ in the frame of the crystal axes. The recorded signal in the polar plots is then the reflectance $R_{\|}(\theta)$ along the direction of $\epsilon_{\|}(\theta)$ minus the reflectance $R_{\perp}(\theta)$ along the perpendicular polarization state $\epsilon_{\perp}(\theta)$, given by $\Delta R(\theta) := (R_{\|}(\theta) - R_{\perp}(\theta))/R_0$ where R_0 is the average reflectance. The difference is monitored directly by the oscillating component of the reflected light at the polarization modulation frequency f, as measured by a lock-in amplifier, while the average reflectance R_0 is monitored by the DC reflectance as measured by the same photodiode.

In the low-temperature C_2 point group, the the dielectric tensor takes on the form,

$$\epsilon = \begin{pmatrix} \epsilon_{xx} & 0 & \epsilon_{xz} \\ 0 & \epsilon_{yy} & 0 \\ \epsilon_{zx} & 0 & \epsilon_{zz} \end{pmatrix}$$

For light incident along the **c**-axis, the reflectivity tensor is then,

$$\mathbf{r} = \begin{pmatrix} r_{xx} & 0 \\ 0 & r_{yy} \end{pmatrix}$$

where the directions **x**- and **y**- are the principle axes. In the case of the C_2 point group, the principle-axis directions correspond to the unique C_2 axis ($\mathbf{y}$) and the direction perpendicular to the C_2 axis ($\mathbf{x}$). Defining $\theta = 0$ along the **x**-axis, the linear polarization states for the angular-dependent linear dichroism measurements are expressed as:

$$\epsilon_{\|}(\theta) = (\cos(\theta),\ \sin(\theta), 0)\,, \quad \epsilon_{\perp}(\theta) = (-\sin(\theta),\ \cos(\theta),\ 0)$$

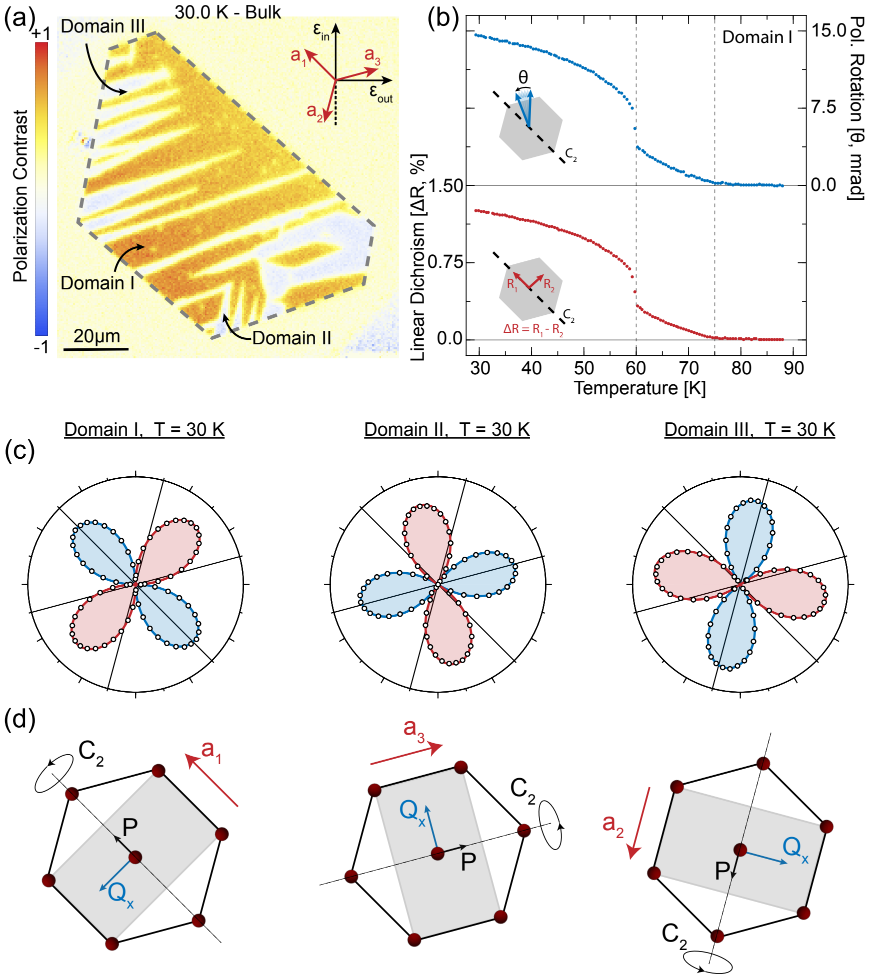

Figure 5.10: (a), Polarized microscopy image of PVD bulk $\mathrm{NiI_2}$. The positions where the optical measurements were performed are labelled as Domain I-III. (b), Comparison of the temperature-dependent birefringence-induced polarization rotation (top) and linear dichroism (bottom) on Domain I. (c), Angular-dependent linear dichroism measurements from the three distinct domains identified in (a). Radial lines indicate the crystallographic a-axes determined from the edges of the as-grown PVD sample. (d), Schematics of the domains as identified from AD-LD measurements in (c), denoting the local C_2 axis orientation, the polar vector P and the in-plane component of the helimagnetic ordering vector $\mathbf{Q}$.

In this case, the angular dependent reflectances for the two polarization states are given by,

$$R_{\parallel}(\theta) = r_{xx}^2 \cos^2(\theta) + r_{yy}^2 \sin^2(\theta), \quad R_{\perp}(\theta) = r_{xx}^2 \sin^2(\theta) + r_{yy}^2 \cos^2(\theta)$$

while the average reflactance $R_0 = (r_{xx}^2 + r_{yy}^2)/2$. The angular-dependent linear dichroism signal, as defined above, is then given by,

$$\Delta R(\theta) = \frac{(r_{xx}^2 - r_{yy}^2)}{R_0} \cos(2\theta) := \delta \cos(2\theta)$$

where δ is the linear dichroism. We see that the resulting angular dependent dichroism signal reaches extrema when $\epsilon_{\|}(\theta)$ lies along one of the principle axes, displaying a positive peak when along the more reflective axis and a negative peak when along the less reflective axis.

In the case of our measurements, both in the bulk and the single-layer sample, the registered curves are fit well to the expected $\propto \cos(2\theta)$ dependence on polarization angle, and display maxima oriented along the **a**-axes of the high-temperature rhombohedral phase. In the low-temperature phase, three-fold rotational symmetry about the **c**-axis is broken and one of the three **a**-axes becomes the unique C_2 axis of the monoclinic phase. Therefore the angular-dependent linear dichroism measurement directly identifies the three possible orientations of the local in-plane C_2 axis and confirms the principle axis orientation along the a-axis of the high temperature rhombohedral phase.

For the temperature-dependence of the three-fold rotational symmetry breaking in few-layer samples, we achieved a higher signal-to-noise ratio by measuring the birefringence-induced polarization rotation. In this case, a linear incident polarization state at an angle θ_i with respect to the crystal axes is reflected off the sample with a different polarization angle θ_f, where $\theta := \theta_i - \theta_f$ is the birefringence-induced polarization rotation.

For initial polarization,

$$\epsilon = (\cos(\theta_i),\ \sin(\theta_i),\ 0)$$

the birefringence induced polarization can be expressed in terms of the linear dichroism above as

$$\theta = \cos^{-1}\left(\frac{\sqrt{1+\delta}\ \cos^2(\theta_i) + \sin^2(\theta_i)}{\sqrt{(1+\delta)\ \cos^2(\theta_i) + \sin^2(\theta_i)}}\right) \simeq \frac{\delta}{4}\sin(2\theta_i)$$

expanded for small difference in reflectivity δ. Therefore, the dichroism-induced polarization rotation is zero when the incident polarization is aligned along one of the principle axes, but has a non-zero value for all other incident polarization states and is directly proportional to the linear dichroism.

In the case of our measurements on the few-layer samples, temperature-dependence was recorded on domains such that the incident polarization made an angle of either ±30° or ±45° with respect to the principle axes. This leads to typical values of the polarization rotation of 1-2 mrad in the 1L, 3-4 mrad in the 2L and 6-7 mrad in the 4L samples.

Point group analysis of the low-temperature phase

Our observations of birefringence in the **a**-**b** plane, the resolution of the principle axes of the birefringence as well as an electric-dipole allowed second harmonic generation together provide strong restrictions for the possible point groups in ground state of bulk and few-layer NiI_2. The high-temperature point group symmetry is $\bar{3}m$, for which both **a**-**b** plane birefringence and electric-dipole active SHG are symmetry forbidden. The development of birefringence necessitates the breaking of the 3-fold rotational symmetry about the **c**-

axis, while SHG requires the breaking of inversion-symmetry. Among the possible sub-point groups of the parent phase, there are only three possible crystallographic (non-magnetic) points groups consistent with our observations of both of these effects: C_1 (1), C_i (m), and C_2 (2). All of these possible sub-point groups are polar as shown in the following table.

Point Group	**Birefringence in the a-b plane:**	**Electric-dipole SHG:**	**Polar?**
$\bar{3}m$ (D_{3d})	Forbidden	Forbidden	No
$\bar{3}$ (S_6)	Forbidden	Forbidden	No
$2/m$ (C_{2h})	Allowed	Forbidden	No
$3m$ (C_{3v})	Forbidden	Allowed	Yes
32 (D_3)	Forbidden	Allowed	No
3 (C_3)	Forbidden	Allowed	Yes
2 (C_2)	Allowed	Allowed	Yes
m (C_s)	Allowed	Allowed	Yes
$\bar{1}$ (C_i)	Allowed	Forbidden	No
1 (C_1)	Allowed	Allowed	Yes

In the bulk, the totality of data are consistent with an assignment of the C_2 point group below $T_{N,2} = 60$ K. The distinction between the possible points groups is demonstrated by the SHG rotational anisotropy patterns for laser wavelengths below the band-gap where the signal is of pure electric-dipole origin (with the absence of magnetic-dipole SHG contributions). For this case, the SHG-RA patterns are well described by the C_2 point group tensor restrictions (see Fig. 5.8). The SHG-RA patterns also uniquely determine the C_2 axis, which is parallel to the crystallographic **a**-axis of the $\bar{3}m$ structure, and forms the unique monoclinic **b**-axis in the low-temperature phase. The angular-dependent linear dichroism measurements further confirm this situation, which demonstrate three domains with principle axes oriented along the crystallographic **a** direction and relatively rotated by 120 degrees. These measurements show that the C_2 axis is the more highly reflective axis, displaying a strong dichroism of positive sign between the **a** axes and the perpendicular $\mathbf{b}^*$ axes.

In the few-layer samples, a consistent behavior is found with the point group symmetry observed in the bulk. Our results demonstrate that E1 SHG is allowed down to the monolayer limit in addition to the presence of a strong birefringence. These observations restrict to the same three possible point groups for the ground state in the atomically-thin limit. The AD-LD measurements registered on three mono-domain regions of a monolayer sample confirm an identical behavior to the bulk, showing 3-domains with principle axes relatively oriented by 120 degrees. Furthermore, the axes with higher reflectivity are in close agreement with the **a**-axes (as determined by the as-grown edges of the samples), as opposed to the 30 degree rotated $\mathbf{a}^*$ axes, the same as found in the bulk. These observations, along with the smooth trend of these signatures as the layer number is reduced to the monolayer limit, strongly support the same assignment of the C_2 non-magnetic point group for low-temperature phase of few- and single-layer NiI_2.

5.6 Afterward

Significant additional work has been completed since the original publication of this article [37]. First, a criticism has been raised [209] to which we have subsequently responded [210]. A summary of the main criticism is that optical evidence alone cannot constitute definitive proof of the ferroelectric component of the underlying multiferroic state and that both LD and SHG can become non-zero from the magnetic degrees of freedom.

The LD and SHG measurements presented above evidence a polar magnetic order that is single-$\mathbf{Q}$ and breaks inversion symmetry surviving the monolayer limit. It is worth noting that in bulk $\mathrm{NiI_2}$, switchable ferroelectricity has been observed [45], and that this polarization emerges directly from the corresponding spin-spiral magnetic state. From the optical evidence, there are two central questions. First is which degree of freedom is being measured by each technique and thus where the symmetry breaking being measured is originating. Second is whether the mechanism of ferroelectricity becomes inoperative in the monolayer limit.

From the SHG data, we have shown above that the degree of freedom being measured changes depending on the probing wavelength. The standard (most common) fundamental wavelength is a Ti:Sapphire oscillator at $\lambda \sim 780 - 800$ nm. In this energy regime, one is close to resonance with *dd* transitions and the charge transfer threshold (see Ref. [190] and also Chapter 8). In this condition, one measures a multicomponent SHG resulting from both standard E1 and additional M1 mechanisms related to the lattice and the magnetic order, respectively. The result is an angular dependent pattern without a clear in-plane two fold axis, which apparently breaks (vertical) mirror symmetry due to the E1 and M1 interference [211]. With wavelength tuned to a transparency region within the *dd* transition energy range ($\lambda \sim 991$ nm), a single component SHG is observed which can be fit to an E1 contribution originating from the lattice degrees of freedom consistent with the in-plane 2-fold axis in the C_2 structure, thus evidencing a polar crystallographic structure. While established in the bulk, we utilized the same wavelength for the thin layers. Since the optical excitations in this energy regime are highly localized and related the local $\mathrm{NiI_6}$ octahedral cluster, we do not anticipate the optical response to change drastically in this energy regime (see Chapter 8), and thus the (lack of) resonant conditions should be preserved. Thus, the same conclusions of a polar inversion symmetry breaking in the lattice should hold for the wavelength dependent SHG in the few-layer limit.

The LD data is also complex. LD can in principle come from the rotational-symmetry-breaking magnetism, the ferroelectricity, or the structure, which must all have compatible principle axes of the dichroic tensor since the orders are microscopically coincident and driven by the same primary order (magnetic) [Fig. 5.10]. The LD we measure is large (up to several percent) and the bulk spin spiral state does not possess a unique global spin axis, as in simple collinear antiferromagnets. This almost certainly rules out a direct second-order magneto-optical effect (e.g. magnetic linear birefringence) which is generally weak and related to the angle between the polarization and the local spin direction [164]. However, as has been noted before in $FePS_3$, one can measure a magnetic-origin LD signal, instead related to the anisotropic effect of magnetism on the electronic structure [165]. This general mechanism agrees with our measurements, however in our case, the LD is possibly multi-component. Evidence for a magnetic contribution without ferroelectric or lattice components comes from the observation of LD within the intermediate phase ($T_{N,2} < T < T_{N,1}$). In this temperature range, our measurements confirm that there is no observable symmetry breaking of the lattice (Chapter 7) and ferroelectricity is also not observed [45]. Meanwhile, an incommensurate single-$\mathbf{Q}$ magnetic order is observed, as we report in Chapter 7. Therefore, a magnetic contribution to LD is likely dominant in the intermediate temperature range, while both magnetic, structural and ferroelectric orders may contribute below $T_{N,2}$. Resolving which order dominates the optical response would require microscopic modeling and direct comparison between the different order parameters, since each can contribute with the same symmetry to the dielectric tensor. A dominant structural contribution can likely be ruled out at $T_{N,2}$ due to the relatively weak structural anisotropy (order of 0.1% difference in bond lengths with respect to $R\bar{3}m$, see Ref. [42] and Chapters 6/7). Meanwhile, the ferroelectric polarization is weak, leading only to a very subtle (static) dielectric anomaly [45]. Thus, the LD is most likely primarily measuring the magnetically-induced electronic anisotropy due to the single-$\mathbf{Q}$ magnetic state, similar to reports in the transition metal thiophosphates [165].

In the end, whether from magnetic or lattice degrees of freedom, our optical measurements provide strong evidence for a type-II multiferroic phase resulting from a polar magnetic ground state persisting to the few layer limit. This is because the magnetic degrees of freedom are the primary order parameter which drives the symmetry breaking among all degrees of freedom (as discussed in Chapters 6 and 7), and other mechanisms including phononic driven structural or ferroelectric orders have been ruled out. Thus, the structural and ferroelectric phase transitions must be seen as resulting from the magnetic order, driven respectively by magneto-structural coupling and spin-charge coupling. Therefore, experimental evidence of the driving magnetic order with the correct (polar) symmetry constitutes evidence for the underlying multiferroic state provided that the mechanism of spin-induced ferroelectricity is unaltered.

Each of the secondary orders (ferroelectric and structural) are observed in the bulk, and the microscopic mechanism driving the spin-induced ferroelectricity is a nearest-neighbor effect acting within the triangular lattice layer [37, 143]. Thus, it is unlikely that this mechanism becomes inoperative in the monolayer limit due to dimensionality arguments alone. What *can* change is the symmetry of the magnetic order in the few layer limit due to the different contribution of the interlayer exchange interactions (see Chapter 7). However, our optical measurements restrict the magnetic ground state to a polar state which allows ferroelectricity through the same mechanism in the bulk [Fig. 5.3]. Furthermore, as observed in other ultrathin ferroelectrics, increased screening of the ferroelectric polarization could contribute due to depolarization fields. However, this is mainly observed for oxide ferroelectrics with out of plane polarization. In our case, the electric polarization is in plane and has a smaller magnitude, leading to an expected weaker depolarization field as generally observed for vdW ferroelectrics [212].

In this vein, independent studies provide supporting evidence of a magnetic phase transition in the monolayer limit through magnetoresistance [213] and scanning tunneling microscopy measurements [143]. In particular, the STM results show the real space modulation of the spin-induced local polarization, which oscillates at a period of half the magnetic spiral pitch in agreement with the microscopic theory of spin-induced ferroelectricity [33] (see Chapter 3). This provides evidence for unscreened charge dipoles in monolayer NiI_2 (with some caveats, discussed towards the end of Chapter 3), supporting the viability of ferroelectricity and consistent with our conclusions. The magnetoresistance studies also largely confirm the layer-dependent transition temperatures from optical measurements [Fig. 5.2]. Furthermore, while the bulk magnetic order has an ordering wavevector along the ΓM reciprocal lattice direction ($(h, 0)$ r.l.u.), STM provides evidence for a wavevector along ΓK ((h, h) r.l.u.) which is in agreement with our first-principles calculations above [Fig. 5.3] and those of Ref. [47]. The difference in magnetic ground state in the bulk/few-layer and the monolayer limits is explored more thoroughly in Chapters 6/7 and is associated to the role of the interlayer exchange interactions.

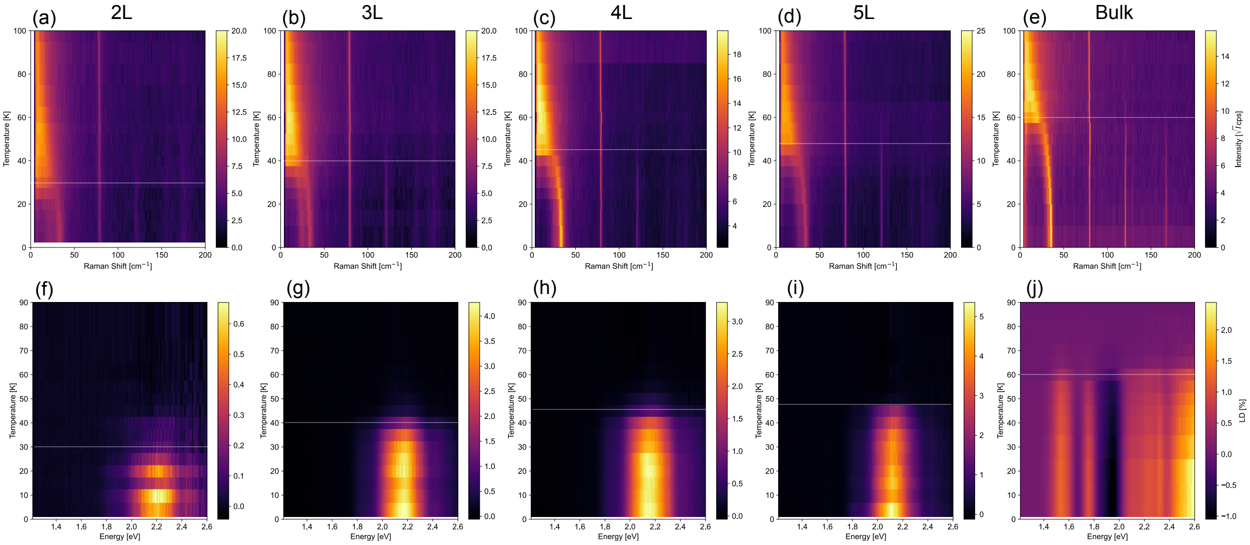

Figure 5.11: (a)-(e) Cross-polarized Raman spectra and (f)-(j) linear dichroism spectra on mechanically exfoliated CVT single crystal NiI_2 on a 285nm SiO_2/Si substrate with thicknesses of 2L, 3L, 4L, 5L and bulk, respectively. Horizontal dashed lines indicate the estimated $T_{N,2}$ transition temperatures, which agree well between the two techniques. Raman excitation wavelength is $\lambda = 532$ nm. Details of the linear dichroism spectroscopy measurements can be found in the Methods section of Chapter 6.

The STM measurements also show that the spin spiral wavevector is consistent with intralayer Heisenberg exchange parameters J_1/J_3 that place the system close to a spiral/ferromagnetic phase boundary [41]. This may reconcile the different observations between our study (Ref. [37]) and a contemporaneous study of NiI_2 (Ref. [186]), which largely agree in observed layer-dependent T_c except for the notable absence of SHG in the monolayer in the latter from which an absence of a magnetic transition was claimed. In the above paper, we have measured few-layer flakes grown on hBN substrates by physical vapor deposition (PVD). The STM work of Ref. [143] measured flakes grown on graphite substrates by molecular beam epitaxy (MBE). Meanwhile, the work of Ref. [186] measured mechanically exfoliated flakes from single crystals grown by chemical vapor transport (CVT). It is possible that the discrepancies in the transition of monolayer NiI_2 is due to a difference in the sample preparation conditions. Provided the proximity to the spin spiral/FM phase boundary revealed by Ref. [143], small differences in local strain (easily introduced during mechanical exfoliation) could push the system out of the spin spiral state. Resolving the dependence on sample preparation conditions is an important issue to resolve moving forward.

Along these lines, we have performed additional Raman spectroscopy and linear dichroism spectroscopy measurements on exfoliated CVT samples down to the bilayer limit of NiI_2, shown in Figure 5.11. The observed transition temperatures are in close agreement with the results we reported above with $T_{N,2} \simeq 30, 40, 45, 47.5, 60 \pm 2.5$ K for 2L, 3L, 4L, 5L, and bulk, respectively. Thus, other experimental factors, such as local laser heating or sample quality, may be required to explain the discrepancy between different works [37, 186]. Importantly, our additional optical spectroscopy results provide additional evidence that SHG and LD reported above are intrinsic properties of NiI_2, and improve upon our previously reported Raman evidence of the magnetic phase transitions in few-layer samples grown by PVD samples on hBN substrates [Fig. 5.7].

In conclusion, evidence is mounting to confirm the measurements presented in this chapter, namely that a spin-spiral magnetic order persists to the monolayer limit of NiI_2, which is accompanied by a spin-induced ferroelectric order as observed in the bulk. There do exist some conflicting claims which need to be resolved, namely supporting proof from, e.g. diffraction measurements, to directly interrogate the long-range magnetic order along with a need for more direct measurements of the ferroelectric order in the ultrathin limit with correspondent proof of switching by electric fields. Furthermore, there remain conflicting reports on transition temperatures in the ultrathin limit, which may be related to sample quality or a high-sensitivity of the samples to local perturbations introduced by sample preparation, such as strain [143] or doping. Significant work therefore remains to reach a consensus on the multiferroic properties of NiI_2 in the monolayer limit, as well as the microscopic physics of the bulk which we partly address in subsequent chapters. Nonetheless, NiI_2 is an intriguing representative material for studying spin-induced ferroelectricity and chiral magnetic order in the ultrathin limit.

Chapter 6

Pressure-enhanced helimagnetic order in van der Waals multiferroic NiI_2

This chapter is adapted from a pre-print posted to arXiv (Ref. [214]) with modifications and corrections.

This is a co-first author work between the present author (C.A.O.) and Luiz G. P. Martins. C.A.O. and L.G.P.M. prepared/characterized the samples, performed the high-pressure Raman and LD measurements, with assistance of Qian Song, and performed the high-pressure diffraction measurements, with assistance of Jesse S. Smith and Joshua J. Sanchez. Q.S. grew the PVD and CVT NiI_2 samples. Experiments were supervised by Jing Kong and Riccardo Comin. Theoretical support was provided by Jesse Kapeghian, Danila Amoroso, Paolo Barone, Bertrand Dupé, Matthieu J. Verstraete and Antia S. Botana. A more thorough treatment of the theoretical results is reported separately in *Physical Review B* in Ref. [126].

6.1 Introduction

Transition metal dihalides are an emerging class of 2D van der Waals (vdW) materials presenting non-collinear magnetism and associated type-II multiferroic order [12, 37, 45–47, 186, 189, 213, 215, 216]. Type-II multiferroics exhibit strong magnetoelectric effects and are therefore of broad interest as constituents in vdW devices [14, 17, 33, 45, 180, 213, 217, 218]. NiI_2 is a promising candidate towards these goals, hosting a type-II multiferroic phase from the bulk to the single-layer limit [37, 45, 186, 213]. The spin-induced ferroelectricity is closely linked to the symmetry of the magnetic order [33, 45, 219]. Therefore, understanding the origins of non-collinear magnetism and the magnetic ground state of NiI_2 is critical and remains under active debate [37, 46, 125, 126, 129, 131, 141, 143, 186, 189, 213].

In the bulk, NiI_2 undergoes two magnetic transitions, first to an antiferromagnetic (AFM) state at $T_{N,1} \simeq 75$ K and then to a single-$\mathbf{Q}$ helimagnetic phase below $T_{N,2} \simeq 60$ K [37, 42] with wavevector $Q \simeq (0.138, 0, 1.457)$ reciprocal lattice units (r.l.u.) [42]. The single-$\mathbf{Q}$

helimagnetic phase is accompanied by a rhombohedral to monoclinic structural phase transition [37, 42, 45, 186] and a magnetic-field-tunable spin-induced ferroelectricity [45]. $T_{N,2}$ decreases continuously to 20 K in the monolayer which is attributed to a dimensionality-controlled reduction of the net interlayer exchange [37], as commonly observed in van der Waals magnets [6]. While this suggests that interlayer exchange promotes long-range helimagnetic order in the bulk limit, a comprehensive assessment of the interlayer exchange, crystallographic symmetry and their coordinated impact on the magnetic ground state is absent.

From this perspective, significant open questions remain regarding the origin of the helimagnetic state in bulk and atomically-thin $\mathrm{NiI_2}$. Non-collinear magnetic structures in triangular lattice magnets are primarily induced by exchange frustration between (isotropic) ferromagnetic (FM) nearest-neighbor $J_1^{\|}$ and AFM third-nearest neighbor $J_3^{\|}$ exchange, but these interactions alone fail to predict the ground state of bulk $\mathrm{NiI_2}$ [42, 131]. Notably, the frustrated intralayer interactions introduce a near-degeneracy of multiple magnetic states with different in-plane propagation vectors and spin textures [47, 129]. It was recently suggested that anisotropic, symmetric exchange (e.g. Kitaev interactions) may resolve this discrepancy [47, 125, 131]. However, recent STM measurements evidence that the ground state of monolayer $\mathrm{NiI_2}$ is $Q \sim (hh)$ r.l.u. [143], different from the bulk and in agreement with the prediction from isotropic $J_1^{\|}/J_3^{\|}$ exchange frustration and first principles calculations [37, 47, 125, 129]. These observations suggest a different mechanism, independent from the interactions within the triangular lattice plane, which stabilizes the unique spin structure of multilayer $\mathrm{NiI_2}$.

Here, we identify the central role of the interlayer exchange interactions and their coupling to the interlayer stacking symmetry for determining the ground state of multilayer $\mathrm{NiI_2}$ using high pressure experiments. Hydrostatic pressure is a powerful tuning parameter to reveal the coupling among the structural, magnetic and electronic degrees of freedom, particularly for vdW materials given the large interlayer compressibility [20, 216, 220–225]. We report high-pressure Raman spectroscopy and optical linear dichroism measurements of bulk and few-layer $\mathrm{NiI_2}$, revealing a large enhancement of helimagnetic phase with pressure, increasing over a factor of 3 up to 10 GPa and down to the 5-layer limit. The combined layer- and pressure-dependence provides experimental evidence that pressure-enhanced interlayer exchange interactions are central to this transition temperature enhancement, as supported by first principles calculations [126]. In addition, high-pressure x-ray diffraction (XRD) measurements reveal that the monoclinic crystallographic phase transition tracks the presence of helimagnetic order up to 10 GPa and is characterized by a significant interlayer shear and c-axis compression, demonstrating significant interlayer magneto-structural coupling in the helimagnetic phase. These results suggest that interlayer exchange interactions provide the microscopic mechanism energetically favoring the helimagnetic ground state of multilayer $\mathrm{NiI_2}$, thus driving its large enhancement with hydrostatic pressure.

6.2 Results

6.2.1 Raman spectroscopy and optical linear dichroism of bulk and few-layer NiI$_2$ at high pressures

We first discuss the pressure- and temperature-dependent optical spectroscopic experiments on a bulk-like ($\sim$ 100 nm thick) single crystal (Sample 1) grown by physical vapor deposition (PVD), shown in Fig. 6.1(a) [37, 189]. The sample was loaded into a diamond anvil cell (DAC, Almax CryoDAC-ST) using 4:1 methanol-ethanol as the pressure transmitting medium (PTM). Representative cross-polarized (XY) Raman spectra (acquired with $\lambda = 532$ nm) at $P_1 = 0.5$ GPa across both the $T_{N,1}$ and $T_{N,2}$ transitions are shown in Fig. 6.1(b). Besides the two Raman-active phonon modes (E_g/A_g), additional features associated to magnetism appear: a magnetic quasi-elastic scattering (mQES) above $T_{N,1}$, which evolves into a finite-frequency soft mode (SM) below $T_{N,1}$ and further splits to two distinct modes electromagnon modes (EM$_{1/2}$) below $T_{N,2}$, which are spectroscopic signatures of multiferroic order [37, 67]. Higher-energy magnon modes (M$_{1,2}$) also appear between $T_{N,1}$ and $T_{N,2}$ [37, 189]. These spectroscopic features provide a robust signature of the magnetic phase transitions.

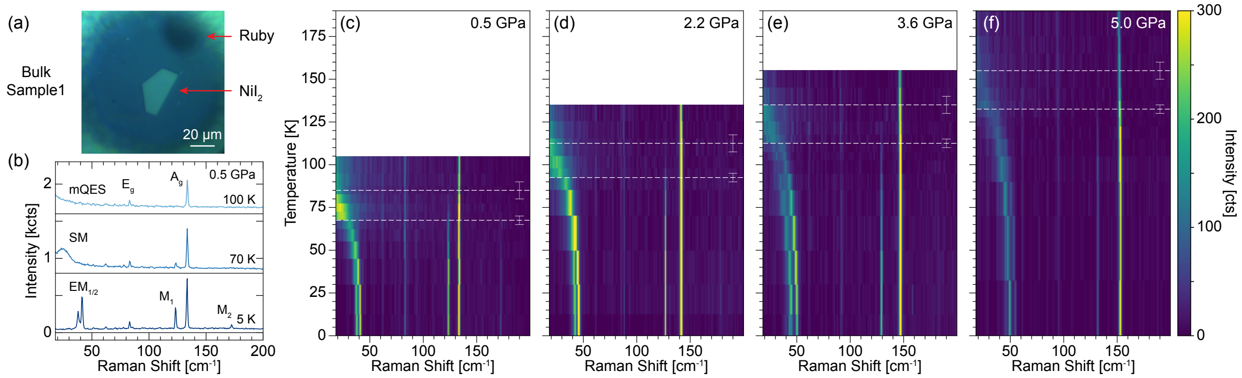

Figure 6.1: (a), Optical image of single-crystal bulk NiI$_2$ (Sample 1) sample inside the DAC used for the optical measurements. (b), Raman spectra at $P_1 = 0.5$ GPa at 100 K ($T > T_{N,1}$), 70 K ($T_{N,2} < T < T_{N,1}$) and 5 K ($T < T_{N,2}$). The phonon modes (E_g/A_g) and the modes associated to magnetic order (mQES, SM, EM$_{1/2}$, and M$_{1/2}$) are indicated (see text). Curves are offset for clarity with zero baselines indicated. (c)-(f), Temperature-dependent Raman maps for pressures P_1-P_4. The $T_{N,1}/T_{N,2}$ transitions are identified with the upper/lower horizontal dashed lines, respectively, with error bars indicated.

Temperature-dependent XY-polarized Raman maps with increasing pressure between $P_1 = 0.5$ GPa and $P_4 = 5.0$ GPa are shown in Figs. 6.1(c)-(f). At all measured pressures, the spectra are qualitatively similar to the results at ambient pressure [37, 189], with a clear increase of both the $T_{N,1}$ and $T_{N,2}$ transition temperatures. The linear evolution of the Raman mode frequencies up to 5 GPa and their spatial homogeneity across the sample at 5 GPa confirm quasi-hydrostatic pressure conditions without significant deviatoric stresses

[225]. The transitions are indicated by dashed white lines for each pressure, determined from the EM and $M_{1/2}$ modes as discussed more below. From these results, we immediately observe a clear increase of both the $T_{N,1}$ and the $T_{N,2}$ transition temperatures from 75/60 K at ambient pressure [37] to $155 \pm 5/\ 132.5 \pm 2.5$ K at $P_4 = 5.0$ GPa, suggesting that both the AFM and the helimagnetic/multiferroic states are rendered more stable upon increasing pressure.

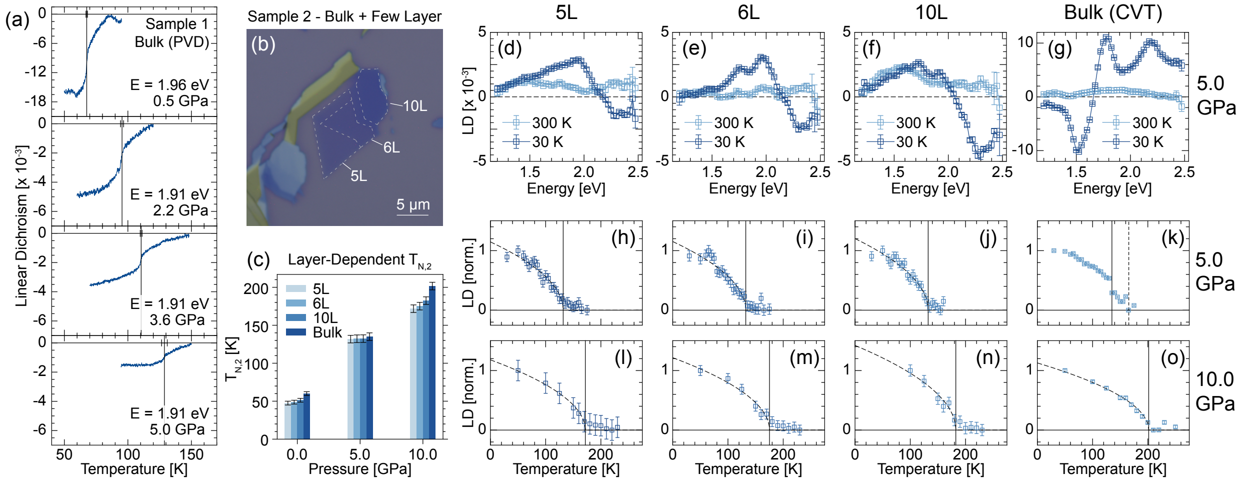

Figure 6.2: (a), Temperature-dependent LD for P_1-P_4 for bulk (Sample 1). The $T_{N,2}$ transitions are marked by vertical lines, with error bars indicated. Photon energy to record LD at each pressure is indicated. (b), Optical image of the NiI_2 sample containing 5-, 6-, 10-layer and bulk flakes (Sample 2) before loading into the DAC. (c), Helimagnetic/multiferroic transition temperature $T_{N,2}$ as a function of pressure for the flakes from Sample 2.(d)-(g), LD spectra vs. photon energy at 30 K and 300 K at 5 GPa for 5, 6, 10-layer and bulk, respectively. (h)-(o), Temperature-dependent LD at 5 and 10 GPa for 5-layer [(h),(l)], 6-layer [(i),(m)], 10-layer [(j),(n)] and bulk [(k),(o)], respectively. Vertical black bars indicate the $T_{N,2}$ temperature.

The multiferroic transition is also characterized by significant breaking of lattice symmetries, including the loss of both three-fold rotational symmetry and inversion symmetry, induced by the polar single-**Q** helical spin order [37, 42, 45, 219]. The former can be detected through optical linear dichroism [37, 65, 190]. To verify the pressure-induced enhancement of the helimagnetic order, we performed temperature-dependent LD measurements as a function of pressure [Fig. 6.2(a)], at the same pressure conditions as the corresponding Raman data on a separate thermal cycle, using a fixed probing wavelength. At all pressures (P_1-P_4), a sharp transition in the LD signal indicates a stabilized $T_{N,2}$ transition as pressure is increased [Fig. 6.2(a)], in agreement with the independently determined $T_{N,2}$ values from Raman.

We next investigate the effect of dimensionality on the evolution of the HM/MF phase under compression. To do so, we performed HP LD spectroscopy measurements on a mechanically exfoliated NiI_2 sample (from chemical vapor transport (CVT) grown single crystal) containing 5, 6, 10-layer and bulk flakes (Sample 2) (Fig. 6.2(b)). LD spectroscopy is used for the the detection of smaller optical signals in thinner samples. Figures 6.2(d)-(g), show the LD spectra vs. photon energy at $T = 30$ K and 300 K and $P = 5$ GPa for each thickness. We note the clear energy-dependent contrast in the LD spectra of the HM/MF phase (30K) compared to room temperature (300K). To extract the transition temperature, we calculate the difference of LD intensity in the spectral regions showing positive and negative contrast compared to spectra above $T_{N,2}$ at each temperature . The resultant temperature-dependent LD is shown in Figs. 6.2(h)-(o) at 5 GPa and 10 GPa for each thickness.

We first note that the LD results are reproduced for exfoliated CVT [Fig. 6.2(k)] and PVD grown [Fig. 6.2(a)] bulk samples, with $T_{N,2} \simeq 135$ K at 5.0 GPa. Similarly to the bulk case, the appearance of finite LD in the 5-,6-, and 10-layer flakes indicates a phase transition occurring at increasing temperatures as pressure increases from 5 to 10 GPa. We extract the corresponding helimagnetic transition temperatures, indicated by the black vertical lines in Figs. 6.2(h)-(o), and plot their values as a function of pressure for each flake in Fig. 6.2(c). In general, $\mathrm{T}_{N,2}$ decreases as the thickness decreases; however, this effect is more pronounced at 10 GPa, as discussed more below. Crucially, a robust signature of pressure-enhancement of the helimagnetic transition is confirmed down to the 5-layer limit and up to 10 GPa.

6.2.2 Pressure-dependent XRD

Having established the pressure enhancement of helimagnetism in bulk and few-layer samples, we next aim to understand the interplay of magnetic and crystallographic symmetry across the helimagnetic transition using high-pressure, temperature dependent XRD on a powder. XRD measurements were performed at Sector 16-ID-B of the Advanced Photon Source, Argonne National Laboratory, using an incident energy $E = 29.2$ keV, neon PTM and high-quality $\mathrm{NiI_2}$ powder grown by CVT. Temperature- and pressure-dependent diffraction was acquired with monotonically-decreasing temperature sweeps from above the transition to the base temperature $\simeq 40$ K at fixed pressure. The pressure was carefully stabilized using an *in-situ* double-sided membrane-driven DAC and monitored via ruby fluorescence.

For all pressures up to 10 GPa, the high-temperature structure remains trigonal and can be indexed to the $R\bar{3}m$ space group [42, 126]. To analyze the low-temperature magneto-structural transition, we focus on the $(2, 0, 8)$, $(0, 0, 12)$ and $(1, 1, 0)$ reflections ((h, k, l) in reciprocal lattice units of the high-symmetry $R\bar{3}m$ cell). Figs. 6.3(c)/(d) show the temperature-dependence of these reflections at representative pressures $P = 5.0$ GPa and 10.0 GPa, respectively. At all pressures, we observe a sharp change in the $(0, 0, 12)$ 2θ position which is nearly concomitant with the splitting of the in-plane $(2, 0, 8)$ peak. These structural distortions respectively correspond to an interlayer compression and a reduction of three-fold rotational symmetry, consistent with the conclusions of previous ambient pressure diffraction studies [42] and those reached from optical LD measurements (Fig. 6.2(a),(h)-(o)).

Closer inspection of the XRD data reveals the dominance of interlayer shearing ($\beta > 90°$), rather than distortions of the planar triangular lattice, in the reduction of structural

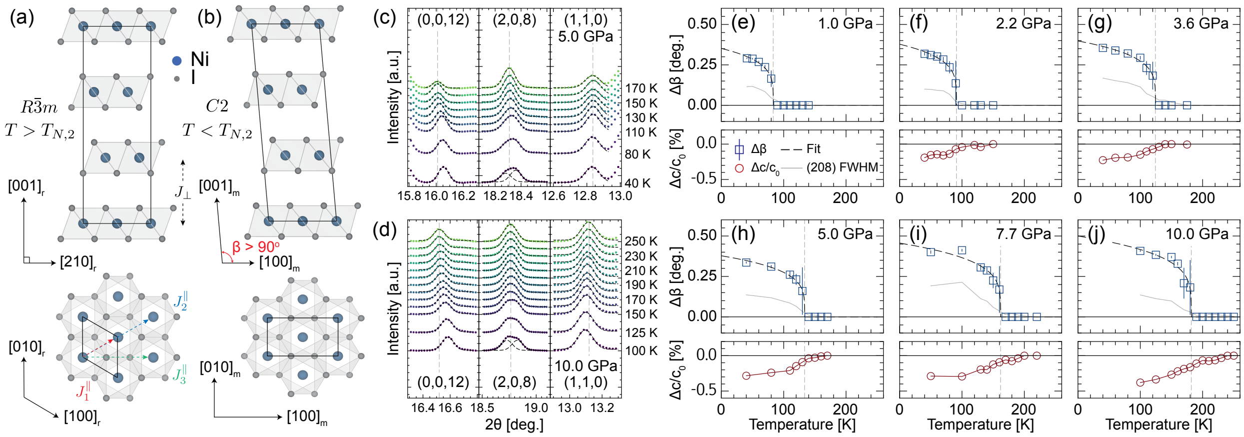

Figure 6.3: Side and top view for the (a) high-temperature rhombohedral (R$\bar{3}$m) and (b) monoclinic (C2) phases of NiI$_2$, defining the crystal axes and β angle. Interlayer ($J_\perp$) and intralayer ($J_i^\parallel$) exchange paths are indicated. Temperature-dependent XRD of the $(0, 0, 12)$, $(2, 0, 8)$ and $(1, 1, 0)$ reflections at (c), 5.0 GPa and (d), 10.0 GPa. Dashed black lines are Gaussian fits. (e)-(j), Temperature-dependence of $\Delta\beta$ $(90 - \beta)$ (top) and $\Delta c/c_0$ (bottom), where c_0 is the high-temperature c-axis length in the trigonal phase, for pressures between 1.0-10.0 GPa. The FWHM of the $(2, 0, 8)$ peak from a single-peak fit is shown as a grey line overlaid on the $\Delta\beta$ plots. Black dashed lines are order parameter fits of the form $|T/T_{N,2} - 1|^\alpha$, with $\alpha = 0.23$. The transitions ($T_{N,2}$) for each pressure are marked by vertical dashed grey lines.

rotational symmetry. As illustrated in Fig. 6.3(a)-(b), changes in both in-plane lattice parameters (Δa) and the interlayer stacking ($\Delta\beta$) are allowed in the monoclinic phase. Which component dominates, if any, can be determined by considering different reflections. As shown in Fig. 6.3(c)-(d), neither the pure-in plane $(1, 1, 0)$ nor the pure out-of-plane $(0, 0, 12)$ XRD peaks split upon cooling down, whereas the hybrid in-plane and out-of-plane $(2, 0, 8)$ peak splits, consistent with a predominant interlayer shearing which becomes more pronounced at elevated pressures. The observation of interlayer magneto-structural coupling has also been observed in other vdW magnets (e.g. CrI$_3$ [18–20] and FePS$_3$ [226, 227]), and reveals a close relationship between the interlayer structural symmetry and helimagnetic phase of NiI$_2$.

We thus extract the corresponding pressure- and temperature-dependent lattice parameters to determine $\Delta\beta$ (Figs. 6.3(e)-(j), top) and the interlayer compression $\Delta c/c_0$ (Figs. 6.3(e)-(j), bottom). The onset of these anomalies occurs at higher temperatures with increasing pressure. We estimate the corresponding transition temperatures ($T_{N,2}$), revealing a pressure-stabilized magneto-structural transition which tracks the values of $T_{N,2}$ from optical measurements.

6.3 Discussion

To summarize, the results of all measurements in the bulk are shown in the magneto-structural phase diagram in Fig. 6.4(a). In the low pressure regime (≤ 5 GPa), a nearly linear increase of both the AFM ($T_{N,1}$) and the multiferroic ($T_{N,2}$) transitions is observed, with rates of 15.3 and 14.4 K/GPa, respectively, with strong agreement among all techniques and among the three measured bulk samples. We also show the relative pressure enhancement as a function of layer number in Fig. 6.4(b), showing that the helimagnetic phase is stabilized by over a factor of 3 in all studied thicknesses between 0 and 10 GPa.

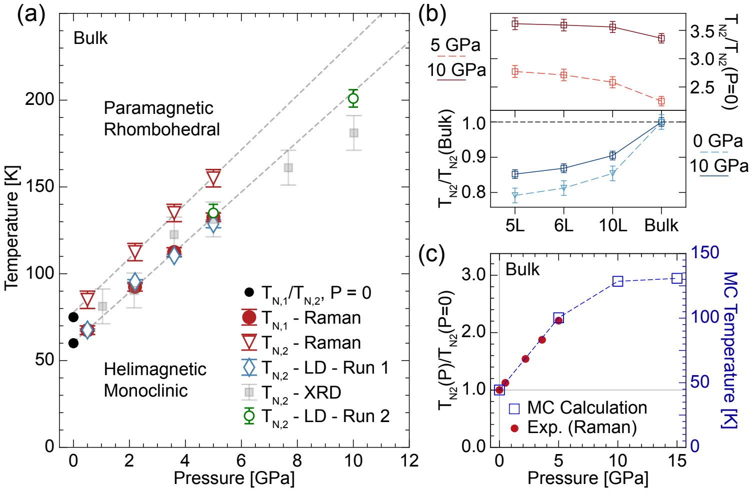

Figure 6.4: (a), Experimental phase diagram compiled from Raman, LD and XRD data for bulk NiI$_2$. Ambient pressure data are from Ref. [37]. Dashed grey lines are linear fits to $T_{N,1}$ and $T_{N,2}$ vs pressure. (b), $T_{N_2}/T_{N,2}$(Bulk) (top) and $T_{N,2}/T_{N,2}(P = 0)$ (bottom) versus layer number at 5/10 and 0/10 GPa, respectively. (c), Comparison of bulk experimental $T_{N,2}$ values from Raman experiments normalized by the ambient pressure value (left axis), compared to Monte Carlo calculations of $T_{N,2}$ vs. pressure for bulk NiI$_2$ from Ref. [126].

To understand the mechanism of these enhancements, we consider the pressure-dependence of the exchange interactions, which was recently studied from first-principles in Ref. [126]. The helimagnetic phase arises from competition between the intralayer first- ($J_1^{||}$) and third-nearest neighbor ($J_3^{||}$) exchange interactions, and is further stabilized by the interlayer exchange ($J_\perp$) [Fig. 6.3(a)]. Calculations show that while $J_1^{||}$ is weakly pressure-dependent, $J_3^{||}$ and $J_\perp$ are strongly enhanced by pressure. The cooperative effect of these interactions leads to a significant enhancement in the ordering temperature as determined from Monte Carlo (MC) calculations, which captures well the relative enhancement of $T_{N,2}$ in the bulk up to 5 GPa [Fig. 6.4(c)].

While both intralayer and interlayer exchange interactions contribute to this enhancement, we can experimentally confirm a key role of interlayer exchange by considering the combined effects of pressure and dimensionality in Fig. 6.4(b), where we plot $T_{N,2}$ vs layer number at ambient and high pressures. The reduction of $T_{N,2}$ with reduced layers at 0 GPa was attributed to a dimensionality controlled interlayer exchange, determined by the ratio $J_\perp/J_\parallel$ [37], given that $J_\parallel$ is hardly modified with decreasing layer number, while $J_\perp$ gets significantly reduced. We observe a similar reduction in $T_{N,2}$ with layer number at 10 GPa [Fig. 6.4(b)], suggesting that the interlayer exchange interaction is the dominant factor for the stability of the MF phase, both at ambient and high pressures. We also observe a significant enhancement of $T_{N,2}$ for the few-layer samples compared to the bulk, as can be seen by comparing $T_{N,2}/T_{N,2}(P=0)$ in Fig. 6.4(b). This relative enhancement likely suggests a non-negligible role of pressure-enhanced intralayer interactions, as well as a possible role of different interlayer compressibility and shear energy as thickness is reduced, discussed more below.

Finally, it is worth noting that the cycloidal phase of isostructural $NiBr_2$ is substantially destabilized with increasing pressure at a rate of -22.5 K/GPa [228], in contrast to what we observe in NiI_2. The ground state of $NiBr_2$ has a distinct in-plane propagation vector $[(h,h)]$ [228] to NiI_2 $[(h,0)]$ [42]. Therefore, increased interlayer interactions with either pressure or chemical tuning may favor the ground state observed in NiI_2, supporting our conclusions. It will be interesting to directly investigate the effects of pressure on the magnetic propagation vector with neutron scattering. Further, it will be critical for direct measurements of the ferroelectric polarization to resolve how pressure impacts the multiferroic nature of NiI_2.

In conclusion, we report a large enhancement of the helimagnetic/multiferroic phase in bulk and few-layer NiI_2 samples by over a factor of 3 between 0 and 10 GPa. The layer dependent transition temperatures show that this enhancement is mostly driven by interlayer exchange. A concomitant structural transition demonstrates a significant coupling of the interlayer distance and stacking symmetry to the helimagnetic order. These results identify the central role of the interlayer exchange interactions for the helimagnetic phase of NiI_2, both in the ground state and in the mechanism of its large stabilization under pressure.

6.4 Methods

Sample prepration

For sample 1 (Fig. 6.1) a bulk-like flake (thickness $\sim$ 100 nm) with dimensions $\sim$ 40×20 μm was grown by physical vapor deposition (PVD). For sample 2 (Fig. 6.2), bulk-like and few-layer NiI_2 flakes were mechanically exfoliated from single-crystals grown by chemical vapor transport (CVT). The PVD and CVT growth processes are described in Ref. [37].

Few-layer samples were exfoliated on 285 nm SiO_2/Si substrates in a high-purity nitrogen-filled glovebox. Samples of the desired thicknesses were identified with optical contrast and confirmed by atomic force microscopy (AFM, AFMWorkshop HR) (Fig. 6.5). The few-layer samples for high pressure measurements were double encapsulated in $\sim$ 10 nm thick hexagonal boron nitride (hBN) and placed on an exfoliated graphite substrate.

Since NiI_2 crystals are hygroscopic, they were handled with care for minimal air exposure.

The samples were transferred directly onto the diamond culet using dry-transfer techniques within a nitrogen-filled glovebox. For the optical measurements we used an Almax CryoDAC-ST. A Be-Cu (stainless steel) gasket for sample 1 (2) was loaded with a ruby crystal for pressure-calibration and an anhydrous 4:1 methanol-ethanol mixture for the PTM, which is well within the quasi-hydrostatic limit in the pressures studied for the optical measurements [229, 230]. The DAC was closed outside of the glovebox with less than 2 minutes of air exposure of the NiI_2 samples. No degradation of the samples was observed.

For the X-ray measurements (Fig. 6.3), pure NiI_2 powder was grown using CVT. The powder was loaded into a custom double-sided membrane-driven DAC for high pressure XRD inside an argon-filled glovebox. The DAC was closed with a neon gas PTM with no ambient exposure of the powder sample. Majority phase of anhydrous NiI_2 is confirmed in the XRD measurements, with a possible small minority of the hydrated phase ($NiI_2 \cdot 6H_2O$) resulting from air exposure, as characterized below.

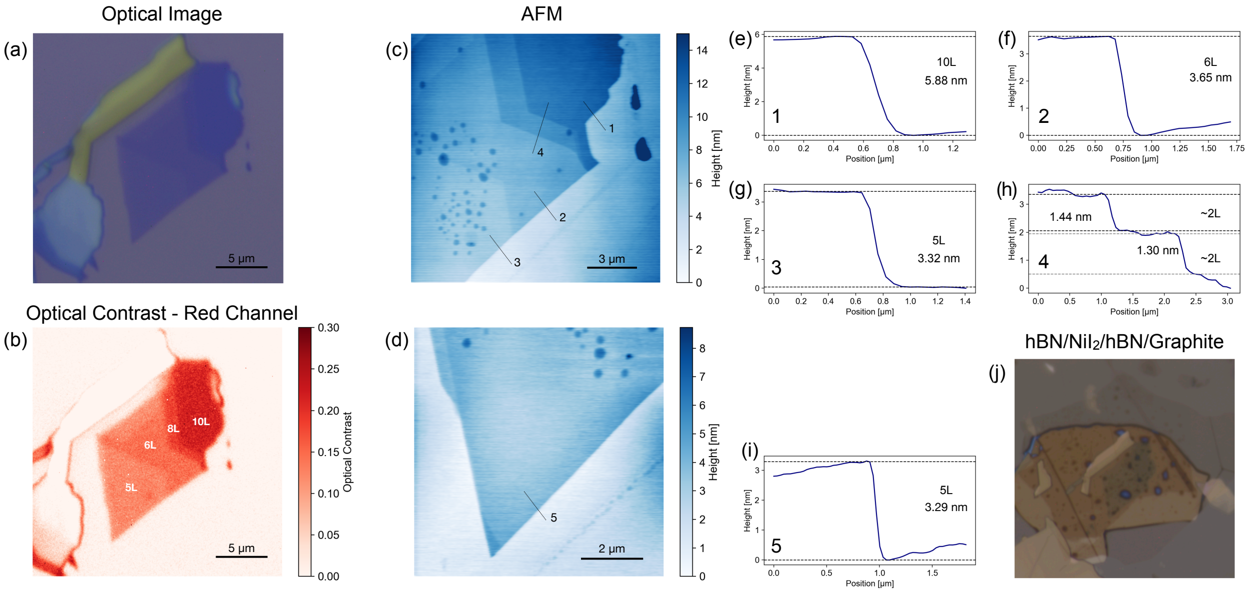

Figure 6.5: (a) Optical image of sample after exfoliation on 285 nm SiO_2/Si substrate. (b) Optical contrast ($-\Delta R/R$) with respect to the substrate in the red channel, with thickness identifications demarcated. (c)/(d), AFM measurements of the same sample in (a)/(b) in two separate regions. Black lines and numbers 1-5 indicate linecuts extracted for thickness determination as shown in the profiles of (e)-(i). (j) Final $hBN/NiI_2/hBN/Graphite$ stack transferred onto the diamond of the DAC before pressurization.

Optical measurements

To perform optical measurements, the DAC was loaded into a Montana Instruments S50 closed-cycle optical cryostat. Raman measurements were performed with a Horiba LabRam HR Evolution spectrometer, using a linearly polarized $\lambda = 532$ nm excitation and an 1800 lines/mm grating. A 50x objective (Olympus SLMPLN-50x) was used to focus the laser to approximately 2 μm spot. The incident power was around 50 μW and the reported spectra were acquired over 15 minutes, with each spectrum recorded twice for averaging. All reported Raman data were acquired in cross-polarized (XY) configuration, using volume Bragg grating filters in order to record Raman shifts down to 5 cm^{-1}. Due to depolarization effects from the DAC, there is a leakage of XX channel into the spectra resulting in a relatively high intensity of the primary A_g phonon line.

Linear dichroism measurements on sample 1 were recorded using either (a) a HeNe ($\lambda = 633$nm) source (for measurements at P_1) or (b) a supercontinuum source (NKT photonics) monochromatized to 650 nm to a 1 nm bandwidth (for measurements at P_2-P_4). The wavelength was changed as it resulted in higher signal-to-noise ratio. An incident power of 10 μW was used for all measurements. For sample 2, we recorded linear dichroism spectra using the supercontinuum source and a monochromator with bandwidth $\sim$ 1nm from 450-1020 nm. In all cases, the incident laser was amplitude-modulated by a mechanical chopper (ThorLabs) and linearly polarized at 45 degrees, before being sent through a photoelastic modulator (PEM, Hinds instruments) with fast axis at 0 degrees. The PEM was modulated at 50 kHz and a retardance of 0.5λ. The light was focused onto the sample using a 50x objective (Olympus SLMPLN-50x for sample 1, Mitutoyo MY50x-825 for sample 2), and the back-reflected light was collected by an amplified photodiode (ThorLabs). The signal was sent to two lock-in amplifiers to measure the linear dichroism signal at the second harmonic of the PEM frequency and the reflectance measured at the chopper frequency, used as normalization.

For the optical measurements on sample 1, the sample was first cooled to base temperature of 5 K. The linear dichroism was then recorded on warming on a slow temperature ramp ($\sim$ 1 K/min), and the pressure was recorded at the end points. The sample was then cooled down to base temperature and Raman measurements were recorded on a second warm up cycle, again measuring the pressure at the end points of the temperature sweep. The sample was then warmed to room temperature to increase the pressure and the process was repeated. All finite pressure measurements were acquired by monotonically increasing pressure. The sample was decompressed after $P_4 = 5$ GPa and an additional temperature dependence was recorded on the recovered sample at ambient pressure to check for consistency with prior measurements [37].

For sample 2, the sample was first cooled to a base temperature of 30 K. Linear dichroism spectra from the bulk, 10L, 6L, 5L, and the graphite substrate reference were recorded at each stabilized temperature on a single, monotonically increasing temperature sweep. At 5.0 GPa, Raman spectra from the bulk were recorded on a subsequent temperature ramp to confirm consistency with the results in the PVD grown bulk (sample 1). Attempts to measure Raman signal from the few layer samples inside the DAC were unsuccessful given their small signals. The pressure was monitored at the end points of each temperature sweep using Ruby fluorescence.

XRD measurements

High-pressure XRD was performed at HPCAT, Advanced Photon Source, Argonne National Laboratory (Sector 16-ID-B). The DAC was loaded with a neon PTM and mounted into a cryostat with a base temperature of 40 K for pressure- and temperature-dependent XRD measurements. At each pressure, the sample was cooled down to approximately 40 K and the XRD diffractograms were recorded. Then, the DAC was warmed up to room temperature and the pressure was increased. A double-sided membrane DAC stabilized the pressure in-situ, such that temperature-variations of the pressure could be corrected. The pressure was monitored with an in-situ ruby fluorescence system. XRD was recorded with an incident energy 29.2 keV.

6.5 Additional Data and Discussion

Linear dichroism spectroscopy data

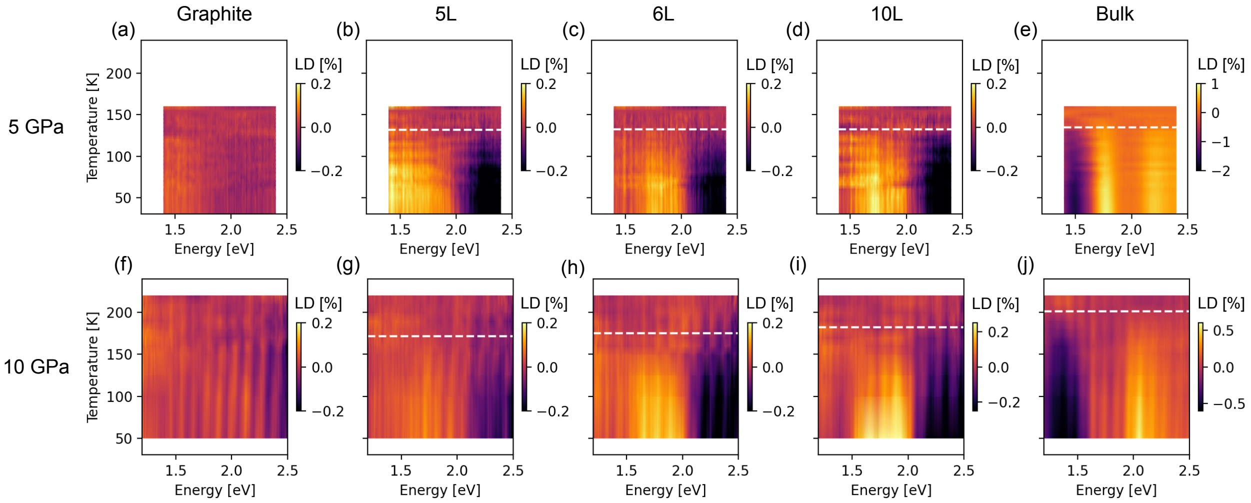

Figure 6.6: Temperature dependent linear dichroism spectra false color maps for, respectively, the graphite substrate, 5L, 6L, 10L and Bulk samples at (a)-(e) 5.0 GPa and (f)-(j) 10.0 GPa. Spectra for each sample at a given temperature and pressure are taken at identical conditions, on the same stabilized temperature point of the same temperature sweep. The color maps for Graphite, 5L and 6L are shown in the same color map scale at both pressures. Horizontal dashed white lines indicate the phase transition temperature $T_{N,2}$ extracted from the data.

Here we show the full data set for the pressure-, layer- and temperature-dependent linear dichroism spectroscopy experiment performed on Sample 2. The full data are presented as false color maps in Fig. 6.6. For thin flakes, the temperature dependent contrast is extracted by integrating the spectral weight in the range 1.7-2.0 eV and 2.0-2.4 eV for 5.0 GPa and 1.6-2.0 eV and 2.0-2.5 eV at 10.0 GPa. For the bulk, integration ranges of 1.4-1.65 eV and 1.65-1.9

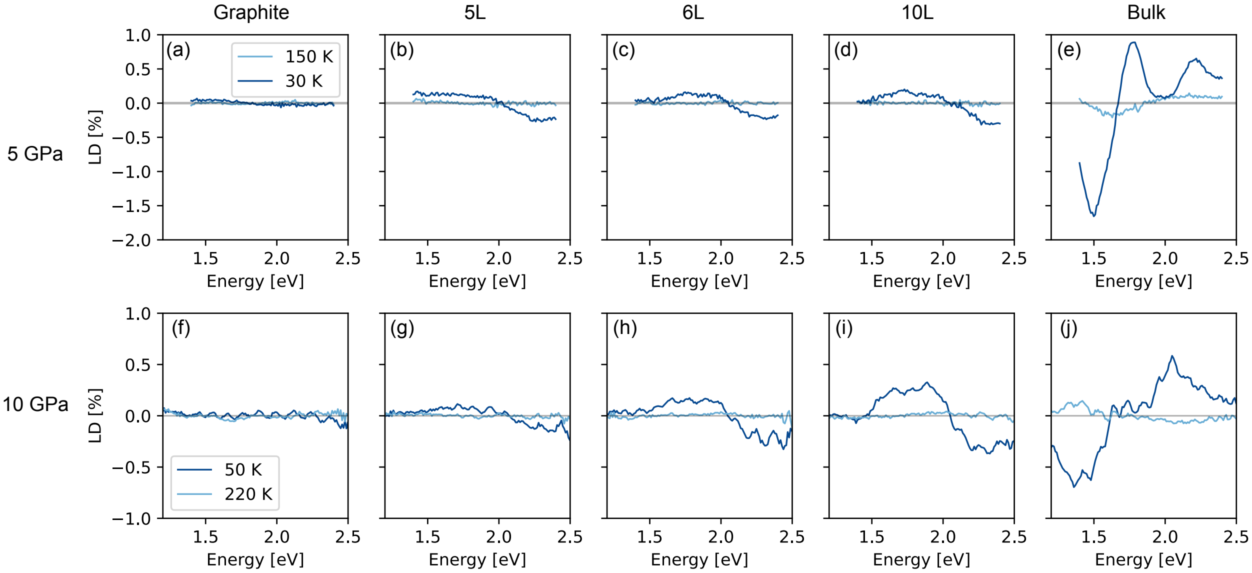

Figure 6.7: Linecuts of the LD spectra at base temperature (30K) and above the helimagnetic transition (150/220 K) for, respectively, the graphite substrate, 5L, 6L, 10L and bulk samples at (a)-(e) 5.0 GPa and (f)-(j) 10.0 GPa. Data are the same as those displayed in the false color maps of Fig. 6.6.

eV for 5.0 GPa and 1.3-1.6 eV and 1.9-2.3 eV at 10.0 GPa were used. The spectra for each flake at base temperature (30/50 K) and above the transition (150/220 K, for 5.0/10.0 GPa, respectively) are shown in Fig. 6.7. The noise level for the experiments is approximately 0.02% in units of linear dichroism, which increases for energies above 2.3 eV due to lower laser power from the supercontinuum laser. We note the appearance of oscillations in the spectra at 10.0 GPa which are seen in Fig. 6.6/6.7. This is not from intrinsic noise of the measurement, but are rather interference fringes from the sample and the top diamond face. The period of the fringes depends on the distance between the diamond culets, which decreases as pressure is increased from 5.0 to 10.0 GPa.

To ensure that the measured spectra are robust from the thin layers inside the DAC, we fabricated a second heterostructure to compare LD spectra at ambient conditions and those collected at high pressures. To do so, we identified another 6L exfoliated NiI_2 based on optical contrast, double encapsulated it in hBN and placed it on a bulk-like graphite flake as a substrate (see Fig. 6.8). We note that using graphite as a substrate for the samples was intentionally chosen to reduce the thin film interference effects, which are known to effect the magneto-optical spectra of 2D materials, particularly on SiO_2/Si substrates. Graphite has a flat reflectivity curve across the full spectral range and is exfoliable, making it a controllable substrate for registering magneto-optical/dichroic spectra of 2D materials. We show a comparison between the ambient pressure LD spectra in the 6L sample of Fig. 6.8(a)/(b) with the finite pressure 6L spectra in sample 2 in Fig. 6.8(c). We find both qualitative and quantitive agreement, with a redshift of the main features near 2.0 eV as a function of pressure being observable. This shows that registered temperature dependent LD spectra are intrinsic to the sample, and not resulting from interference inside the DAC, or the PTM.

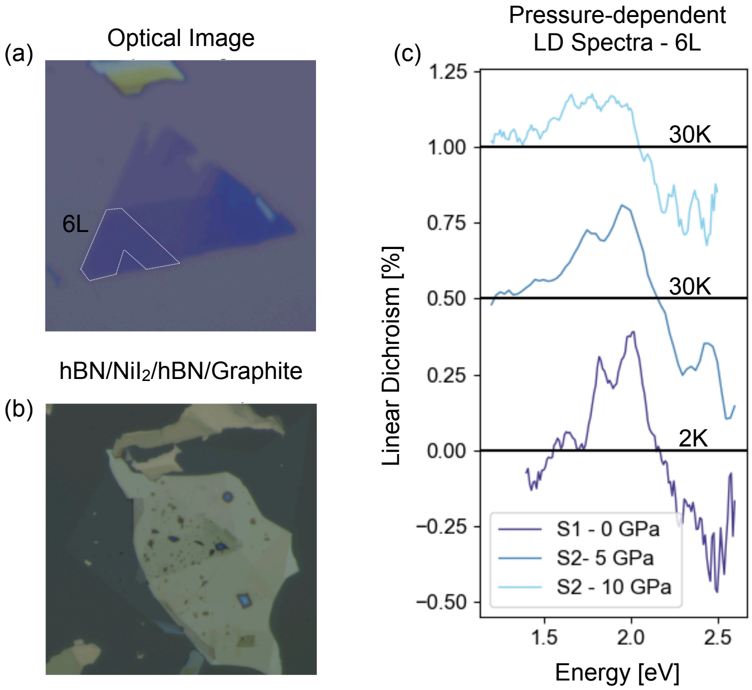

Figure 6.8: (a) Optical image of an additional exfoliated NiI_2 few-layer flake on a 285 nm SiO_2/Si substrate. White dashes outline a 6L flake. (b) The same flake, double encapsulated in hBN on top of an exfoliated graphite flake and transferred onto a sapphire substrate. (c) Linear dichroism spectra of 6L samples as a function of pressure. Data from the 6L region of the sample in (b) is shown in purple, recorded at $T = 2$ K and ambient pressure $P = 0.0$ GPa. This is compared to finite pressure data on the 6L region of Sample 2 at 5.0 and 10.0 GPa and base temperature $T = 30$ K.

Ambient pressure optical data on few-layer samples

In order to determine the ambient pressure transition temperatures of 5L, 6L and 10L flakes, we performed linear dichroism spectroscopy on an additional exfoliated flake on a 285nm SiO_2/Si substrate. The flakes and optical contrasts are shown in Fig. 6.9(a)/(b). Temperature dependent linear dichroism values, extracted from LD spectroscopy experiments, are reported in (c), determining the layer-dependent transition temperature at ambient pressure for the thicknesses of relevance to this study. The values determined here are used for comparison to the layer-dependence of the transition temperatures at finite pressure (Fig. 6.4). To confirm the correspondence between the transition temperature $T_{N,2}$ as determined by LD spectroscopy and Raman experiments in few-layer samples, we also performed temperature dependent cross-polarized Raman on the 5L region, the thinnest sample addressed in this study. These results are reported in Fig. 6.9(d)/(e). A transition temperature of $T_{N,2} = 47.5 \pm 2.5$K is confirmed from both techniques. This confirms that the electromagnon excitations appear at the same temperature that finite LD arises in the 5L sample, justifying the use of LD spectroscopy as an optical signature for the helimagnetic phase in few-layer samples at elevated pressures.

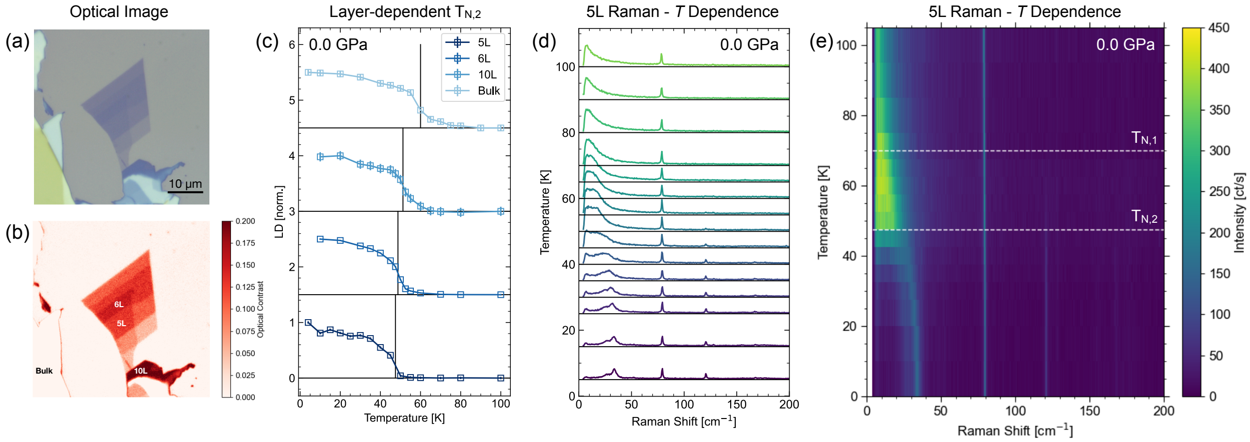

Figure 6.9: (a) Optical image of a dedicated sample for ambient pressure measurement of the layer dependent transition temperatures for 5L, 6L, 10L and bulk. (b) Optical contrast ($-\Delta R/R$) of the flake in (a). (c), Layer- and temperature-dependent linear dichroism measurements on 5L, 6L, 10L and bulk at ambient pressure, using the same linear dichroism spectroscopy method as for the few-layer samples at high pressure. Transition temperatures are indicated by vertical black lines. (d) Temperature dependent XY polarized Raman spectra for the 5L sample and (e) corresponding color map. The transitions $T_{N,1}$ and $T_{N,2}$ are indicated by horizontal white lines. $T_{N,2}$ of $\sim 47.5 \pm 2.5$K is confirmed from both Raman and LD measurements on the 5L sample at ambient pressure.

High pressure Raman data and analysis procedure

We show the raw Raman spectra versus pressure and temperature in Fig. 6.10. The finite-pressure data is the same as those displayed in Fig. 6.1. Here, we show the raw line cuts for clarity. A constant background was subtracted from all spectra determined from the high-frequency data above 300 cm^{-1}, depicted as red lines in Fig. 6.10. The temperature dependent constant background results from a broad, featureless fluorescence of the PTM. We also show corresponding data from the recovered sample at $P'_{00} = 0$ GPa, acquired by decompression of the DAC from $P_{04} = 5.0$ GPa. All spectra were recorded with XY polarization conditions and the relative alignment of the incident polarization with respect to the crystallographic axes were kept the same throughout all experiments. The incident polarization is vertical ($E_i \parallel y$) in the image of the sample loaded in the DAC in Fig. 6.1(a). XY polarization was used to reduce the elastic line and fluorescence background from the DAC and PTM, while giving access all salient Raman features with high signal-noise ratio.

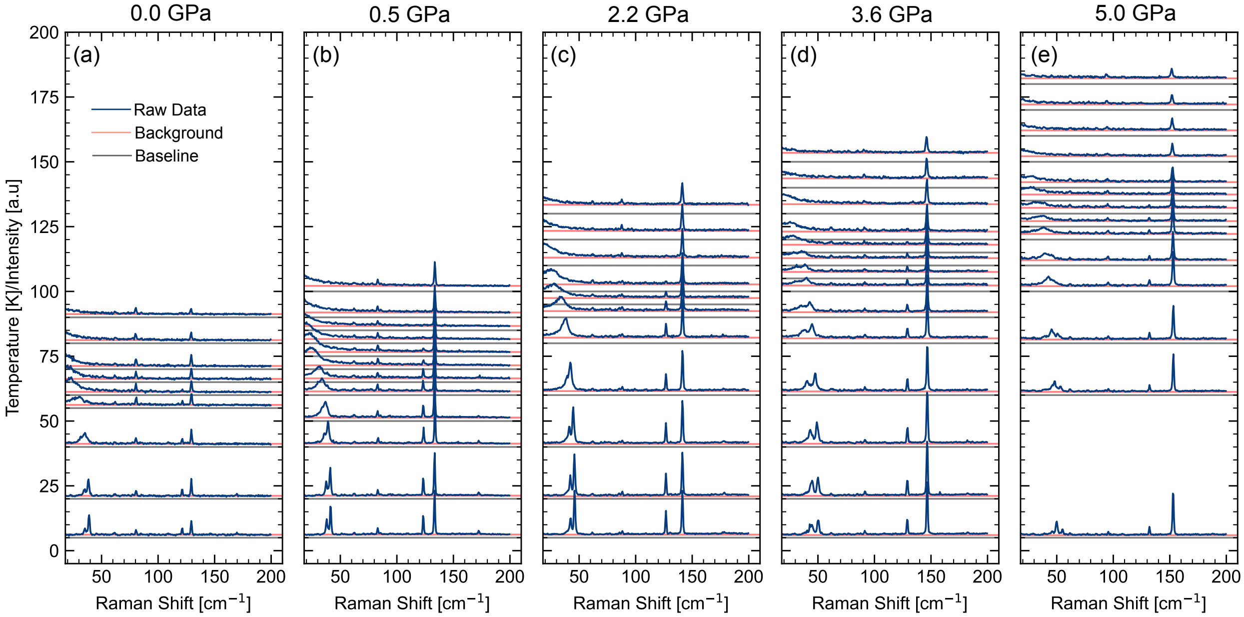

Figure 6.10: Raman spectra in XY polarization versus pressure and temperature for sample 1. The spectra are shifted vertically by the temperature for clarity. For each spectrum we show the raw data (dark blue), the baseline (grey) and the constant background from temperature-dependent PTM fluorescence (red). The ambient pressure data were recorded from the same sample after decompression, which is consistent with previously reported ambient pressure spectra [37]. The other spectra were recorded with monotonically increasing pressure from P_{01} to P_{04}.

We also provide higher detail of the evolution of the Raman spectra in the vicinity of the transitions $T_{N,1}$ and $T_{N,2}$ to highlight the definitions of the two transitions from Raman data in Fig. 6.11. We define the transition temperatures based on the evolution of Raman spectra observed at ambient pressure [37]. Upon warming up from base temperature, $T_{N,2}$ is characterized by a clear discontinuity in the energy of the low-energy modes (electromagnon), indicated by the red arrows imposed on the data in Fig. 6.11. For $T_{N,2} < T < T_{N,1}$, the low-energy mode remains peaked at finite energy (indicated by black arrows), before softening to zero energy and leaving only the tail of a quasielastic line for $T \geq T_{N,1}$. Separately, the M_1 mode decreases in intensity above $T_{N,2}$ before disappearing at $T_{N,1}$. Together, these features define the $T_{N,1}$ transition temperature. $T_{N,1}$ is less sharply defined than $T_{N,2}$ and thus we assign a correspondingly higher error (±5K).

To provide more detail on the temperature dependence of the M_1 mode for determination of $T_{N,2}$ and $T_{N,1}$, we extracted the temperature-dependent intensity of the A_g and the M_1 modes versus pressure in Fig. 6.12. The latter was shown to be an indicator of the magnetic phase transition, rising between $T_{N,1}$ and $T_{N,2}$ [37] upon cooling down, thus providing a secondary signature of the phase transition in addition to the soft modes which were used to estimate the transitions above. While the A_g phonon shows a gradual decrease with temperature upon warming up, at all pressures, the M_1 mode goes to zero in vicinity of

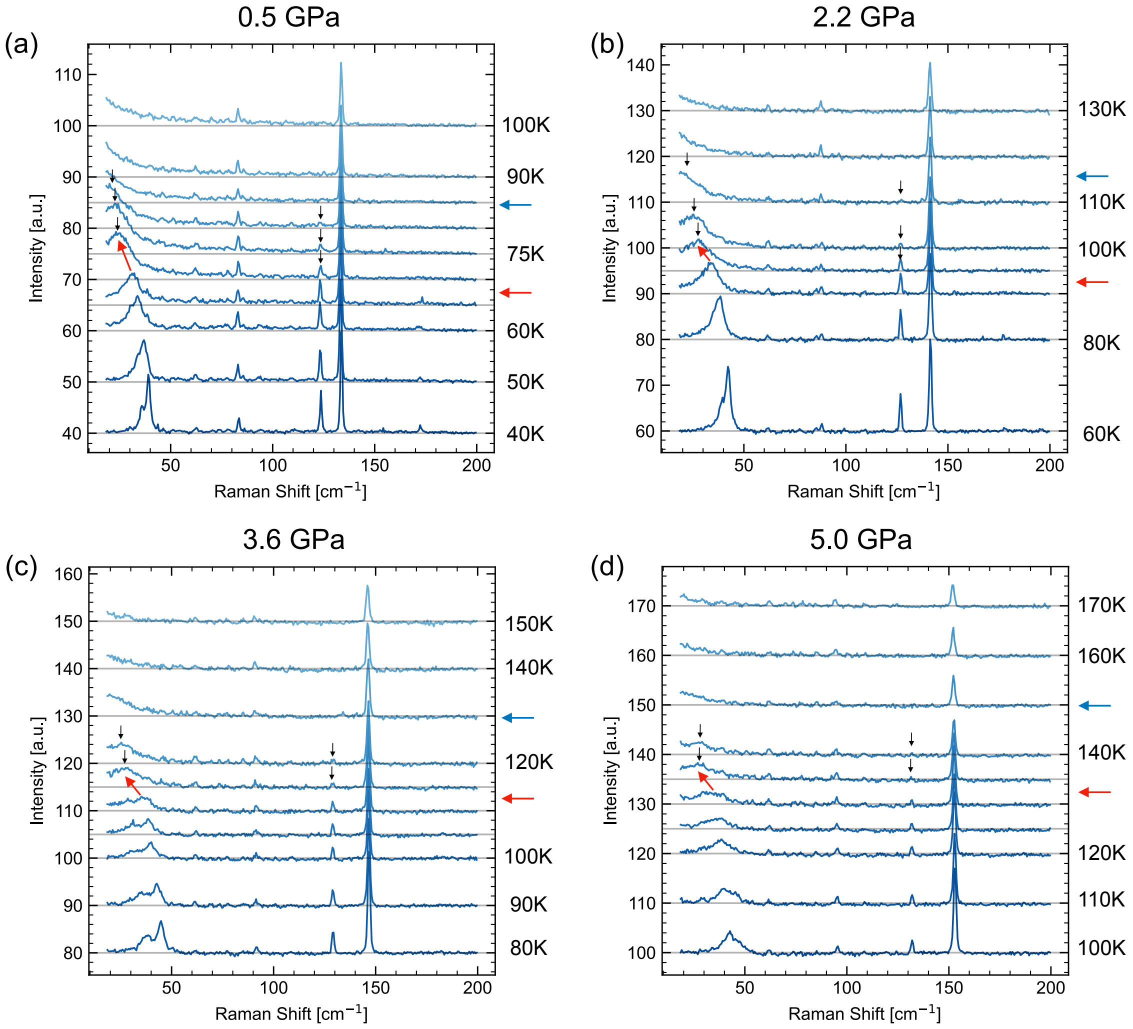

Figure 6.11: Temperature-dependent XY polarized Raman spectra in the vicinity of the transitions $T_{N,1}$ and $T_{N,2}$ for (a) 0.5 GPa, (b) 2.2 GPa, (c) 3.6 GPa, and (d) 5.0 GPa on sample 1. Red arrow overlaid on spectra indicates the discontinuity in the energy of the low-energy excitation, defining $T_{N,2}$ (indicated by red arrow on right hand side of the temperature axis). Above $T_{N,2}$, black arrows overlaid on the spectra highlight the finite energy soft mode and the M_1 mode that persist between $T_{N,1}$ and $T_{N,2}$. $T_{N,1}$ is then defined as the temperature when the soft mode energy goes to zero, leaving just a quasielastic tail centered at zero energy transfer, and the M_1 peak disappears. $T_{N,1}$ is indicated by a blue arrow on the right hand side temperature axis.

the transition temperatures determined from the soft modes (shown as vertical lines in Fig. 6.12). This is consistent with the ambient pressure results reported previously [37] and bolsters our identification of pressure-stabilized magnetic phase transitions from the Raman data. We note that while the A_g mode can acquire finite XY channel intensity due to the reduced symmetry across the trigonal-to-monoclinic phase transition, this effect is likely small as shown in a previous ambient pressure Raman investigation [37] and cannot explain the relatively large intensity observed here at all pressures. Instead, we associate the finite A_g intensity to a depolarization effect from the diamond anvil cell which causes a mixture of the XX and XY polarization channels.

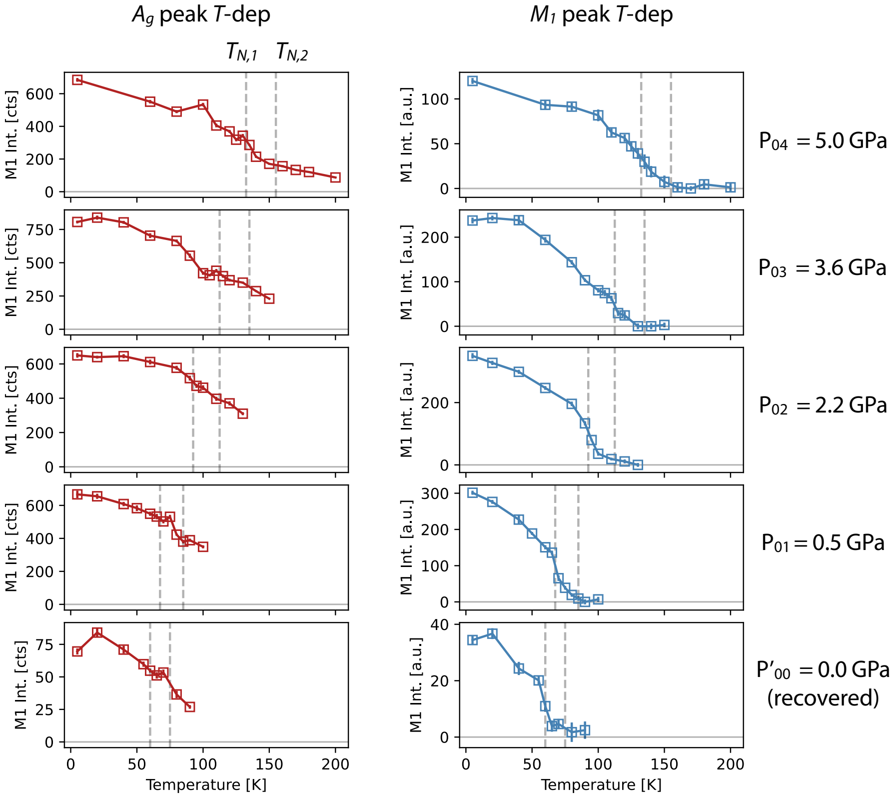

Figure 6.12: Temperature dependence of the A_g (left, red) and M_1 (right, blue) peaks as a function of pressure and temperature. Values represent the amplitude of single gaussian peaks fit to the data shown in Fig. 6.10. Vertical dashed lines indicate the transition temperatures $T_{N,1}$ and $T_{N,2}$ independently determined from the soft mode excitations and linear dichroism.

High pressure XRD data and analysis procedures

All of the raw XRD data used for the temperature- and pressure-dependent structural analysis are shown in Fig. 6.13. Besides the full range diffractograms, we also show zoom-ins of the peaks used for specific analysis of peak splitting and the c-axis magnetostriction. For the former, the (208) peak was used since it is high in 2θ, increasing sensitivity to small distortions, and for its relative isolation from other peaks. For the c-axis length, we used the (0012) peak except for P_{01} where we used the isolated (003) peak since the (0012) overlaps with the $(20\bar{4})$ at this pressure. We note some limitations of the P_{01} data which shows significant pressure variations and thus a large variation in the lattice parameters as a function of temperature despite a nominally fixed pressure. For the P_{01} temperature sweep, we used

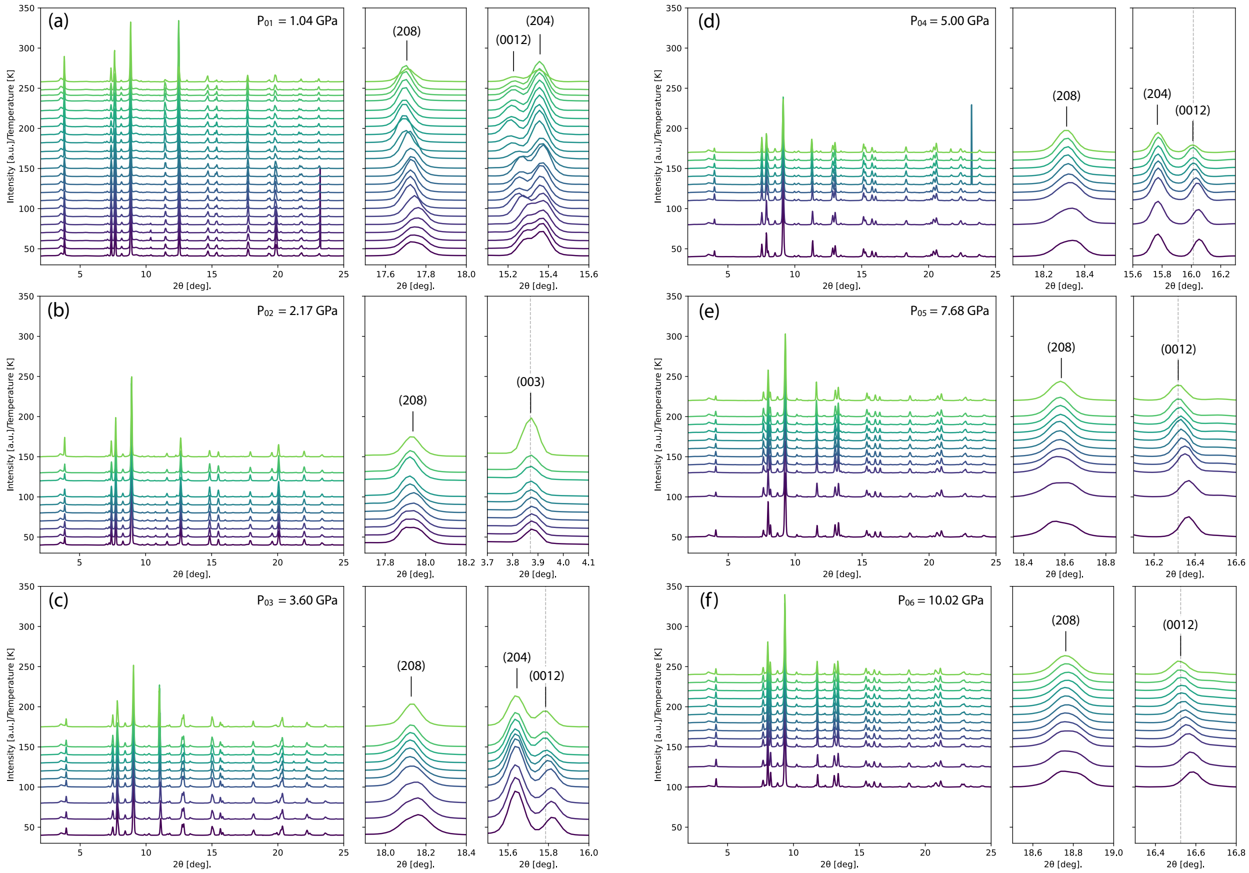

Figure 6.13: Full temperature and pressure-dependent XRD data from (a), $P_{01} = 1.04$ GPa to (f) $P_{06} = 10.02$ GPa. From left to right in each subplot is (i) the full XRD spectra, and zoom-ins of (ii) the in-plane and (iii) out-of-plane peaks used for analysis of the monoclinic phase transition and c-axis magnetorestriction. Except for P_{02}, the latter two are the (208) and (0012) reflections. At P_{01} it was necessary to use the isolated 003 peak for out-of-plane analysis due to an overlap of the (0012) and (20$\bar{4}$) peaks at that pressure. Data in each plot are independently normalized by a constant factor and are shifted vertically proportional to the temperature for clarity.

a smaller thermalization time between temperature points and we conjecture that this was insufficient for stabilization of the position and pressure inside the cell to a consistent value across all temperatures. For $P_{02} \rightarrow P_{06}$ we used a different protocol with significant ($\simeq 5$ min) thermalization time at each temperature which fixed the issue. While this precludes analysis of the temperature dependent lattice parameters with sufficient accuracy at P_{01}, the width and spitting of the (208) peak is a robust quantity.

All peaks were fit with Gaussian lineshapes. The c-axis length versus T was directly determined from single-peak fit of the corresponding (003)/(0012) peak for each pressure. For the (208) we used a two-step procedure to determine the phase transition temperature. We began by fitting the (208) to a single Gaussian peak with free parameters of width, position and amplitude. From these fits, it was found that the width of the peak suddenly

P (GPa)	1.04	2.17	3.60	5.00	7.68	10.02
a (Å)	3.891	3.863	3.823	3.793	3.745	3.717
c (Å)	19.240	18.881	18.578	18.311	17.951	17.691

Table 6.1: Pressure dependent lattice parameters of NiI_2 at $T = 200$ K.

increases at low temperature and the lineshape is clearly double peaked at base temperature (Fig. 6.13). We then used a reduced χ^2 analysis to fit the spectra to single- and two-Gaussian peak models, with the model chosen by optimal χ^2 per fitting parameter. These determined the finite peak splitting curves in Fig. 6.3. The width of the single-peak fit model and the peak-splitting from the two-peak model are directly compared in Fig. 6.3, showing good agreement and bolstering our assignment of the transition temperature. Error bars for $T_{N,2}$ were fixed to the temperature step size (10 K) which are larger than the statistical fitting error bars from the order parameter $|T/T_c - 1|^\alpha$ fits to the T-dependent peak splitting shown in Fig. 6.3.

In Fig. 6.14 we show the evolution of the XRD spectra at $T = 200$ K for pressures $P_{01} \rightarrow P_{06}$. We report the spectra here as the square root of total counts to highlight smaller intensity peaks. Note that $T = 200$ K is above the identified magneto-structural transition for all considered pressures. The spectra are compared to structure factor calculations for the $R\bar{3}m$ structure shown as black bar plots below the spectra. We note that most peaks and their relative intensities are well captured by the predicted pattern for $R\bar{3}m$ symmetry, which is the same as the high-temperature structure at ambient pressure [42]. The ambient pressure atomic positions are kept the same for all pressures with pressure-dependent lattice parameters a/c determined from the (208) and (0012) reflections. The pressure dependent lattice parameters up to $P_{06} = 10.02$ GPa are summarized in Table 6.1. Smaller additional peaks that are not indexed could be due to small minority phase of degraded sample, discussed below, while the peak appearing between 11-12 deg. is diffraction from the solidified Ne PTM above 3.60 GPa. Importantly, the majority phase is $R\bar{3}m$ at all pressures, showing that the structural symmetry remains trigonal up to at least 10.02 GPa, in agreement with the Raman results.

Structural analysis of lattice distortion below $T_{N,2}$

The low temperature space group at ambient pressure has been previously reported by Kuindersma et al. [42]. The authors report a transition from a rhombohedral cell at high temperature, to a centered monoclinic cell below $T_{N,2}$ as depicted in Fig. 6.3. The low-temperature monoclinic phase has two important structural distortions: (i) a splitting of the triangular lattice constants within the plane along the orthonormal monoclinic axes (a_M/b_M), reducing the planar rotational symmetry and (ii) an interlayer shearing, deviating the interlayer stacking order from the high-symmetry rhombohedral configuration. In principle, both distortions occur in the monoclinic phase. We here parameterize these intra- and inter-layer stuctural distortion components as $\delta a/a$ and β, respectively.

In the high-pressure XRD data, we observe a clear splitting of the (208) reflection (indexed to the high-temperature structure). In principle, this splitting could be due to either structural distortions of the type $\delta a/a$ or the interlayer shear β. To quantify these distortions independently, we consider a pure in-plane peak, $(2\bar{1}0)$.

The interlayer shear only splits reflections of the type (hkl), for $l > 0$, while the intralayer lattice parameter distortion splits all (hkl) peaks for any l with h or $k \neq 0$. We show this diagramatically in Fig. 6.15(a)-(d) using the (208) and $(2\bar{1}0)$ as representatives. We first consider a monoclinic distortion dominated by the interlayer shearing ($\beta > 0$ and $\delta a/a \sim 0$) and confirm that this results in a (208) splitting while $(2\bar{1}0)$ reflections remain degenerate (Fig. 6.15(a)/(b)). Separately, we consider the opposite scenario with $\beta = 90°$ in the high-symmetry interlayer stacking and instead consider distortions of the type $|\delta a/a| > 0$, showing the expected splitting of both the (208) and the $(2\bar{1}0)$ reflections.

We now consider the data at 10.02 GPa as an example and look at the peak widths of the $(208)/(104)/(2\bar{1}0)/(0,0,12)$ reflections as a function of temperature. The raw data are depicted in Fig. 6.3. We consider the full width half maximum (FWHM) width of these peaks determined by fits to a single Gaussian function. If the peak displays an observable splitting, one expects an increase in the FWHM. This is clearly observed for the (208) peak at all pressures, as shown in Fig. 6.3 and for 10.02 GPa in Fig. 6.15(e). A smaller but observable increase in the FWHM of the (104) reflection is also observed. Meanwhile, the $(2\bar{1}0)$ and $(0,0,12)$ reflections do not display any observable broadening, consistent with an intralayer structural distortion that is small compared to our experimental Q resolution and ruling out an inhomogeneous interlayer strain yielding extrinsically broadened diffraction peaks for $l > 0$. We note that the expected splitting of the $(2\bar{1}0)$ reflection should be greater than the (208) if intralayer distortions dominated, the latter of which is experimentally $\sim$ 0.1 degrees, and thus should be easily observable if present. We conclude that the dominant structural distortion at high pressures, in terms of change in interatomic distances, comes from the interlayer shear. The change in the stacking configuration naturally explains the concomitant shrinking of the c-axis parameter. These observations together suggest a key coupling between both the interlayer distance and stacking symmetry with the helimagnetic ground state of $\mathrm{NiI_2}$.

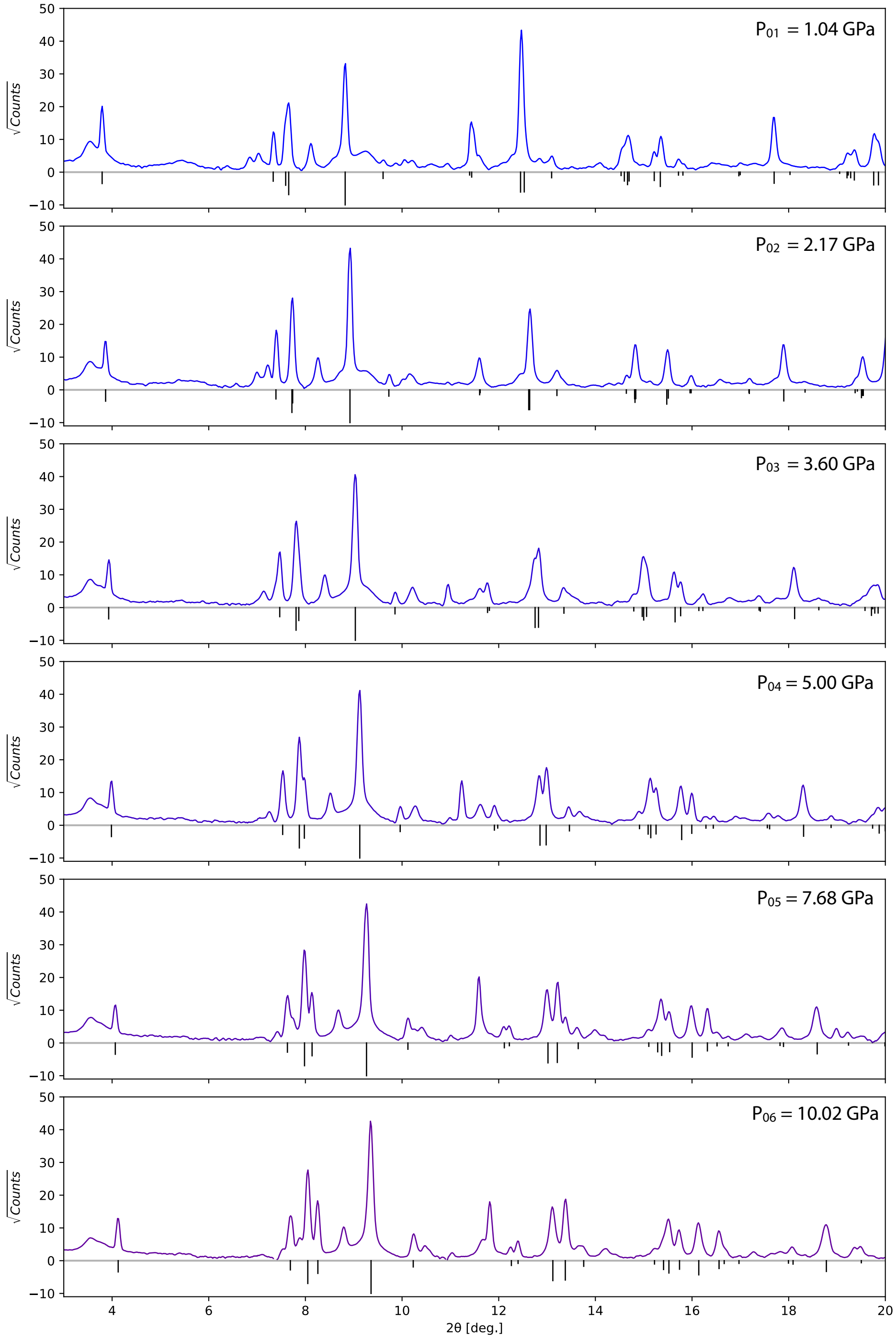

Figure 6.14: Pressure dependence of the XRD spectra between $P_{01} = 1.04$ GPa (top) and $P_{06} = 10.02$ GPa (bottom) at $T = 200$ K. Spectra are reported $\sqrt{I}$ in counts for clarity. These are compared to structure factor calculations based on the high-temperature ambient pressure $R\bar{3}m$ structure with appropriately modified lattice parameters (see text), indicated by black bars in arbitrary units below the experimental spectra.

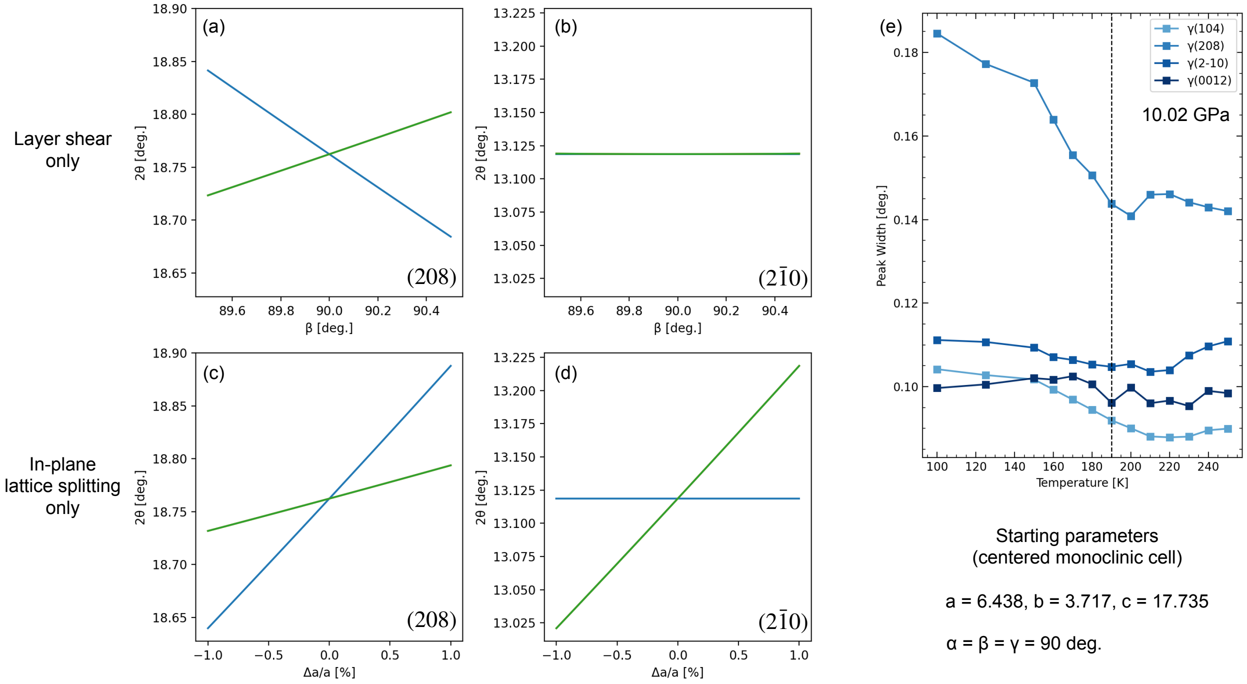

Figure 6.15: Comparison of the splitting behavior of $(h0l)$ and $(hk0)$ type reflections with different possible lattice distortions in the low temperature monoclinic phase. Splitting of the (a) (208) and (b) $(2\bar{1}0)$ reflections as a function of the interlayer shear parameter β. Splitting of the (c) (208) and (d) $(2\bar{1}0)$ reflections as a function of the in-plane lattice distortion $\delta a/a$. Values are calculated assuming a centered monoclinic cell with parameters determined for the high symmetry phase at 10.02 GPa. (e) Full width half maximum of the $(208)/(104)/(2\bar{1}0)/(0,0,12)$ reflections as a function of temperature at 10.02 GPa.

Chapter 7

Interlayer-shear driven helimagnetism in NiI_2

The work in this chapter is a co-first author work with Yi Tseng and the present author (C.A.O.). Y.T. and C.A.O. performed the resonant diffraction measurements with the assistance of Ronny Sutarto, Jiarui Li and Sahaj Patel. Y.T. and C.A.O. performed the structural diffraction with the assistance of Christie Nelson, Raúl Acevedo-Esteves, and Meghna Shankar. Qian Song grew the samples. C.A.O. performed the ground state calculations. Additional theoretical support was provided by Paolo Barone and Silvia Picozzi. Experiments were supervised by Riccardo Comin.

7.1 Introduction

In the previous chapter, we showed using a combination of high-pressure and optical techniques including optical linear dichroism, Raman spectroscopy and X-ray diffraction that (a) there is a large enhancement of the helimagnetic transition temperature with hydrostatic pressure at a rate of ~ 14 K/GPa in the bulk and (b) there is a significant coupling between interlayer stacking symmetry and the single-$\mathbf{Q}$ helimagnetic state.

The large enhancement rate is attributed to a pressure-enhancement of the interlayer exchange interactions, which is demonstrated by the layer-dependence of the transition temperature at different pressures. Specifically, we previously showed that at ambient pressure the layer-dependent $T_{N,2}$ value can be fit to an empirical relation related to the ratio $J_\perp/J_\parallel$ where thicker layers display a higher transition temperature due to a dimensionality-tuned contribution of the net interlayer exchange in the Hamiltonian [37] (Chapter 5). Thus, the characteristic decreasing trend of $T_{N,2}$ vs. layer number up to 10 GPa provides an experimental signature that the interlayer interactions are primarily responsible for the enhancement of T_N with pressure. This implies that the observed helimagnetic ground state with $\mathbf{Q} = (0.138, 0, 1.457)$ r.l.u. is promoted by increasing the interlayer exchange.

On the other hand, as we increase the interlayer interactions and the transition temperatures with pressure, we also observe that the rhombohedral-to-monoclinic structural transition is enhanced alongside the helimagnetic order [42]. This shows that the structural transition is closely linked to the presence of helimagnetic order, rather than being an independent structural distortion driven by, e.g., a non-magnetic lattice instability. Critically, we showed that the monoclinic distortion is characterized by a change of the stacking symmetry of different triangular lattice layers, corresponding to an interlayer shear quantified by the monoclinic crystallographic angle β deviating from the rhombohedral value of 90° (Chapter 6). At the same time as the interlayer shear, we also observe a pronounced compression of the interlayer distance. The close coupling of this structural transition to the magnetism, and the dominant interlayer nature of the crystallographic distortion, suggest that this is a magneto-structural transition and that the magnetic ground state is closely linked the interlayer exchange interactions and the stacking symmetry. This conclusion fits naturally with the stabilization of this phase with increasing interlayer exchange vs. pressure, as well as with the role of interlayer interactions for stabilizing the helimagnetism as a function of layer number at ambient pressure [37].

From these observations, we argue that the observed magnetic ground state with $\mathbf{Q} = (0.138, 0, 1.457)$ r.l.u. in bulk $\mathrm{NiI_2}$ is stabilized by the interlayer exchange interactions, breaking the degeneracy between other closely lying magnetic wavevectors (Fig. 7.1). As we showed, the interactions stabilizing the observed bulk ground state have not been clarified from a theoretical standpoint, with calculations always predicting a phase with in-plane wavevector $\mathbf{Q}_{\parallel} = (h, h)$, which is what is observed in isostructural $\mathrm{NiBr_2}$ [228] and the expected result for a Heisenberg exchange-frustration model with FM/AFM $J_1^{\parallel}/J_3^{\parallel}$, respectively (Fig. 7.1) and negligible $J_2^{\parallel}$ (Chapter 3). Furthermore, it is recently reported that monolayer $\mathrm{NiI_2}$ has a wavevector of $\mathbf{Q} \parallel (h, h)$ r.l.u. [143], suggesting that interactions stabilizing the bulk ground state are not originating from within the triangular lattice layers.

Along these lines, we note that there are significant open questions regarding the sequence of magnetic phase transitions in *bulk* $\mathrm{NiI_2}$ even at ambient pressure. As previously mentioned, magnetometry results show that there is a two-stage magnetic phase transition in $\mathrm{NiI_2}$. With decreasing temperature, a peak in the susceptibility signals the second-order-like transition to an AFM type state below $T_{N,1} = 75$ K. Secondly, a sharp drop in the susceptibility at $T_{N,2} \simeq 60$ K indicates a first-order-like transition to a second state. Early Mössbauer results indicate that the ground state below $T_{N,2}$ is characterized by an average transferred hyperfine field onto the iodine sites making an angle of $\simeq 62^\circ$ $(\pm 10^\circ)$ with respect to the c-axis [188]. Data was only recorded at base temperature of 4 K and the Mössbauer results do not restrict a unique ground state, only the cell averaged relative orientation of the nickel moments. It was later shown from powder neutron diffraction that the ground state below $T_{N,2}$ is consistent with a helical magnetic state with wavevector $\mathbf{Q} = (0.138, 0, 1.457)$[42]. Analysis of the neutron cross section and comparison to the Mössbauer results show that a consistent magnetic structure is a helical type spin structure (see Chapter 3 and 5) where the spins rotate within a fixed plane making an angle of $\simeq 55^\circ \pm 10^\circ$ with respect to the

c-axis, also consistent with the lack of a net magnetization.

As far as the initial studies, this constitutes nearly the totality of information regarding the magnetic ground state of NiI$_2$. In particular, there is no direct experimental evidence for the magnetic structure in the intermediate magnetic phase $T_{N,2} < T < T_{N,1}$, although it is hypothesized [45, 46] that it is a simple layered AFM state with $\mathbf{Q} = (0, 0, 3/2)$. This is the magnetic structure observed for NiCl$_2$ below its (single) Néel temperature $T_N \simeq 45$ K [124] and the intermediate magnetic phase of NiBr$_2$ between 22.5 and 52 K [231] which are directly confirmed by neutron diffraction measurements. Nonetheless, further characterization of this intermediate state has received little interest, likely because (a) it is natural to expect an isostructural phase to NiBr$_2$ and NiCl$_2$, (b) the more interesting magnetic structure is the low temperature incommensurate phase and (c) later measurements show that the intermediate phase does not have the same multiferroic properties and spin-induced ferroelectricity [37, 45, 186]. Despite this, resolving the nature of the intermediate phase is critical for determining the mechanisms of the multiferroic ground state of NiI$_2$ and establishing the proper spin Hamiltonian.

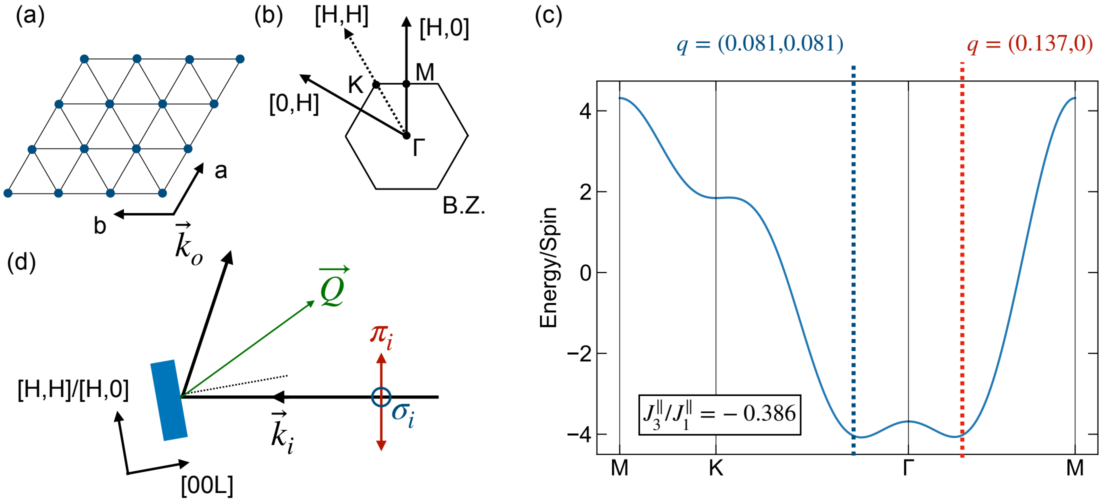

Figure 7.1: (a) Triangular lattice of Ni^{2+} ions in NiI$_2$ and (b) the reciprocal lattice (Brillouin zone) defining the principle wavevector directions (h, h) along ΓK and $(h, 0)$ along ΓM. (c) Calculation of the exchange energy in a single triangular lattice layer with $J_3^{\parallel}/J_1^{\parallel} = -0.386$, with units normalized to $J_1^{\parallel}$ per spin. Indicated are the two closely lying minima in the exchange energy for $q = (0.081, 0.081)$ (blue) and $q = (0.137, 0)$ (red). (d) Scattering geometry for the RXD measurements, showing the incident/outgoing wavevectors $\mathbf{k}_i/\mathbf{k}_o$, respectively, and the incident polarization states π_i/σ_i. Also indicated are the sample axes in rlu, and the orientation of the magnetic wavevector $\mathbf{Q}$ in the diffraction condition.

In this chapter, we investigate the properties of this intermediate phase more directly, as well as the change of the magnetic structure across the structural transition at $T_{N,2}$, using resonant magnetic X-ray scattering (RMXS) at the Ni-L_3 edge (Chapter 4). Surprisingly, we find that the intermediate magnetic phase is not a simple AFM order, but is rather an incommensurate phase with approximately the same magnitude of $|\mathbf{Q}|$ as the ground state, but with a distinct in-plane propagation vector along $\mathbf{Q}_{\parallel} = (h, h)$. The phase arises at $T_{N,1}$ before a first order transition at $T_{N,2}$ where the magnetic wavevector rotates 30° in-plane. Additional crystallography measurements confirm the low temperature monoclinic distortion [42] with a pronounced interlayer shear that occurs concomitantly with the transition between (h, h) and $(h, 0)$ magnetic states at precisely $T_{N,2}$ with a first-order-like structural order parameter. Using a mean-field spin-exchange model for incommensurate magnetic states including interlayer interactions and their modification through the structural transition, we confirm that the monoclinic distortion provides an energetic favorability to change the in-plane propagation vector. Along with the results of hydrostatic pressure in Chapter 6, these results conclusively demonstrate that interlayer interactions and spin-lattice coupling drive the ground state spin structure of NiI_2. Combining information from the polarization-dependence in RMXS (Chapter 4), symmetry-resolved optical probes (Chapter 5) and previous measurements of the multiferroic properties [45], we conclude the intermediate phase of NiI_2 between $T_{N,2} < T < T_{N,1}$ is likely an amplitude modulated, single-$\mathbf{Q}$ spin-density wave (Chapter 3) which breaks rotational but not inversion symmetry. These results isolate the key interactions driving the multiferroic ground state in NiI_2 and provide insight into the crossover of the magnetic ground state in the ultrathin limit.

7.2 Results

7.2.1 Resonant magnetic X-ray scattering of helimagnetic order in bulk NiI_2

Resonant diffraction measurements on single-crystal NiI_2 grown by chemical vapor deposition (CVD) grown and intermediate thickness ($\sim$ 15 nm) flakes grown by physical vapor deposition (PVD) were performed at the REIXS beamline at the Canadian Light Source. The diffraction geometry is shown in Fig. 7.1 (d), with tunable incident photon energy near the Ni-L_3 edge and controllable polarization perpendicular (σ_i) and parallel (π_i) with respect to the scattering plane. The outgoing polarization is not resolved and is the sum of σ_o/π_o contributions.

We begin by discussing the magnetic response below $T_{N,2}$, at $T = 20$ K. With photon energy tuned to the peak of the Ni-L_3 edge, an intense incommensurate reflection is observed near $h \simeq 0.144$ and $l \simeq 1.47$ rlu (Fig. 7.2 (a)/(b)), along the in-plane $(h, 0)$ direction. Notably, this is near the wavevector predicted from previous neutron scattering results [42], with small quantitative discrepancies. To confirm the magnetic origin of the peak and association to the nickel moments, we perform energy scans across the Ni-$L_{3,2}$ edge while fixing the momentum transfer $\mathbf{Q} \simeq (0.144, 0, 1.47)$ (Fig. 7.2(c)). A clear resonant enhancement is observed at the Ni edge, which is highlighted by comparison to the XAS spectrum in total fluorescence yield (TFY) reported in Fig. 7.2(d). The XAS spectrum agrees with previous

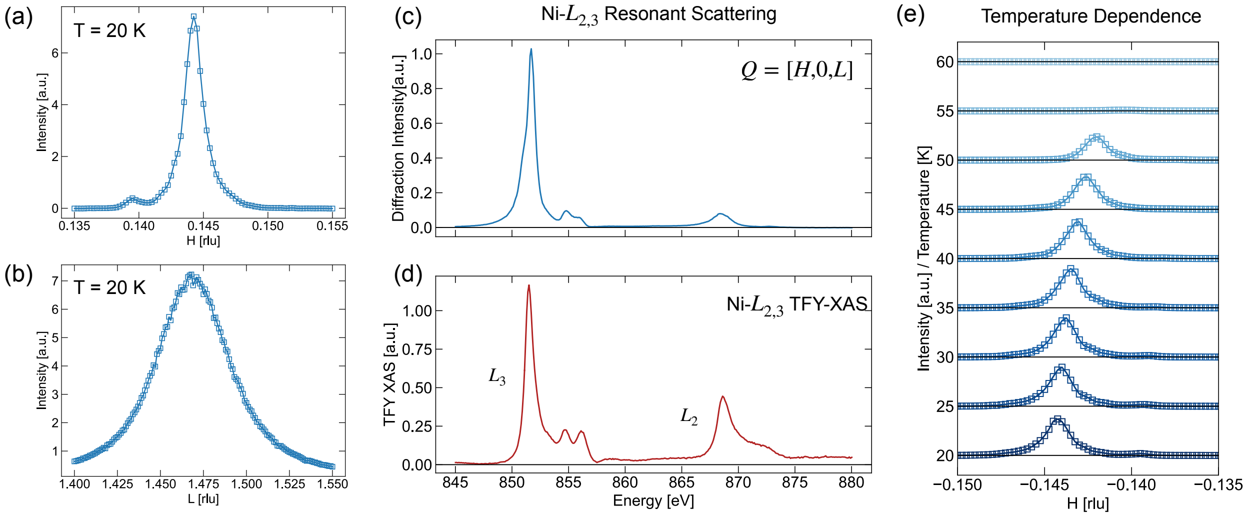

Figure 7.2: Ni L_3 edge resonant diffraction in NiI$_2$ at $T = 20$ K. (a) h and (b) l scans of the helimagnetic wavevector at $T = 20$ K with incidence energy tuned to the peak of the Ni L$_3$ absorption, confirming a $\mathbf{Q} \simeq (0.144, 0, 1.47)$ rlu magnetic ground state. (c) Energy scan at fixed wavevector of the magnetic peak in (a)/(b), showing a resonance behavior at the Ni $L_{2,3}$ edges, compared to (d) the Ni $L_{2,3}$ edge total fluorescence yield (TFY) absorption. (e) Temperature-dependence of the helimagnetic order, showing that the peak disappears at $T_{N,2}$.

results confirming the quality of the samples [155].

We next perform temperature-dependent h scans across $T_{N,2}$, and observe that the peak disappears abruptly between 50 and 55 K. There is also a weak temperature-dependence of the incommensurability factor, decreasing from $h \simeq 0.144$ at 20 K to $\simeq 0.142$ at 50 K. Along with the clear resonance behavior (Fig. 7.2(c)), these results confirm that the observed reflection is the helimagnetic order. This is already one critical result, as the wavevector direction was only inferred from calculations in the previous neutron study [42], which only measured powder samples and is thus only sensitive to $|\mathbf{Q}|$.

Having established the ground state spin order with RMXS, we next aim to study the magnetic order in the intermediate phase with $T_{N,2} < T < T_{N,1}$. We began by checking the hypothesized $\mathbf{Q} = (0, 0, 3/2)$ ordering, corresponding to a layered AFM state with a FM intralayer order. This ordering wavevector was checked systematically on multiple samples throughout this study, but no peak was observed at any temperature. However, we do observe a new peak appearing at 60 K along the (h, h) in-plane direction, with $h \simeq 0.086$ and $l \simeq 1.49$ (Fig. 7.3(a)/(b)). This corresponds to a relative rotation of the wavevector by 30° in the triangular lattice plane with respect to the ground state propagation vector. Notably, the magnitude of the spiral pitch is nearly the same in both cases,

$$|(0.086, 0.086)| = 0.276\ \text{Å}^{-1} \rightarrow 22.8\ \text{Å}$$

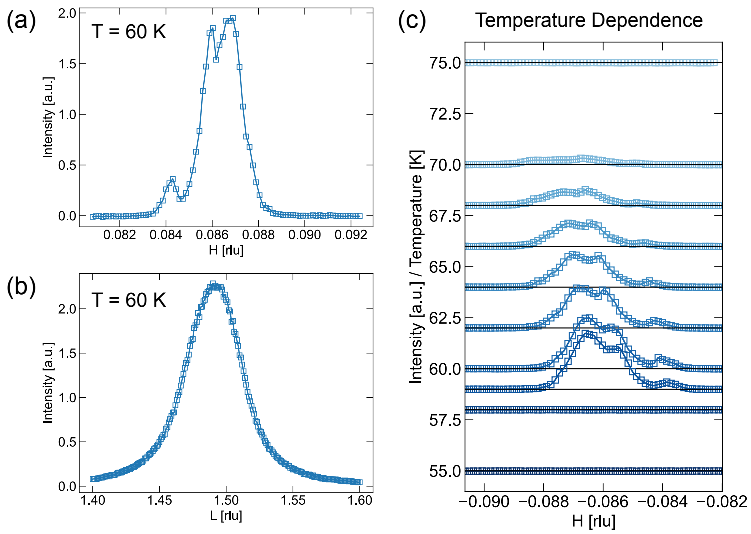

Figure 7.3: Ni L_3 edge resonant diffraction in NiI$_2$ in the intermediate phase $T_{N,2} < T < T_{N,1}$. (a) h and (b) l scans of a magnetic peak at $T = 60$ K with incidence energy tuned to the peak of the Ni L_3 absorption. The observed peak is $\mathbf{Q} \simeq (0.086, 0.086, 1.49)$ rlu. (c) Temperature-dependence of the intermediate phase magnetic order, showing that the peak appears near $T_{N,1}$ and suddenly disappears when cooling below $T_{N,2}$.

$$|(0.144, 0)| = 0.267\ \text{Å}^{-1} \rightarrow 23.6\ \text{Å}$$

which is reminiscent of the nearly degenerate magnetic states along ΓM and ΓK predicted by the simple $J_1^{\parallel}/J_3^{\parallel}$ exchange model shown in Fig. 7.1(c), discussed more below.

We further perform temperature-dependent h scans of this reflection (Fig. 7.3(c)). This peak shows a non-trivial temperature dependence, appearing on cooling between 75 and 70 K ($T_{N,1}$) and suddenly disappearing below $\simeq$ 58 K. This unique temperature dependence provides strong evidence that this peak corresponds to the intermediate magnetic phase observed in magnetometry and optical experiments, while the layered AFM state can be ruled out. The magnetic phase diagram determined by RMXS is thus summarized in Fig. 7.4. On cooling, the sample transitions first to a magnetic state with $\mathbf{Q} \sim (h, h, l)$ with a second-order like transition. Then, there is a first-order like transition at $T_{N,2}$, characterized by a discontinuous change in the $\mathbf{Q}$ vector, rotating 30° degrees in plane to $\mathbf{Q} \sim (h, 0, l)$, with nearly the same magnitude of $\mathbf{Q}_{\parallel}$ in each case. The first order nature of the crossover is further confirmed by a continuous temperature scan (solid red line in Fig. 7.4) of the (h, h, l) order, showing a transition width on the order of 0.1 K. The slight discrepancy of the onset of the $(h, 0, l)$ peak, appearing near 55 K, could be due to either a different probed distribution of single-$\mathbf{Q}$ domains which can have a complex temperature dependence close to the transition (see Chapter 5) or due to more complex evolution of the wavevector near the transition which we do not resolve.

Additional information on the symmetry of the underlying magnetic order at each reflection can be gleaned from the polarization dependence (Chapter 3). Thus, we investigated

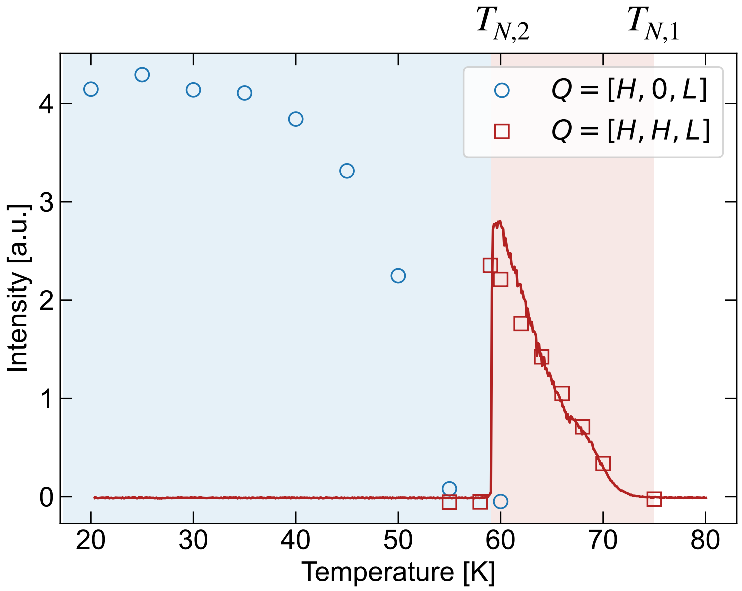

Figure 7.4: Magnetic phase diagram of NiI_2. Below $T_{N,2}$, the ground state is a helical state with $\mathbf{Q} = (h, 0, l)$, with $h \simeq 0.144$ rlu and $l \simeq 1.47$ rlu (blue data points). Between $T_{N,2}$ and $T_{N,1}$, a magnetic order with $\mathbf{Q} = (h, h, l)$ with $h \simeq 0.086$ rlu and $l \simeq 1.49$ rlu is observed, with a first order like transition near $T_{N,2}$ (red data points). Data points are the integrated intensity from temperature-dependent h scans of the magnetic peaks, and the continuous red line is a temperature-dependent scan of the (h, h, l) peak at fixed momentum transfer.

the scattering intensity (I) in each channel with incident linear vertical/horizontal (σ/π) and circular left/right (σ^+/σ^-) polarizations (Fig. 7.5). Beginning in the high-temperature phase with $\mathbf{Q} = (h, h, l)$ for $T_{N,2} < T < T_{N,1}$, we observe that the intensity is much stronger with incident π compared to σ, while the intensity is approximately equal in σ^+/σ^- (Fig. 7.5(a)/(b)). The same situation is observed upon reversing the sign of the in-plane component at the $\mathbf{Q} = (-h, -h, l)$ reflection, besides an overall reduced intensity likely associated to self-absorption effects [232].

In the low-temperature phase, a different response is observed. While both the $\mathbf{Q} = (h, 0, l)$ and $\mathbf{Q} = (-h, 0, l)$ reflections show a similar dependence on linear polarization as the (h, h, l) reflection, a finite circular dichroism (CD) is observed (Fig. 7.5 (c)/(d)). Notably, the CD reverses sign upon reversal of $\mathbf{Q}_{\parallel}$, with $I(\sigma^+) > I(\sigma^-)$ and $I(\sigma^-) > I(\sigma^+)$ for the $(h, 0, l)$ and $(-h, 0, l)$ reflections, respectively. This behavior is consistent with a finite spin helicity, as expected from a spin-helical or cycloidal state (Chapter 3), which is known to be directly reflected in the CD response of RMXS [233]. While more detailed calculations are ongoing work, these observations provide an important restriction on the intermediate magnetic state, discussed more below, and are consistent with a spin spiral state with finite spin helicity in the multiferroic phase below $T_{N,2}$.

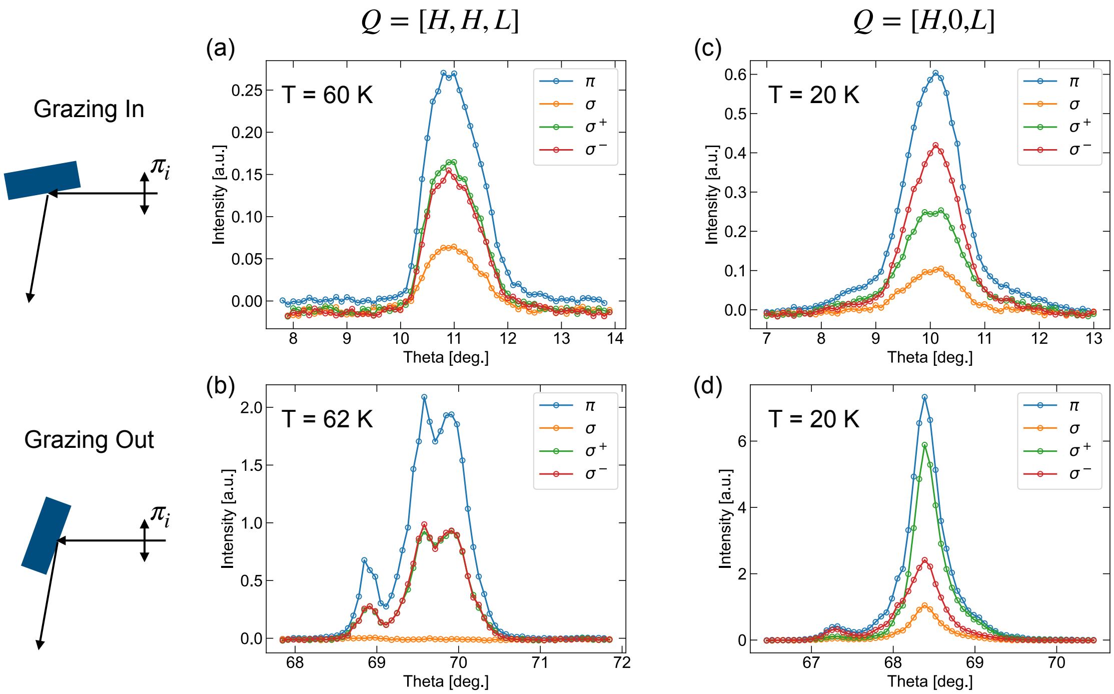

Figure 7.5: Polarization dependence of the magnetic scattering in NiI_2. Polarization dependent θ-scans at $T = 60$ K and at the (a) (h, h, l) reflection (grazing out) and (b) $(-h, -h, l)$ reflection (grazing incidence) for the intermediate magnetic phase $T_{N,2} < T < T_{N,1}$. Polarization dependent θ-scans at $T = 20$ K and at the (c) $(h, 0, l)$ reflection (grazing out) and (d) $(-h, 0, l)$ reflection (grazing incidence) for the low-temperature magnetic phase $T < T_{N,2}$. The respective scattering geometries for grazing out/incidence are shown schematically on the left, indicating the orientation of incident linear horizontal light (π_i) lying within the scattering plane. Linear polarizations are labelled σ (orange, linear vertical) and π (blue, linear horizontal) while circular polarizations are labelled σ^+ (green, circular left) and σ^- (red, circular right). In all cases, the outgoing polarizations are not resolved.

7.2.2 Characterization of the structural phase transition

The results of the previous section show that the physics of NiI_2 is likely distinct from both $NiCl_2$ and $NiBr_2$, which both display a simple layered AFM state in their respective magnetic phase diagrams. Furthermore, in $NiBr_2$, the transition to the ground state spiral structure behaves as a second-order phase transition, while in NiI_2 a first-order transition is observed. As we hypothesized, the change of magnetic ground state is likely mediated by spin-lattice interactions and the associated magneto-structural transition, which is observed in NiI_2 but not in the other nickel dihalides.

To confirm this scenario, we more closely inspect the monoclinic structural phase transition which was previously reported [42]. While the transition temperature was observed, the data quality is poor (using powder samples with a standard Cu K_α source) which precludes a precise determination of the order parameter and refinement of the crystal structure.

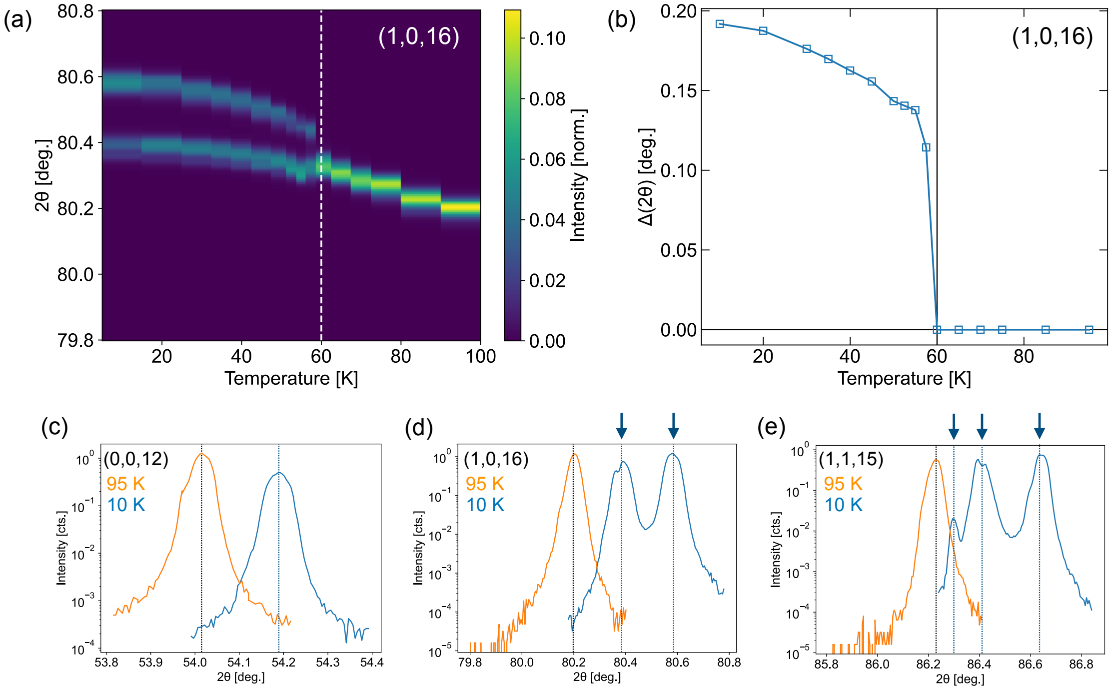

Figure 7.6: Temperature-dependent structural analysis of single-crystal bulk NiI_2 recorded with incident energy of 8.33 keV. (a) Temperature-dependent θ-2θ scans near the $(1, 0, 16)$ structural reflection, showing a splitting at $T_{N,2} = 60$ K. (b), Temperature-dependence of the order parameter for the monoclinic structural transition, showing a first-order like transition at 60 K. θ-2θ scans near the (c), $(0, 0, 12)$, (d), $(1, 0, 16)$ and (e), $(1, 1, 15)$ reflections at $T = 95$ K (orange) and $T = 10$ K (blue). Black arrows indicate the observed split components of these reflections below $T_{N,2}$.

Thus, we have performed additional high-resolution structural diffraction on CVT-grown single crystals of NiI_2 at the 4ID-ISR beamline at the National Synchrotron Light Source II, Brookhaven National Laboratory, using monochromatic X-rays with an incident energy of $E = 8.33$ keV ($\lambda = 1.4884$ Å).

To determine the crystal structure, we focus on the $(0, 0, 12)$, $(1, 0, 16)$ and $(1, 1, 15)$ reflections. At $T = 95$ K, all of the reflections are single peaked and are consistent with the high-temperature $R\bar{3}m$ cell, with lattice parameters shown in Table 7.1. Meanwhile, at $T = 10$ K, the $(1, 0, 16)$ and $(1, 1, 15)$ reflections split into 2 and 3 components, respectively Fig. 7.6(d)/(e). These splittings can be fit to a centered monoclinic cell with either $C2$ or $C2/m$ space group, with lattice parameters shown in Table 7.1. The reported values are close to those reported in Ref. [42].

To register the structural transition, we focus on the $(1, 0, 16)$ reflection versus temperature (Fig. 7.6(a)). A clear first-order like transition is observed at precisely $T_{N,2} = 60 \pm 2.5$ K. Additionally, no lattice distortion is observed in the intermediate magnetic phase. We extract the splitting, proportional to the order parameter of the structural transition, which

T (K)	SG	a (Å)	b(Å)	c(Å)	α (deg.)	β (deg.)	γ (deg.)
95 K	$R\bar{3}m$	3.9103	3.9103	19.665	90	90	120
10 K	$C2(/m)$	6.7585	3.9130	19.610	90	90.23	90

Table 7.1: Lattice refinement of $\mathrm{NiI_2}$ at $T = 10$ K and 95 K.

is displayed in Fig. 7.6(b). These results confirm that the structural transition is first-order like, compatible with the transition between the $(h,0,l)$ and (h,h,l) magnetic states occurring at the same temperature (Fig. 7.4). This provides strong evidence for a connection between the change of ground state and the change of the underlying lattice symmetry, consistent with the conclusions reached from high-pressure experiments in Chapter 6.

7.2.3 Magnetic scattering from nanometer-thickness $\mathrm{NiI_2}$ flakes

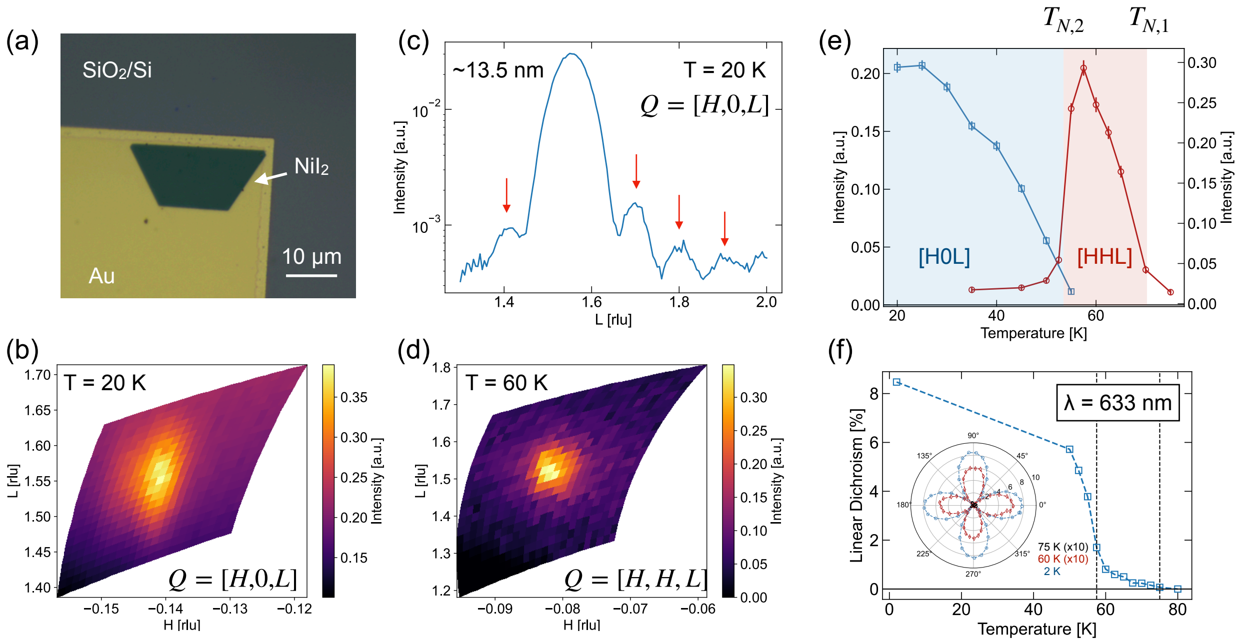

Figure 7.7: Resonant magnetic scattering in $\sim$ 15nm thick $\mathrm{NiI_2}$. (a), Optical image of a trapezoidal shaped $\mathrm{NiI_2}$ flake grown by PVD and transferred onto a Au contact on $\mathrm{SiO_2/Si}$. Scale bar: 10 μm. (b), $(h,0,l)$ reciprocal space map (RSM) of the helimagnetic peak at $T = 20$ K. (c), Long-range l scan of the helimagnetic peak in log scale, showing the presence of Laue oscillations resulting from finite flake thickness along the c-axis. (d), RSM of the (h,h,l) reflection in the intermediate phase at $T = 60$ K. (e), Temperature-dependence of the $(h,0,l)$ and (h,h,l) reflections across $T_{N,1}$ and $T_{N,2}$, showing similar behavior as the bulk. (f) Temperature-dependent linear dichroism in the same 15 nm flake with wavelength $\lambda = 633$ nm. Inset: Angular dependent LD at $T = 2$ K (blue), 60 K (red) and 75 K (black). The curves for 60 and 75 K are multiplied by 10.

One of the major advantages of resonant soft x-ray scattering is its sensitivity to magnetic order from small samples volumes, down to few atomic layers [74, 158, 159, 234, 235]. Thus, this technique has great promise for the characterization of long-range magnetic order in vdW magnets, overcoming the limitations of the weak neutron scattering cross-section. We demonstrate this here by performing the same RMXS experiments on a thin flake of $\mathrm{NiI_2}$ grown by PVD with a thickness of approximately 15 nm. An optical image of the $\sim 10 \times 20$ μm dimension sample is shown in Fig. 7.7(a). The sample is transferred onto the corner of Au contact deposited on a $\mathrm{SiO_2}$/Si substrate, and is spatially isolated from nearby flakes by around 500 μm. The conditions provide a practical method for identifying the flake position with the X-ray beam, and ensuring that diffraction is only collected from the sample of interest. Furthermore, the Au contact is crucial to allow for heat/charge dissipation from the flake to prevent sample damage.

At $T = 20$ K, we observe a resonant reflection near the expected $(h, 0, l)$ position, with $h \simeq 0.142$ rlu and $l \simeq 1.56$ rlu, as shown in the 2D reciprocal space map (RSM) in Fig. 7.7(b). This is in general agreement with the results of the bulk reported in Fig. 7.2. We further performed high-statistics and long-range scans along the l direction, shown in log scale in Fig. 7.7(c). These measurements show the presence of clear Laue oscillations, related to the finite thickness along the c-axis. We can estimate the sample thickness from the periodicity of these fringes ($\Delta l \simeq 0.15$ rlu) as ~ 13.5 nm, in rough agreement with the thickness determined by optical contrast and AFM measurements. This provides direct evidence for resonant magnetic scattering from the identified flake in Fig. 7.7(a), rather than other thicker nearby flakes.

We also characterized the cross-over of the magnetic transition in these flakes. It was previously suggested from SHG measurements [186] that mesoscale thickness flakes ($\sim 10-20$ nm) display a rotation of the magnetic wavevector to the (h, h, l) direction in the ground state. Thus, considering our results in the bulk, we explicitly verify the magnetic phase diagram within this mesoscale regime. At $T = 60$ K, we observe a reflection along the (h, h, l) direction, summarized in the RSM of Fig. 7.7(d), in agreement with intermediate phase of the bulk. We performed temperature-dependence of both the $(h, 0, l)$ and (h, h, l) reflections and find a similar phase diagram for the ~ 15 nm flake as observed in bulk (Fig. 7.7(e)). This rules out a potential rotation of the ground state wavevector at these thicknesses. We also note that these results were confirmed down to 10 nm thickness, not shown here. Extension of these data to the thinner limit should be feasible, and is the process of ongoing work.

One notable distinction in the bulk and thin limit is that the transition at $T_{N,2}$ becomes broader and less well-defined. This is also observed in the temperature-dependence of both linear dichroism (LD) and second harmonic generation (SHG) [37] (Chapter 5). We directly compare the magnetic phase diagram determined from RMXS with optical LD measurements on the same flake in Fig. 7.7(f) (for experimental details see the Methods section of Chapter 5). Optical measurements show a broadened $T_{N,2}$ transition around 57.5 K, in agreement with RMXS transition to the $(h, 0, l)$ state. We also note that finite LD signal is observed in the intermediate phase, but it is much weaker than the LD below $T_{N,2}$. We also perform angular dependent LD in each phase shown as the inset in Fig. 7.7(f), showing that the principle anisotropy axes of the intermediate state are the same as the ground state. These observations and their implications for the intermediate phase spin structure are discussed more below.

7.2.4 Analysis of the ground state and the coupling between interlayer shear and exchange interactions

We now build a microscopic model of the exchange Hamiltonian including a minimal set of interlayer exchange interactions in order to justify the claim that the structural transition can change the magnetic ground state. For these calculations, we will consider the following Hamiltonian,

$$H = -\sum_{\langle i,j\rangle_n} J_n^{\parallel} \mathbf{S}_i \cdot \mathbf{S}_j - \sum_{\langle i,j\rangle_n} J_n^{\perp} \mathbf{S}_i \cdot \mathbf{S}_j \tag{7.1}$$

where $\langle i,j\rangle_n$ refer to sums over pairs of n^{th} nearest neighbors with intralayer exchange interactions $J_n^{\parallel}$ and interlayer exchange interactions $J_n^{\perp}$, respectively. We will work in a model considering classical local spin moments $\mathbf{S}_i$. In this limit, one can calculate the ground state magnetic wavevector by minimizing the classical energy of the system with respect to $\mathbf{q}$ by taking the Fourier transform of the exchange integrals (Chapter 3):

$$J_n(\mathbf{q}) = \sum_{\langle i,j\rangle_n} J_n e^{-i\mathbf{q}\cdot\mathbf{r}_{ij}} \tag{7.2}$$

For the exchange interactions, we use take the leading contributions determined from theoretical calculations. In all cases, the triangular lattice geometry for Ni^{2+} ions consistently gives ferromagnetic $J_1^{\parallel}$, negligible $J_2^{\parallel}$ and antiferromagnetic $J_3^{\parallel}$ for the intralayer exchange [46, 47, 126, 143]. These can be easily justified by the Goodenough Kanamori rules, with J_1 being determined by $\simeq 90°$ Ni-I-Ni bonds, while J_3 is a Ni-I-I-Ni bond with predominant direct transfer between the involved iodine orbitals (Chapter 3). We note that the original isotropic Heisenberg models used to justify the ground state of NiI$_2$ with $\mathbf{Q}_{\parallel} \sim (h, 0)$ assumed a large value of $J_2^{\parallel}$ [42]. However, more recent numerical calculations are all consistent in finding that the magnitude of $J_2^{\parallel}$ is too small for this to be the interaction responsible for the observed ground state.

The interlayer interactions are all of the type Ni-I-I-Ni, mediated by two ligands. Due to the large spatial extent of the iodine orbitals in the case of NiI$_2$ (as well as the large metal-ligand hybridization and small metal-ligand charge transfer gap, see Chapter 8), the interlayer interactions are predicted to be large [37, 126]. The main contributions are the first- and second-nearest neighbor exchange interactions $J_1^{\perp}$, $J_2^{\perp}$, which are weak FM and strong AFM, respectively, as determined by first-principles calculations in bilayers [126] and as discussed microscopically in Chapter 3.

For a minimal model, we take as non-zero $J_1^{\parallel}$, $J_3^{\parallel}$ and $J_2^{\perp}$ and consider the classical ground states. The expressions for $J(\mathbf{q})$, expressing $\mathbf{q}$ in terms of (h,k,l) reciprocal lattice units on the triangular lattice, are

$$J_1^{\|}(\mathbf{q}) = 2J_1^{\|}\left(\cos(2\pi h) + \cos(2\pi k) + \cos(2\pi(h+k))\right) \tag{7.3}$$

$$J_3^{\|}(\mathbf{q}) = 2J_3^{\|}\left(\cos(4\pi h) + \cos(4\pi k) + \cos(4\pi(h+k))\right) \tag{7.4}$$

$$\begin{aligned} J_2^{\perp}(\mathbf{q}) =& 2J_2^{\perp}\left(\cos\left(\frac{2\pi(2h+4k+l)}{3}\right) + \cos\left(\frac{2\pi(2h-2k+l)}{3}\right)\right) \\ &+2\left(J_2^{\perp}\right)'\cos\left(\frac{2\pi(-4h-2k+l)}{3}\right) \end{aligned} \tag{7.5}$$

The two terms of $J_2^{\perp}(\mathbf{q})$ correspond to two sets of bond lengths/exchange paths which become inequivalent in monoclinic symmetry, discussed below. We first consider the case of the high symmetry $R\bar{3}m$ structure with $J_2^{\perp} = \left(J_2^{\perp}\right)'$. To calculate the phase diagram we express $j_3^{\|} = J_3^{\|}/J_1^{\|}$ and $j_2^{\perp} = J_2^{\perp}/J_1^{\|}$ and calculate the ground state versus $j_3^{\|}$ and $j_2^{\perp}$.

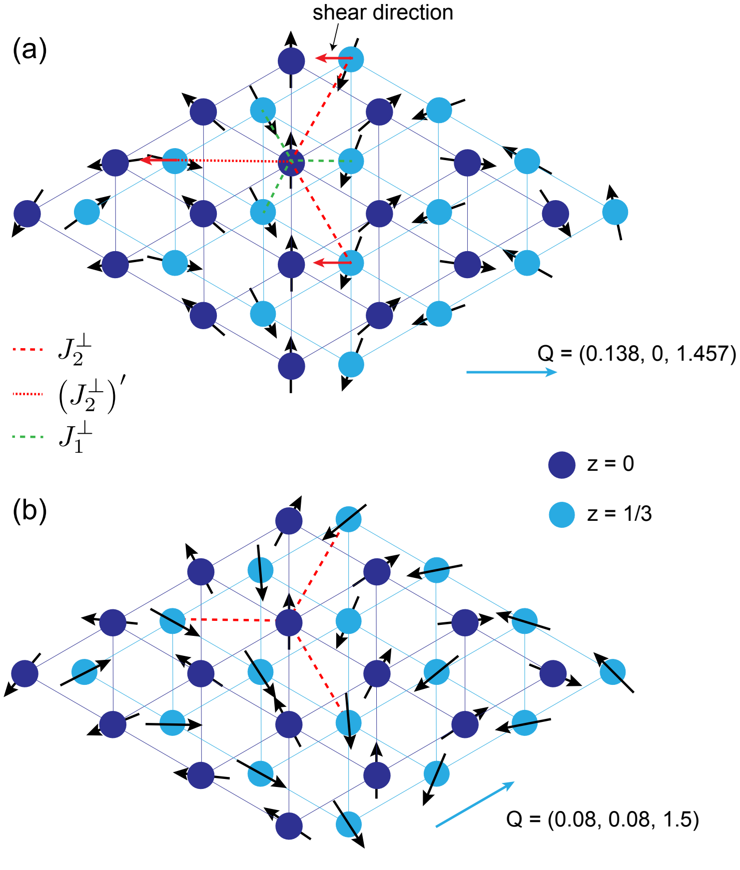

Figure 7.8: Magnetic ground state schematics and definition of interlayer J terms.

We plot the classical magnetic ground states for $R\bar{3}m$ symmetry in Fig. 7.9. We consider separately wavevectors of the type $\mathbf{Q} = (h,h,l)$ (Fig. 7.9 (a,b)) and $\mathbf{Q} = (h,0,l)$ (Fig. 7.9 (c/d)), and then determine the overall ground state as the minimum between these two

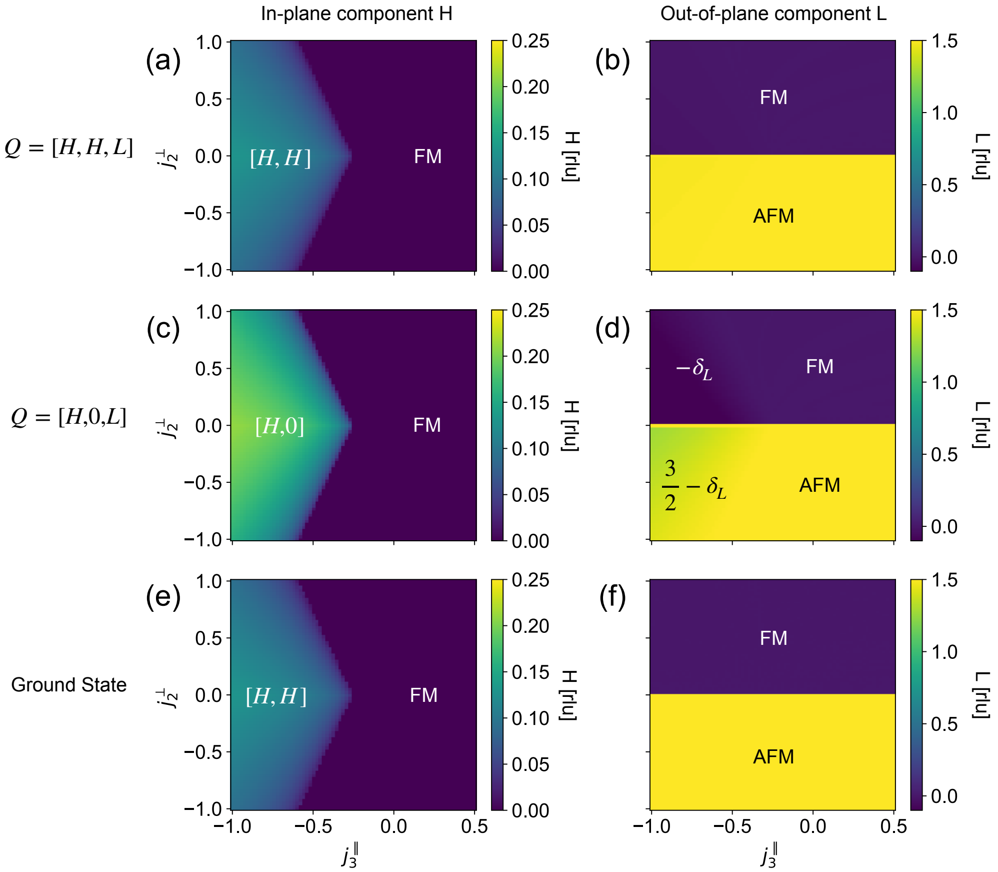

Figure 7.9: Classical ground state of $R\bar{3}m$ stacked triangular lattice with second-nearest neighbor interlayer interactions. All plots expressed versus $j_3^{\parallel}$ (horizontal) and $j_2^{\perp}$ (vertical). (a) h and (b) l components of the ground state for $\mathbf{Q} = (h, h, l)$. (c) h and (d) l components for $\mathbf{Q} = (h, 0, l)$. (e) h and (f) l for the overall ground state, which in this case is always of either FM intralayer order or in-plane incommensurate states of the type (h, h, l).

possibilities (Fig. 7.9 (e/f)). First, we note that the overall ground state is always either FM in plane ($(h, k) = (0, 0)$), or an incommensurate spiral state with $\mathbf{Q} = (h, h)$. Notably, the $(h, 0, l)$ phase of $\mathrm{NiI_2}$ cannot be stabilized simply by including interlayer interactions alone.

A few general features can be noted. First, the sign of the interlayer exchange determines AFM/FM interlayer stacking ($l = 3/2$ and $l = 0$, respectively), as expected. Secondly, increasing interlayer interactions shifts the phase boundary between the FM and spin spiral structures, relatively stabilizing the simple intralayer FM state and increasing the critical value of $j_3^{\parallel}$ required to stabilize the (h, h) or $(h, 0)$ phases. Finally, we note that while the $\mathbf{Q} = (h, 0, l)$ state is not the ground state, the interlayer interactions uniquely predict that this state has an incommensurate value of $l = 3/2 - \delta$, while the (h, h, l) phase is always commensurate out-of-plane with $l = 1.5$. This is in general agreement with the observations, since the (h, h, l) state of $\mathrm{NiBr_2}$ is commensurate, while $\mathrm{NiI_2}$ has a small incommensuration of $\delta \simeq 0.05$ rlu out-of-plane.

Finally, we plot the energy difference between $\mathbf{Q} = (h, h, l)$ and the $(h, 0, l)$ states in Fig. 7.10. This shows that while the (h, h, l) state is the overall ground state, the energy separation is on the order $\Delta E \simeq 10^{-2} J_1^{\parallel}$ near the phase spiral/FM boundary. In physical units, $J_1^{\parallel}$ is around 5 meV/Ni atom [46, 47, 125, 126], thus the energy difference between the states in on the order of $\simeq 100\mu$eV/Ni.

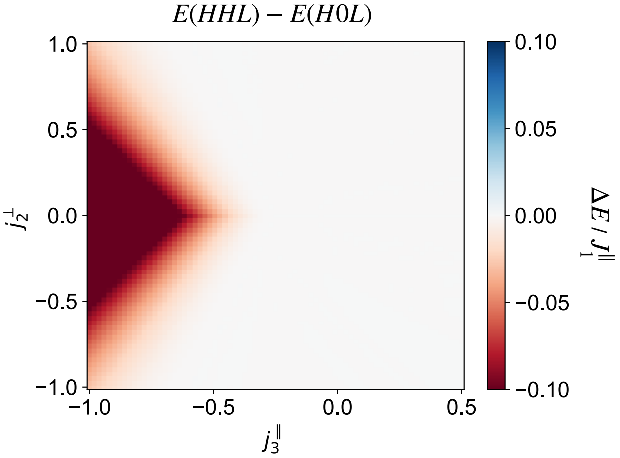

Figure 7.10: Energy difference of (h, h, l) and $(h, 0, l)$ states in $R\bar{3}m$ symmetry.

We next move to the case of monoclinic symmetry with $(J_2^{\perp})' \neq J_2^{\perp}$ (Fig. 7.8). We account for the difference by introducing a symmetric proportional splitting, e.g. $j_2^{\perp} = (1 + \Delta)\bar{j}_2^{\perp}$ and $(j_2^{\perp})' = (1 - \Delta)\bar{j}_2^{\perp}$. We begin by setting a splitting of 2% and calculate the ground states, which are shown in Fig. 7.11. We observe that near the spiral-FM phase boundary with $\Delta > 0$ that the ground state becomes $(h, 0, l)$ before switching back to (h, h, l) as the spiral state becomes more stabilized by increasing $j_3^{\parallel}$ or decreasing $j_2^{\perp}$. This indicates that a small deviation from rhombohedral symmetry can energetically favor the $(h, 0, l)$ state observed in NiI$_2$, and that small changes in parameters can change the ground state between (h, h, l) and $(h, 0, l)$, in principle.

To further demonstrate the cross over in the ground state, we calculate the dependence on $\Delta j_2^{\perp}$ at fixed values of $j_3^{\parallel} = -0.55$ and $\bar{j}_2^{\perp} = -0.40$ in Fig. 7.12. For these parameters, we observe a continuous change in the energy difference ΔE between the two states before the ground state changes at $\Delta j_2^{\perp} \simeq 2.5$ %. Furthermore, the ordering wavevectors of each state show a significant change with increasing Δ. For $(h, 0, l)$, both h and l change significantly, while for (h, h, l) the value of h is approximately constant but becomes incommensurate along l for deviations from rhombohedral symmetry. This allows a mechanism through which the spin-lattice interactions can change the incommensurability factor, and lead to a temperature-dependence of the wavevector.

Finally, we estimate a reasonable parameter range for the splitting $\Delta j_2^{\perp}$. To do so, we calculate the change in the interatomic distance between the interlayer second nearest neighbors across the monoclinic phase transition, using the refined lattice parameters in the previous section. We then estimate the corresponding change in the exchange parameters

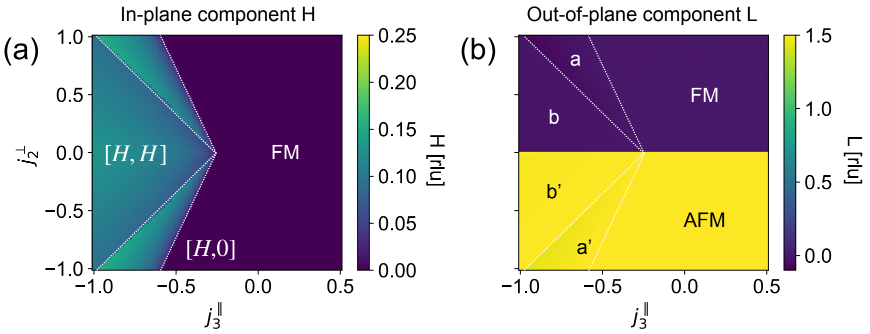

Figure 7.11: (a) h and (b) l components of the ground state of a monoclinic stacked triangular lattice with second-nearest neighbor interlayer interactions. The h value for the (h, h, l) state is multiplied by $\sqrt(3)$ for direct comparison to $(h, 0, l)$. All plots are expressed versus $j_3^\parallel$ (horizontal) and $j_2^\perp$ (vertical). The value of $\Delta j_2^\parallel = 2\%$.

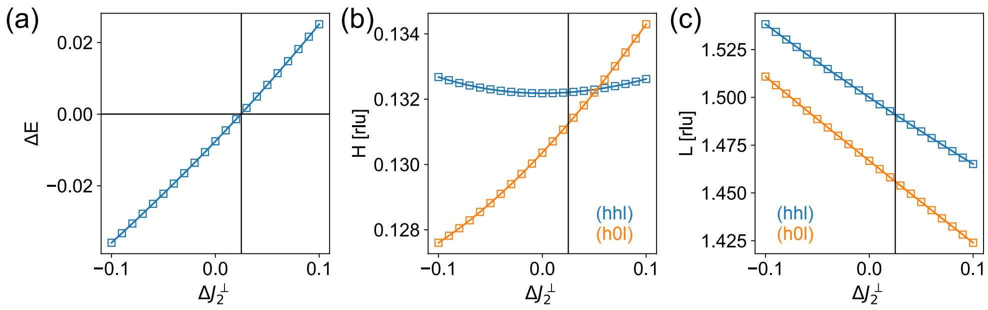

Figure 7.12: Ground state crossover versus $\Delta j_2^\perp$ in monoclinic symmetry. (a) Energy difference (ΔE) of the (h, h, l) and $(h, 0, l)$ ground states and (b) h and (c) l components of the wavevector for both (h, h, l) (blue) and $(h, 0, l)$ (orange) states. The vertical line indicates the value of $\Delta j_2^\perp \simeq 0.025$ which leads to a change of ground state. All plots for $j_3^\parallel = -0.55$ and (average) $j_2^\perp = -0.40$.

using results of first-principles calculations at high-pressures which modifies the exchange through compressive strain [126][1].

Using the crystallographic parameters in Tab. 7.1, we find that the $J_2^\perp$ bonds have a length $r = 7.93765$ Å and the $(J_2^\perp)'$ bond is $r' = 7.95469$ Å, corresponding to a difference in bond length $\Delta r/r \simeq -0.21\%$. Meanwhile, the value of $j_2^\perp$ between 0 and 5 GPa increases rapidly at a rate $\simeq 15.6$ $(\% j_2^\perp)/(\%$ strain). Thus, we estimate a maximal splitting of the exchange parameters from the crystallographic distortion to be around $\Delta j_2^\perp \simeq 3\%$, which is in reasonable agreement with the approximate values used in the above analysis.

---

[1] The electronic structure, in particular the band gap and Ni-I charge transfer gap, also change with pressure which we do not expect to be significantly modified by small lattice displacements. Thus, the comparison to pressure is only meant as an order of magnitude estimate.

7.3 Discussion

Thus, we have shown that a minimal microscopic model that accounts for an interlayer shear can effectively drive the observed ground state of bulk $\mathrm{NiI_2}$ through the interlayer interactions. It was noted that the magnetic wavevector of the monolayer observed by STM places the system close to the spiral-FM phase boundary [143], with a value of $j_3^{\parallel} \simeq -0.263$, close to the critical value in the absence of interlayer interactions $j_3 = -0.25$ for the FM-spiral state. Meanwhile, including interlayer interactions pushes the system even closer to this boundary, as we noted before. The proximity to this phase boundary is important within our analysis, as this is the same region where small $\Delta j_2^{\perp}$ can drive the change in ground state. The further away from this phase boundary, the larger value of $\Delta j_2^{\perp}$ would be required, which is bounded to a few percent because of the small change in the interatomic distances.

We propose the scenario by which the bulk $\mathrm{NiI_2}$ first transitions into an incommensurate magnetic state with wavevector $(h, h, 3/2)$ with parameters near the spiral-FM phase boundary. Then, a magneto-structural transition occurs simultaneously with the transition to the $(h, 0, 3/2 - \delta)$ state, mediated by a spin-lattice interaction whereby the structural distortion and corresponding change of magnetic ground state can minimize the total energy of the system. The magnitude of the structural distortion would be counterbalanced by the cost of elastic energy for the interlayer shear. Quantifying this elastic energy would require more dedicated studies of the elastic moduli and phonons of $\mathrm{NiI_2}$ which is the subject of future work. Nonetheless, this scenario is fully consistent with our observations and is supported directly by our minimal microscopic model.

There are several outstanding questions for the nature of this intermediate state. In particular, inversion symmetry breaking [37, 186] and ferroelectric polarization along any axis [45] is not observed above 60 K. This immediately gives strong restrictions on the magnetic state, because the reported SHG measurements are also sensitive to the magnetic order for the right choice of wavelength [37] (Chapter 5). Thus, an inversion-symmetry breaking single-**Q** spiral state in the intermediate phase is unlikely, as otherwise SHG and/or ferroelectric polarization would almost certainly be observed given the ubiquity in isostructural systems with the same magnetic wavevector [33, 38, 44]. Meanwhile, there is a clear optical linear dichroism signal above the $T_{N,2}$ transition, observed both by us [37] (Chapter 5) and in older optical literature [190]. This suggests that C_{3z} rotational symmetry is broken while, crucially, the lattice remains in high-symmetry rhombohedral phase as directly evidenced from our high-resolution diffraction measurements (Fig. 7.6). This is apparently at odds with the lack of inversion symmetry breaking, because the breaking of C_{3z} symmetry by the magnetic order is also compatible with a single-**Q** state. Finally, the observation of finite CD in RMXS in the $(h, 0)$ phase, but not the (h, h) phase (Fig. 7.5), evidences that the intermediate phase magnetic structure may not possess a net spin helicity. This would be consistent with a non-spiral magnetic state between $T_{N,2} < T < T_{N,1}$.

One possibility is that the intermediate phase is a triple- or double-$\mathbf{Q}$ state [47]. The model we presented here acts as a mechanism to stabilize the single-$\mathbf{Q}$ state through the monoclinic distortion, with the ground state having a propagation vector aligned to the shear direction which can occur along one of three equivalent axes (Fig. 7.6). Meanwhile, in the rhombohedral phase, the three different $\mathbf{Q}$ states (with $\mathbf{Q}_{\|}$ along $\pm(h, h)$, $\pm(-2h, h)$, $\pm(h, -2h)$) are degenerate. Thus, single-$\mathbf{Q}$ states must be stabilized by different interactions or chosen by a spontaneous symmetry breaking.

One possible solution consistent with all current experimental evidence and the ground state analysis presented above is that the intermediate state is an amplitude-modulated SDW phase (Chapter 3). Such a state can viewed as the addition of two spin spiral phases with opposite signs of the magnetic wavevector ($\pm\mathbf{Q}$) and opposite spin helicity [236]. Such a phase breaks rotational symmetry but not inversion, consistent with the optical data, and has been observed as a competing phase in several type-II multiferroics above the spiral transition, including $TbMnO_3$ [237, 238], CuO [239, 240] and $AgFeO_2$ [241]. In particular, an SDW phase *preceding* a spiral phase at a lower temperature is commonly observed, as a single-$\mathbf{Q}$ state with definite single helicity requires coupling to the lattice to break the degeneracy between states of opposite helicity whose wavevectors are selected by the magnetic exchange. This situation is precisely what we observe in NiI_2, and naturally explains why the structural transition occurs at $T_{N,2}$ rather than $T_{N,1}$. Thus, the difference between the in-plane propagation directions favored by the magnetic exchange ((h, h)), the near degeneracy of the (h, h) and $(h, 0)$ magnetic states, and the lowest-energy direction of the lattice shear ([210] real space direction) are all critical ingredients to explain how spin-lattice coupling leads simultaneously to a change in magnetic ground state and the presence of finite spin helicity (Fig. 7.5).

More generally to the physics of NiI_2, one must recall the importance of two-site anisotropy (or Kitaev terms) [47, 131], which favor specific local spin directions (or spin rotation planes) which can also energetically affect the propagation vector. Particularly, Ref. [131] argued that Kitaev interactions are the mechanism driving the $(h, 0)$ state of NiI_2. However, this bond anisotropy term acts within the triangular lattice layer, thus predicting the same ground state for the monolayer and the bulk, which disagrees with the observations of [143]. Therefore, Ref. [131] likely overestimates the contribution of Kitaev interactions, but their importance for determining the spin rotation plane cannot be ignored (Chapter 3). These may relatively stabilize the single-$\mathbf{Q}$ state and corresponding rotation plane, but are not strong enough on their own to make this the ground state, requiring an additional stabilization from the interlayer interactions through the mechanism we identified here. We note that the interlayer shear and Kitaev mechanisms should be cooperative as they both stabilize $(h, 0)$ order near the spiral-FM phase boundary. This cooperative effect should reduce the required splitting of the interlayer exchange interactions within our model, supporting the viability of this mechanism. At these energy scales, it is also crucial to include the smaller exchange interactions $J_2^{\|}$, $J_1^{\perp}$, and $J_3^{\perp}$ [126] as these are on the same order of the energetic difference between the $(h, 0)$ and (h, h) states, although their inclusion in $R\bar{3}m$ symmetry alone does not change the ground state [131].

In conclusion, by directly probing the long-range magnetic order of NiI_2 using RMXS, we have confirmed the ground state spin structure and revealed the nature of the intermediate magnetic state which was not previously resolved. Through additional analysis of the structural phase transition and its coupling to the underlying spin Hamiltonian, we have found that the ground state spin structure is likely driven by the interlayer shear of the triangular lattice layers. This points to the critical role of the interlayer exchange interactions and the stacking symmetry for determining the ground state of NiI_2. These observations provide direct experimental evidence for the proper spin Hamiltonian of NiI_2 and resolves the debate surrounding the discrepancy between the ground state of the monolayer and the bulk in relation to predictions from theoretical calculations [47, 125, 126, 129, 131, 143].

More generally, these results demonstrate that in frustrated layered magnets with long-range magnetic interactions, the interlayer interactions can not only modify the *interlayer* magnetic order [6, 19], but also the *intralayer* spin texture. The control of complex spin textures through interlayer exchange engineering could lead to intriguing results in vdW heterostructures, particularly through the spatially modulated interlayer interactions in moiré superlattices [31, 32]. Finally, we have shown the feasibility to use RMXS scattering to probe the long-range magnetic order of vdW magnets with nanometer thickness. This methodology can be extended to the ultrathin limit, possibly permitting the direct confirmation of long-range magnetic order in the single- and few-layer limit of vdW materials.

Chapter 8

Nature of excitons and their ligand-mediated delocalization in nickel dihalide charge transfer insulators

This chapter is adapted from a pre-print posted to arXiv (Ref. [242]) with modifications and corrections.

This paper is a co-first author work between the present author (C.A.O.) and Yi Tseng. C.A.O. and Y.T. initiated the project in discussion with Jonathan Pelliciari and Riccardo Comin. C.A.O., Y.T., J.P. and Valentina Bisogni performed the RIXS measurements. Qian Song grew and characterized the $NiBr_2$ and NiI_2 samples. Mark Blei and Seth Ariel Tongay grew and characterized the $NiCl_2$ samples. The charge transfer multiplet calculations were performed by C.A.O., with additional theoretical support provided by Hebatalla Elnaggar and Frank M. F. de Groot. R.C. supervised the project.

8.1 Introduction

The recent demonstration of magnetic order in correlated transition-metal van der Waals (vdW) materials to the ultrathin limit has led to an increased interest in their excitonic responses and coupling to magnetism. In contrast to uncorrelated, direct bandgap semiconductors exhibiting Wannier-type interband excitons [50], the below bandgap excitations of strongly correlated transition-metal compounds are typically interpreted in terms of localized transitions between distinct spin/orbital configurations of the transition-metal ions. Also known as *dd* or ligand-field transitions [60], such excitations may be equivalently described as Frenkel-type excitons [243]. Of particular interest is the utility of *dd* excitation optical responses for measuring and tuning magnetic states, as exemplified by the observation of helical ligand-field luminescence in ferromagnetic Cr trihalides [48, 64], the linearly polarized absorption/emission from excitons in the Ni^{2+} vdW magnets NiI_2 [65] and $NiPS_3$ [56, 66, 68, 69, 244], and associated photo-induced magnetic properties [59, 71, 72]. Clarifying the microscopic origin of such excitonic states, particularly their coupling mechanism to the local spin degree of freedom and long-range magnetism, is essential for continued progress towards functional applications and for the optical characterization of magnetic ground states in vdW materials.

Here, we focus on the triangular-lattice nickel dihalide antiferromagnets $\mathrm{NiX_2}$ (X = Cl, Br, I) based on $\mathrm{Ni^{2+}}$ ions ($3d^8$) to study their multiplet spectra versus ligand, temperature and momentum using Ni-L_3 edge resonant inelastic X-ray scattering (RIXS). The ligand-field spectra of $\mathrm{Ni^{2+}}$ systems have been the subject of intensive study in classical optical literature [43, 190, 245–249] and more recent studies [9, 56, 65, 66, 68, 69, 71, 72, 244]. Specifically, several recent investigations report the emergence of sharp excitons below the magnetic transition temperatures of correlated $\mathrm{Ni^{2+}}$ vdW magnets [56, 65, 66, 68, 69, 244] These excitons were associated to spin-entangled Zhang-Rice triplet-to-singlet excitations stabilized by long-range magnetic order and magnetic coherence [56, 65]. The Zhang-Rice mechanism is motivated by the charge-transfer insulator nature of the electronic ground state in $\mathrm{Ni^{2+}}$ systems [154, 155]. The electronic states are an admixture between local $3d^8$ and $3d^9\underline{L}$ configurations, where $3d^9\underline{L}$ represents self-doped ligand hole electronic configuration [110, 154, 155]. From this configuration, analogs to Zhang-Rice states may arise as observed in doped copper oxides [15, 250, 251]. Despite this, the reported excitons bear a strong resemblance to optically spin-forbidden multiplet transitions previously revealed by optical spectroscopy [43, 190, 245–249, 252, 253]. Based on this dichotomy, the proposed Zhang-Rice mechanism for stabilizing these exciton states and the role of long-range magnetic order requires further scrutiny.

The nickel halides provide a platform to assess each of these aspects directly. First, the nickel dihalides are vdW magnets exhibiting distinct ligand-tuned magnetic ground states, ranging from C-type antiferromagnetic (AFM) to non-collinear spin structures [37, 43, 65, 124, 128]. Furthermore, they constitute an archetypal series of charge transfer insulators with systematically tuned Ni-X covalency and charge-transfer gap, Δ, as previously revealed through both X-ray photoemission and X-ray absorption spectroscopy (XPS/XAS) [154, 155]. However, the impact that this strongly ligand-tuned Δ has on the ground state multiplet excitations has not been investigated in detail. As we show in this work, the simultaneous tuning of magnetic order and self-doped ligand holes through the charge-transfer gap establishes their roles in the emergence of the exciton states, and in their fundamental parameters (namely dispersion, microscopic nature, and temperature effects). While dd excitations are nominally dipole forbidden in optics, RIXS provides direct spin- and dipole-allowed sensitivity to the zero-boson multiplet excitations [110]. Such measurements are thus crucial to unravel their microscopic nature, and intrinsic evolution with both temperature and momentum to inform a proper interpretation of their manifestation in optical experiments.

From our RIXS measurements, we observe sharp (nearly resolution-limited) excitonic peaks in all $\mathrm{NiX_2}$ (X = Cl, Br, I) compounds, confirming their universality in $\mathrm{Ni^{2+}}$ charge-transfer insulators. The ubiquity of these excitons stems from their microscopic nature, which we assign as spin-singlet ($S = 0$) multiplet (dd) excitations of $^1A_{1g}/^1E_g$ symmetry [1]. These features are characteristic of Ni^{2+} ions in octahedral symmetry, and are broadly consistent with their original identification through optical spectroscopy [43, 190, 245–249, 252, 253]. Crucially, while the energies of these singlet excited states are strongly affected by the ligand and their ionic character, the existence of these excitons does not necessitate particular charge-transfer contributions or long-range magnetic order [110, 257]. Using charge-transfer multiplet (CTM) theory, we show the strong ligand-dependence results from an effective screening of the intra-atomic Hund's exchange interaction (e.g. nephelauxetic effect) [61, 110, 154, 258, 259] due to the increasing contribution of self-doped ligand hole ($3d^9\underline{L}$) states at small Δ. This systematically establishes the primary effects of the metal-ligand hybridization/covalency, and provides a complete description of the multiplet structure in the highly ionic ($NiCl_2$) and strongly covalent (NiI_2) limits. This evidence resolves key discrepancies in the peak assignments and their microscopic interpretations found throughout the literature.

Additionally, we uncover a finite momentum dispersion of the spin forbidden $^1A_{1g}/^1E_g$ multiplets. As the charge-transfer energy is reduced by changing the halogen ligand, their dispersive bandwidth increases. This dispersion is independent from the magnetic dynamics, demonstrated through a direct comparison to the spin-excitation dispersions. Furthermore, the excitons and their dispersive behavior persist far above the magnetic ordering temperatures, demonstrating an exciton delocalization regardless of the presence of long-range magnetism. To explain this, we propose a simple charge-transfer induced exciton delocalization mechanism, determined from the dominant ligand-mediated orbital hopping pathways on the 2D triangular lattice. This effect can be viewed as a natural consequence of the increased metal-ligand hybridization in a crystalline environment. Our results demonstrate that the microscopic interactions stabilizing these excitons are the multielectron interactions at the nickel site and its local symmetry. This demonstrates how their fundamental energies and degree of delocalization may be tuned through the charge transfer gap.

8.2 Results

We performed XAS and RIXS measurements on high-quality single crystals of NiX_2 compounds grown by chemical vapor transport (see Sec. 8.4). The RIXS and XAS data were acquired at the 2-ID SIX beamline of the National Synchrotron Light Source II, Brookhaven National Laboratory [161]. RIXS measurements were performed with an energy resolution of $\Delta E = 31$ meV at the Ni-L_3 edge and XAS was recorded in total fluorescence yield (TFY). The samples were aligned with the $\mathbf{a}^*$ reciprocal lattice direction aligned in the scattering plane [Fig. 8.1(a)], with grazing incidence geometry, σ incident polarization, and $T = 40$

---

[1] Throughout the paper, we will use the terms exciton/multiplet/dd-excitation interchangeably. Such terminology is consistent with the usage of "Frenkel excitons" in reference to multiplet transitions in the early optical literature [190, 243, 245, 246, 252, 254–256]. However, referring to these states as multiplet transitions avoids confusion with excitons of distinct microscopic origin (e.g. Wannier excitons) routinely observed in semiconductors.

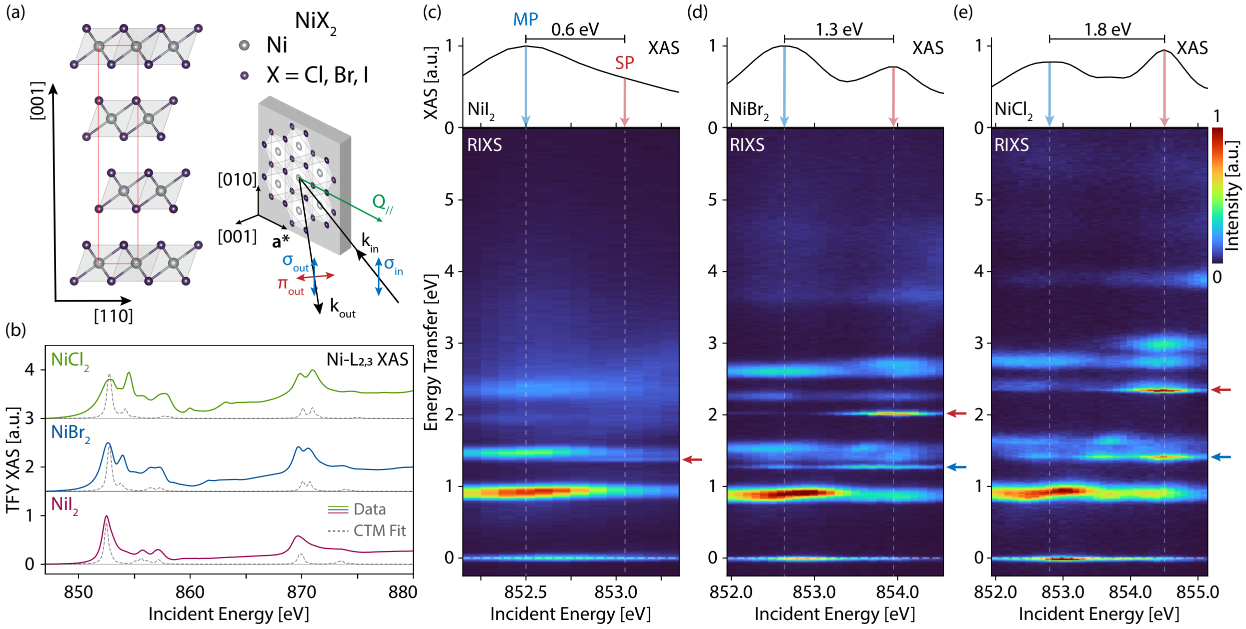

Figure 8.1: (a), The layered rhombohedral (space group $R\bar{3}m$) structure of NiX$_2$ dihalide compounds, highlighting the triangular lattice of magnetic Ni^{2+} ions and the RIXS scattering geometry at grazing incidence (see text). (b), Ligand-dependent Ni-L_3/L_2 edge XAS spectra at $T = 40$ K. Corresponding XAS fits from charge transfer multiplet calculations are the dashed grey lines (see text). (c-e), Incident-energy dependent RIXS maps for each compound across the main and side peaks at the Ni-L_3 edge (bottom) with the corresponding TFY XAS spectra (top). The XAS spectra indicate the main/side peak (MP/SP) XAS resonances with blue and red arrows, respectively, along with the MP-SP incident energy splitting for each compound. Red/blue arrows on the right axis of each RIXS map indicate the $^1A_{1g}$ - ^1E_g spin-singlet multiplets, resonant at the XAS SP.

K unless otherwise specified. The temperature was chosen to be below the magnetic phase transitions for each compound.

8.2.1 Evolution of RIXS/XAS Spectra versus Ligand

We begin by discussing the evolution of the Ni L_3-edge RIXS and XAS spectra versus ligand (X) for NiX$_2$ (X = Cl, Br, I). Figure 8.1(b) shows XAS spectra across the Ni L_3/L_2 edges for each compound. At the L_3 edge, a clear double-peaked structure is observed for all compounds corresponding to a "main" peak (MP) around 852.7 eV, followed at higher energy by a "side" peak (SP) at 854.5 eV, 854.0 eV, and 853.1 eV for NiCl$_2$, NiBr$_2$, and NiI$_2$, respectively [see Fig. 8.1(c-e), top]. We note the pronounced self-absorption effect in the TFY XAS spectra [155, 260–262], leading to suppression of the main L_3 edge peak intensity. The energy separating the MP and SP increases with the ionic character of the compound. The latter is directly linked to higher charge-transfer gaps, Δ, as discussed below. Additionally, several broader peaks are observed at higher energies ($E_i \simeq 855 - 860$

eV) and associated to charge-transfer satellites [110, 155, 259]. An overall similar qualitative behavior is observed at the L_2 edge.

We subsequently measure RIXS spectra versus incident energy across the MP and SP resonances at the Ni L_3 edge for each compound [Fig. 8.1(c-e)]. For Ni^{2+} in O_h crystal field, the ground state electronic configuration is ${}^3A_{2g}$ with $t_{2g}^6 e_g^2$ orbital occupation and $S = 1$ arrangement of the half-filled e_g states [60, 263]. Around $\Delta E = 950$ meV energy transfer, we identify a predominant Raman-like excitation which is nearly independent of ligand. This excitation is connected to the fundamental $t_{2g} \rightarrow e_g$ spin preserving ($\Delta S = 0$) crystal field excitation (${}^3T_{2g}$), suggesting a similar O_h crystal field energy scale ($10Dq$) across the series [257]. The independence of this energy scale with ligand can be rationalized by the balance of charge-transfer and metal-ligand hybridization contributions, both of which affect the covalent crystal field splitting as captured by our CTM calculations and discussed below [15, 264, 265]. At higher-energies ($\Delta E = 1 - 3$ eV), rich excitation profiles are resolved with a strong ligand-dependence. These peaks are linked to the multiplet structure of Ni^{2+} in O_h symmetry [60, 110, 257, 266]. We highlight the uniquely sharp excitations around 1.38, 2.04, and 2.37 eV in I/Br/Cl [red arrows, Fig. 8.1(c-e)], respectively. Remarkably, these peaks are nearly resolution-limited and resonant near the SP. Additional sharp excitations at the SP near $\Delta E = 1.3/1.45$ eV in Br/Cl (blue arrows) are also revealed.

The ligand-dependent RIXS spectra at the MP and SP resonances are summarized in Fig. 8.2(a). The individual dd transitions are assigned with term symbols in O_h symmetry for $\mathrm{NiCl_2}$ (top), based on our CTM calculations. Specifically, the higher/lower energy sharp peaks resonant at SP are ascribed to the spin flip $\Delta S = 1$ and ${}^1A_{1g}/{}^1E_g$ multiplet terms, respectively [257, 266], which preserve the ground state $t_{2g}^6 e_g^2$ orbital configuration. These spin-singlet multiplets are equivalent to the previously identified excitons in the optical regime, appearing at the same energies [43, 56, 65, 190, 245, 252, 253]. The salient features of the ligand dependence can be summarized by (i) a reduction of the MP-SP splitting in XAS, (ii) a reduction of multiplet energies that is most pronounced in the spin-singlet ${}^1A_{1g}$ and ${}^1E_g$ excitations, and (iii) the resonant behavior of the $\Delta S = 1$ excitations at the ligand-dependent SP resonance.

8.2.2 $\mathrm{NiX_6}$ Cluster Calculations

We next aim to quantitatively describe these ligand-dependent spectroscopic features and to provide a robust assignment of the electronic ground states and excitations. To do so, we employ CTM calculations as implemented in Quanty [113, 267, 268]. The model reduces to a multielectronic calculation of a single $\mathrm{NiX_6}$ cluster with O_h symmetry, accounting for the Ni-$3d$ orbitals and the corresponding symmetrized ligand X-np molecular orbitals [110, 155, 267] (see Sec. 8.4). We restrict the present analysis to octahedral symmetry, while potential effects of the trigonal distortion are discussed below in Sec. 8.5. Figure 8.2(b) shows the evolution of low-energy multiplets for the $3d^8 + 3d^9\underline{L} + 3d^{10}\underline{L}^2$ configuration as a function of Δ. The evolution of the ${}^1A_{1g}$ and the ${}^1E_g$ excited states as a function of ligand

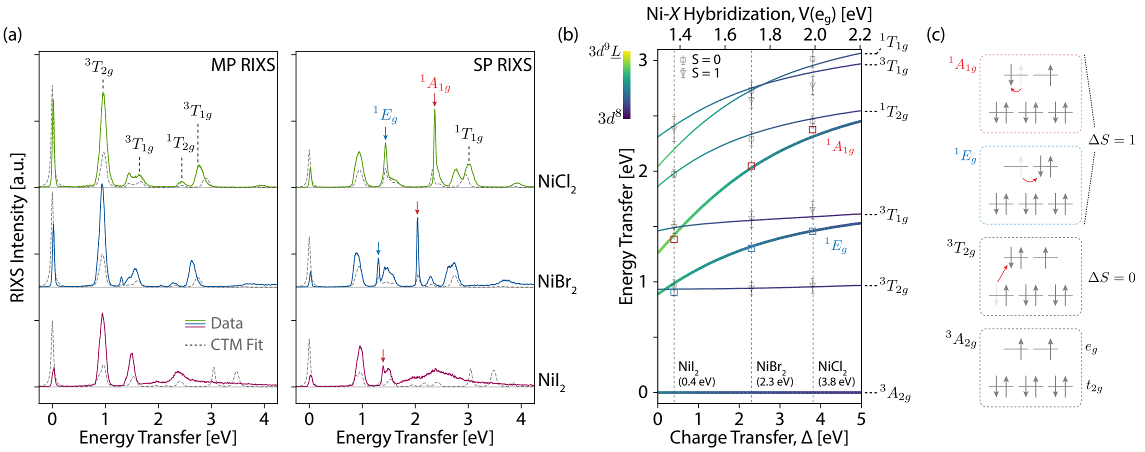

Figure 8.2: (a), Ligand-dependent RIXS spectra at the MP (left) and SP (right) resonances. Intensity for each spectrum has been normalized by the total inelastic signal (0.5 → 5.0 eV). The peaks are labelled with their corresponding multiplet term symbol in O_h symmetry (see text). The sharp spin-singlet excitations (^1E_g and $^1A_{1g}$) are indicated for each compound with blue/red arrows, respectively. Corresponding CTM calculations are shown as dashed grey lines overlaid with each experimental spectrum. The sharp features in the CTM calculations for NiI$_2$ above 3 eV are charge-transfer transitions, which are broad and overlap with fluorescence-like background in experiment (thus not well-resolved). The lower energy 3d^8 multiplets in all NiX$_2$ samples are sharp and well-captured by CTM calculations. (b), Energy level diagram calculated from the CTM model as a function of charge transfer gap Δ and Ni-X hybridization $V(e_g)$ in O_h symmetry (spin-orbit coupling excluded for simplicity). The $^1A_{1g}$ and ^1E_g term energies are highlighted with thick lines, and all calculated excitations are colored based on the $3d^8/3d^9\underline{L}$ character, as indicated by the color bar. Experimental energies for the $^1A_{1g}/^1E_g$ peaks are shown as red/blue data points with other experimental multiplets indicated with triangles/squares for triplet/singlet terms, respectively. Optimal fit values of Δ for each compound are indicated with vertical dashed lines. (c), Schematic representation of the low-energy $\Delta S = 0/\Delta S = 1$ $3d^8$ multiplet terms in O_h symmetry.

charge-transfer are highlighted with thick lines [Fig. 8.2(b)]. These excitations correspond to a nearly pure spin-flip $\Delta S = 1$ within the $|e_g\rangle$ manifold without transfer of orbital weight between the t_{2g}-e_g states. Thus, they are stabilized from the $^3A_{2g}$ ground state by the intra-atomic Hund's exchange [60] (see also [2]). Their preservation of the $t_{2g}^6 e_g^2$ ground state orbital configuration, in conjunction with their low-degeneracy, naturally accounts for their characteristically sharper linewidths compared to the other inter-configurational multiplets [61, 245, 254, 255].

We identify the optimal parameters for each compound based on a minimal parameter fitting while keeping the Coulomb interactions at the nickel site fixed (for a detailed description

---

[2] We note the distinction between these local spin-state transitions (e.g. $S = 1 \rightarrow S = 0$) and the single-/two-magnon excitations [257, 269, 270]. The former, considered here, are dd excitations stabilized by Hund's exchange. The latter are transitions of the spin projection $\Delta m_s = 1$ within the triplet ground state, with characteristic energies determined by the effective spin exchange [60, 110, 266].

of the model and parameters, see Sec. 8.5). The optimized ligand-dependent CTM parameters Δ and the metal-ligand hybridization $V(e_g)$ are summarized in Table 8.1 and indicated as vertical dashed lines in Fig. 8.2(b), with the experimental values of multiplet energies overlaid. The refined parameters are broadly consistent with previous reports from XPS and XAS [154, 155], while our calculations are further restricted by the multiplet spectra which more accurately reflect the ground state Hamiltonian. The simulated XAS/RIXS spectra determined from these parameters are shown as grey lines on top of the experimental data in Figs. 8.1(c) and 8.2(a). They reveal a good agreement with all salient features of the ligand dependence, including the peak energies [Fig. 8.2(b)], their resonance behavior/relative intensities [Fig. 8.2(a)], as well as the MP-SP and charge transfer satellite structures in the XAS (Fig. 8.1(b), for calculated RIXS maps to compare to experiments in Fig. 8.1(c-e), see Sec. 8.5).

Ligand (X)	Δ [eV]	$V(e_g)$ [eV]	β_{eff}	J_H^{eff} [eV]
Cl	3.80	1.99	0.75	0.850
Br	2.30	1.72	0.64	0.722
I	0.40	1.37	0.44	0.496

Table 8.1: Ligand-dependence of Δ and $V(e_g)$ from CTM calculations. Coulomb interactions are fixed to atomic values and ionic contribution to $10Dq = 0.55$ eV is fixed for all ligands. The on-site Coulomb repulsions are fixed to $U_{dd} = 5.0$ eV and $U_{pd} = 7.0$ eV from photoemission experiments [154]. Also shown is the phenomenological, effective ground state nephelauxetic reduction (β_{eff}) and intra-atomic Hund's exchange (J_H^{eff}) determined from corresponding ionic calculations discussed in Sec. 8.5.

A consequence of reduced Δ is a larger mixing of the $3d^9\underline{L}$ configuration into the ground and excited state $3d^8$ multiplets [56, 65, 110, 120, 155, 257, 259, 271]. The energy level diagram in Fig. 8.2(b) shows the evolution between $3d^8$ and $3d^9\underline{L}$ character resolved to each excitation. The ligand-hole character is excitation-dependent, with higher-energy excitations within a given orbital configuration (e.g. $t_{2g}^6 e_g^2$ vs. $t_{2g}^5 e_g^3$) displaying larger ligand character at a given Δ, with the $|3d^9\underline{L}\rangle$ weight roughly commensurate to the energetic renormalization of each excitation. A similar situation determines the energy-dependent ligand-hole character and MP-SP reduction in the XAS intermediate states. Besides this energetic renormalization, all excitations remain direct analogs of the corresponding $3d^8$ multiplets as they stem only from the electronic configuration and point group symmetry.

We conclude that the dominant role of ligand-hole states at the level of a single NiX$_6$ cluster is a renormalization of the intra-atomic Coulomb interactions in both the initial and final RIXS states. This is induced by delocalization of electronic density onto the ligand states (e.g. nephelauxetic effect [61, 110, 154, 258, 259]). This screening effect captures the evolution of the sharp singlet excitations, their resonance behavior, and the MP-SP evolution, which can be mapped to properties of Ni^{2+} ions in O_h symmetry without invoking emergent properties from the $3d^9\underline{L}$ configuration. From this assessment, the relevance of the recently

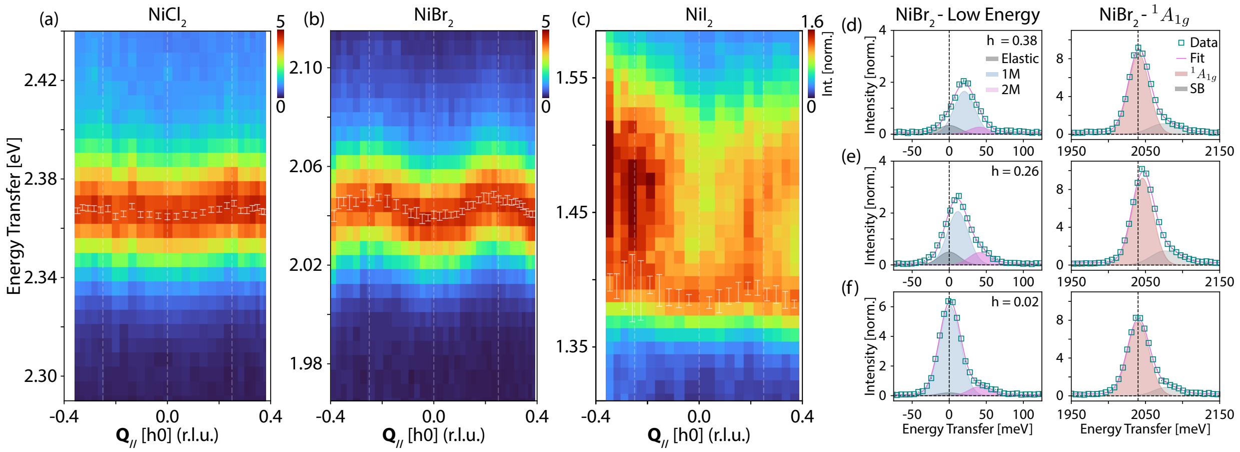

Figure 8.3: Momentum-dependence of the $^1A_{1g}$ peak as a function of ligand at $T = 40$ K in panels (a, b, c) for Cl/Br/I respectively along the ΓM direction. Momentum is reported as $\mathbf{Q}_{\parallel} = [h0]$ with h expressed in reciprocal lattice units (r.l.u.). Color maps are normalized to the integrated intensity of the displayed region in (a, b) and to the region 1.35-1.42 eV in (c). Fitted points for the $^1A_{1g}$ peak are shown as overlaid white data points with error bars determined as standard errors from the fits. Figures (d-f) are example raw data along ΓM with $h = 0.38$, 0.26, and 0.02, respectively, for NiBr$_2$ both in the low-energy transfer (left) and $^1A_{1g}$ spectral regions (right), highlighting fits to the elastic (grey), single-/two-magnon (1M/2M, blue/purple, respectively) contributions, and the $^1A_{1g}$ peak (red) and its side band (SB, grey), with overall fit depicted in purple. Statistical error bars are indicated, which are smaller than the data points.

proposed Zhang-Rice mechanism for these excitations can be ruled out [68]. Thus, the sharp $^1A_{1g}$ and ^1E_g peaks are Ni^{2+} dd-excitations arising from multielectronic interactions of a $3d^8$ electronic configuration in O_h crystal field. One may therefore expect such excitations to be ubiquitous in isoelectronic systems close to the ionic limit [56, 61, 65, 110, 245, 257, 258, 272]. These conclusions are directly supported by calculations restricted to the purely ionic limit with $3d^8$ configuration and excluding charge-transfer processes. Indeed, the effect of ligand holes on the multiplet excitations can be captured by an effective nephelauxetic effect (β_{eff}), as summarized in Table 8.1.

8.2.3 Exciton Dispersion and Relation to Magnetism

Having established the presence and properties of the exciton peaks in NiX$_2$ as a function of ligand, as well as their hybridized Ni/halogen nature, we now investigate their dependence on momentum and temperature to assess their delocalization beyond pure on-site dd excitations [123, 273, 274] and their connection to the magnetic order.

We first report the dispersion of the $^1A_{1g}$ excitation for each ligand in Fig. 8.3(a-c), measured at $T = 40$ K with momentum transfer along the $\mathbf{a}^*$ direction ([$h0$] in reciprocal lattice units, r.l.u.) and with incident energy tuned to the SP resonance (Figs. 8.1 and

8.2). We resolve an electronic dispersion with bandwidth $\delta E \simeq 3.4 \pm 1.2$ meV in $\mathrm{NiCl_2}$, $\simeq 8.2 \pm 1.3$ meV in $\mathrm{NiBr_2}$, and $\simeq 9.6 \pm 3.0$ meV in $\mathrm{NiI_2}$. Representative fits for spectra at selected momentum-transfer points for $\mathrm{NiBr_2}$ are shown in Fig. 8.3(d-f) showing both the elastic/magnon and ${}^1A_{1g}$ spectral regions. Both spectral regions are from the same spectra at a given $\mathbf{Q}_{\parallel}$, recorded at the SP resonance where single- and two-magnon contributions are observed [257, 266, 269, 270]. The spectra are relatively aligned using $\Delta S = 0$ multiplet excitations, which assumes these excitations are non-dispersive. This assumption can be justified by their high-multiplicity, significant phonon broadening, and the relatively low contribution of the $3d^9\underline{L}$ configuration, leading to the same spectral center of mass (i.e., lack of apparent dispersion). The corresponding analysis is discussed further in Sec. 8.5 alongside additional discussion of polarization cross-section/multiplet fine structure effects. Momentum-dependence for the ${}^1E_g$ excitation is also resolved in $\mathrm{NiCl_2}$ and $\mathrm{NiBr_2}$.

To elucidate the microscopic origin of the exciton dispersion and its reciprocal space structure in more detail, we perform momentum-dependent RIXS measurements across the magnetic phase transition and along different high-symmetry directions in reciprocal space, with a focus on $\mathrm{NiBr_2}$. In Fig. 8.4(a,b), we plot the fitted energy dispersion for the low-energy magnon and ${}^1A_{1g}$ mode in $\mathrm{NiBr_2}$, with comparison along the ΓM ($[h0]$ r.l.u.) and ΓK direction ($[hh]$ r.l.u.). The magnon and ${}^1A_{1g}$ exciton dispersion along ΓM are further compared at 40 K and 70 K, representing the layered AFM and paramagnetic phase of $\mathrm{NiBr_2}$, respectively [43, 128, 245]. From these data, we infer marginal differences in the ${}^1A_{1g}$ dispersion across the magnetic phase transition [Fig. 8.4(b)], with the primary temperature effect being an overall broadened linewidth with increasing temperature (as discussed below). This implies that the exciton dispersion is present regardless of long-range magnetic order, and therefore is likely not mediated by it.

The magnon dispersions are compared with linear spin-wave (LSW) calculations ([Fig. 8.4(a)]) based on inelastic neutron scattering (INS) in the layered AFM phase [128], showing good quantitative agreement (for similar comparisons in $\mathrm{NiCl_2}$ [124] see Sec. 8.5). Importantly, the magnon and the ${}^1A_{1g}$ peaks have qualitatively distinct dispersions along ΓK and ΓM. From Fig. 8.3(a-c), we also note the qualitatively similar functional form of the ${}^1A_{1g}$ dispersion across all compounds, which is independent of the disparate magnetic structures or spin excitation dispersions (see also Sec. 8.5). These aspects support our assignment of a genuine dispersion of the ${}^1A_{1g}$ excitations. To quantify this, we construct a minimal tight-binding (TB) model based on isotropic hopping parameters t_n up to $n = 3$ nearest-neighbor (NN) [243, 255, 275, 276]. We find that the ${}^1A_{1g}$ dispersion is well-described by considering only the third-NN contribution, with the single parameter (t_3) fit for $\mathrm{NiBr_2}$ shown in Fig. 8.4(b). We note that the spin-excitations persist above the long-range ordering temperatures [Fig. 8.4(a)], suggesting the presence of short-range magnetic correlations persisting to high-temperatures [277–279]. An effect of these short range magnetic correlations for determining the spin-singlet multiplet dispersion cannot be ruled out directly, although we will argue for a more natural mechanism as evidenced by the ligand dependence (discussed below).

To further underscore the independence of the $\Delta S = 1$ multiplets from the magnetic order, we measure the temperature dependence at fixed momentum transfer across the magnetic phase transitions in each compound as reported in Fig. 8.4(c-f). A monotonic linewidth broadening is revealed for both the $^1A_{1g}$ and ^1E_g modes without any significant change of spectral profiles across the magnetic phase transition temperatures for each NiX$_2$ compound [Fig. 8.4(d-f)]. For NiBr$_2$ [Fig. 8.4(c)], additional spectral weight at higher energies (∼30-40 meV) above the $^1A_{1g}$ peak is apparent, which is attributed to two-phonon side bands, consistent with previous optical experiments [43, 245–249]. Importantly, the linewidth and intensity of the singlet peaks are independent of the magnetic phase. In addition, we do not observe any clear correlation between the thermal broadening slope or extrapolated zero-temperature linewidth with the either the magnetic transition temperatures (as may be expected for magnetic coherence) or with the $|3d^9\underline{L}\rangle$ character of the excitations [Fig. 8.4(d-f)]. Instead, we attribute the thermally-activated broadening to a Franck-Condon phonon-coupling effect [245, 263, 280].

Before moving on, we summarize the experimental observations and what they imply regarding the role of magnetism for these multiplet states. At the level of localized excitations, the charge transfer multiplet calculations identify the energy scale stabilizing the $^1A_{1g}/^1E_g$ exciton states as the Hund's exchange. Therefore, their microscopic origin is independent of magnetic order but the relationship of these excitations to the local spin degree of freedom at the nickel site is clarified. At the next level detail, the independence of the fine structure of these excitations from magnetic order is corroborated by their temperature-dependencies at fixed momentum, revealing no anomalies in the linewidth or intensity across the long-range magnetic ordering temperatures. This establishes that the multiplet excitations are independent of long-range magnetic order, and sufficient to microscopically describe the excitons in NiX$_2$.

Separately, we observe a finite dispersion of the $^1A_{1g}/^1E_g$ excitations for all ligands, independent of the disparate spin structures of the different compounds and qualitatively distinct from the spin excitation dispersions. In NiBr$_2$, both the spin excitations and multiplet dispersions are observed to persist above the long-range ordering temperature. This allows the possibility for a role of short-range correlations in the multiplet dispersion. However, the totality of experimental evidence strongly suggests that at leading order, there is no direct effect of either short- or long-range magnetic order on the bare multiplet states, or in their dispersive character. This leads us to consider a mechanism of exciton delocalization that is independent of magnetism, but instead directly connected to increased contributions of the self-doped ligand holes with reduced Δ. Even if magnetism would enter a more exhaustive description, our data directly evidence that strong emphasis must be placed on the self-doped ligand holes.

8.2.4 Origin of Exciton Dispersion

To examine the origin of the finite $^1A_{1g}$ dispersion, we consider the ligand-dependence of the dispersive bandwidth (t_3). This is displayed in Fig. 8.5(a), extracted from the $\mathbf{a}^*$ dispersion

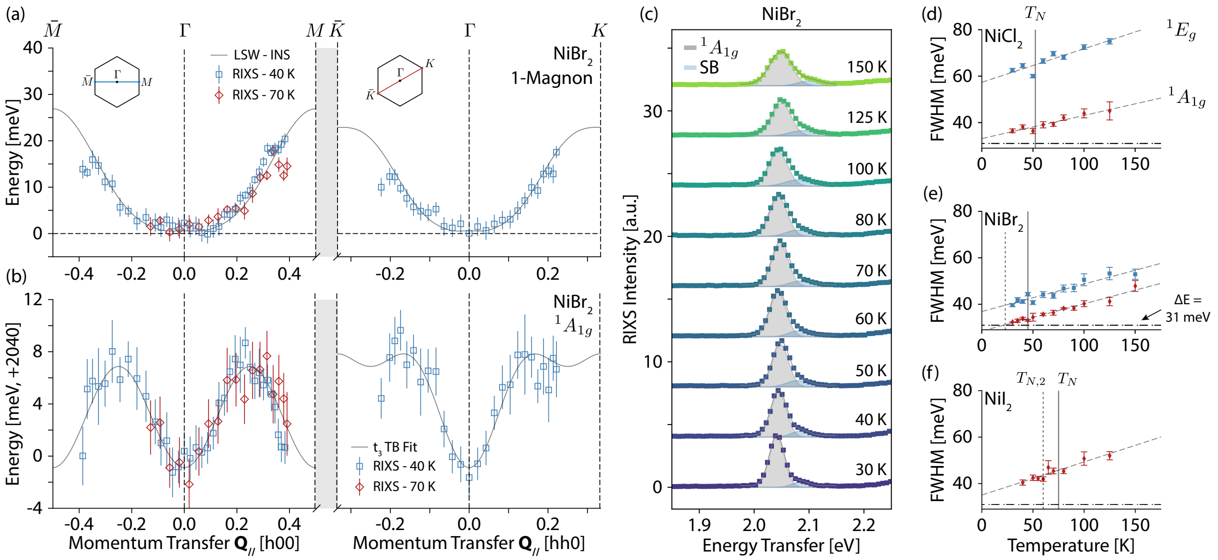

Figure 8.4: Momentum-dependence of the single-magnon (a), and the $^1A_{1g}$ excitation (b) in NiBr$_2$ along the ΓM (left) and ΓK (right) momentum-space cuts. Blue squares, $T = 40$ K and red diamonds, $T = 70$ K. Experimental single-magnon energies are compared to LSW theory, accounting for intra-layer exchange up to third nearest neighbor (J_3) using experimentally-determined parameters from Ref. [128]. The $^1A_{1g}$ data is fit along both ΓM and ΓK with a tight-binding (TB) model considering only third-nearest neighbor hopping (t_3). The LSW and TB curves are shown as solid grey lines in (a, b), respectively. (c), Representative temperature-dependence of the $^1A_{1g}$ excitation in NiBr$_2$ highlighting the temperature-dependent linewidth. Gaussian fits to the $^1A_{1g}$ and its side-band (SB, see text) are the filled grey/blue curves, respectively. Temperature-dependent linewidth of the $^1A_{1g}$ (red) and ^1E_g (blue) peaks for (d) NiCl$_2$, (e) NiBr$_2$ and (f) NiI$_2$. Linear fits (dashed lines) highlight a linear broadening of each peak with increasing temperature. Horizontal dashed lines denote the experimental resolution ($\Delta E = 31$ meV) for all measurements. Vertical solid lines indicate the C-type AFM transition temperature $T_N \simeq 52$, 45, and 75 K for Cl/Br/I, respectively, and dashed lines indicate the non-collinear magnetic phases $T_{N,2} \simeq 22$ and 60 K for Br/I, respectively [42, 43, 124].

in Fig. 8.3(a-c), revealing an increase of the bandwidth with decreasing Δ. The ligand-dependent bandwidth follows the trend of the projected $3d^9\underline{L}$ character of the ${}^1A_{1g}$ state [$|\beta^2|$ in Fig. 8.5(a)], implicating a ligand-mediated delocalization mechanism. This is also suggested by the dominance of third-NN interactions evidenced by the functional form of the dispersion, suggesting long-range interactions beyond direct $d \rightarrow d$ overlap. We interpret these features in analogy to the evolution of magnetic exchange interactions throughout the dihalide series, which have been analyzed in detail in the literature [37, 42, 47, 124, 128]. The spin exchange is dominated by superexchange [46, 120], with moderate ferromagnetic J_1, negligible J_2 and antiferromagnetic J_3 parameters restricted to the 2D triangular lattice plane where J_n is n^{th} Ni-Ni neighbor exchange [47]. While J_1 exhibits moderate stoichiometric dependence, J_3 is strongly ligand-dependent and is responsible for the difference in magnetic ground states across the series, including the non-collinear magnetic states in X = Br, I [37, 41, 47, 128]. Specifically, J_3 is mediated by superexchange pathways involving ligand X-np molecular orbitals with large σ-type overlap [120], as depicted in Fig. 8.5(b).

From this picture, a dominance of the t_3 TB component in the ${}^1A_{1g}$ dispersion can be explained by the stronger $pp\sigma$ ligand-ligand transfer integrals between third-NN $3d^9\underline{L}$ e_g-symmetry molecular orbitals, in conjunction with the lowering of the charge transfer gap which mediates pd electron transfer and increases the self-doped $3d^9\underline{L}$ character [110, 120, 154, 271]. While superexchange occurs between Ni atoms in the ${}^3A_{2g}$ ground state, the dispersion we observe originates from interactions between an excited ${}^1A_{1g}$ impurity and a surrounding bath of ${}^3A_{2g}$ [254, 255] [Fig. 8.5(b)]. The enhancement of $3d^9\underline{L}$ character upon excitation of the effective ${}^1A_{1g}$ defect compared to the ${}^3A_{2g}$ ground state [Fig. 8.5(a)] could contribute to these observations due to selective enhancement of the excited state third-NN interactions, which are more sensitive to the ligand-hole contribution compared to nearest neighbor interactions [120].

These considerations are not unique to the ${}^1A_{1g}$ state, as a finite dispersion was also resolved for the ${}^1E_g$ state (see Sec. 8.5). For ${}^1E_g$, the dispersion is weaker and with opposite sign relative to the ${}^1A_{1g}$ but of a similar qualitative (sinusoidal) form with increased bandwidth from $NiCl_2$ to $NiBr_2$ (see Sec. 8.5). This suggests the sensitivity of the proposed hopping processes to the relative spin-orbital character of the excited and ground states, again in analogue to Pauli-restricted virtual hopping processes leading to superexchange [15, 120, 255]. We note that since the ${}^1E_g$ and ${}^1A_{1g}$ states are $S = 0$ (non-magnetic), this should be interpreted as a multiplet-dependent effective transfer integral that is independent of the relative alignment of the surrounding ${}^3A_{2g}$ ground state spins – that is, independent of the long-range magnetic order. This scenario is consistent with the insensitivity of the spin-singlet multiplets and their dispersion to the magnetic transitions (Fig. 8.4).

We stress a distinction between the role of magnetism on the multiplet state and its dispersion from the effects of dispersive excitons on the surrounding magnetic order. We have shown that the excitons and their dispersion are independent from magnetic order. Meanwhile, the dispersion reveals the microscopic pathway mediating non-local interactions of the locally excited $S = 0$ magnetic defect with the surrounding magnetic sites. This

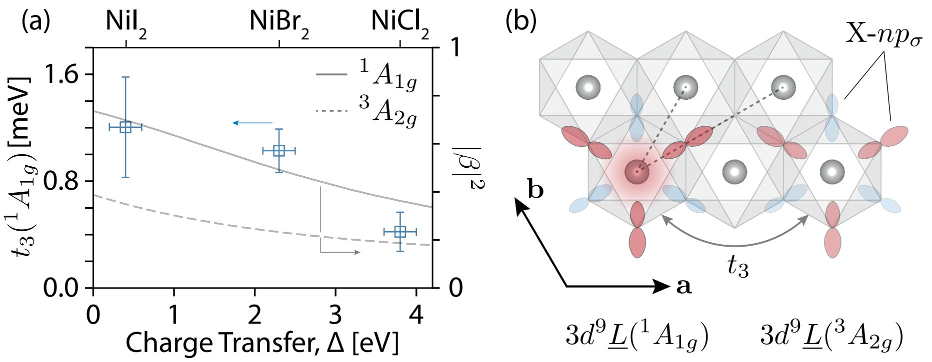

Figure 8.5: (a), Ligand-dependence of the t_3 TB parameter from fits to the $\mathbf{a}^*$ dispersion data presented in Fig. 8.3 (a-c) (left axis, blue), along with the $3d^9\underline{L}$ character ($|\beta|^2$) of the excited state $^1A_{1g}$ (solid) and the ground state $^3A_{2g}$ (dashed) multiplets extracted from the CTM calculations in Fig. 8.2 (b) (right axis). (b), Schematic of the hopping pathways in the triangular lattice plane (t_1-t_3) and the proposed third-neighbor hopping mechanism between the $3d^9\underline{L}(^1A_{1g})$ excited state and $3d^9\underline{L}(^3A_{2g})$ ground state, mediated by ligand *p*-*p* overlapping σ-bonding molecular orbitals.

was previously elaborated for excited state exchange interactions and their relevance to exciton-magnon absorption sidebands in optical experiments [62, 254–256, 281, 282]. Further theoretical investigations are required to clarify the essence of this exciton delocalization and its coupling to electronic degrees of freedom through, e.g., dynamical mean field theory [121]. Nonetheless, the mode-resolved and Δ-dependent dispersive behavior presented here provides key constraints for reaching a consistent microscopic description of excitonic dispersion in charge transfer insulators.

8.3 Discussion

Our results reveal the momentum-dependence of spin-singlet *dd* excitations in NiX$_2$ compounds and we propose a ligand-mediated delocalization mechanism analogous to superexchange. Specifically, the microscopic interactions that give rise to the $^1A_{1g}/^1E_g$ excitations are rooted in the $3d^8$ electronic configuration in octahedral symmetry, i.e. *dd* excitations. Meanwhile, increasing metal-ligand charge transfer induces two intertwined, but distinct, effects. First, it renormalizes the intra-atomic Coulomb interactions at the Ni site and induces a corresponding reduction of the fundamental multiplet energies (Figs. 8.1, 8.2). Second, the excitations simultaneously develop an increasingly delocalized and propagating nature, independent of the magnetic phase (Figs. 8.3-8.5). These conclusions provide a self-consistent and comprehensive picture of the influence of metal-ligand charge transfer on the properties of multiplet excitations in charge-transfer insulators.

The importance of measuring the exciton dispersion for unraveling its underlying nature has been stressed in several different contexts, including the alkali halides [283], spin-state transitions in cobaltites [121], fractionalization in low-dimensional cuprates [123, 273, 274], molecular excitons [275, 284–286] and the description of exciton-magnon sidebands in optics [43, 245, 247–249, 254–256, 281]. For the latter, the momentum-dependence of the exciton state contributes to the sideband structure and also determines the mechanisms of intersite exciton-magnon coupling [243, 254, 255], which are of strong relevance for interpreting photo-induced magnetic responses in transition-metal/vdW materials [57, 59, 69–71, 254, 255, 287–290]. While the momentum-dependence of spin-flip excitons has been indirectly inferred in optical experiments, our results provide the first direct evidence of their dispersive behavior. We note that the observed multiplet dispersion is distinct from the the case of fractionalized orbital excitations (orbitons) observed in cuprate spin chains [123, 273], which is an emergent effect from low dimensionality. Instead, we expect the dispersion of the spin-flip excitons observed here to be a general phenomenon for the electronic excitations of charge-transfer insulators.

More broadly, our temperature-dependent RIXS results (Fig. 8.4) provide important context for the observation of these spin-flip *dd* excitations in the optical regime [43, 56, 65, 68, 190, 246, 252]. These multiplet transitions are optically dipole- and spin-forbidden, and therefore sensitive to the lowering of symmetry across (magnetic) phase transitions that are typically inferred from optical side-bands of bosonic origin (e.g. phonon, magnon [245–249]). The complexity of such rich side-band structure, as well as the large energetic reormalization of the spin-forbidden peaks as a function of charge-transfer gap, has precluded consistent peak assignments and interpretations in the optical literature which we conclusively resolve. One consequence of the coupling to bosons is that the optical response of these exciton side-bands can be sensitive to the coherence of the magnon excitations [247–249]. The proposed effects of magnetic coherence are then likely attributed to the (magnetic) $^3A_{2g}$ ground state rather than the (non-magnetic) $^1A_{1g}/^1E_g$ excited states. Conversely, the fundamental spin-flip multiplets, generally a high cross-section and direct RIXS process at the transition-metal L-edges, are well-defined and independent of magnetic order with lineshape limited only by a temperature-dependent Franck-Condon phonon broadening [Fig. 8.4(c-f)].

Finally, we have demonstrated several key design principles for tuning the functional exciton properties. We note that only the isolated $^1A_{1g}$ peak in NiBr$_2$ has a resolution-limited behavior at the lowest measured temperature (T = 30 K). This contrasts with the $^1A_{1g}$ excitations of NiCl$_2$ and NiI$_2$ which are broader than the experimental resolution and are partially/fully overlapped with multiplets. We hypothesize that a spin-orbit coupling induced hybridization of closely lying multiplets with distinct orbital configurations (e.g. $t_{2g}^6 e_g^2$ and $t_{2g}^5 e_g^3$) may be an important aspect limiting the intrinsic (low-T) linewidths. Furthermore, for making these modes optically bright with large oscillator strength, details of multiplet level sequencing (particularly the lowest excited state) and relative energetic proximity of different multiplet terms are known to be essential through, e.g., inter-system crossing and intensity borrowing mechanisms [61]. These are actively employed in the ligand-field engineering of spin-flip luminescence transitions in molecular systems [61, 272, 291], which are direct molecular analogs to the spin-flip multiplets elaborated here. In this work, we have shown how the fundamental multiplet energies and their sequencing can be tuned by ligand field engineering and the charge transfer gap in the solid state. These underlying design principles could be fruitful for bringing on-demand and deterministic optical properties into the field of vdW materials.

In conclusion, we have extensively investigated the properties of the sharp, spin-singlet multiplet excitations of the nickel dihalides (NiX_2) using RIXS. We demonstrated that nearly resolution-limited *dd* excitations are ubiquitous features of octahedrally-coordinated Ni^{2+}, which can be systematically tuned by the ligand and charge transfer gap. We have further established the roles of the self-doped ligand hole/charge transfer states and magnetism, ruling out a Zhang-Rice mechanism and revealing that the fundamental multiplet peaks are independent from long-range magnetic order. Most importantly, we provide the first direct experimental evidence demonstrating that these excitations are dispersive. We connected this behavior to an emergent effect of the increased self-doped ligand hole character of these excitations upon reduction of the charge transfer gap. Finally, we identified a potential mechanism for this exciton delocalization that is mediated by the ligand states in analogy to superexchange. Our RIXS results thus firmly establish the microscopic nature of these exciton states and provide a fundamentally distinct approach for tailoring collective electronic excitations in charge transfer insulators through their momentum dispersion.

8.4 Methods

Sample growth and preparation

All samples were prepared using chemical vapor transport (CVT). $NiCl_2$ was synthesized using stoichiometric ratios of Nickel powder (Sigma Aldrich, 99.9%) and $TeCl_4$ (Sigma Aldrich, 99.8 %), at a temperature gradient of 760 °C to 730 °C for 72 hours before being cooled naturally to ambient conditions. The temperature ramp-up time was 72 hrs. Single-crystal $NiBr_2$ was grown from $NiBr_2$ powder (anhydrous, > 99.9%, Sigma-Aldrich), at a temperature gradient 650 °C to 600 °C. Single-crystal NiI_2 was grown from elemental precursors with molar ratio Ni:I = 1:2, at a temperature gradient 700°C to 500°C as described previously [37]. The magnetic susceptibility was measured using a magnetic property measurement system (MPMS-3, Quantum Design Inc.) for NiI_2/$NiBr_2$ and a physical property measurement system (PPMS, Quantum Design Inc.) using the vibrating sample magnetometer (VSM) option for $NiCl_2$. The magnetic susceptibility of the bulk crystals confirm magnetic transitions at $T_N = 53$ K for $NiCl_2$, $T_{N,1} = 45$ K and $T_{N,2} = 22$ K for $NiBr_2$ and $T_{N,1} = 75$ K and $T_{N,2} = 60$ K for NiI_2. Magnetic susceptibility data are shown in Sec. 8.5 for $NiCl_2$ and $NiBr_2$ and in Ref. [37] for the NiI_2.

The samples were aligned using a Bruker-GAADS Co-K_α ($\lambda = 1.7902$ Å) x-ray diffractometer to place the $\mathbf{a}^*$ direction in the scattering plane for RIXS experiments. The lattice parameters were determined to be $a = 3.465(12)$ Å and $c = 17.304(46)$ Å for $NiCl_2$,

$a = 3.648(13)$ Å and $c = 18.412(52)$ Å for $NiBr_2$ and $a = 3.934(15)$ Å and $c = 19.809(61)$ Å for NiI_2 which were determined by single crystal diffraction from the (006) and (104) reflections. Samples are aligned in air, cleaved in a high-purity nitrogen-filled glovebox (H_2O and $O_2 < 0.1$ ppm) and stored in vacuum for transport to the X-ray beamline. For NiI_2, we left the as-grown surface uncleaved for XRD alignment, with air exposure of approximately 15 minutes. Cleaving of the as-grown surface inside a nitrogen-filled glovebox after alignment revealed protected surfaces without visible degradation. The sharp multiplet features in agreement with optical spectra [190, 245, 252] and low diffuse scattering of the soft X-ray beam confirms high-quality samples and flat vdW surfaces for all samples.

X-ray absorption and resonant inelastic X-ray scattering experiments

XAS and RIXS measurements at the Ni L_3-edge (852 eV) were carried out at the 2-ID SIX beamline at the National Synchrotron Light Source II, Brookhaven National Laboratory. σ polarization was applied for the incident X-rays for all measurements. XAS was recorded in total fluorescence yield (TFY) using a photodiode inside the soft X-ray chamber. RIXS spectra were recorded with high-resolution of $\Delta E = 31$ meV for all measurements. The sample temperature was kept at 40 K unless specified. Laboratory-prepared and sealed samples were transferred from vacuum into the ultra-high vacuum (UHV) loadlock of the X-ray chamber with minimal air exposure and kept under UHV conditions for the duration of X-ray experiments. NiI_2 samples are more hygroscopic, and were loaded into the vacuum chamber within a high-purity nitrogen environment.

Charge-transfer multiplet calculations

We performed charge transfer multiplet (CTM) and crystal field multiplet (CFM) calculations using the Quanty software [113, 267, 268]. For the CFM calculations, we consider the Ni-$3d$ orbitals in the basis set with an octahedral crystal field (O_h CF). For CTM calculations, the symmetrized $X =$ Cl/Br/I molecular orbitals of t_{2g} and e_g symmetry are explicitly included. Core-level spectra for the Ni-$L_{2/3}$ edges are calculated by considering $2p \rightarrow 3d$ dipole transitions using the Green's function formalism [113, 267, 268]. All spectra are calculated in the experimental polarization conditions.

The parameters for the multiplet calculations include the Coulomb interactions at the Nickel site, parameterized as the direct Slater integrals F^2_{dd}/F^4_{dd} in the initial/final RIXS state ($3d^8$) and by the direct integrals $F^2_{dd}/F^4_{dd}/F^2_{pd}$ and exchange integrals G^1_{pd}/G^3_{pd} in the intermediate RIXS state ($2p^5 3d^9$). The atomic spin-orbit coupling (SOC) in the $3d$ and $2p$ nickel states are also included. The Slater integrals and SOC parameters for each electronic configuration are taken from Hartree-Fock values tabulated by Haverkort [292]. For CTM calculations, all Slater integrals are uniformly scaled to atomic values (80% of HF values). Additional parameters include the Coulomb repulsion parameters $U_{dd}/U_{pd} = 5.0/7.0$ eV, respectively (taken from photoemission experiments [154, 155]), the charge transfer energy Δ and the metal-ligand hybridization $V(e_g)/V(t_{2g})$. We use the empirical relation $V(t_{2g}) = 3/5 \times V(e_g)$ and fit the XAS/RIXS spectra using $V(e_g)/\Delta$.

8.5 Additional Data and Discussion

Sample characterization

Fig. 8.6 shows the magnetic susceptibility data for $NiBr_2$ and $NiCl_2$ of crystals from the same growth batch used for the RIXS experiments. Data for NiI_2 is shown in Ref. [37]. This confirms the expected antiferromagnetic transitions at $T = 53$ K for $NiCl_2$ [124] and at $T = 22/45$ K for $NiBr_2$ [127, 128].

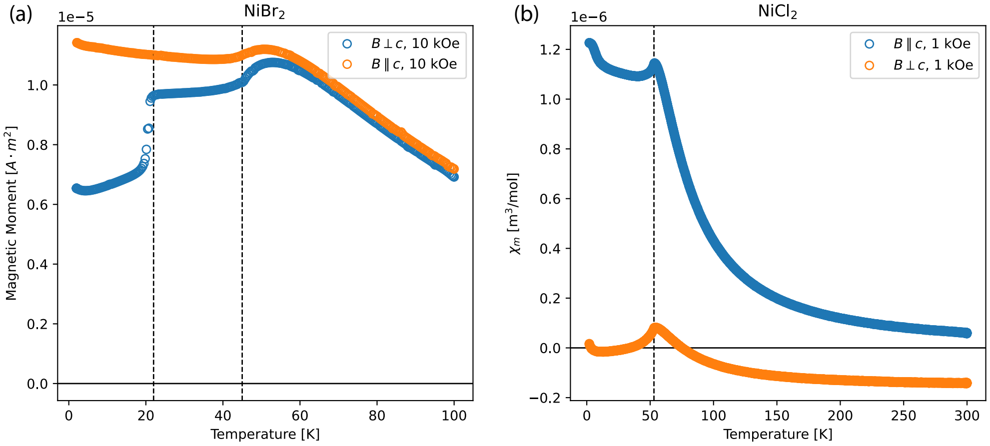

Figure 8.6: Magnetic susceptibility data for (a) $NiBr_2$ and (b) $NiCl_2$ measured with applied field parallel/perpendicular to the c axis and with a magnitude of 10/1 kOe for each sample, respectively. Dashed vertical lines denote the antiferromagnetic transitions previously reported [124, 127, 128]. $NiCl_2$ data is expressed as molar susceptibility with sample mass 0.6(1) mg. The mass of $NiBr_2$ sample was not able to be precisely measured, and the data are provided in units of magnetic moment.

Temperature-dependent data for ^1E_g and $^1A_{1g}$ multiplets

Here we report the temperature dependence of the ^1E_g and $^1A_{1g}$ multiplets for each compound in Fig. 8.7. These are the same measurements analyzed in Fig. 8.4(c-f), where here we report the raw linecuts and fits for each compound. The measured data were taken at maximum momentum transfer (grazing-incidence geometry) along the ΓM momentum space cut, with σ incident polarization and with energy tuned the respective side peak (SP) resonance in the XAS, as reported in Fig. 8.1. The multiplets were fit with a single Gaussian peak to determine the full width at half maximum (FWHM) as a function of temperature.

Additional neighboring multiplets and additional spectral weight appearing as side bands (particularly visible on the higher energy loss side of the $^1A_{1g}$ peak in $NiCl_2$ and $NiBr_2$, discussed below) were fit with additional Gaussian peaks in addition to a constant background. The grey dashed lines in the FWHM plots indicate linear fits. Error bars are determined from the standard error of the fits.

In the case of $NiCl_2$ and $NiBr_2$, the ^1E_g has an energy close to the $^3T_{1g}$ multiplet which appears at higher energy loss in the displayed regions of Fig. 8.7, while the ^1E_g peak is not resolved in NiI_2. The additional spectral weight in the higher energy-loss side of the $^1A_{1g}$ peaks in $NiCl_2$ and NiI_2 are associated to the $^1T_{2g}$ and $^3T_{1g}$ multiplets, respectively. These assignments are supported by our cluster calculations in Fig. 8.2. Meanwhile, additional spectral weight appearing as a side band at higher energy-loss of the $^1A_{1g}$ peak in $NiBr_2$ cannot be directly accounted for in the localized multiplet excitation spectrum. These are associated to two-phonon or magnon side bands, consistent with their identification in optics experiments [245–249].

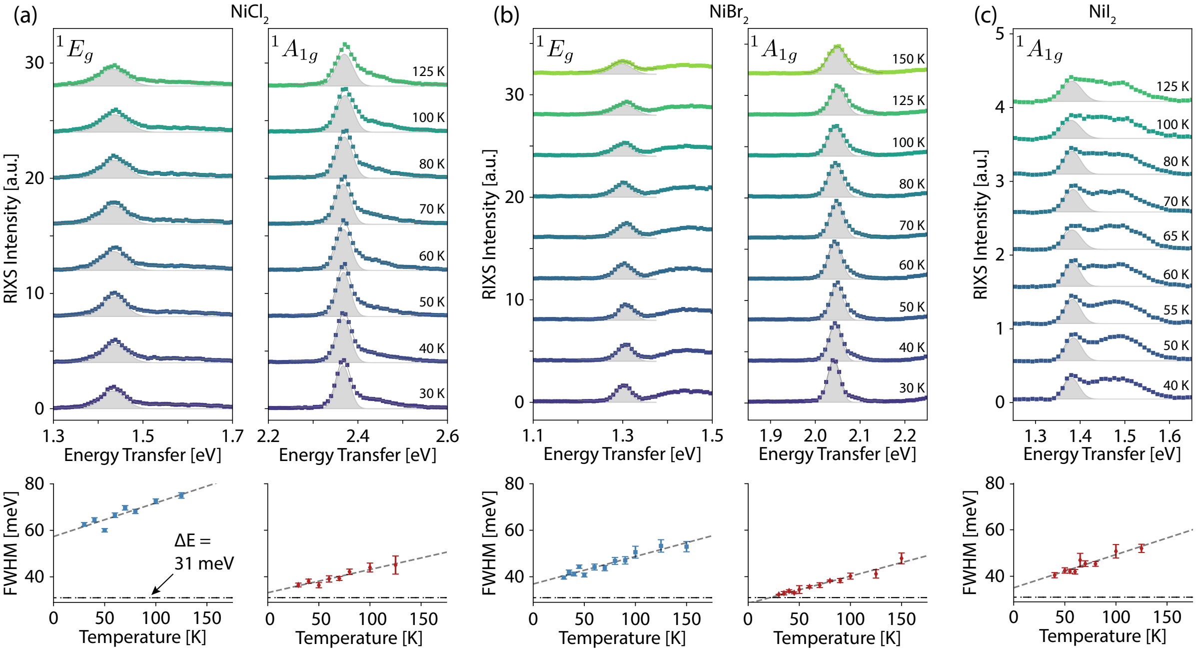

Figure 8.7: Raw temperature dependent line cuts and fits for the ^1E_g and $^1A_{1g}$ multiplets in (a) $NiCl_2$, (b) $NiBr_2$, and (c) NiI_2. The full width half maximum of each peak as a function of temperature, determined from Gaussian fits, is shown below each respective plot. The dashed line indicates the experimental resolution of $\Delta E = 31$ meV for all measurements. The spectra are all normalized by the counting time.

Additional momentum-dependence data

In Figs. 8.8-8.12, we show additional momentum-dependence on all samples at different energy regions and temperatures. In particular, we report the dispersion of the ^1E_g peak and the spin-excitation dispersion in $NiBr_2$ and $NiCl_2$. The multiplet excitations were fit by single Gaussian functions with amplitude, position and width as free parameters, along with a constant background contribution and additional Gaussians to account for other nearby excitations.

For the low-energy spin excitations, we note that the elastic line is relatively weak away from specular condition, precluding a consistent fitting of the elastic for aligning the zero-energy loss at each momentum. The zero energy loss for all samples was thus aligned at different $\mathbf{Q}$ by aligning the center of mass of dd excitations, specifically the $^3T_{2g}$ for $NiCl_2$ and NiI_2 and the high energy $^3T_{1g}$ peak in $NiBr_2$. With this procedure, we were then able to fit the specular elastic line near $\mathbf{Q}_{\|} \simeq 0$ as well as the magnon and elastic lines at maximum positive/negative $\mathbf{Q}_{\|}$ which showed a consistent alignment at the endpoints. After this, we fit the low energy spectral weight first by a single Gaussian peak. Already at this stage, the center of mass and best-fit full width half maximum (FWHM) of the single-peak model showed good agreement with the expected spin-wave dispersion from inelastic neutron scattering (INS) [124, 128], suggesting that the single-magnon contribution is the dominant contribution to this spectral region.

To minimize the number of parameters, we then fit to a three-Gaussian model, including an assumed non-dispersive peak fixed to zero energy loss, a dispersive single-magnon excitation, and an assumed non-dispersive two-magnon excitation. The latter was motivated by the clear non-dispersive spectral weight near 40 meV that is most apparent near zero momentum transfer, as well as from previous studies which reported that while the single-magnon contributions are collective (dispersive), the multi-magnon contributions are non-dispersive [269, 270]. We also note that the presence of a prominent two-magnon peak may be expected in our case since we measure at the SP resonance of the XAS, which was previously elucidated in the case of NiO [257]. We thus fixed the energy of the two-magnon contribution empirically to near twice the maximum $\mathbf{Q}$ single-magnon energy. Finally, we note that near $\mathbf{Q}_{\|} = 0$, there is significant overlap between the increasing specular elastic contribution and the low energy single-magnon contribution. Thus, there is a large cross correlation between the intensities of these quantities. To account for these uncertainties, we have added a 2 meV error in quadrature with the standard error of the fit value of the single-magnon energy. We note that (a) the good agreement of fit spin wave dispersions with previously reported INS data in $NiBr_2$ and $NiCl_2$, (b) the qualitatively distinct functional forms of the dispersions for the spin excitation, ^1E_g and $^1A_{1g}$ peaks and (c) the consistency of the procedures across different momentum cuts, samples and temperatures all testify to the robustness of our elastic alignment.

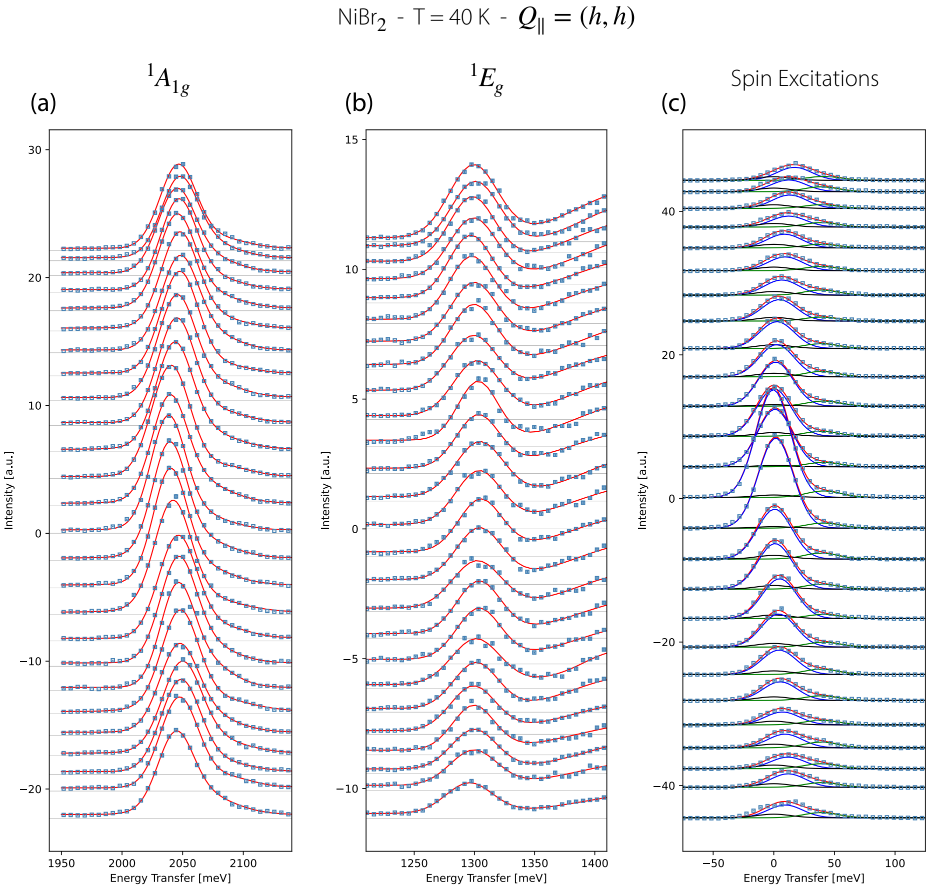

Figure 8.8: Momentum-dependent RIXS line-cuts near the (a) $^1A_{1g}$, (b) ^1E_g, and (c) elastic/spin-excitation regions for NiBr$_2$ at $T = 40$K and $\mathbf{Q}_\parallel = [h,h]$. Data are normalized by the total inelastic weight (integrated between $0.2 \rightarrow 3.0$ eV). Data points are shown as blue squares. Statistical (Poisson) error bars are indicated, but smaller than the used data points. Total fits are shown in red (see text). In (c), fit components for the elastic, single-magnon and two-magnon excitations are shown as black, blue and green solid lines, respectively. Zero baselines for each curve are shown as horizontal grey lines. Data are shifted vertically for clarity, proportionally to the momentum transfer h times an arbitrary factor.

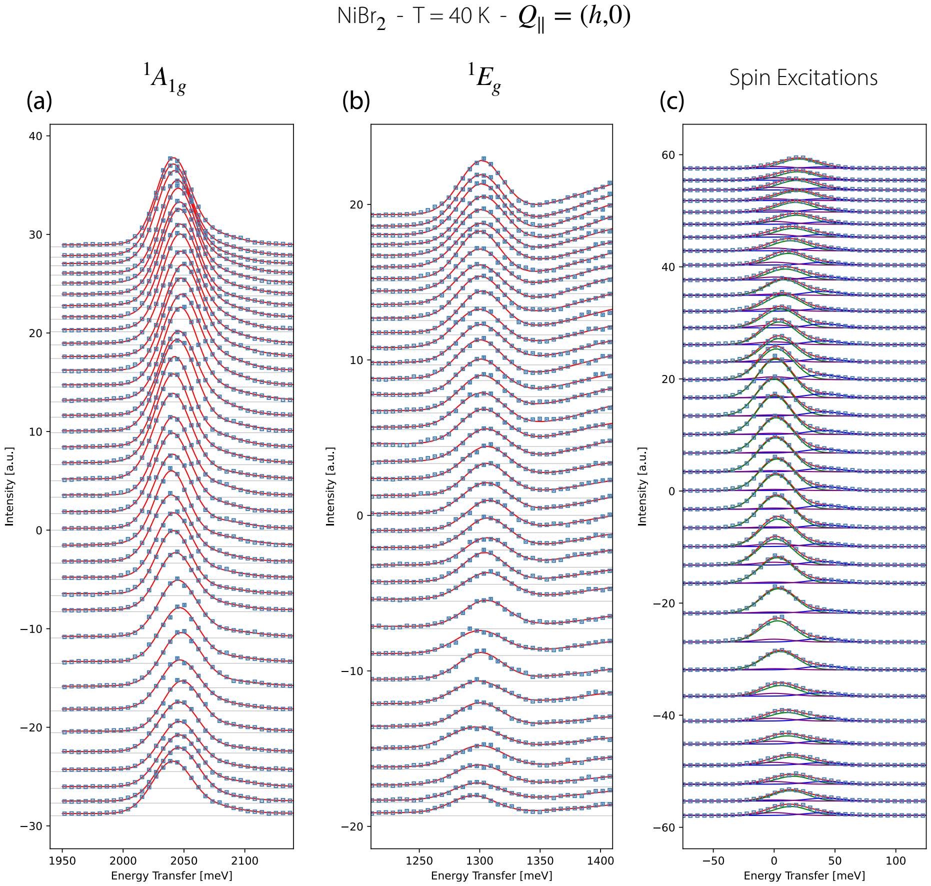

Figure 8.9: Momentum-dependent RIXS line-cuts near the (a) $^1A_{1g}$, (b) ^1E_g, and (c) elastic/spin-excitation regions for NiBr$_2$ at $T = 40$K and $\mathbf{Q}_{\|} = [h, 0]$. Data are normalized by the total inelastic weight (integrated between $0.2 \rightarrow 3.0$ eV). Data points are shown as blue squares. Statistical (Poisson) error bars are indicated, but smaller than the used data points. Total fits are shown in red (see text). In (c) fit components for the elastic, single-magnon and two-magnon excitations are shown as black, blue and green solid lines, respectively. Zero baselines for each curve are shown as horizontal grey lines. Data are shifted vertically for clarity, proportionally to the momentum transfer h times an arbitrary factor.

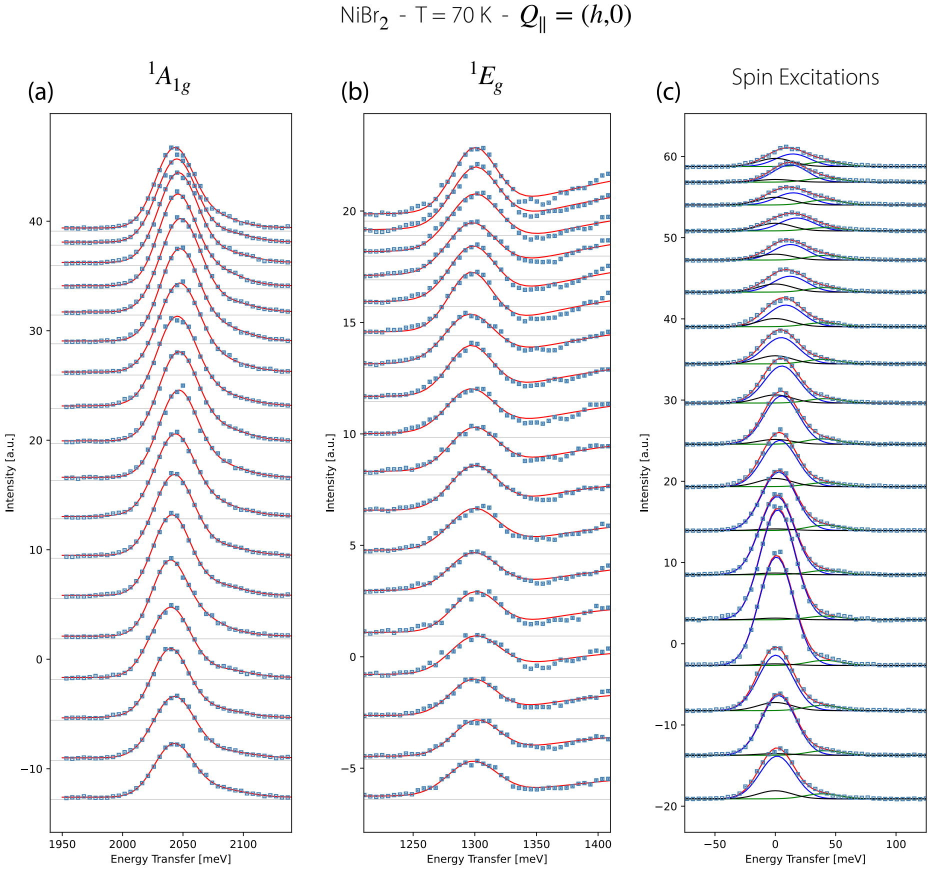

Figure 8.10: Momentum-dependent RIXS line-cuts near the (a) $^1A_{1g}$, (b) ^1E_g, and (c) elastic/spin-excitation regions for NiBr$_2$ at $T = 70$K and $\mathbf{Q}_\parallel = [h, 0]$. Data are normalized by the total inelastic weight (integrated between $0.2 \rightarrow 3.0$ eV). Data points are shown as blue squares. Statistical (Poisson) error bars are indicated, but smaller than the used data points. Total fits are shown in red (see text). In (c) fit components for the elastic, single-magnon and two-magnon excitations are shown as black, blue and green solid lines, respectively. Zero baselines for each curve are shown as horizontal grey lines. Data are shifted vertically for clarity, proportionally to the momentum transfer h times an arbitrary factor.

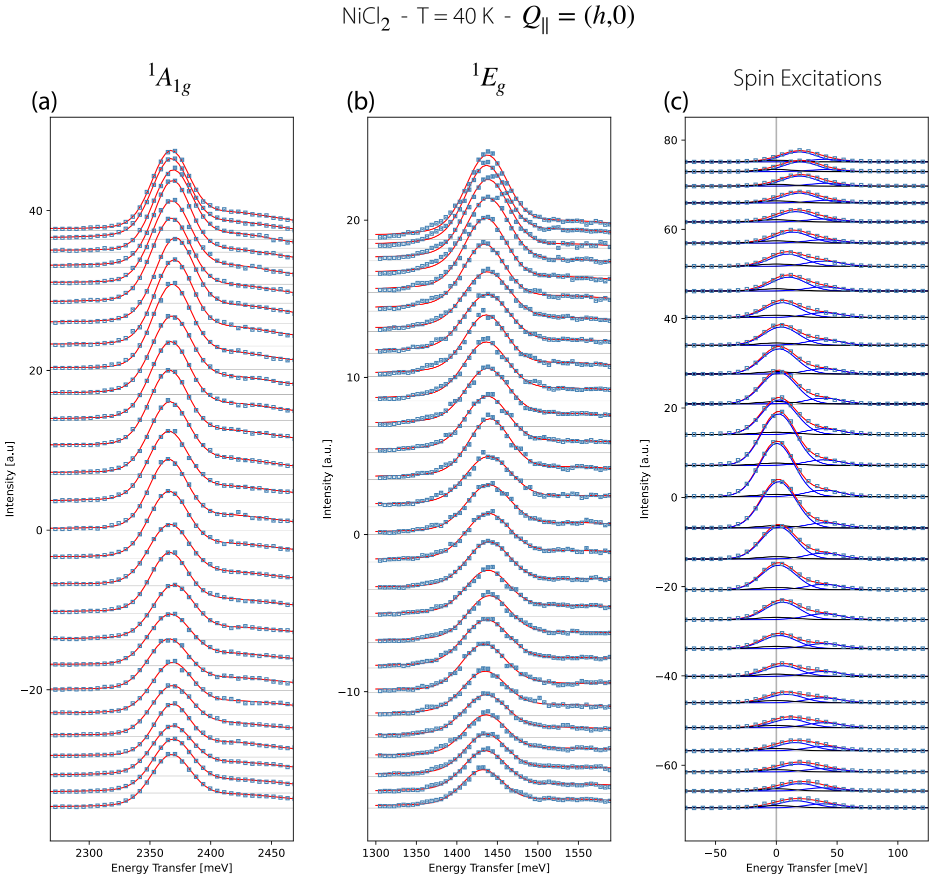

Figure 8.11: Momentum-dependent RIXS line-cuts near the (a) $^1A_{1g}$, (b) ^1E_g, and (c) elastic/spin-excitation regions for NiCl$_2$ at $T = 40$K and $\mathbf{Q}_\parallel = [h,0]$. Data are normalized by the total inelastic weight (integrated between $0.2 \rightarrow 3.0$ eV). Data points are shown as blue squares. Statistical (Poisson) error bars are indicated, but smaller than the used data points. Total fits are shown in red (see text). In (c) fit components for the elastic, single-magnon and two-magnon excitations are shown as black, blue and green solid lines, respectively. Zero baselines for each curve are shown as horizontal grey lines. Data are shifted vertically for clarity, proportionally to the momentum transfer h times an arbitrary factor.

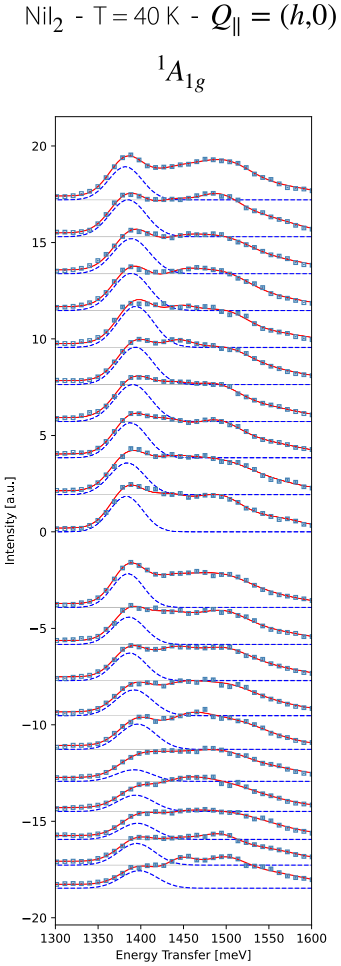

Figure 8.12: Momentum-dependent RIXS line-cuts near the $^1A_{1g}$ region for NiI$_2$ at $T = 40$K and $\mathbf{Q}_{\parallel} = [h, 0]$. Data are normalized by the total inelastic weight (integrated between 0.2 → 3.0 eV). Data points are shown as blue squares. Statistical (Poisson) error bars are indicated, but smaller than the used data points. Total fits are shown in red (see text). Dashed blue lines indicate the Gaussian function corresponding to the $^1A_{1g}$ fit component. Zero baselines for each curve are shown as horizontal grey lines. Data are shifted vertically for clarity, proportionally to the momentum transfer h times an arbitrary factor.

Tight-binding analysis for exciton dispersion

To phenomenologically understand the dominant hopping pathways from the qualitative form of the $^1A_{1g}$ dispersion, and to quantify the ligand-dependence of the dispersive bandwidth, we employed a standard tight-binding model restricted to the triangular lattice planes up to the third nearest neighbor. We determined that the dominant hopping pathway evidenced from the data is the third-nearest neighbor (t_3) contribution corroborated by a previous core-level X-ray spectroscopy study [120], also revealed by the clear two-fold periodicity within the first Brillouin zone. The single-parameter fit functional form of the dispersion to fit the data [Fig. 8.4(b)] is,

$$\omega(h,k) = 2t_3\left[\cos(4\pi h) + \cos(4\pi k) + \cos(4\pi(h+k)\right] \tag{8.1}$$

where h, k are in-plane momenta expressed in reciprocal lattice units (r.l.u.). The high symmetry momentum points are $\Gamma = (0,0)$, $M - \bar{M} = (\pm 1/2, 0)$ and $K - \bar{K} = (\pm 1/3, \pm 1/3)$. This functional form was used to estimate the t_3 hopping parameter for the $^1A_{1g}$ peak versus ligand, reported in units of meV in Fig. 8.5(a). We show additional fits to the ^1E_g and $^1A_{1g}$ peaks to the t_3 tight-binding (Eq. 8.1) for $NiBr_2$/$NiCl_2$/NiI_2 in Fig. 8.13. We also show an analogue to Fig. 8.5(a), including the bandwidth and $3d^9\underline{L}$ character of the ^1E_g state extracted from the multiplet calculations in Fig. 8.13(f).

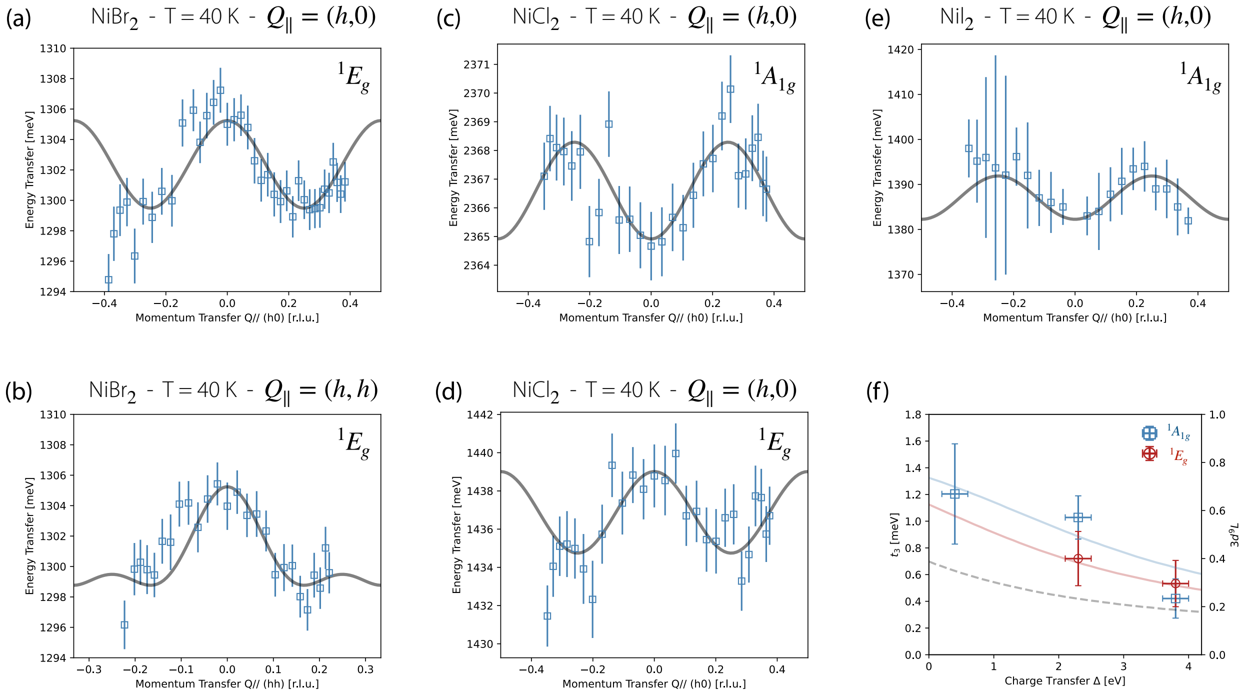

Figure 8.13: Additional fittings of the ^1E_g and $^1A_{1g}$ momentum dependencies to the tight-binding model. In (a-e) experimental data are shown as blue squares with error bars determined from standard errors of the fits (see Figs. 8.9-8.12) and the solid grey lines are the best fits to the third-nearest neighbor tight binding (TB) function along the appropriate momentum space cut (see text). (f) Extension of Fig. 8.5(b) to include the t_3 TB parameter for the ^1E_g dispersion. Note, the values are reported as absolute value of t_3 (left axis) which is negative for the $^1A_{1g}$ (blue squares) and positive for the ^1E_g (red squares) for all ligands. Also shown are the $3d^9\underline{L}$ ligand-hole characters ($|\beta|^2$, see text) for the $^3A_{2g}$ (dashed grey line), $^1A_{1g}$ (solid blue line) and ^1E_g (solid red line) versus charge transfer gap extracted from charge transfer multiplet (CTM) calculations. An approximate uncertainty range for the charge transfer gap of ±0.2 eV is given as horizontal error bar [estimated based on the energy renormalization of the $^1E_g - {}^1A_{1g}$ states, Fig. 8.2(b)], along with the standard error of the TB fit as vertical error bar. Note that the ^1E_g peak is not resolved in NiI$_2$.

Linear spin wave calculation of spin excitation dispersion in $\mathbf{NiX_2}$

The spin wave dispersions of $NiBr_2$ and $NiCl_2$ have been investigated with inelastic neutron scattering [124, 127, 128] and interpreted in terms of isotropic exchange interactions in the triangular lattice plane up to the third nearest neighbor as previously analyzed [41], with the following Hamiltonian

$$H = -\sum_{i,j} J_{ij}(\mathbf{S}_i \cdot \mathbf{S}_j) + D\sum_i (S_i^z)^2 \tag{8.2}$$

where $J_{ij} = J_1, J_2, J_3$ are isotropic first-, second-, and third-nearest neighbor intralayer exchange, respectively, $J_{ij} = J'$ is the interlayer exchange, and D is the single-ion anisotropy. This model results in a satisfactory agreement between the experimental spin-wave dispersions and the magnetic ground states of the nickel dihalides [41, 42, 124, 127, 128]. For comparison to RIXS data, we have reproduced the calculated spin-wave dispersions in the paramagnetic phase ($T < 52$ K in $NiCl_2$ and 22 K $< T <$ 45 K in $NiBr_2$), consistent with the magnetic ground states at the measured temperature of $T = 40$ K in RIXS experiments. The parameters determined from INS are summarized in Table 8.2.

Table 8.2: Exchange parameters from Refs. [124, 127] for $NiBr_2$ and $NiCl_2$. All units in meV. Positive sign $J > 0$ is ferromagnetic and negative $J < 0$ is antiferromagnetic interaction.

	J_1	J_2	J_3	J'	D
$NiBr_2$	1.56	-0.02	-0.41	-0.18	0.08
$NiCl_2$	1.87	-0.42	0.00	-0.066	0.035

The spin-wave dispersion is then determined as, from Ref. [41],

$$\omega(\mathbf{q}) = 2S\left[J(\mathbf{k}_0) + \frac{(J(\mathbf{q}+\mathbf{k}_0) + J(\mathbf{q}-\mathbf{k}_0))}{2}\right]^{1/2}\left[J(\mathbf{q}) - J(\mathbf{k}_0) + D\left(1 - \frac{1}{2S}\right)\right]^{1/2} \tag{8.3}$$

For comparison to experiments, we used the magnetic structure with wavevector $\mathbf{k}_0 = (0, 0, 3/2)$ corresponding to the layered AFM phases common to both $NiCl_2$ and $NiBr_2$ at the measurement temperature $T = 40$ K. These results are used for comparison to the spin wave dispersion measured by RIXS in $NiBr_2$ in Fig. 8.4(a) along the ΓM and ΓK momentum space directions. The corresponding comparison for $NiCl_2$ along the ΓM direction is shown in Fig. 8.14. We find a similar good agreement between the previously published exchange parameters and the experimental spin-excitation dispersion in RIXS. The spin wave spectra have not yet been reported for NiI_2 and a detailed analysis is beyond the scope of the current paper.

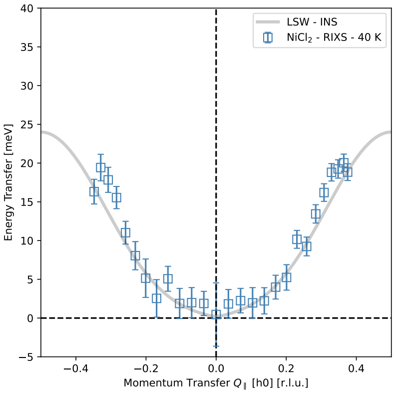

Figure 8.14: Comparison between fit spin excitation dispersion along the ΓM direction in NiCl$_2$ at $T = 40$ K (blue squares) and linear spin wave (LSW) calculation (grey line) based on parameters from inelastic neutron scattering (INS) (see text).

Details of charge transfer multiplet calculations

Here we provide additional details of the charge transfer multiplet (CTM), crystal field multiplet (CFM) calculations, and the ligand-dependent best-fit parameters. The basis set for the CFM calculations are the Ni-$2p$ orbitals (for calculating Ni-L_2/L_3 edge core-level spectra), the Ni-$3d$ orbitals, as well as symmetrized ligand molecular orbitals for the CTM model.

The atomic Hamiltonian to describe the ground state multiplet structure of the ionic limit ($3d^8$) electronic configuration includes multipolar Coulomb interactions parameterized by the direct (F^n_{dd}) Slater integrals, the spin-orbit coupling (SOC) ζ_{3d} in the initial state, and a phenomenological crystal field splitting ($10Dq$ in octahedral symmetry). Additional parameters in the intermediate RIXS ($3d^9 2p^5$) state include the direct F^n_{dd}-F^n_{pd} and exchange G^n_{pd} Slater integrals, the atomic SOC ζ'_{3d} in the intermediate slate and the core-level $2p$ SOC ζ_{2p} which determines the L_3/L_2 edge splitting.

The Slater integrals are acquired from Hartree-Fock values, with scaling factors F_k and G_k for the direct and exchange contributions, respectively. The atomic values are empirically determined to be 80% of the Hartree- Fock (HF) values which have been tabulated by Haverkort [292]. For CTM calculations, where additional screening is captured by the mixture of ligand hole states, we leave the Slater integral scaling to atomic values ($F_k = G_k = 0.8$). The $3d$ SOC is always maintained at the Hartree-Fock values and is not rescaled.

The coordination symmetry of the nickel site in the nickel dihalides is a trigonally-distorted octahedron, with a dominant octahedral (O_h) crystal field (CF) contribution. This splits the five $3d$ orbitals into a higher energy e_g symmetry doublet and a lower energy t_{2g} symmetry triplet. In first-order approximation, a small trigonal (D_{3d}) distortion leads to a further splitting of the O_h-t_{2g} levels into a singlet a^π_{1g} and a doublet e^π_g level, while the O_h-e_g levels remain degenerate (which we denote as e^σ_g in D_{3d} symmetry). Trigonal symmetry also allows a mixing term between the e^π_g and e^σ_g orbitals. For most calculations, we consider only

O_h CF unless otherwise specified, while the effects of the trigonal distortion are investigated separately below (Fig. 8.21).

Config.	F^2_{dd}	F^4_{dd}	ζ_{3d}	F^2_{pd}	G^1_{pd}	G^3_{pd}	ζ_{2p}
$3d^8 2p^6$	12.233	7.597	0.083	-	-	-	-
$3d^9 2p^5$	13.005	8.084	0.102	7.720	5.783	3.290	11.507

Table 8.3: Hartree-Fock parameters from Ref. [292] in the ground ($3d^8 2p^6$) and intermediate state ($3d^9 2p^5$) of Ni^{2+} used for all calculations. Units are in eV.

The description provided so far defines the approximation of CFM calculations, which do not explicitly include the ligand states or charge transfer processes. Additional parameters for CTM calculations include the charge transfer energy (Δ), the Coulomb parameters in the initial (U_{dd}) and intermediate (U_{pd}) states as defined in the Zaanen-Sawatsky-Allen scheme [154, 155], and the hybridization between the ligand molecular orbitals and the Ni-$3d$ states of e_g [$V(e_g)$] and t_{2g} [$V(t_{2g})$] symmetry. The charge transfer Δ and metal-ligand hybridization $V(e_g) - V(t_{2g})$ are then used as fit parameters to the XAS and RIXS spectra while leaving the Slater integrals of the nickel site fixed to atomic values ($F_k = G_k = 0.8$).

For fitting the data in the CTM model, we employed a minimal fitting procedure where we fix the empirical ratio $V(t_{2g}) = 3/5 \times V(e_g)$ and scale the hybridization V and charge-transfer Δ to match experiment. We take the parameters U_{pd} and U_{dd} from photoemission experiments which we fix to $U_{dd} = 5.0$ eV and $U_{pd} = 7.0$ eV [155]. Furthermore, the bare O_h-symmetry Ni-$3d$ crystal field splitting ('ionic' CF) is fixed to $10Dq = 0.55$ eV for all compounds. It was found that best fit to each ligand is an approximately linear relation between Δ and $V(e_g)$, given by $V = 0.181 \times \Delta + 1.301$, which was used to generate Fig. 8.2(b). The overall parameters for the ligand dependence are summarized in Table 8.4. The reported values are in good agreement with previous reports from XPS and XAS measurements [155], but are further restricted in our case by the RIXS data.

	Δ	$V(e_g)$
$\mathrm{NiCl_2}$	3.80	1.99
$\mathrm{NiBr_2}$	2.30	1.72
$\mathrm{NiI_2}$	0.40	1.37

Table 8.4: Ligand-dependence of Δ and $V(e_g)$ from CTM calculations. Coulomb screening parameters are fixed to atomic values $F_k = G_k = 0.80$ and the ionic O_h CF is fixed to $10Dq = 0.55$ eV for all compounds.

Besides these CTM calculations, we also performed CFM calculations to investigate the role of the ligand-hole states. We fixed the O_h symmetry crystal field to $10Dq = 0.95$ eV based on the lowest energy ${}^3T_{2g}$ multiplet observed in all compounds. We then adjust the direct Slater integral scaling F_k to find the optimum agreement with all other multipet excitations in the RIXS spectra. Finally, we fix F_k and vary the exchange integral scaling G_k, which is only included in the intermediate state Hamiltonian, to optimize the XAS profile, in particular the MP-SP splitting in the XAS. The optimized values for each compound are reported in Table 8.5.

	F_k	G_k
$NiCl_2$	0.60	0.68
$NiBr_2$	0.51	0.51
NiI_2	0.35	0.22

Table 8.5: Ligand-dependence of Coulomb screening parameters from optimized charge transfer multiplets (CTM) calculations. The O_h crystal field (CF) is fixed to $10Dq = 0.95$ eV. Values are percent of Haetree-Fock (HF) values, where $F_k = G_k = 0.80$ correspond to atomic values. Uniform scaling of all parameters is used across the initial and intermediate states.

We compare the calculated XAS and ground state energy level diagrams within the CTM and CFM frameworks in Fig. 8.15. From these comparisons, we conclude that the evolution of the ${}^1A_{1g}$ and the ${}^1E_g$ peaks, as well as the MP-SP evolution, can be effectively mapped onto an ionic model and result from the intra-atomic Coulomb interactions at the nickel site. The near resolution-limited behavior of these highlighted ${}^1A_{1g}$ and ${}^1E_g$ multiplets results from their low-degeneracy: the ${}^1A_{1g}$ is both a spin- and orbital singlet, while the ${}^1E_g$ is an orbital doublet and spin-singlet state. As both of these spin-orbital excitations involve a rearrangement of the electronic configuration within the half-filled e_g crystal field states, they are not sensitive to the crystal field distortion, but are rather stabilized from the ${}^3A_{2g}$ ground state directly through the intra-atomic Hund's exchange interactions which are here parameterized by the Slater integrals $F^2_{dd} - F^4_{dd}$ in the initial state. This intra-configurational excitation nature also results in a smaller coupling to phonons [245, 247–249], which contributes to the qualitatively smaller linewidths compared to the other inter-configurational (e.g. $t^6_{2g}e^2_g \rightarrow t^5_{2g}e^3_g$) multiplets.

In the CFM model, the screening of the intra-atomic Coulomb interaction, or nephalauxetic effect, is accounted for by a direct reduction of the Slater integrals (e.g. $F_k - G_k$ scaling factors), while in the CTM calculations an effective reduction of the Coulomb interactions are induced by an enhanced self-doped ligand ($3d^9\underline{L}$) hole character which naturally increases as the charge transfer gap is decreased [see Fig. 8.2(c)]. Thus, as electronic density is transferred to the surrounding ligands, the electronic interactions stabilizing the spin-singlet multiplets are reduced. Furthermore, the ${}^1A_{1g}$ and ${}^1E_g$ multiplet degeneracy is not sensitive to the inclusion of SOC, lowered (trigonal) CF symmetry or effective spin-exchange field splitting and they are not endowed with fine-structure broadening, leading to nearly resolution limited behavior across the entire halide series, independent of the ligand-tuned covalency and charge transfer state weight. We note that these conclusions are also consistent with previous observations in NiO [257].

While the essential physics can be accounted from only a $3d^8$ model, the inclusion of charge transfer states more accurately captures the excitation-dependent screening of the intra-atomic electronic interactions compared to a uniform screening introduced phenomenologically through the CFM model, resulting in an improvement in the description of the data. Additionally, higher energy charge transfer side bands in the XAS and additional charge transfer excitations in the RIXS spectra are captured in the CTM model, which are not included in the CFM approximation. In the CFM model, a separate tuning of the direct and exchange Coulomb interactions is required to describe the ligand-dependent screening in both the initial/final (ground, $3d^8 2p^6$) and the intermediate (excited, $3d^9 2p^5$) states in order to accurately describe the $\Delta S = 1$ excitations in the RIXS spectrum and the L_3 edge XAS side-band evolution versus ligand. In contrast, the CTM model allows for a correct description of both features directly through tuning of the charge transfer energy and the orbital-dependent hybridization. The source of these effects come from larger hybridization of higher-energy excitations in both the initial and intermediate RIXS states with the charge transfer states, leading to a larger effective screening of their Coulomb interactions. For this reason, the side band multiplet in the intermediate $3d^9 2p^5$ state reflected in the XAS profile hybridizes more strongly at a given Δ than the main band multiplets, as shown in Fig. 8.16, and similarly for the ${}^1A_{1g}$ excitation in the ground/final $3d^8$ state which occurs at higher energies relative to the ${}^3A_{2g}$ ground state compared to the ${}^1E_g$ excitation. This preferentially large hybridization may lead to the incorrect conclusion that the ligand states are essential to describe the physics of these excitations — however, larger ligand hole state weight in these excitations is a consequence of the details of hybridization within this regime of charge transfer gap, and the dominant effect (as revealed directly through our comparison of ionic and charge transfer calculations) is that hybridization with ligand states induces a nephalauxetic effect [110] which describes all salient features of the data excluding the temperature- and momentum dependence. This is directly proven by our ligand dependent data and calculations and is in agreement with the known spectrochemical trends for halogen ligands [60, 110, 190, 245, 252, 253, 258].

From the charge-transfer and crystal-field multiplet models, the XAS and RIXS core-level spectra at the Ni-L_2/L_3 edges are calculated with the Green's function approach as implemented in the software Quanty [113, 267, 268]. We use a core-hole (Lorentzian) broadening of 500 meV for both XAS and RIXS spectra and a 30 meV Lorentzian broadening on the energy-transfer axis for RIXS spectra. In addition, we introduce a mode-dependent broadening of specific excitations which do couple (inter-configurational, e.g. ${}^3T_{2g}$) and do not couple (intra-configurational, e.g. ${}^1A_{1g} - {}^1E_g$) to the O_h crystal field by averaging several calculations calculated with different values of $10Dq$ with ± 50 meV of the best fit value. This phenomenologically accounts for the distinct linewidths between these types of excitations, related to a differential coupling to phonons which broaden the lineshape of the $10Dq$-coupled excitations. Simulated RIXS maps for each compound in the CTM model are shown in Fig. 8.17(a-c). These show good agreement with the experimental RIXS maps in Fig. 8.1(c-e). We note in both the calculated/experimental RIXS maps an apparent shift of the ${}^3T_{2g}$ peak to higher energies in the XAS post-edge region. This is attributed to intermediate state cross section effects which transfer spectral weight to different fine structure components of the $^3T_{2g}$ state. Such fine-structure can be induced by the combined effects of spin-orbit coupling, effective spin exchange, and the trigonal distortion [266]. We also show a corresponding RIXS map calculation for the CFM model for optimized $NiBr_2$ parameters in Fig. 8.17(d). The latter shows that the resonance of the spin-flip multiplets at the side band is not related to the relative ligand-hole state character in the ground/intermediate state, but is dictated by a cross-section effect related to the $3d^8/3d^9 2p^5$ ground/intermediate state multiplet structure and dipole selection rules determined from Ni^{2+} in O_h symmetry. We note that this cross-section effect may be related to the $\Delta m_s = 2$ (two-magnon) excitations resonant at the side band in NiO [257], as also suggested in our data on $NiCl_2$ and $NiBr_2$.

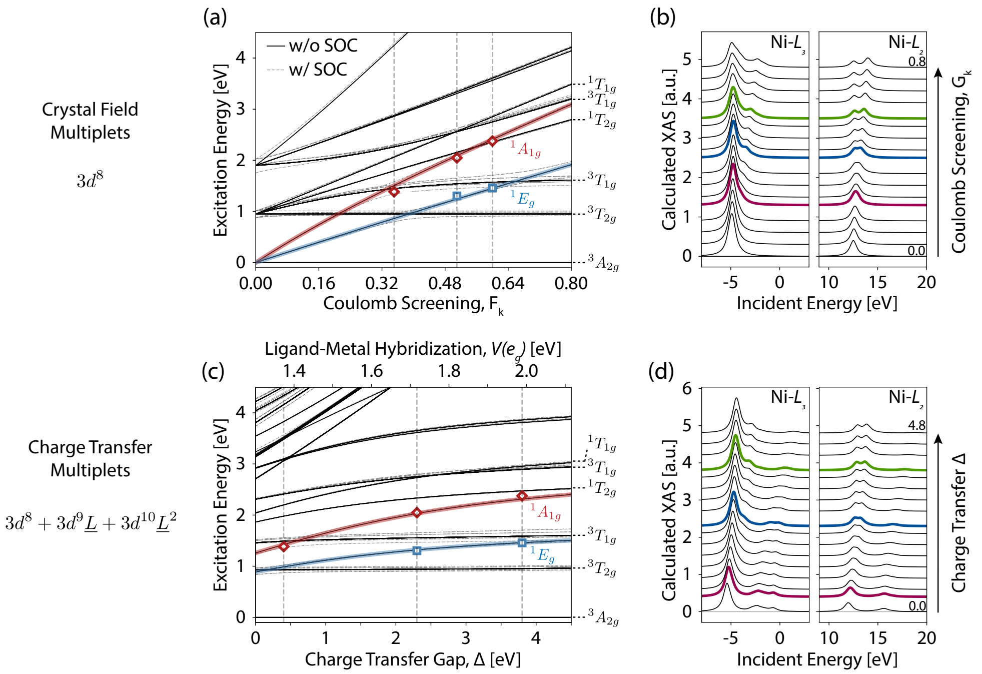

Figure 8.15: Calculations of the multiplet structure within the crystal field (CFM, top row) and charge transfer (CTM, bottom row) models. (a) $3d^8$ multiplet structure with $10Dq = 950$ meV as a function of the intra-atomic Coulomb screening F_k in the initial RIXS state, where $F_k = 0.80$ corresponds to atomic values. (b), The Ni-L_3 (left) and Ni-L_2 (right) simulated XAS spectra (offset vertically for clarity) as a function of co-varied direct (F_k) and exchange (G_k) Slater integrals in the initial and intermediate state. (c), Energy level multiplet diagram in the charge transfer model as a function of covaried charge transfer gap (Δ) and metal-ligand hybridization [$V(e_g)$] along with (d), the simulated XAS spectra. The covariant values $F_k - G_k$ and $\Delta - V(e_g)$ in the CFM and CTM models, respectively, are interpolated linearly between the best fit values of the NiX$_2$ experimental data (see Tables 8.5 and 8.4). In (a) and (c) thick red and blue lines highlight the $^1A_{1g}$ and ^1E_g excitations, respectively, and the experimentally observed excitation energies are shown as open red diamonds/blue squares, respectively for X = I/Br/Cl from left to right. The optimal parameter values are indicated by dashed vertical lines. In (b) and (d), the corresponding XAS spectra for these optimized values are shown in red/blue/green for I/Br/Cl, respectively.

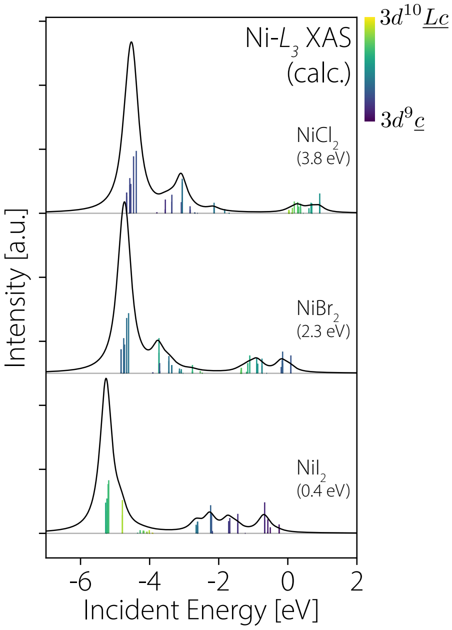

Figure 8.16: Calculated Ni-L_3 edge XAS for optimized values in the CTM model for $\mathrm{NiCl_2/NiBr_2/NiI_2}$ from top to bottom, respectively. The energy axis is with respect to the center energy of $3d^92p^5$ configuration in the calculation. Individual excitations contributing to the XAS profile are shown as bar plots over the corresponding spectra, showing the evolution of each XAS transition between $3d^9\underline{c}/3d^{10}\underline{Lc}$ ligand-hole character as Δ is reduced. The relative weight of each configuration is indicated by the color bar. See also the analogous plot for the ground state multiplets in Fig. 8.2(b).

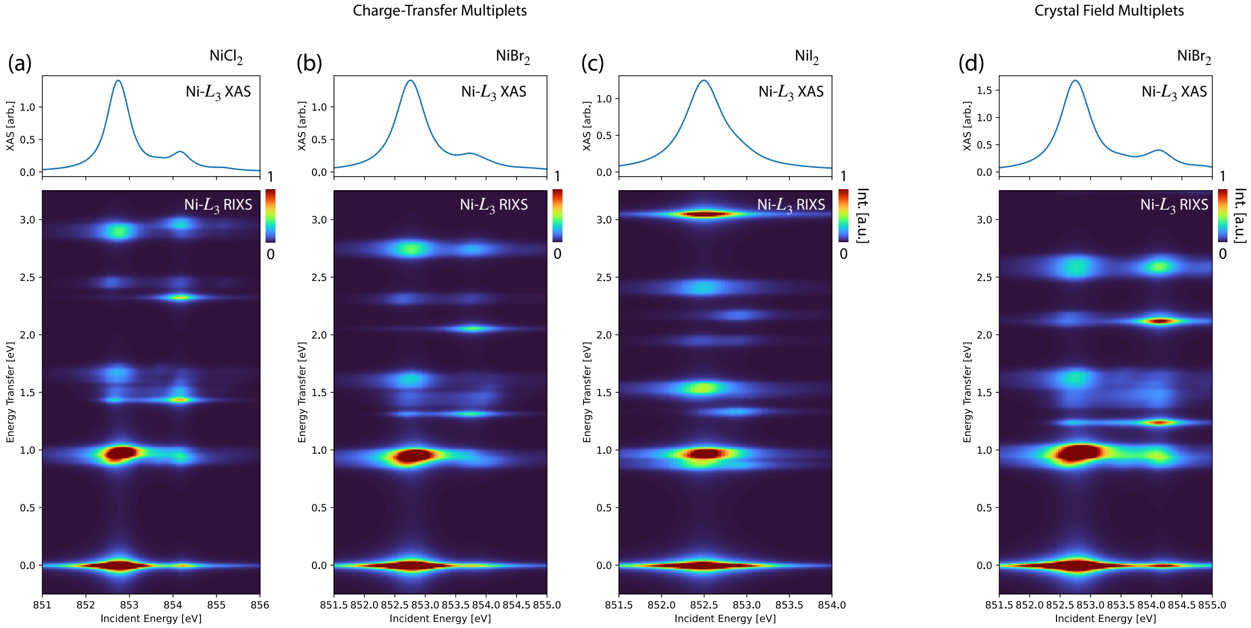

Figure 8.17: Calculated incident-energy dependent RIXS maps across the Ni-L_3 resonance alongside the calculated XAS in the CTM model for (a), NiCl$_2$ (b), NiBr$_2$ and (c), NiI$_2$, as well as the corresponding CFM result for NiBr$_2$ in (d). Parameters are described in the text. Spectra are calculated with Lorentzian broadening of 0.5 eV on the incident energy axis (XAS and RIXS) and by 0.03 eV on the energy transfer axis. In addition, an empirical, mode-dependent broadening is introduced by averaging spectra with different values of $10Dq$ in a range ±0.05 eV around the central best value. Spectra are all calculated in the experimental polarization conditions.

Polarization-dependence and self-absorption

Here we provide an additional assessment of the dependence of the RIXS intensity on incident polarization, including the effects of self-absorption in the RIXS and XAS profiles as well as the intrinsic angular dependence of the multiplet excitations as inferred from cluster calculations. Throughout this section, we will argue that the angular dependencies of the intrinsic cross-section effects on the sample angle θ and the self-absorption effects cannot account for the periodicity of the measured multiplet dispersions, thus ruling out cross-section artifacts to explain the ${}^1E_g$ and ${}^1A_{1g}$ dispersions reported here.

From previous XAS studies on the nickel dihalides [154, 155], we observe strong self-absorption and saturation effects in the total/partial fluorescence yield measurements (TFY and PFY, respectively), most prominent at the Ni-L_3 edge white line/main peak (MP) resonance [260, 261]. The self-absorption gets more pronounced when going from X $=$ I to X $=$ Cl. This is evident from the TFY and PFY data compared in Fig. 8.18, where the white line peak is heavily suppressed. The NiX$_2$ compounds are all highly insulating, and bulk forms of the crystals did not result in strong total electron yield (TEY) signal, except for NiBr$_2$ for which a thin single crystal was used ($\simeq 10$ μm). We show a comparison between the CTM calculation, TEY and TFY signal in NiBr$_2$ in Fig. 8.19, confirming a large self-absorption on the MP resonance of Ni-L_3 edge.

The effects of self-absorption are known to distort the intensity profile of RIXS spectra when the incident energy is tuned above the main resonance [262, 293]. In our case, all momentum dependent data were collected on the SP resonance of the XAS which maximizes the intensity of the ${}^1E_g/{}^1A_{1g}$ peaks (see Fig. 8.18, 8.1, 8.2). In this case, the absolute emitted energy of inelastic (energy loss) peaks may be coincident to the region of maximum absorption (MP) and will be accordingly suppressed by self-absorption. For incident energy ω_i and scattered energy ω_o, it was shown that the appropriate self-absorption correction factor for RIXS experiments is [293],

$$C(\omega_1, \omega_2) = 1 + \frac{\alpha_0 + \alpha(\omega_i)}{\alpha_0 + \alpha(\omega_o)} \frac{\cos(\theta_i)}{\cos(\theta_o)} \tag{8.4}$$

where in $\theta_i - \theta_o$ are the incident/emitted angle with respect to surface normal. Our scattering geometry is depicted in Fig. 8.20(a), where the scattering angle is fixed to $2\theta = 150°$ and the appropriate angles are $\theta_i = \theta - 90°$ and $\theta_o = \theta - 60°$ in terms of the defined angle θ reported for the measurements.

We first extract the intensity of the total inelastic spectral weight as a function of angle by integrating the total intensity from $0.2 \rightarrow 3.0$ eV when normalizing the intensity by the total counting time. These are reported for NiCl$_2$ along $[h, 0]$, NiBr$_2$ along $[h, 0]$ and $[h, h]$, and NiI$_2$ along $[h, 0]$ at $T = 40$ K in Fig. 8.20(b). The solid lines show fits to an assumed emission-energy and emitted-polarization independent self-absorption factor C, showing the average effect of self-absorption on the RIXS intensity. Importantly, the self-absorption intensity is monotonically decreasing when going from grazing incidence $\theta < 75°$ to grazing emission $\theta > 75°$.

For fitting the spectra, we normalized each RIXS spectrum by the total inelastic scattered intensity as reported in Fig. 8.20(b), corresponding to the normalized spectra shown in Figs. 8.8-8.12. The intensity of the fitted ${}^1A_{1g}$ and ${}^1E_g$ peaks along different momentum cuts are reported in Fig. 8.20(c-f). These are compared to the intrinsic angular dependencies expected from corresponding CTM calculations (bottom row), using the optimized values for NiBr$_2$. The angular dependencies can all be described by the functional form:

$$I(\theta) = A\cos^2(\theta - \theta_0) + B \tag{8.5}$$

consistent with the expectations from dipolar selection rules. Importantly, these have a periodicity of 180°. Along $[h, 0]$, the angle dependent intensity of the ${}^1A_{1g}$ peak shows good agreement with the theoretical prediction, as well as along $[h, h]$ for NiBr$_2$ [Fig. 8.20(c,d)]. Meanwhile, the ${}^1E_g$ peak does not agree well for the measured cases, with the experimental data showing a monotonically decreasing intensity. We attribute this discrepancy to the emission-energy dependent self-absorption described by $C(\omega_1, \omega_2)$ above.

We assess this in Fig. 8.18, where we indicate the measurement energy for all temperature and momentum dependent data at the SP (E_{meas}) as well as the corresponding absolute emitted photon energies for the ${}^1E_g$ and ${}^1A_{1g}$ peaks, shown as vertical blue/red lines, respectively. We observe that in all cases, the ${}^1A_{1g}$ peak emission energy is in the pre-edge region of the Ni-L_3 edge, while in NiCl$_2$ and NiBr$_2$, the ${}^1E_g$ emission energy is tuned near the maximum of the Ni-L_3 white line. Thus, while the self-absorption of the ${}^1A_{1g}$ peak in each case may be appropriately accounted by normalizing the average (polarization/emission-energy independent) self-absorption from the integrated inelastic weight in Fig. 8.20(b), the ${}^1E_g$ may be expected to show a higher than average self absorption effect. We argue that this explains the simultaneous agreement of the ${}^1A_{1g}$ and the disagreement of the ${}^1E_g$ angular dependencies to CTM calculations. Given the lack of consistent TEY and TFY comparison data due to the insulating nature of NiX$_2$ compounds, as well as the lack of experimental resolution of the emitted polarization, we leave this description qualitative instead of attempting a full emission-energy dependent self-absorption correction to the data, instead preferring to report the raw data.

To conclude this section, we note that while self-absorption is shown to have a non-negligible effect on the emission spectra, we have shown that a monotonically-decreasing self-absorption effect (with increasing θ) and the intrinsic angular dependence with periodicity of 180° cannot explain the observed momentum-dependent energy of the ${}^1A_{1g}/{}^1E_g$ multiplets, which instead have a two-fold periodicity within a single Brillouin zone and an (approximate) periodicity of 90° with respect to θ. Furthermore, we note that the effects of self-absorption are expected to be most pronounced in NiCl$_2$, which shows the largest self-absorption distortion of the XAS, while the energetic dispersion is smallest in this sample throughout the halide series. The good agreement of the angular dependence of the ${}^1A_{1g}$ peaks with the theoretical prediction bolsters our multiplet assignments and the accuracy of our calculations.

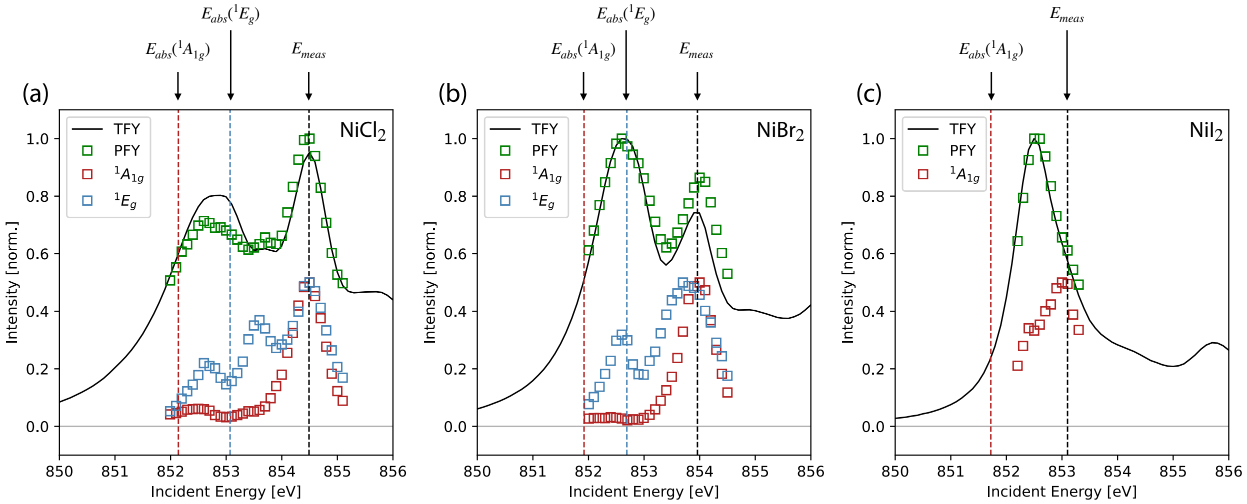

Figure 8.18: Comparison of total integrated inelastic weight [e.g. partial fluorescence yield (PFY), green squares] with the TFY absorption profile (black line) for (a), NiCl$_2$ (b), NiBr$_2$ and (c), NiI$_2$. Also shown are the integrated intensity of the ^1E_g (blue squares) and $^1A_{1g}$ (red squares) excitations. Data for the energy-dependent integrated intensities are from the RIXS maps shown in Fig. 8.1. In addition, we also indicate the incident energy on the side peak (SP) resonance (E_{meas}) for measuring the temperature and momentum dependence of the spin-singlet excitations for each compound (vertical black dashed line), as well as the absolute emission energies $E_{abs}(^1E_g) - E_{abs}(^1A_{1g})$ excitations with incident energy E_{meas} for comparison to the expected emission-energy dependent self-absorption (see text).

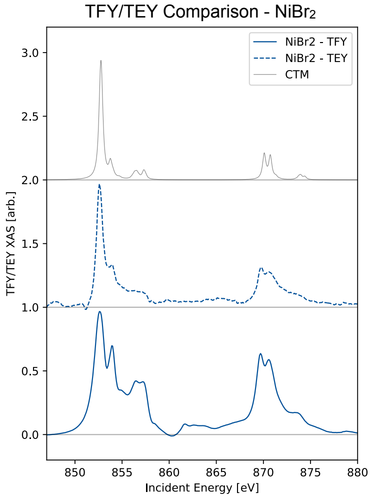

Figure 8.19: Comparison between the XAS spectra measured in TFY (solid, blue) and TEY (dashed, blue) in NiBr$_2$, measured at $\theta = 11^\circ$ and $T = 40$ K. A linear background was subtracted from both experimental spectra. These are further compared to the XAS calculated from CTM calculations using the optimized parameters for NiBr$_2$ (solid, grey) with a uniform (Lorentzian) core-hole broadening of $\Gamma = 0.5$ eV.

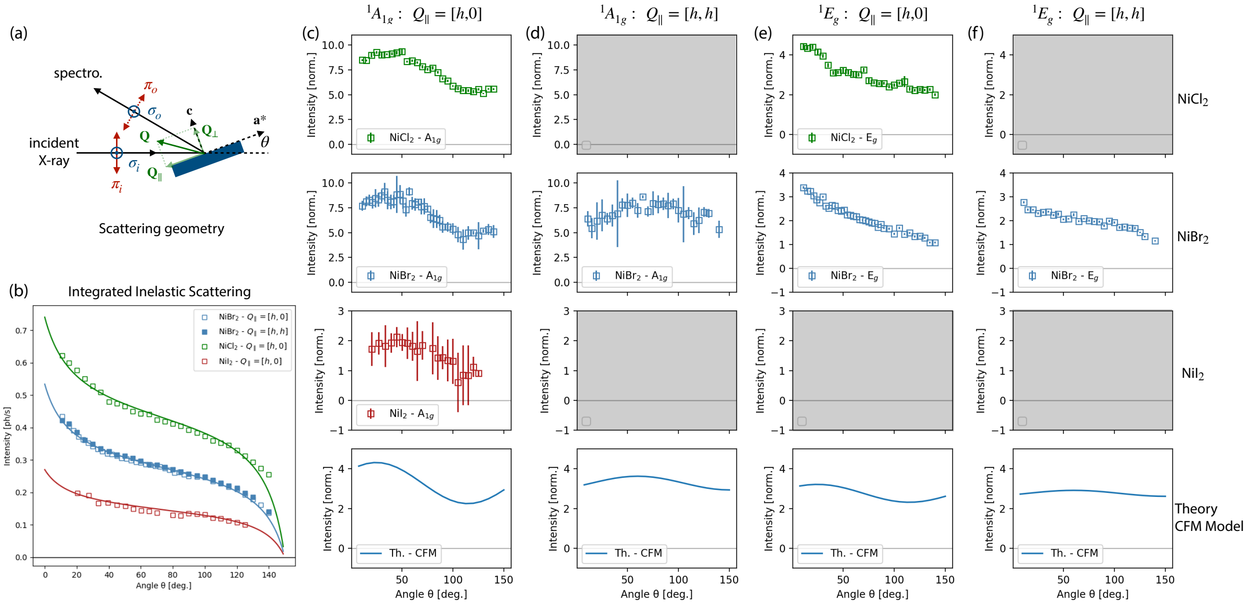

Figure 8.20: (a) Scattering geometry used for all experiments with scattering angle $2\theta = 150°$. (b), Total integrated inelastic weight ($\Delta E = 0.2 \rightarrow 3.0$ eV) normalized to the total counting time for each NiX$_2$ sample (squares) for all data at $T = 40$ K. Solid lines are fits to an effective self-absorption factor $C(\theta)$ without explicit consideration of the emission energy dependence (see text). (c-f) Angle-dependent intensity of the $^1A_{1g}$ and ^1E_g multiplets for each compound (where available, top to bottom: NiCl$_2$/NiBr$_2$/NiI$_2$) from fits shown in Figs. 8.9-8.12 above, after normalizing to the total integrated inelastic weight shown in panel (b). The bottom row of (c-f) are the intrinsic angular-dependencies as calculated within the CFM approximation for optimized parameters of NiBr$_2$ (see text) and with the experimentally utilized polarization states (incident σ polarization and unresolved emitted polarization). Note that all calculated intensity profiles can all be described with a functional form $\propto A\cos^2(\theta - \phi) + B$, consistent with the expected dipole transition selection rules (see text). All plots are reported versus angle θ with respect to the surface as defined in panel (a).

Effect of trigonal distortion

We show the effect of trigonally-distorted crystal field on the multiplet spectrum in the case of O_h symmetry optimized parameters for NiBr$_2$ in the CTM model in Fig. 8.21 below. We observe that the allowed CF terms when reducing symmetry from $O_h \rightarrow D_{3d}$ effect neither the ground state, the ^1E_g, nor the $^1A_{1g}$ fine structure. We note that the $^1A_{1g}$ is a spin and orbital singlet, and thus here is no degeneracy to break with lower symmetry. These results show that trigonal distortion does not induce additional fine structure splitting due to either ground state ($^3A_{2g}$) or excited state ($^1E_g - {}^1A_{1g}$) effects, and thus the observed dispersion of the ^1E_g and $^1A_{1g}$ peaks cannot be attributed to a cross section effect that modulates intensity between closely lying multiplet excitations in the RIXS profile. This is also corroborated by the satisfactory agreement between experiment and the intrinsic polarization dependence predicted in the cluster model, as discussed in the previous section.

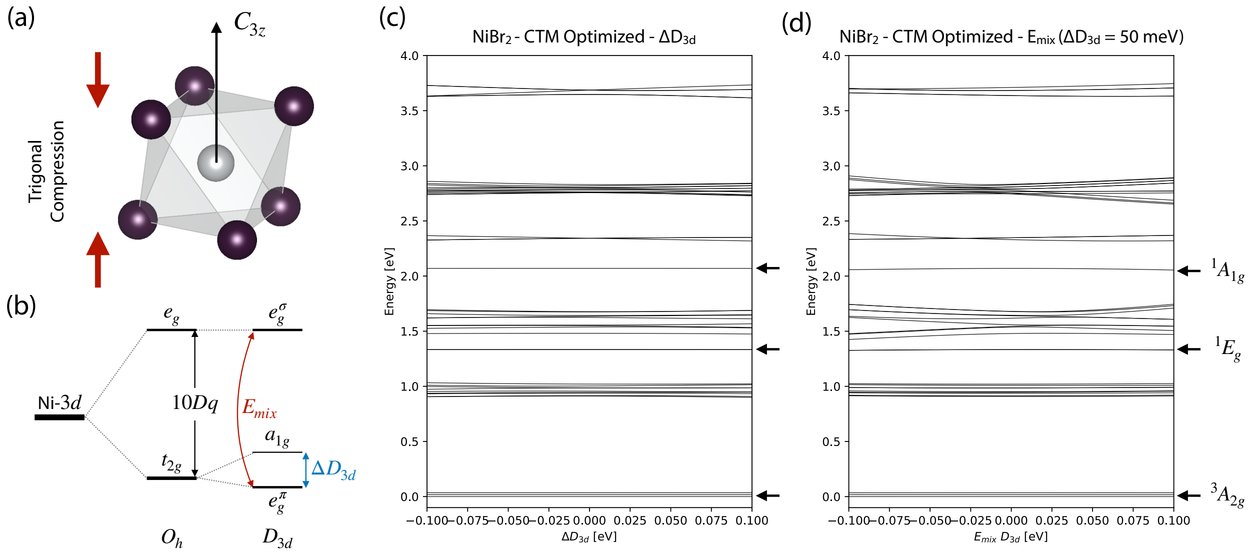

Figure 8.21: (a), Schematic of the local distorted NiX$_6$ octahedron in the nickel dihalides, indicating the three-fold rotation symmetry axis (C_{3z}) which is parallel to the crystallographic c-axis in the $R\bar{3}m$ space group structure of the NiX$_2$ compounds. The trigonal distortion corresponds to either compression or elongation along the C_{3z} axis. (b), Orbital energy diagram for different crystal fields, including O_h symmetry, with e_g-t_{2g} splitting $10Dq$, and the trigonal D_{3d} symmetry. Also indicated are the new CF parameters allowed in trigonal symmetry, including the intra-t_{2g} splitting ΔD_{3d} and a mixing between e_g^π and e_g^σ states (E_{mix}). Energy-level diagrams in the CTM model using optimized parameters for NiBr$_2$ (see text) and an effective spin exchange field of 20 meV, considering the effects on the multiplet states of (c), ΔD_{3d} and (d), E_{mix} parameters, with (d) calculated with a fixed $\Delta D_{3d} = 50$ meV. The ground state $^3A_{2g}$ and excited state $^1E_g/^1A_{1g}$ singlet multiplets are indicated with black arrows. While all other multiplets exhibit additional fine structure due to trigonal distortion, no fine structure in the multiplets of interest is introduced.

Chapter 9

Spontaneous orbital polarization in the nematic phase of FeSe

This chapter is adapted from the corresponding paper published in *Nature Materials* (Ref. [294]) with modifications and corrections.

This paper is a co-first author work between the present author (C.A.O.) and Joshua J. Sanchez. This project was conceptualized and initiated by C.A.O., J.J.S., Gilberto Fabbris, Yongseong Choi, Jong-Woo Kim and Philip J. Ryan. X-ray measurements were performed by C.A.O., J.J.S., G.F., Y.C. J.-W.K. and P.J.R. C.A.O. and J.J.S. prepared the samples and performed the optical birefringence experiments. Qian Song grew the FeSe crystals. Riccardo Comin supervised the project.

An extended introduction to the physics of iron-based superconductors can be found in Chapter 1.

9.1 Introduction

Symmetry-breaking phase transitions in strongly correlated electron systems are characterized by their structural and electronic (spin, charge, and orbital) degrees of freedom [15]. In electronically-ordered phases, these degrees of freedom become intertwined, making an experimental determination of the leading interaction challenging. One striking example of this complex interplay is nematicity, an electronically-driven rotational-symmetry breaking which is widely observed in iron-based superconductors [78]. While static nematic order is found to compete with superconductivity in iron pnictide materials such as Co-doped $BaFe_2As_2$ [78, 85, 86], it may actually help stabilize it in the chalcogenide FeSe [295]. Thus, understanding the origin of nematic order in each class is essential for understanding the nature of superconductivity [296]. Despite sustained efforts, a persistent question is whether nematicity is driven by the spin or orbital degree of freedom. The answer to this question has remained elusive largely due to the complexity of the microscopic relationship between these degrees of freedom and the nematicity-induced structural anisotropy.

The central difficulty in addressing the orbital degree of freedom arises from its close association with the lattice symmetry. This problem is important not just to nematicity in iron-based superconductors, but also to phenomena as diverse as Jahn-Teller distortions in transition-metal oxides [15, 297] and quadrupolar $4f$ ordering in heavy fermion materials [298, 299]. In this work, we introduce a general methodology to distinguish the orbital and lattice degrees of freedom by combining *in situ* tunable strain with x-ray linear dichroism (XLD) and x-ray diffraction (XRD), to directly probe the orbital polarization and strain state of the lattice, respectively. We use this methodology to provide the most direct evidence that orbital ordering drives the nematic transition in the iron-based superconductor FeSe.

FeSe displays a nematic transition at $T_s = 90$ K which results in a small lattice orthorhombicity and a large anisotropy in both orbital occupation and spin fluctuations, as demonstrated by many techniques [95–99, 101, 104, 106, 300–302]. While elastoresistivity measurements have identified an electronic driver for the nematic transition [93, 95, 102, 303, 304], this technique alone cannot uniquely identify the driving interaction [305, 306]. The primary role of the orbital degree of freedom in the nematic phase has been suggested by nuclear magnetic resonance (NMR) [99, 300] and angle-resolved photoemission spectroscopy (ARPES) [95, 104, 106, 301] measurements that reveal anisotropy between the Fe $|3d_{xz}\rangle$ and $|3d_{yz}\rangle$ orbitals. Meanwhile, nematicity in the iron pnictide materials is widely thought to result as a result of antiferromagnetic order [78], and spin-driven nematic fluctuations likely play a major role in the enhancement of superconductivity. However, this spin-nematic model for FeSe is fundamentally challenged by the absence of long-range antiferromagnetic order and by the preservation of nematic order while spin fluctuations are suppressed below the superconducting transition temperature [99, 101]. Intriguingly, these strong spin fluctuations may nonetheless be key to the enhancement of superconductivity while having only a minimal or subdominant role in the formation of nematic order [307].

The investigation of nematicity is further challenged by the presence of structural twin domains, which form below the nematic transition and cause bulk probes to average out the electronic anisotropy. Several recent works have used fixed applied strain to (partially or fully) detwin the nematic domains and probe the spin or orbital anisotropy [96, 98, 308]. However, a fixed strain methodology cannot assess the nature of the coupling between the lattice and electronic degrees of freedom, which is key for understanding what drives the system into a nematic state. Furthermore, any strain applied above the transition induces anisotropy when there is none in equilibrium, while within the ordered phase any excess strain applied beyond full detwinning will increase the anisotropy beyond the equilibrium value. Thus, it is necessary to observe the behavior of the electronic anisotropy as a function of both strain and temperature across the nematic transition [108, 309] in order to establish the microscopic relationship between these two degrees of freedom.

Here, we address this question using strain-dependent XLD at the Fe K pre-edge to probe the local orbital degree of freedom at the Fe site and determine the Fe $3d$ orbital polarization in the nematic state. We use *in situ* tunable applied stress to detwin the structural domains and apply further strain to the lattice. These XLD measurements, along with supporting XRD measurements to quantify the strain state, allow us to determine a robust relationship between the orbital and lattice degrees of freedom as a function of strain and temperature across the nematic phase boundary. A key result of this work is the observation of a saturating XLD signal beyond full detwinning in the nematic phase. This suggests a spontaneously-ordered orbital polarization that serves as a primary nematic order parameter, analogous to a saturating magnetization in a ferromagnet. Further, both the strain susceptibility of the orbital polarization (the orbital polarizability) and the simultaneously measured elastoresistivity diverge on approach to the transition from above, consistent with local nematic fluctuations driven by the orbital degree of freedom. While these measurements do not address the spin degree of freedom directly, the transport measurements reveal a secondary source of resistivity anisotropy which we attribute to inelastic scattering from anisotropic spin fluctuations, which is only activated below T_s and is enhanced with increasing orthorhombicity in a strain regime where the orbital polarization is saturated. These measurements thus isolate the critical role of the orbital-degree of freedom in the nematic phase of FeSe and evidence that nematicity is primarily driven by orbital order.

9.2 Results

9.2.1 XAS and XLD Spectra in Detwinned FeSe

We performed measurements on two samples from the same crystal growth batch. The crystals were cut into rectangular bars with edges parallel to the orthorhombic **a**/**b** directions. The samples were then mounted on a titanium support platform as described in Refs. [303, 310] and fit with transport leads in a four-wire geometry for determining the longitudinal resistivity ρ_{xx} along the applied stress direction (Fig. 9.1(b)). Uniaxial stress was applied to the platform with a Razorbill CS130 strain cell, with the nominal strain ϵ_{xx} determined by the capacitance strain gauge on the stress device (see Methods).

Sample 1 was initially cooled to $T = 25$ K under moderate tensile stress ($\epsilon_{xx} \simeq 0.1\%$) which partially detwins the structural domains that form below T_s. We define the structural A domain (B domain) as that with the longer **a** (shorter **b**) lattice constant aligned parallel to the stress axis (Fig. 9.1(a)). The inset to Figure 9.1(c) shows an XRD measurement of the (114) reflection, revealing a 75% detwinning state, in agreement with the predicted detwinning given the 0.23% orthorhombicity. Figure 9.1(c) shows the Fe K-edge X-ray absorption spectra (XAS), taken at normal incidence with incident linear polarizations LH/LV (parallel to $\vec{a}/\vec{b}$ in the tensionally detwinned state, respectively) and normalized to the main edge jump. The near-edge structure shows three features labeled as A/B/C consistent with previous studies [311–313]. We report the associated in-plane XLD spectrum in Figure 9.1(d), defined as the difference $I_{LV} - I_{LH}$.

The Fe K-edge resonance results from dipole-allowed transitions from Fe $1s$ to Fe $4p$ states, with admixed Fe $3d$ and Se $4p/4d$ orbital character due to hybridization. Feature

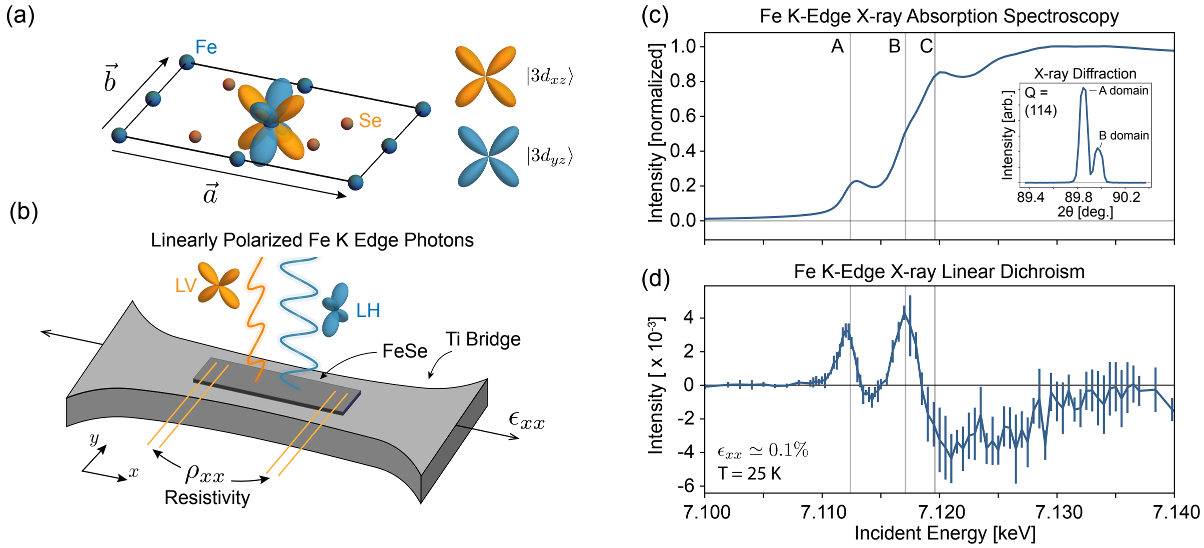

Figure 9.1: Strain apparatus and XLD spectroscopy in FeSe. (a), The orthorhombic unit cell of FeSe, defining the **a**/**b** orthorhombic axes and the orientation of the $|3d_{xz}\rangle/|3d_{yz}\rangle$ orbitals (A domain). (b), Schematic of the strain apparatus and sample, with polarization states (LH/LV) for normal incidence dichroism measurements. (c), Sample 1, the Fe K-edge XAS profile at $T = 25$ K under tension ($\epsilon_{xx} \simeq 0.1\%$). Inset: XRD of (114) reflection shows partial detwinning to the A domain. (d), The corresponding XLD spectrum with error bars determined from the standard deviation of repeated scans.

B is the usual main edge of this transition [311, 312]. Higher incident energies (peak C) are dominated by non-local effects including multiple scattering and encode Fe $4p$/Se $4d$ hybridization. Thus, feature C is sensitive to the Fe-Se bond length and long-range structural distortions [312, 313]. Lower incident energy favors increasingly local electronic states around the absorbing Fe atom [110, 314] and the pre-edge (peak A) coincides with the unoccupied Fe $3d$ density of states near the Fermi level. Due to the local tetrahedral symmetry, the $|3d_{xz}\rangle$ ($|3d_{yz}\rangle$) orbital exhibits strong on-site hybridization with $|4p_y\rangle$ ($|4p_x\rangle$) states [150, 315–317], giving access to $3d$ orbitals through dipole transitions at the pre-edge. In this picture, the positive pre-edge XLD in the tensionally detwinned state (Fig. 9.1(d)) corresponds to a more occupied $|3d_{yz}\rangle$ state (Fig. 9.1(a)), in agreement with the Γ-point occupation anisotropy seen in ARPES [104, 106, 308].

9.2.2 Spontaneous Orbital Polarization

We now discuss the simultaneously recorded XLD, XRD and elastoresistivity data collected at fixed strain values on a compressive-to-tensile strain sweep in Sample 1 at $T = 50$ K (see Methods). Figures 9.2(a)-(d) show the XLD spectra as a function of strain. The XLD at each XAS feature is strain tunable and reverses sign between compression and tension, consistent with the detwinning of nematic domains. The integrated XLD intensity of the pre-edge peak is plotted versus strain in Figure 9.2(d). The XLD increases rapidly before saturating at larger strain, with the saturation occurring near $\epsilon_{xx} \simeq 0.14\%$.

On the same strain loop, we used XRD to measure the strain response of the A domain $\vec{a}$ and $\vec{c}$ lattice constants from which we determine the unidirectional strains $\Delta a/a_0$ and $\Delta c/c_0$ shown in Figure 9.2(e)/(f). The lattice constants exhibit a weak response to small strain before changing rapidly at large tensile strain, indicating a detwinning strain of $\epsilon_{xx} \simeq 0.14\%$ denoted by red vertical lines in Figure 9.2. Thus, strains below the detwinning point act to reorient nematic domains with only a negligible effect on the lattice constants of an individual domain [318]. The crossover in the monodomain lattice response is also concomitant with a sign change in the slope of the simultaneously measured resistivity (Fig. 9.2(g)), discussed in more detail below.

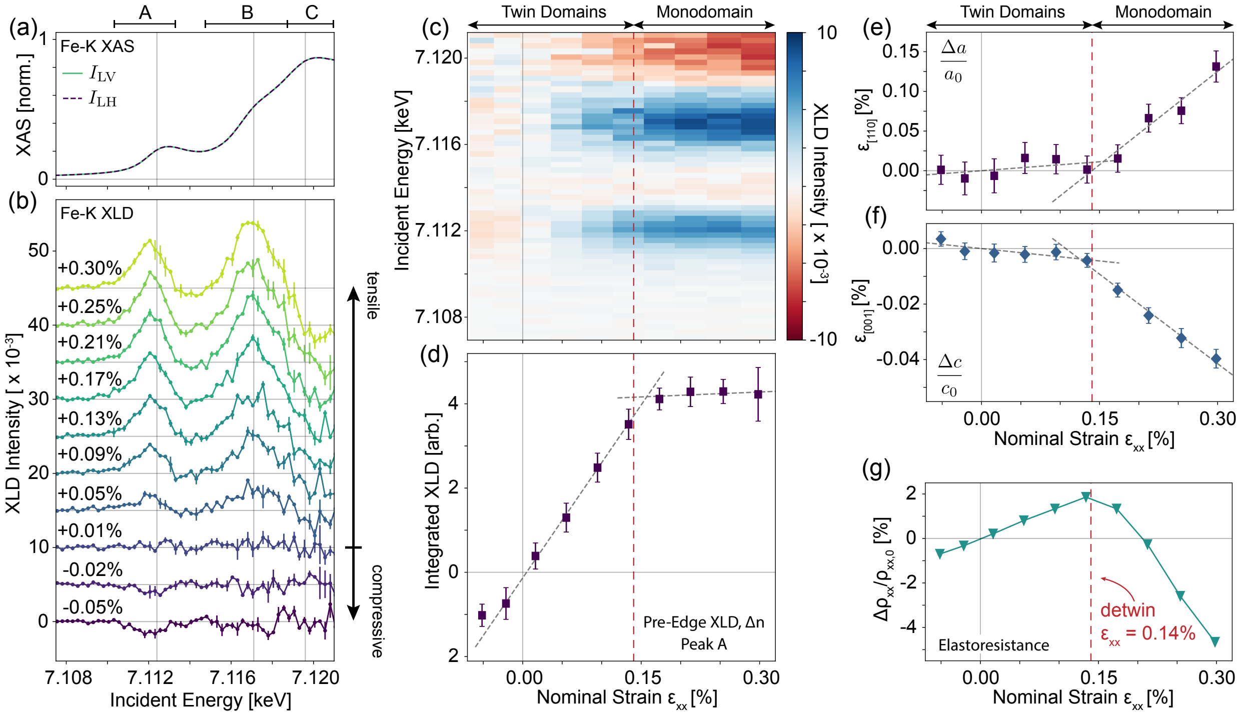

Figure 9.2: Strain-dependent X-ray measurements in the nematic phase. X-ray measurements versus strain on Sample 1 at $T = 50$ K. (a), The Fe K-edge XAS profile for polarizations LH $\parallel \vec{a}$ and LV $\parallel \vec{b}$, with the integration regions for the features A/B/C denoted. (b), In-plane XLD spectra as a function of increasing strain from -0.05% (bottom) to 0.30% (top). (c), Color map of the strain-dependent in-plane XLD spectra in (b). (d), The integrated XLD intensity of the pre-edge A (Δn) as a function of applied strain. XRD measurements of the (e), [110] (parallel to applied strain) and (f), the [001] (out-of-plane) lattice strains versus nominal linear strain ϵ_{xx}. Error bars represent the standard error from Gaussian fits to XRD peaks. (g), Elastoresistance measurements recorded simultaneously with XLD and XRD data, showing a sign-reversal at the detwinning point, $\epsilon_{xx} \simeq 0.14\%$, denoted by vertical red lines in panels (c)-(g). All measurements reported in (a)-(g) are taken at identical strain conditions.

We thus find that the saturation of the pre-edge XLD coincides with the full detwinning of the sample. In contrast, the higher energy XLD features continue to increase with tension past the detwinning point (Fig. 9.2(b)/(c)). This suggests that the higher energy XLD features probe the net lattice anisotropy between the $\hat{x}$ and $\hat{y}$ directions which changes both with detwinning and with strain-enhanced orthorhombicity. Indeed, the structural contributions to the XLD are linear in the orthorhombicity and well-captured by multiple scattering calculations [319]. From these considerations, we conclude that the saturating pre-edge XLD signature (with integrated value Δn) corresponds to a lattice-independent, spontaneous polarization of Fe $3d$ orbitals which is only weakly coupled to further structural distortion.

To further associate the orbital polarization with the emergence of nematicity, we performed XLD measurements on Sample 2 as a function of strain and at fixed temperatures above and below the nematic transition. We plot Δn versus strain in Figure 9.3(c)/(d). At a given tensile strain value, Δn clearly increases with decreasing temperature, while at a given temperature the susceptibility is maximum near zero strain. Using a combination of XRD and optical birefringence measurements, we identify the approximate detwinning strain point at each temperature below T_s, which coincides with the inflection point of Δn. These data indicate an orbital polarization that develops with decreasing temperature below T_s with a diminishing strain-susceptibility beyond full detwinning.

Finally, we characterized the orbital polarizability above the nematic transition in Sample 1. To do so, we measured the temperature dependence of Δn at a moderate fixed tensile strain of $\epsilon_{xx} \simeq 0.2\%$ (Figure 9.4(a)). The constant linear strain state is confirmed by XRD measurements and a fixed orthorhombicity is suggested by the constancy of peak C in the XLD spectrum between 120 K and 90 K, which encodes the structural orthorhombicity. Over this same temperature range, the peak A XLD (Δn) increases strongly (over a factor of 2) before saturating for $T < T_s$. This is quantified with a Curie-Weiss analysis for $T > T_s$, revealing a Curie temperature $T^* = 62.5 \pm 5$ K (Figure 9.4(a)), thus identifying a divergence of Δn as T_s is approached from above. Since this divergence occurs under fixed lattice conditions, we understand Δn as originating from a strain alignment of diverging orbital-origin nematic fluctuations and not as a secondary orbital response to the lattice distortion. Below T_s, the XLD signal appears to be nearly saturated. This is due to both domain detwinning and additional strain-induced orbital polarization. These results demonstrate that a fixed-strain methodology cannot accurately distinguish the equilibrium order parameter from the diverging strain-susceptibility of induced order above T_s. Such measurements instead require a fixed-temperature variable-strain approach as in Figs. 9.2/9.3.

The combined strain- and temperature-dependence reveals two distinct pieces of evidence regarding the nature of the measured orbital polarization. On one hand, the strain-dependent curves as a function of temperature directly show that a lattice-independent orbital polarization emerges in the nematic phase (Fig. 9.3(e) top). At the same time, the strain-susceptibility of the orbital polarization shows a divergence under fixed strain conditions above T_s (Fig. 9.3(e) bottom). This behavior is reminiscent of the magnetization across a para- to ferromagnetic transition, with the magnetic field being replaced by an anti-symmetric strain as the poling field. This identifies the orbital polarization with the primary order parameter of the nematic phase. Therefore, the effect of strain far below the transition is only to reorient 'nematic moments' that are fixed in magnitude and orientationally locked to the underlying structure. Evidence for such a scenario is supported by X-ray pair distribution function experiments [320], which associate local nematic moments with a short-range ordered orbital degeneracy lifting that persists far above the nematic transition, consistent with the temperature- and strain-dependence above T_s in our experiments.

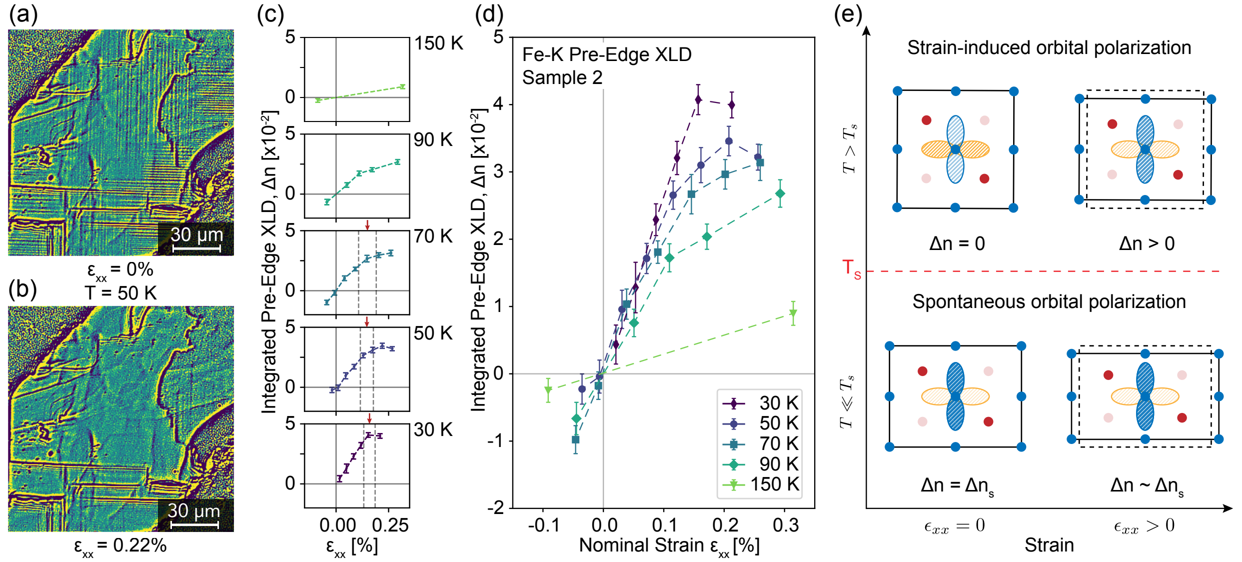

Figure 9.3: Spontaneous orbital polarization across the nematic transition. Optical birefringence images of the nematic domains at $T = 50$ K on Sample 2 at (a), $\epsilon_{xx} = 0\%$ and (b), $\epsilon_{xx} = 0.22\%$ strain showing the full detwinning. Scale bars are 30 μm. (c), Temperature and strain-dependent pre-edge XLD (Δn) across the nematic transition in Sample 2. For $T < T_s$, the approximate detwinning points are indicated by red arrows, determined from independent XRD and optical birefringence measurements. Vertical dashed grey lines indicate the range of uncertainty in the detwinning point. (d), The same data in (c) plotted together to highlight the temperature- and strain-dependence. XLD error bars are as defined in Figs. 9.1/9.2. (e), Above the nematic transition ($T > T_s$, top), the orbital polarization is only nonzero with applied strain. Far below the nematic transition ($T \ll T_s$, bottom), the orbital polarization is nonzero in equilibrium, fully saturated, and is unchanged with applied strain beyond full detwinning, indicating it is not driven by the lattice distortion.

9.2.3 Signatures of Orthorhombicity-Coupled Spin Fluctuations

These conclusions are further supported by simultaneous elastoresistivity measurements, which reveal a close correspondence between the orbital polarization and the resistivity anisotropy above T_s that breaks down within the nematic phase. In Figure 9.4(b), we show the temperature-dependent elastoresistance collected simultaneously with the fixed-strain

XLD measurements (Fig. 9.4(a)). Above T_s, the resistivity anisotropy ($\Delta\rho/\rho_0$) diverges with a Curie-Weiss temperature dependence to $T^* \simeq 61.4 \pm 3.1$ K, consistent with previous elastoresistivity measurements [303, 321] and in close correspondence to the Curie temperature of Δn ($T^* = 62.5 \pm 5$ K). Below T_s, Δn saturates while $\Delta\rho/\rho_0$ decreases rapidly, implying a breakdown in the correspondence between the orbital and transport anisotropies.

This is highlighted in more detail in Figure 9.4(c), where we plot $\Delta\rho/\rho_0$ vs Δn from Fig. 9.2(d)/(g) for Sample 1 at $T = 50$ K. Here, the resistivity increases linearly with the orbital polarization up to the detwinning point, beyond which it decreases rapidly with increasing strain even while the XLD remains saturated. Equivalent data in Sample 2 show the same orbital-transport linearity up to full detwinning, with a strongly temperature-dependent proportionality. In Figure 9.4(c) we plot the slope of $\Delta\rho/\rho_0$ vs Δn from both samples across temperature and phase, for both fixed-strain temperature sweeps and fixed-temperature strain sweeps within the detwinning strain regime. We find a positive and weakly-temperature dependent orbital-transport proportionality above T_s which rapidly diminishes below the transition, with a sign change near $T = 40$ K. Taken together, these results suggest a second source of elastoresistivity which only becomes dominant below T_s and at strains beyond full detwinning.

The elastoresistivity encodes information from several distinct but intertwined contributions. Namely, the orbital polarization primarily creates anisotropy in the Drude weight, while spin fluctuations primarily create anisotropy in the scattering rate [93, 107, 305, 306, 322, 323]. Thus, orbital and spin contributions to the elastoresistivity can in principle behave independently. Our simultaneous XLD and transport measurements enable us to show that the resistivity has a component which closely corresponds to the orbital polarization, both above T_s and within the detwinning strain regime below T_s. We propose that the second component of the elastoresistivity originates from spin scattering. FeSe exhibits the same stripe-type spin fluctuations as found in iron pnictide materials [96–99, 300], which are thought to drive the large negative elastoresistivity in the latter. In the non-magnetically ordered nematic phase of FeSe, a strain-enhanced orthorhombicity is expected to enhance the anisotropy of the spin fluctuations [304, 324] and their effect on transport anisotropy [309, 322], reflecting the propensity of the system to undergo a putative stripe-type magnetic transition. This then can explain both the decreasing magnitude of the elastoresistivity below T_s as well as the distinct proportionality in the detwinning and post-detwinning strain regimes. A strain-transport study of FeSe using a more direct probe of spin fluctuations with a tunable strain state would be needed to confirm this scenario.

9.3 Discussion

Due to the intertwined nature of spin and orbital degrees of freedom, two general routes have been invoked to explain the nematicity in FeSe. In the spin-nematic picture, divergent orbital-selective spin fluctuations drive the nematic ordering and consequently induce

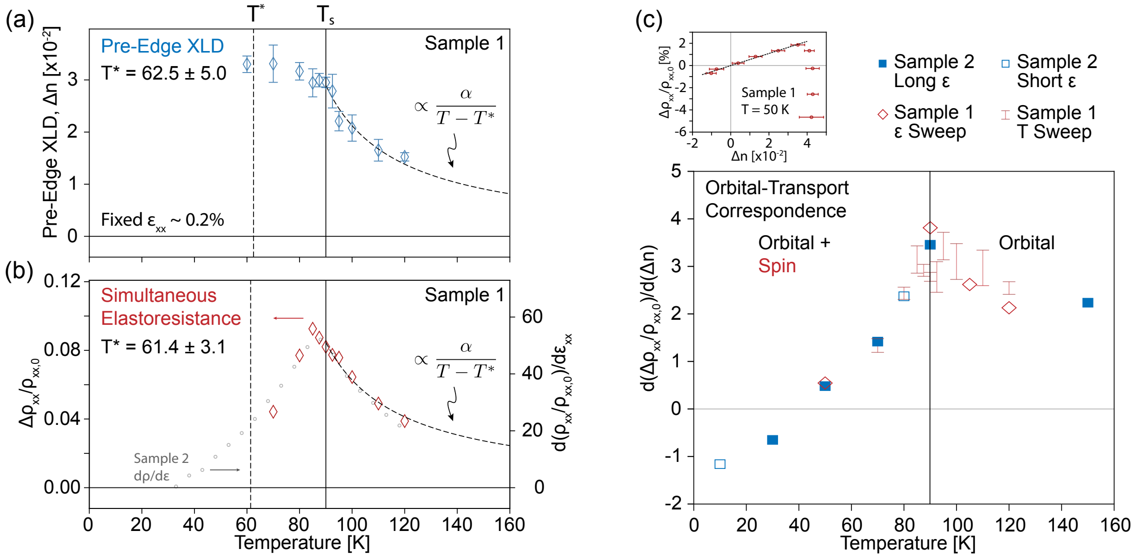

Figure 9.4: Divergent orbital polarizability and correspondence between orbital and transport anisotropy. (a), Δn and (b), the simultaneous elastoresistance (red diamonds, left axis) versus temperature across T_s at a fixed $\epsilon_{xx} \simeq 0.2\%$ for Sample 1. Dashed curves are Curie Weiss fits to the data at $T \geq T_s = 90$ K, indicating CW temperatures of $T^* \simeq 62.5 \pm 5$ K and 61.4 ± 3 K, respectively. Also shown in (b) is the longitudinal elastoresistivity coefficient about zero strain in Sample 2 (grey circles, right axis) for comparison. (c), Ratio of the normalized resistivity to the pre-edge XLD versus temperature, taken from the slope of the linear fit of normalized resistivity at $T = 50$ K from (c) (inset), additional temperatures in Sample 1 (red diamonds), equivalent data from Sample 2 (from Fig. 9.3(c), blue squares), and from the fixed-strain temperature sweep in Sample 1 (Fig. 9.4(a)/(b)) (red bars). Inset: Normalized resistivity versus XLD in Sample 1 at $T = 50$ K using data from Fig. 9.2(d)/(g). Error bars in (a)/(c) are determined from the statistical errors of the XLD signal, and are the size of the data point where not indicated.

a splitting between $|3d_{xz}\rangle$ and $|3d_{yz}\rangle$ bands. Our observation of (i) a large nematic-phase spontaneous orbital polarization, (ii) its divergence behavior above T_s and (iii) the direct correspondence between the orbital polarization and the transport anisotropy above T_s overall suggests that nematicity is instead driven by orbital order.

In this case, the increasing Fermi surface anisotropy below T_s enhances strongly anisotropic spin fluctuations (as evidenced by elastoresistivity) which can themselves act as a mechanism for further momentum-dependent evolution of the Fermi surface [105–107]. The change of the Fermi surface topology and orbital content at the hole and electron pockets observed by ARPES [104, 106], the associated suppression of B_{1g} charge fluctuations in Raman [302, 325], the increase of the spin-relaxation rate in NMR [99], the abrupt sign-change in the Hall coefficient [103, 304], and the unusual sign-changing elastoresistivity [95, 102, 304], all manifesting only *below* T_s, may be the clearest signs of this effect. This sequence of events, where orbital-dependent spin fluctuations are triggered below T_s by the onset of nematicity driven by spontaneous orbital order may reconcile the apparently disparate conclusions reached by previous studies and is consistent with our experimental observations. Indeed, inelastic neutron scattering has shown that the spin frustration between Néel order (with C_4 rotational symmetry) and stripe-type order (with C_2 rotational symmetry) is partially lifted by the nematic transition and its accompanying orthorhombic structural distortion [326]. Thus, our proposed notion of orthorhombicity-stabilized spin fluctuations is consistent with the available experimental evidence from more direct probes of the spin degrees of freedom [96–98, 326]. However, additional data utilizing the tunable strain methodology introduced here is required to fully assess how spin fluctuations modulate the properties of the orbital nematic state.

Finally, several observations stand as key indicators that nematicity and superconductivity are driven by distinct degrees of freedom in FeSe. Below the onset of superconductivity, spin fluctuations are diminished for both Co-doped $BaFe_2As_2$ [86] and FeSe [97, 99], but the orthorhombicity is only suppressed for the former [85] while being apparently unaffected in the latter [101]. In addition, optimal superconductivity is not found in the vicinity of the nematic quantum critical point in FeSe under hydrostatic pressure [327] or S-doping [102, 307], in clear contrast to the observation of iron pnictides. This may be naturally understood in our interpretation of orbital nematicity, as this regime of the phase diagram does not then correspond to the critical spin fluctuations thought to drive the unconventional pairing in the pnictides [78]. Instead, the presence of an orbital nematic state may affect other aspects of superconductivity in FeSe, including the anisotropy of the superconducting gap and the orbital dependence of the pairing mechanism [295, 328]. These results disentangle spin fluctuations from nematicity in FeSe, and thus allow a refocusing towards the more relevant part of phase diagram for optimizing chalcogenide superconductivity.

9.4 Methods

Sample preparation

Single crystals of FeSe with typical dimensions of 2.0 x 2.0 x 0.05 mm were grown using the KCl-ACl_3 flux method as described in Ref. [97]. The resulting samples were cut with a $\lambda = 1064$ nm laser cutter (spot size of 10 μm) into rectangular bars with dimensions of 1.0 x 0.15 mm with the long axis along the tetragonal [110] (orthorhombic $\vec{a}$) direction. The samples were then mounted onto pre-fabricated Titanium platforms (following the specifications outlined in Refs. [303] and [310]) using Stycast 2850LT epoxy, cured at 80° C for 12 hours. After the epoxy was cured, the sample surface was cleaved several times to reduce the thickness to $\simeq 25$ μm and 25 μm gold wires were affixed near the ends of the long axis of the sample in a four-wire geometry using Epotex H20E silver epoxy. The silver epoxy was cured in a nitrogen-filled glovebox at 120° C for 15 minutes for Sample 2 and at 80° C in ambient conditions for 2 hours for Sample 1. The Ti platform with the wired FeSe bars was then fastened to a Razorbill CS130 strain cell.

XAS, XLD and XRD Measurements

X-Ray absorption and diffraction measurements were performed at the 4-ID-D endstation of the Advanced Photon Source, Argonne National Laboratory. The strain cell was mounted into an Advanced Research Systems Displex closed-cycled cryostat with a base temperature $T \simeq 10$ K. The cryostat was mounted in a 6-circle diffractometer to allow sample manipulation for XRD, as well as precise alignment of the incident beam to the surface normal of the sample for in-plane XLD measurements. XAS spectra were recorded in partial fluorescence yield at the Fe-Kα emission line in a quasi-backscattering geometry with a Hitachi Vortex detector. The incident energy was varied across the Fe K-edge resonance, and at each incident energy the polarization was rapidly switched between linear polarization states using diamond phase plates in the sequence LV/LH/LH/LV in order to determine the linear dichroism spectrum with high signal-to-noise ratio.

All reported XAS spectra were normalized to the main edge jump using reference XAS/XLD spectra acquired up to 7.140 keV. The reported XLD is calculated as the direct difference of the normalized XAS spectra at different polarizations. For the high-statistics near-edge XLD spectra used for Figure 9.2 and Figure 9.3, 2-3 spectra were acquired back to back and averaged, in the energy range of 7.107 - 7.121 keV with a step size of 250 meV. The standard deviation of these subsequent scans is used for the error bars of the XLD data. XRD measurements were performed with an incidence energy above the Fe K-edge resonance, with an energy of 7.200 keV and 7.400 keV for Sample 1 and Sample 2, respectively. The X-ray measurements are performed with a beam size of 50×50 μm^2 and are bulk sensitive, and thus average over multiple twin domains when present [93] (Fig. 9.3(a)/(b)).

Strain-Temperature Sweep Procedures

All data reported were taken by sweeping the voltage of the piezo stacks of the strain device continuously from maximum compression to maximum tension. Before changing temperature, the voltage on the piezo stacks was fixed to zero. This ensured a consistent nominal zero-strain capacitance reading throughout the experiment. Once at target temperature, the sample would be initialized by moving to maximum tension and back to maximum compression before initializing the sweep. This consistent initialization procedure accounts for any effects of detwinning hysteresis or hysteretic effects of the piezo-actuators/Ti bridge, ensuring consistent and comparable strain-dependent measurements throughout the experiment.

For the strain sweep data in Figure 9.2, the sample was initialized with the above procedure at $T = 50$ K and strain was increased monotonically from maximum compression to tension. At each strain point, XAS/XLD spectra at normal incidence and XRD measurements of the (114) and (004) were performed at an identical strain condition before moving to the next increased tensile strain point. The resistivity values were stable at fixed strains and the reported resistance values were averaged over the duration of corresponding XLD measurements.

For the XLD temperature dependence recorded in Sample 2 (Fig. 9.3), the measurements were completed from the same, single cooldown of the cryostat, starting at low temperature (10 K) and increasing monotonically to the highest measured temperature (150 K). Reported resistance measurements were again averaged over the duration of the XLD measurements, and thus the reported quantities are under identical strain conditions. XRD measurements were also performed in Sample 2. These were performed on subsequent strain loops at the same temperature conditions, immediately after the XLD/resistance strain loops. The sample was consistently initialized, and separate strain sweeps following the same compressive-to-tensile strain loop as the XLD measurements were repeated for separate measurements of the (114) and (004) reflections.

Determination of Nominal Strain

All reported data are plotted versus nominal linear strain ϵ_{xx}. For XLD measurements, the nominal zero-strain was determined by the capacitance readout of the strain cell gap corresponding to the interpolated value for zero XLD signal, signaling a fully twinned sample below T_S, or an unstrained tetragonal phase above. Since XLD is bulk sensitive, this provides the most consistent measure of the true zero strain value. The conversion of the change in the strain cell gap distance with respect to this zero, monitored by change in the capacitance across the gap, was determined by strain transmission data at $T = 90$ K of the [110] lattice parameter, calculated from the combined XRD of the (114) and (004) reflections. The temperature $T = 90$ K was chosen for strain transmission data since the lack of orthorhombic domains results in a linear strain transmission, as opposed to the highly non-linear effects observed within the nematic phase (Fig. 9.2(e)/(f)) due to details of the detwinning process.

Optical Birefringence Measurements

Optical birefringence and additional elastoresistivity data were acquired on Sample 2 with identical sample preparation conditions. Polarized images were acquired using a monochrome camera with a broadband LED light source which was passed through a $\lambda = 600$ nm long-pass filter (ThorLabs) in order to increase the birefringence contrast [93]. The incident light was polarized with a broadband Glan-Thompson polarizer (ThorLabs) along the tetragonal [100] direction. To resolve the birefringence-induced polarization rotation, another Glan-Thompson polarizer was placed before the camera and detuned by $\simeq 1^\circ$ from the cross-polarized configuration (with respect to the polarizer) in order to optimize the birefringent domain contrast. The images were recorded using both 20x and 50x objectives (Olympus).

9.5 Additional Data and Discussion

Characterization of XLD Signal

Here we provide additional XLD data to corroborate our measurement of XLD purely within the Fe-Fe rectangular lattice plane. FeSe is tetragonal above the nematic phase, and thus at all temperatures possesses a large structural anisotropy between the out-of-plane direction (**c** axis) and the **a**-**b** plane. We report measurements assessing this effect in Figure 9.5, acquired on Sample 1 at $T = 25$ K. In order to measure the out-of-plane component, we rotated the sample about the $\vec{a}$ axis so that the incoming beam makes an angle of $\theta = 50^\circ$ with respect to the surface normal of the sample. In this geometry, LV polarization acquires a finite projection along the $\vec{c}$ axis while LH polarization remains oriented along $\vec{a}$. The resulting XLD spectrum ("out-of-plane" XLD), is shown in Figure 9.5(b), showing a large dichroism of the order 10^{-1} which is visually inferred from the direct XAS profiles in LH/LV polarizations in Fig. 9.5(a). For comparison, we also show the normal incidence XLD spectrum in a partially detwinned sample with LV/LH parallel to $\vec{b}/\vec{a}$ orthorhombic (Fe-Fe direction) axes, respectively ("in-plane" XLD spectrum).

While the in-plane XLD is over an order of magnitude weaker, the spectral shape is distinct from the out-of-plane XLD corroborating a distinct origin, ruling out any small misorientation of the sample and parasitic contributions from the out-of-plane spectrum into the in-plane XLD spectra reported here. In the case of our measurement, the surface normal was aligned to the incoming wavevector to an accuracy exceeding 1°, using a diffractometer and the experimentally determined orientation matrix of the sample. XRD was also used to accurately align the orthorhombic axes to lie parallel to LV/LH polarizations for the in-plane XLD measurements.

We also acquired in-plane XLD spectra in the fully detwinned state of Sample 1 at $T = 50$ K in two sample orientations to associate the measured XLD spectra to an intrinsic response of the sample. We first acquired XLD spectra at an angle $\phi = 0^\circ$ corresponding to LV $\parallel \vec{b}$ and LH $\parallel \vec{a}$, and then rotated the sample to $\phi = 90^\circ$ in a plane perpendicular to the incoming beam, with the second state corresponding to LV $\parallel \vec{a}$ and LH $\parallel \vec{b}$. The measurement procedures and the strain state of the sample were held under identical conditions. The two spectra are shown in Fig. 9.6. The two spectra are reversed in sign with respect to each other and quantitatively similar in magnitude and spectral shape. The results of Fig. 9.5 and 9.6 confirm that the in-plane XLD is genuine and is not resulting from an extrinsic effect related to misorientation or normalization errors in the incoming polarization states. For the strain-dependent curves in Fig. 9.2(b), this also confirms there is not any constant offset from the instrumentation in a fixed geometry as was done for all reported data unless explicitly specified. For the XLD reported in Fig. 9.2(a)-(d), we also show the strain-dependence of the XLD spectra resolved into the individual spectral features A/B/C in Fig. 9.7.

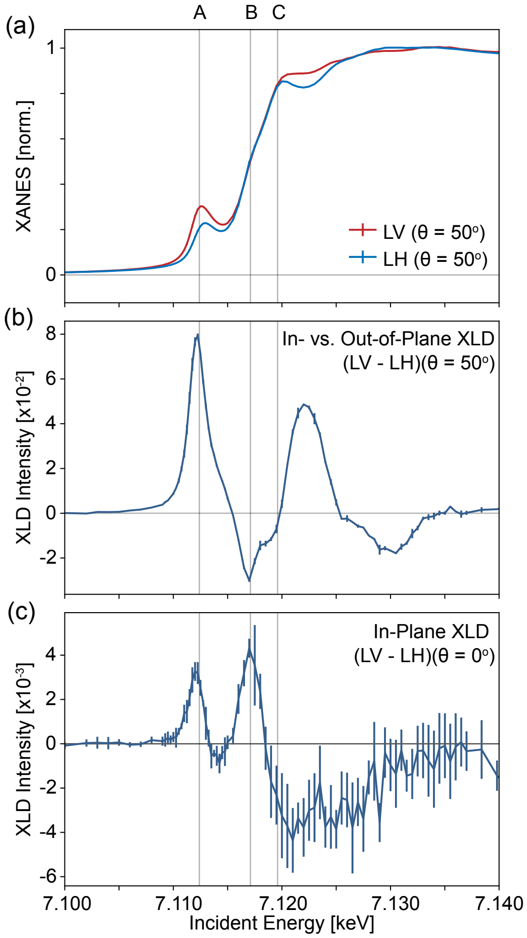

Figure 9.5: A comparison of the pure in-plane and the out-of-plane linear dichroism spectra. (a) XAS spectra in LH/LV polarizations with the beam incident at an angle $\theta = 50°$ with respect to the surface normal within the $\vec{b}$-$\vec{c}$ plane (see text). (b) The out-of-plane XLD spectrum corresponding to the polarized XAS spectra in (a), compared to (c), the pure in-plane XLD spectrum with LV $\parallel \vec{b}$ and LH $\parallel \vec{a}$ with the beam at normal incidence along the $\vec{c}$ crystallographic direction. Note: the out-of-plane XLD spectrum is expressed in units of 10^{-2} while the in-plane are expressed in units of 10^{-3}.

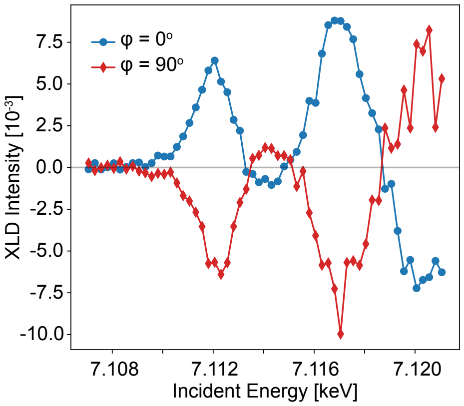

Figure 9.6: In-plane XLD signal at normal incidence of the fully-detwinned Sample 1 at $T = 50$ K for two different sample orientations rotated around the $\vec{c}$ axis by a relative angle ϕ of 90 degrees. $\phi = 0°$ corresponds to LV/LH parallel to $\vec{b}/\vec{a}$, respectively, and vice versa for $\phi = 90°$.

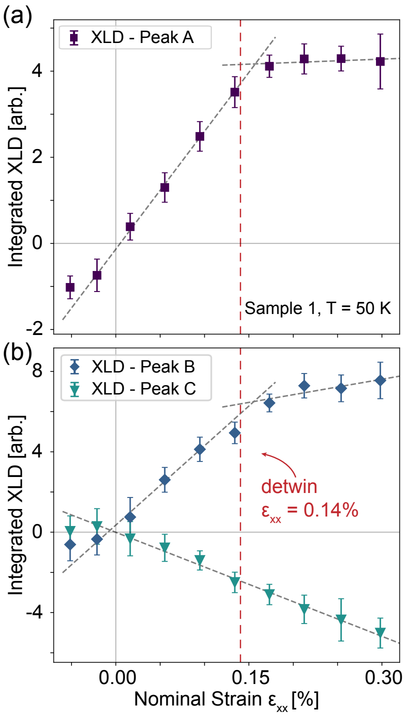

Figure 9.7: Strain-dependent XLD signal from Sample 1 at $T = 50$ K resolved into the individual XAS features A/B/C. (a), The pre-edge signal saturates for strains larger than the detwinning strain, indicated by the dashed vertical red line at $\epsilon_{xx} \simeq 0.14\%$. (c), The higher energy peaks show increasing XLD signal past the detwinning point, with peak C XLD being nearly linear across the whole strain range, while peak B shows a slope change at the detwinning point, but without complete saturation as observed at the pre-edge.

FDMNES Calculations

FDMNES calculations were performed using the experimentally determined lattice parameters at base temperature ($a = 5.331$ Å, $b = 5.305$ Å, $c = 5.485$ Å) using the $Cmma$ space group for orthorhombic FeSe [329]. The Se atomic height of $z = 0.2673$ was used. The Fermi level was set self-consistently and the convergence with respect to cluster radius was checked up to 12 Å within the Muffin Tin approximation. Only small changes were found above 7 Å cluster radius in both the simulated XLD and XAS. For the reported calculations, a cluster radius of 7.3 Å was chosen in order to include the full shell of 11^{th} nearest neighbor Fe atoms. This value is consistent with previous reports for FDMNES calculations in Fe-based superconductors [330]. Unless explicitly specified, both quadrupole and dipole transition intensities are included in the calculations.

We compare the polarized XAS and XLD spectra output from FDMNES to the experimental data in Figure 9.8. For comparison to the experimental data, the Fermi level was set to an edge energy of $E = 7.1124$ keV and the energy axes of the calculations were stretched by 15%, as argued in Ref. [311]. A satisfactory agreement is found for the XAS spectra, as well as the overall spectral shape and magnitude of both the in-plane and out-of-plane XLD spectra. The experimental data and the calculated curves are both normalized to the main edge jump using the same procedure. The in-plane experimental data in Fig. 9.8(b) corresponds to Sample 1 at $T = 50$ K and is in the fully detwinned state, while the out-of-plane data in Fig. 9.8(d) is from Sample 1 at $T = 25$ K. The out-of-plane XLD spectrum is purely structural in origin and is well-captured by the calculations, resulting from the large anisotropy determined from the high-temperature tetragonal structure. The XLD magnitude is slightly overestimated by the calculation. The expected structural contributions at higher energy features (peak B/C) for the in-plane XLD are also well reproduced, although again overestimated compared to experiment. For the pre-edge peak A, the spectral shape is not captured well, and the overall intensity is far underestimated. We note that without the introduction of electronic correlations, the disagreement could be due to an improper treatment of the $3d$ orbitals by a single-particle code such as FDMNES [311]; however, general agreement has been found between multiple scattering codes and the more strongly correlated $L_{2,3}$ XAS spectra in Fe-based superconductors [319, 331, 332]. This suggests a non-structural mechanism that is not captured by the FDMNES calculations to explain the pre-edge XLD spectrum, which is attributed to properties of the localized orbitals derived from Fe $3d$, Se $4p$ and an admixed Fe $4p$ character, as has been recently suggested [315].

To support this further, we investigate the origin of the pre-edge peak in more detail. Figure 9.9 shows the same calculation of the in-plane XLD, but resolved into the dipolar transitions ($1s \rightarrow 4p$) and the quadrupolar transitions ($1s \rightarrow 3d$). The quadrupolar matrix elements are calculated for wavevector $\mathbf{k_i} \parallel \mathbf{c}$ as in the normal incidence measurements for the in-plane XLD configuration executed experimentally. The quadrupole transition intensity is largest at the pre-edge, which may be anticipated as this corresponds to the region of the unoccupied Fe $3d$ states just above the Fermi level. However, even at the pre-edge, the direct quadrupolar transition is approximately a factor of 40 weaker than the dipole contribution in both the XAS and XLD spectra. Thus, the signal measured in experiment is almost purely dipole in origin as has been concluded previously for the Fe K pre-edge [311–313, 316, 330, 333]. The increase in the dipolar intensity is due to the both local tetrahedral environment and hybridization with the ligand Se $4p$ states. In the tetrahedral crystal field, a local on-site mixing of the Fe $4p$ orbitals with the Fe $3d$ states becomes allowed (discussed more below). This corresponds to an orbital localization effect as suggested in Ref. [315] and is supported by both experiments [312, 316] and Wannier projection of the $3d$ orbitals [317].

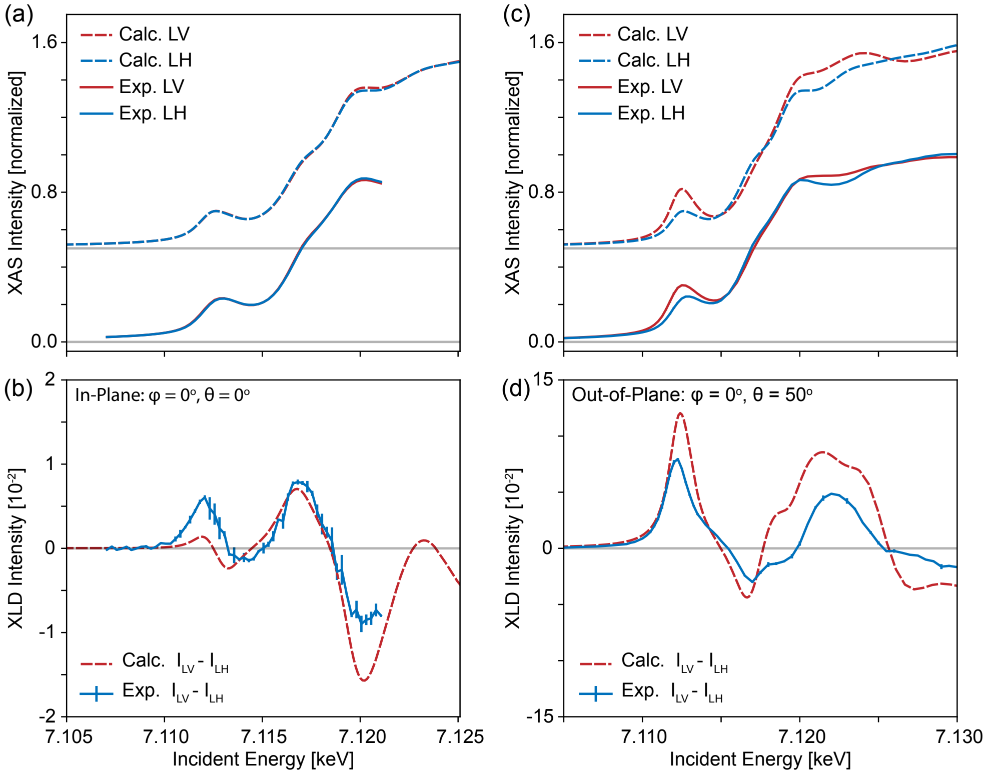

Figure 9.8: FDMNES calculations of Fe K-edge polarized XAS in FeSe. (a), XAS and (b), XLD for the in-plane configuration with $\phi = 0°$ and $\theta = 0°$ as described in Fig. 9.5. (c), XAS and (d), XLD in the out-of-plane configuration with $\phi = 0°$ and $\theta = 50°$. In all panels, dashed lines correspond to calculations and solid lines are experimental data in Sample 1. The in-plane data is the fully detwinned data at $T = 50$ K from Figure 9.2(b). The out-of-plane data is at $T = 25$ K reproduced from Figure 9.5. Curves in (a)/(c) are offset for clarity.

As a final check, we performed calculations as a function of the structural orthorhombicity δ. In experiment, the orthorhombicity at base temperature is approximately $\delta = 0.24\%$. The in-plane XLD spectra for several δ are shown in Figure 9.10. As can be seen, the predicted structural XLD is linear in δ at each XAS spectral feature. This is in contrast with the behavior of the pre-edge found in experiment, both from the strain dependence (Figures

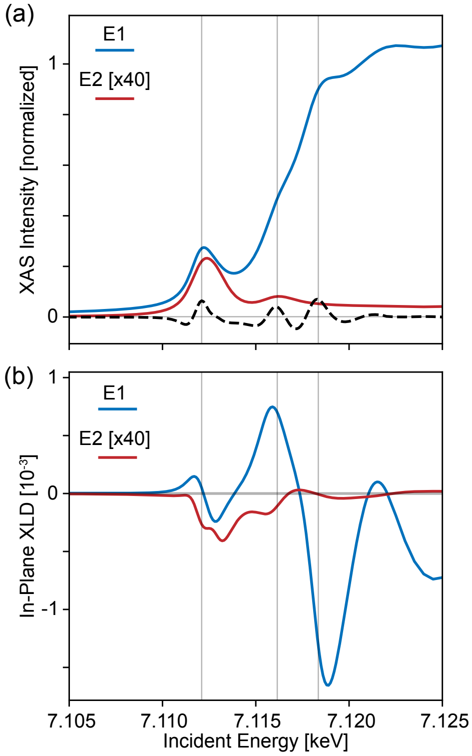

Figure 9.9: Calculations comparing the transition weights corresponding to dipolar (E1, $1s \rightarrow 4p$) and quadrupolar (E2, $1s \rightarrow 3d$) transitions. (a), XAS and (b), XLD for the in-plane configuration resolved into the dipole (purple) and quadrupolar (green) contributions. In both cases, the quadrupolar is multiplied by a factor of 40 for clarity. The dashed line in (a) is the second derivative for identifying the features A/B/C.

9.2/9.5) and the temperature dependence (Figures 9.3/9.4). As a function of strain below T_s, only the higher energy features continue to increase beyond the detwinning point as the structural anisotropy is increased beyond the equilibrium value. Furthermore, when lattice orthorhombicity is externally imposed by strain above T_s, the relative ratio of the high-energy (B/C) and the pre-edge (A) features changes with respect to the nematic phase, with similar magnitudes in the higher energy features but a suppressed intensity at the pre-edge (see Figure 9.4(a)). These aspects imply an orbital polarization that is independent from the lattice that arises below T_s.

The overall interpretation of the pre-edge sensitivity to the $3d$ states is shown in Figure 9.11, provided (a) the dipolar origin of the in-plane XLD signal and (b) the localization effects beyond single-particle approximations suggested in Ref. [315]. The local tetrahedral environment around the central Fe atom breaks the local inversion symmetry which allows an on-site hybridization of Fe $3d$ and Fe $4p$ states. This effect has been experimentally verified [316] and is the reason why the Fe K pre-edge of tetrahedrally coordinated Fe is more intense, due to the increase of the dipolar $1s \rightarrow 4p$ contribution which is forbidden in higher symmetry (e.g. octahedral) compounds [150]. Even with small mixing, the dipole

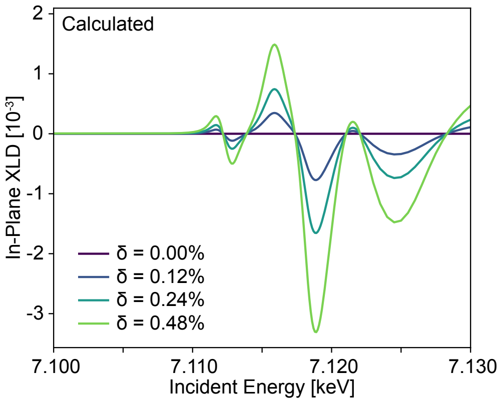

Figure 9.10: Calculations comparing the expected in-plane XLD as a function of the lattice orthorhombicity (δ). The base temperature orthorhombicity in FeSe is $\delta = 0.24\%$ as measured in experiment at $T = 10$ K in both Sample 1/2. The structural XLD contributions are all linear in δ.

transition amplitude is several orders of magnitude larger than the quadrupole one, and therefore quickly becomes dominant. It has been argued recently that this corresponds to an effective orbital localization of the Fe 3d states by reducing the Fe 3d anti-bonding character with respect to hybridization with the neighboring Se 4p states [315]. This effect has been shown to be common in the Fe-based superconductors, but is particularly pronounced in the chalcogenides as inferred through comparison of the Se K- and the Fe K-edge XAS polarization dependence [312, 315].

In the case of iron pnictides and chalcogenides, Wannier orbital analysis of the 3d states near the Fermi level confirms that the Fe states in the t_{2g} sector hybridize most strongly with orbitals of p character that are oriented perpendicular to the plane of the given 3d state [334]. This is shown for the case of the $|3d_{yz}\rangle$ orbital in Fig. 9.11(a), which mixes most strongly with the $|4p_x\rangle$ orbital leading to a hybrid orbital at the far left where the 3d lobes are deviated towards the nearest neighbor Se atoms (see Fig. 9.11(b)). In this situation, the dipolar transition at the pre-edge corresponds to a final state of the $|4p_x\rangle$ component of the hybridized orbital, which may be selected with linear polarized light along the $\vec{a}$ direction (Figure 9.11(b), right). Also shown is the analogous situation for the $|3d_{xz}\rangle$ orbital, which mixes strongest with the $|4p_y\rangle$ state and may be accessed through dipolar transitions with linear polarization along $\vec{b}$ (Figure 9.11, left). With these assignments, the positive XLD at the pre-edge (corresponding to $I_{LV} - I_{LH}$ with LV/LH parallel to $\vec{b}/\vec{a}$, respectively) corresponds to a higher occupation of the $|3d_{yz}\rangle$ orbital. While the mixing of 4p character may be sensitive to the bond-lengths, the saturating XLD signature with strain past the detwinning point suggests that the change in hybridization is a subdominant effect compared to the orbital occupation mismatch of the 3d orbitals.

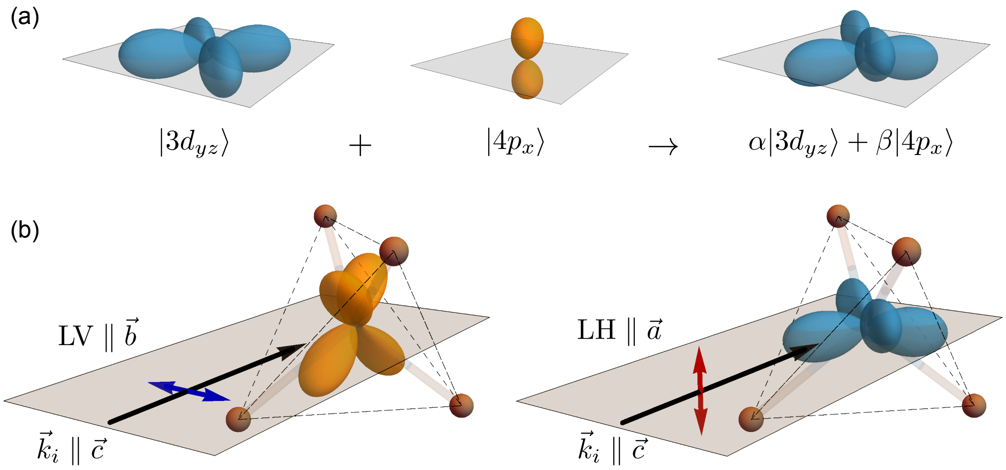

Figure 9.11: Schematic describing the sensitivity of the Fe K pre-edge measurements to the Fe-3d states. (a), Schematic showing the on-site Fe 3d/Fe 4p mixing induced by hybridization in the tetrahedral environment. (b), the $3d_{xz}$ orbital (orange) within the FeSe$_4$ tetrahedral environment is selected by polarization parallel to the $\vec{b}$ axis and (c) the $3d_{yz}$ orbital (blue) is selected by polarization parallel to $\vec{a}$. The distortions of the orbitals are exaggerated and for illustration purposes only (for quantitative details, see Refs. [334] and [315]).

Interpretation of Strain Dependent X-Ray and Transport Data

Here we explain the overall interpretation of the strain-dependent transport and XLD data utilized in this chapter. In Figure 9.12 (a)-(c), we show a schematic of the strain dependent orthorhombic domain populations, the net orbital polarization, and longitudinal resistivity, respectively. In Fig. 9.12(d) we show the orientation of the A and B domains below T_s. In this figure, positive tensile strain is applied along the x (vertical) direction which increasingly favors the A domain with the longer $\vec{a}$ axis aligned to the strain direction. In this case, $\vec{a}/\vec{b}$ always refer to the longer/shorter microscopic lattice parameters of the orthorhombic unit cells, while domain A/B refer to the respective orientation of the unit cell within a fixed lab frame defined as $\hat{x}/\hat{y}$.

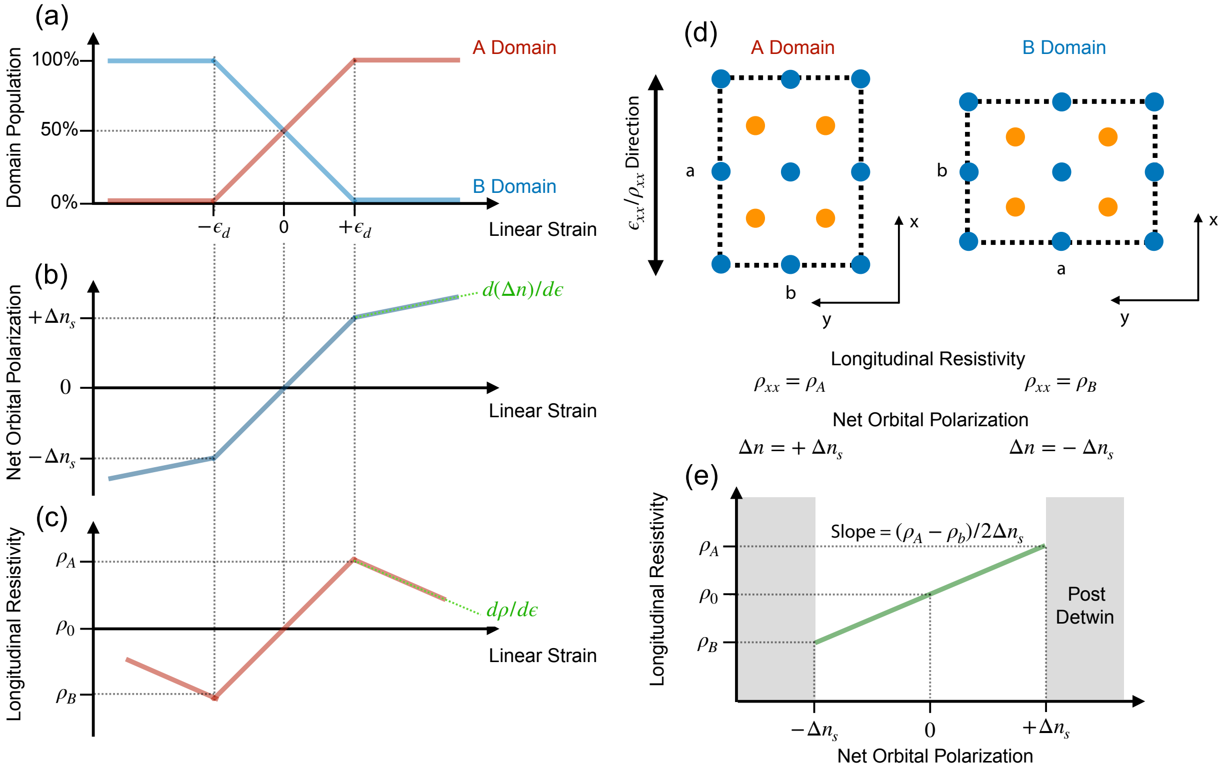

Figure 9.12: Schematic of the framework used to interpret the nematic-phase strain-dependent data throughout this chapter. (a), The relative volume fraction of the A and B domain populations, with full detwinning strains defined as $\pm\epsilon_d$. (b), The net orbital polarization measured in a fixed XLD geometry, with values $\pm\Delta n_s$ at $\pm\epsilon_d$ and post-detwinning strain susceptibility $d(\Delta n)/d\epsilon$. (c), The longitudinal resistivity, with values of ρ_A and ρ_B at $\pm\epsilon_d$ and post-detwinning strain susceptibility $d\rho/d\epsilon$ (i.e. elastoresistivity). (d), Schematic of the twin domains in relation to a fixed reference frame (x/y) and measurement geometry, with defined quantities for the orbital polarization Δn_s and resistivity ρ_A/ρ_B. (e), Schematic of the behavior of the longitudinal resistivity versus the net orbital polarization within the twin domain region, demonstrating the expected linearity and its relation to the resistivity anisotropy $\Delta\rho_s = \rho_A - \rho_B$ and the orbital polarization $\Delta n_s = n_x - n_y$.

We consider the net orbital polarization as the difference along $\hat{x}$ and $\hat{y}$ directions and the longitudinal resistance measured along the strain axis ρ_{xx} as executed experimentally. With these definitions, we define a positive spontaneous orbital polarization of $+\Delta n_s$ for the A domain, with the opposite sign for the B domain $-\Delta n_s$. Similarly for the resistance, we define ρ_A/ρ_B as the resistivity ρ_{xx} measured in the perfectly detwinned A/B domain, along the $\vec{a}/\vec{b}$ lattice parameter, respectively. The difference is related to the spontaneous resistivity anisotropy, defined as $\Delta\rho_s = \rho_A - \rho_B$.

We now consider how these quantities relate to the observed strain dependence of the measured longitudinal elastoresistance and the XLD probe of orbital polarization. At zero strain, the domain populations are equal, the net orbital polarization (XLD signal) is zero and the resistivity is ρ_0. As positive (negative) strain is applied the domain populations evolve linearly in favor of the A (B) domain until the detwinning strain $+\epsilon_d$ $(-\epsilon_d)$ is reached. Within the "twin domain region" defined as $-\epsilon_d < \epsilon < \epsilon_d$, both the net orbital polarization and the longitudinal resistivity evolve linearly, interpolating between the spontaneous values of the B and A domains, with values $-\Delta n_s/\rho_B$ at $-\epsilon_d$ and $+\Delta n_s/\rho_A$ at $+\epsilon_d$. We note that these observables only hold under the assumption of a linear evolution of the domain populations and that within the twin domain region, the microscopic lattice parameters within each domain are unperturbed. These assumptions are directly confirmed in our experiment (see Figure 9.2). For the resistivity, the linearity would also be affected by the presence of domain wall scattering in the twin domain region, however our experiments reveal a consistent linearity in this regime across all temperatures, arguing against such a contribution.

Past the detwinning points, a monodomain state is formed and the applied strain begins affecting the microscopic lattice parameters. In this regime, a distinct dependence of the orbital polarization and resistance would be observed (defined as $d(\Delta n)/d\epsilon$ and $d\rho/d\epsilon$) corresponding to the intrinsic strain-susceptibility in the monodomain. We note that these quantities are distinct from the spontaneous values which determine the strain dependence in the twin domain regime. Thus, probing the strain tunability of the resistivity anisotropy in either the twin domain strain regime or beyond the detwinning strain measures two different quantities (i.e. $\rho_{A/B}$ vs $d\rho/d\epsilon$), which results in sharp changes in the resistivity behavior across the detwinning point, as is seen in experiment. The elastoresistance past the detwinning point ($d\rho/d\epsilon$) was estimated from birefringence imaging experiments in Sample 2 and the strain-susceptibility of the orbital polarization ($d(\Delta n)/d\epsilon$)) past the detwinning point was estimated in Sample 2.

Most importantly, we wish to highlight the significance of the slope of the longitudinal elastoresistance to the orbital polarization within the twin domain regime. This is shown schematically in Fig. 9.12(e) and is the subject of Figure 9.4(c) and Figure 9.13 from experimental data. While each quantity is linear when plotted versus strain under the assumption of a linear evolution of domain populations, when plotting the quantities against each other the relationship is expected to be linear, independent of the precise details of the detwinning process or the precise strain state of the sample. The linearity does not necessarily hold post-detwinning, which is seen most clearly in the data of Figure 9.13(f) of Sample 1 at $T = 50$ K, and which signals the presence of a lattice-independent, saturating spontaneous orbital polarization in contrast to a lattice-coupled elastoresistivity.

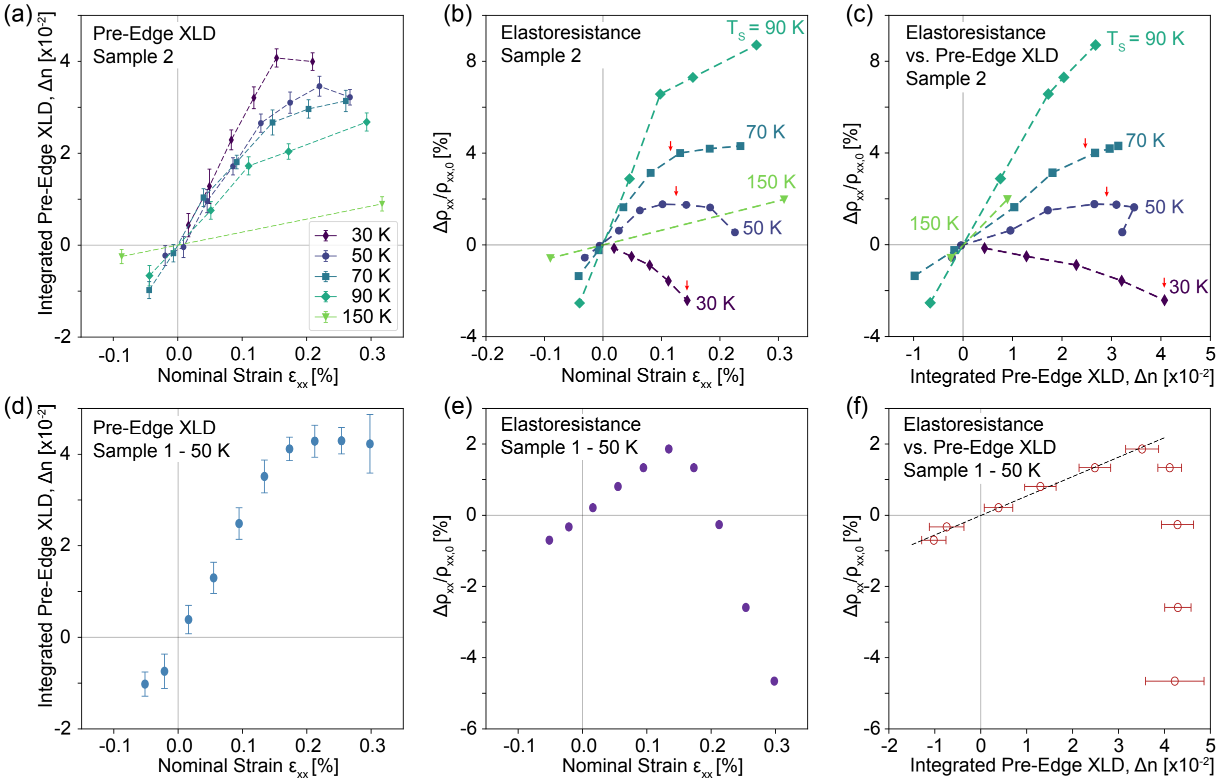

Figure 9.13: Elastoresistivity versus XLD data in Samples 1 and 2. (a), XLD and (b), elastoresistance versus strain and temperature from Sample 2. The XLD data is reproduced from Fig. 9.3(c)/(d) and the elastoresistance data is collected simultaneously to the XLD data. (c), The same data in (a)/(b), plotted as elastoresistance versus XLD. Red arrows denote the approximate detwinning point. The analogous data for Sample 1 at $T = 50$ K is shown in panels (d)-(f) which is reproduced from Fig. 9.2(d)/(g) for comparison between the samples. The slopes of the elastoresistance versus XLD within the detwinning regime are used for Fig. 9.4(c) summarizing the correspondence between the orbital and transport anisotropies.

The slope of the resulting line within the detwinning regime provides a direct relationship between the resistivity anisotropy and the orbital polarization as shown in Fig. 9.13(e) with a slope of $\Delta\rho_s/2\Delta n_s$. This is the quantity of interest which is plotted versus temperature in Figure 9.4(c). We note that this slope is rigorous since both XLD and elastoresistivity are bulk probes and sensitive to similar sample volumes. Thus, even if regions of the sample are pinned or otherwise unresponsive to strain, these regions will not contribute to the net anisotropy probed by either technique and the slope will be the same, with the endpoints at the detwinning point being scaled by the responsive fraction of the sample volume. This is clearly seen in experiment as well: while the quantitative values of the bare anisotropies as measured by XLD and resistivity measurements have slight quantitative discrepancies, the slopes extracted relating these two quantities are in excellent quantitative agreement between both samples (Fig. 9.4(c)). This analysis thus gives a robust assessment of the relationship between the orbital polarization and the resistivity anisotropy and highlights the strength of a technique that can directly relate two strain-dependent quantities *in situ*.

Using the framework presented above, we now present simultaneous measurements of the integrated pre-edge XLD intensity (Δn) and the normalized resistivity ($\Delta\rho/\rho_0$) vs the nominal strain (ϵ_{xx}) at fixed temperature for Sample 2 (Fig. 9.13 (a)/(b)) and Sample 1 (Fig. 9.13(d)/(e)). We find that both quantities show a nonlinear dependence on nominal strain due to the combined effects of domain detwinning (revealing the spontaneous anisotropies below T_s) and the strain-induced orbital polarization and elastoresistivity (for strains beyond full detwinning below T_s, and for all strains at and above T_s). However, when plotting $\Delta\rho/\rho_0$ against Δn (Fig. 9.13(c)/(f)) we find that the transport is linear to the orbital polarization within the detwinning regime. The temperature dependence of this linear proportionality is shown in Fig. 9.4(c) for both samples.

Chapter 10

Conclusion

In this thesis, we have shown that intrinsic non-collinear magnetic states can survive down to the single-layer limit, as demonstrated in the vdW type-II multiferroic NiI_2 (Chapter 5). We elaborated the ground state magnetic interactions which stabilize the various incommensurate magnetic states observed in this material, as established from experimental probes including optical and x-ray spectroscopy/scattering and through extreme conditions of high-pressure (Chapters 6 and 7). These results provide a comprehensive assessment of the physics of NiI_2 in the bulk and how it is modified through reduced dimensionality down to the monolayer.

Additionally, we have demonstrated the microscopic origin of sharp excitons which appear below the band gap in Ni^{2+} magnets (Chapter 8), establishing them as a set of intra-configurational multiplet excitations of octahedrally-coordinated Ni^{2+} which get significantly modified by metal-ligand charge transfer/covalency. We reported the first observation of the dispersive nature of these excitations using $\mathbf{q}$-resolved RIXS measurements, and showed how this delocalization occurs through the same ligand-to-metal charge transfer processes underlying interatomic superexchange. This provides the foundation for future investigations into the nature of optical excitons in strongly correlated 2D materials, which is relevant for the (magneto-)optical response of a majority of insulating/semiconducting 2D magnets.

Finally, we have introduced a new technique using *in-situ* tunable strain with multimodal X-ray absorption spectroscopy, X-ray diffraction, and transport measurements to characterize the relationship between the orbital, structural and electronic anisotropy in strongly correlated systems (Chapter 9). We used this technique to resolve the intrinsic $3d$ orbital anisotropy of the iron-based superconductor (IBSC) FeSe, which displays electronic nematicity in proximity to unconventional superconductivity. These measurements provide strong evidence that the orbital degree of freedom acts as the primary order parameter of the nematic phase in FeSe. This resolves key outstanding questions regarding the relationship between spin, structural and orbital anisotropy in FeSe, and their relevance to both nematic order and superconductivity in IBSCs.

Each of these advancements open significant future opportunities for the fields of vdW magnets, excitons and strongly correlated systems, which we outline below.

10.1 Future opportunities

10.1.1 Non-collinear magnetism and frustration in two dimensions

Our report of non-collinear magnetism (NCM) persisting to the single-layer limit opens many exciting opportunities for the field of vdW materials. First, it significantly broadens the classes of vdW magnetic materials which can retain long-range magnetic order down to the single-layer limit beyond the examples of Ising-type FM [6, 7] or (commensurate) Néel-type AFMs [24, 25]. Additionally, these NCMs are important functional materials because of their ability to generate spin-induced ferroelectric order, thus allowing large magnetoelectric effects which could be essential for device applications. Indeed, controlling magnetism at the nanoscale is a major thrust of the study of vdW magnetic materials. In many realizations and theoretical proposals, the mutual control of magnetism and electrical properties are induced through interfacial effects in heterostructures. Instead, intrinsic multiferroic order in pristine samples, as the case of type-II multiferroics, allows these additional degrees of freedom (e.g. heterostructure or moiré engineering) to be explored independently, rather than for the purpose of introducing interfacial magnetoelectric coupling.

In this context, a natural extension of the work presented here is to explore the effect of moiré heterostructures of NiI_2 or $NiBr_2$. Moiré heterostructures of 2D magnets - at leading order - induce a spatial modulation of the interlayer exchange interactions $J_\perp(\mathbf{r})$, which was recently demonstrated in moiré CrI_3 [31]. In this case, NCM may be induced through spatial modulation of the sign of $J_\perp$ [32], while locally retaining an intralayer Ising-like FM character. We elaborated how the interlayer interactions in frustrated triangular lattices can have a more dramatic effect on the magnetic ground state than simply determining the relative arrangement of spins in neighboring layers. Instead, these materials have many closely lying magnetic structures owing to the frustrated exchange interactions and we showed that the in-plane magnetic wavevector, spin texture, and the presence (or not) of ferroelecticity can be modified through the effects of interlayer interactions and the crystallographic stacking symmetry (Chapters 6,7). Thus, moiré heterostructures of, e.g., NiI_2 may show highly non-trivial behavior, with a possible competition between different in-plane spin spiral states induced by $J_\perp(\mathbf{r})$ in the length scale of the moiré unit cell $\mathcal{O}(10\text{ nm})$. This could lead to more complex mesoscale spin textures which do not have direct analogs in bulk materials. This carries the potential for an associated spatial modulation of the spin-induced ferroelectric order due to its microscopic connection to the magnetic wavevector ($\mathbf{q}$, Chapter 7). Finally, by introducing significant frustration between different single-$\mathbf{q}$ magnetic states, one may stabilize a triple-$\mathbf{q}$ state to minimize the single- and two-ion anisotropy. This could be a promising avenue to stabilize spontaneous topological spin structures in 2D systems (e.g. skyrmions), without the need for an external magnetic field [47]. These finite-momentum orderings may be probed by resonant magnetic X-ray scattering in the ultrathin limit (Chapter 7).

On a more fundamental level, there are significant opportunities to study the nature of low-dimensional spin systems beyond the case on long-range ordered magnetism. While much of the field has thus far focused on long-range order, 2D magnets may also realize idealized spin models, such as quantum spin liquids (QSLs), where instead one wants to suppress the tendency towards long-range order. This is exemplified by the case of the 2D XY model and associated Berezinskii-Kosterlitz-Thouless (BKT) transition, which was recently claimed for the case of the honeycomb vdW antiferromagnet $NiPS_3$ in the monolayer [25, 335]. Another route towards this goal is in frustrated triangular lattice magnets in the ultra-thin limit. A compound related to the nickel dihalides is layered $NiGa_2S_4$ with NiS_2 triangular lattice layers, which has been proposed as a quantum spin liquid candidate [336] and is (likely) exfoliable [337]. This material is more covalent than NiI_2, with longer-range exchange interactions and increased magnetic frustration [120]. It lacks long-range magnetic order to the lowest temperature but shows short-range incommensurate correlations for $T < 10$ K [336, 338], in agreement with the ground states analyzed in Chapter 3. Besides the need to minimize sample disorder, it is possible that these short-range correlations could be suppressed by exfoliation down to the single layer limit through reducing the interlayer exchange interactions (Chapter 5-7), the latter of which likely favor long-range order. Such physics have also been recently investigated for the case of the vdW honeycomb Kitaev spin liquid candidate $RuCl_3$ [339].

Finally, a promising opportunity is to tune the triangular lattice systems towards a quantum phase transition (QPT), either through doping or pressure. QPTs are characterized by significant zero-temperature fluctuations in the degree of freedom related to the incipient order. Indeed, above the transition temperature in NiI_2, Raman spectroscopy reveals significant quasielastic magnetic scattering (Chapter 5), which is likely related to short-range spin correlations persisting to temperatures far above T_N. Realizing a QPT should be possible in the doping series $Ni(Br_{1-x}I_x)_2$ [340] or applying pressure to $NiBr_2$ [228]. As we discussed (Chapter 7), the magnetic ground states of $NiBr_2$ and NiI_2 are different, with the former having in plane spiral vector of $\mathbf{q}_{\parallel} = [h, h]$ [128] while the latter has $\mathbf{q}_{\parallel} = [h, 0]$ in the bulk [42]. It is observed that under pressure, the $[h, h]$ phase of $NiBr_2$ decreases in its transition temperature rapidly (-22.5 K/GPa) [228], meaning that the transition should go to $T = 0$ K at a relatively low pressure ~ 1 GPa. The crossover region between the two stable in-plane wavevectors $[h, 0]/[h, h]$ could result in a disordered ground state with significant spin fluctuations (or short-range order) persisting to the lowest temperatures. Characterization of spin disordered states in the 2D limit will require more refined probes of spin excitations in ultra-thin materials, including thermodynamic probes of quantities like the magnetic specific heat or the magnetic susceptibility extended to few-layer materials. These may be addressable by inelastic spectroscopies such as quasielastic Raman scattering, resonantly-tuned magneto-optics, or RIXS (Chapter 4).

10.1.2 Tunable excitonic optical properties and determining the nature of excitons through dispersion

Identifying the nature of excitations from optical data alone can be a challenging endeavor. This is related to ambiguities in the optical selection rules, its $\mathbf{q} \simeq 0$ nature, and intermediate sensitivity to both localized electronic states (e.g., *dd* transitions) and itinerant excitations (e.g., Wannier excitons and interband transitions). We have shown that the use of local **q**-resolved probes, such as RIXS, can provide crucial complementary information, which we used here to identify the microscopic origin of sharp excitons in $\mathrm{NiX_2}$.

Our conclusion is that the sharp excitons are essentially spin singlet intra-configurational multiplets of $\mathrm{Ni^{2+}}$ (Chapter 2), which are stabilized purely through multielectronic effects (intra-atomic Hund's coupling). While ligand field theory and *dd* transitions have been extensively utilized in the past for describing optical spectra [60, 62], these spin-forbidden transitions pose a formidable task to quantitative theory. The emerging standard approach for describing the optical spectra of vdW materials is the Bethe-Salpeter equation (BSE), employed as a post-density-functional-theory (DFT) calculation of the optical spectra including excitonic effects [341]. These have been successful in describing, e.g., the optical response of the chromium trihalides [57, 342] and more recently the Wannier type excitons in vdW AFM CrSBr [49, 58, 343]. However, the singlet-to-triplet transitions we observe here are not accessible in the current BSE formalism, due to the approximation of the input DFT restricting to a single multielectronic configuration. That is, DFT can account for changes in Δm_s (spin-polarization), but not ΔS excitations [344].

Therefore, additional studies are needed to capture these types of excitations from the prevailing theoretical models, wherein work is beginning to be performed in the context of both chemistry and condensed matter systems [344, 345]. While the cluster models we presented can predict the energy, and take into account the effects of metal-ligand covalency at the first order of approximation (at the level of a single octahedral cluster), it is likely that the hybridization of localized d/f electrons with the band-like states formed by the ligand orbitals are important for describing the oscillator strengths quantiatively. Any such model must take into account the electronic correlations of the d levels in an exact way (e.g. dynamical mean field theory, DMFT), beyond the effective single particle treatment of DFT + U.

We note that spin-preserving *dd* excitations have been claimed to be captured by the BSE [57, 342, 345]. However, there is a conceptual difference between how such localized excitations are treated in the approaches of BSE and ligand-field theory. In the former, one constructs excitonic wavefunctions from a summation of **k** states in the vicinity of the band extrema, and the energy of the excitation is expressed as a binding energy with respect to a (phenomenological) band gap with self-energy effects included. Meanwhile, ligand field theory predicts a well-defined absolute energy of the excitation built only from localized electronic parameters. The relationship between these quantities is far from clear, and it is not clear a priori if pure Frenkel-type excitons will emerge from the BSE picture with a quantitative accuracy. As discussed for DFT-input multiplet models, DFT captures well the effects of covalency (e.g. metal-ligand hybridization and covalent contributions to the crystal field splitting), but is poor at accounting for the local cluster properties. Reconciling these two viewpoints will be crucial moving forward.

Beyond these challenges, there are exciting opportunities for utilizing these *dd* excitations for controlling the optical response. Optically driving multiplet excitations of triplet-to-singlet spin character may be an efficient mechanism to optically perturb magnetic order. The excitation of these multiplets quenches the local spin moment, becoming essentially a non-magnetic defect. Additionally, the fact that these excitations disperse means that they have interaction between different sites in the crystal, likely in a process similar to superexchange. It follows that there may be a coupling between such multiplets and the long-range magnetic order. There has been some evidence for this possibility shown in the literature [71, 290], but more work is needed to get a better understanding of the precise coupling mechanism and to optimize the optical properties of these excitations. Extending such photomagnetic effects to the equilibrium/metastable regime will be critical for real applications, as has begun to be demonstrated with all-optical magnetization switching in ferromagnets [59].

Towards these goals, our work shows how one can tune the energy of these excitons through the ligand environment and corresponding change in the charge transfer gap. This ends up being a very efficient tuning knob of the energy of spin-forbidden multiplets by changing the degree of screening of the Coulomb interactions at the transition metal site. It also provides hints towards enhancing the cross section of these multiplets, which will also be critical for applications. Increasing hybridization with the ligand states endows these excitations with significant ligand-centered character as we have analyzed in a cluster basis of localized ligand orbitals. In real materials, the ligand *p* orbitals are highly covalent and are better approximated by itinerant bands with large band width. Thus, the increasing metal-ligand hybridization endows the *dd*-transitions with a significant band component, which may act as an additional mechanism to relax the selection rules [345], as discussed above. The use of heavy ligands such as I or Br may help additionally relax the spin selection rule through significant ligand SOC (Chapter 4).

Significant work also remains regarding the role of magnetism in these multiplets. The original studies have claimed that these excitons are activated by the long-range magnetic order [56, 65], however our RIXS measurements show that they are independent of magnetic order (Chapter 8). This conclusion is compatible with their microscopic origin. However, large dichroic responses on these excitons are observed within the magnetically-ordered phase, which are likely connected to the local spin degree of freedom [65, 70]. This is also reconcilable within the picture of *dd* excitations, provided that transitions of the type $^3A_{2g} \rightarrow {}^1A_{1g}$ may have selection rules related to the projection S_z of the $S = 1$ ground state, which may set the unique axis for the dipole moment of the transition through SOC. Notably, this mechanism requires a magnetic order with a well defined local spin direction, but is a purely local process. Despite this, the role of magnetism in the optical cross section, and the sharp linewidths [56], remains unknown quantitatively. Our work shows that resolving this issue is specific to details of the optical cross section and not the microscopic origin of the excitations themselves, thus requiring more detailed and systematic optical measurements. One route to answer these questions is through hydrostatic pressure, which modifies both the charge transfer gap and the magnetic transition temperature (Chapter 6), thus allowing one to address their individual roles in the oscillator strength and temperature dependence across the long-range ordering temperature independent from the characteristic phonon energy scale resulting in Franck-Condon broadening.

Finally, the observation of the dispersion of these excitons opens new opportunities to study the properties of excitons in 2D materials more broadly, including their degree of localization, how they propagate through the lattice, and how they are coupled to long-range order (e.g. magnetism). These properties are not directly accessible by optical probes, instead relying on theoretical calculations such as BSE, which can provide the excitonic wavefunctions. It will interesting to extend our work beyond the case of multiplet excitations to Wannier excitons, particularly those with large binding energies as typically encountered in low-dimensional vdW materials. Due to the different sensitivity to local/itinerant electronic states and differences in the excitation processes of RIXS and optical reflectivity/absorption, it is unclear if such states can be detected. Nonetheless, monitoring the dispersion and momentum-space structure with RIXS may provide more direct information on the atomic/orbital character of the excitonic wavefunctions, as well as their spatial extent/delocalization, which may be subsequently compared to BSE calculations. Such measurements will thus provide a critical experimental test for identifying the nature of excitons. Along with the extension to spin-flip multiplets studied in the present work, this will guide theoretical efforts towards a complete description of the optical responses of correlated materials.

10.1.3 Disentangling the microscopic nature of the ground state in strongly correlated materials

Our use of *in-situ* tunable strain along with multiple independent measurements (XLD, XRD, transport) introduces a new method to disentangle the relationship between the structural and orbital degrees of freedom. This method demonstrates that the orbital anisotropy is independent of the structural distortion in FeSe. Beyond the case of IBSCs, the problem of such coupled order parameters is a general feature of strongly correlated systems. For instance, orbital-ordering is always accompanied by a corresponding structural distortion of the local transition-metal environment, know as Jahn-Teller distortions [15]. Therefore, the origin of signals attributed to orbital order are under debate in many systems, such as the manganites [157, 297], particularly whether the orbital order is simply a result of the structurally-induced anisotropy, or if an orbital order exists independently. Such distinctions currently require theoretical calculations and quantitative comparison to the magnitudes of the effects which can be experimentally difficult. As we demonstrated here, a direct and independent tuning of the lattice through an appropriate uniaxial strain along with a direct spectroscopic measurement of the orbital degrees of freedom may be an alternative route to resolve the interplay of coupled orbital and structural orders in correlated systems.

There are also opportunities for the study of frustrated magnetism, such as the triangular lattice systems studied throughout this thesis. On one hand, we have shown that spin-lattice coupling is a critical ingredient for the magnetic ground state of $\mathrm{NiI_2}$ (Chapter 6,7). In particular, this coupling switches the magnetic ground state from a collinear state without spin-induced ferroelectricity to a single-$\mathbf{Q}$ phase with type-II multiferroic properties (Chapter 5). It is therefore possible that a symmetry resolved tuning parameter, such as uniaxial strain, may be an efficient modulation of the multiferroicity in $\mathrm{NiI_2}$, which could lead to potentially useful properties such as a large effective piezoelectricity. In a practical sense, this would also allow using strain to detwin the single-$\mathbf{Q}$ domains as we utilized in the case of FeSe in Chapter 9 for studying electronic nematicity. This would allow macroscopic probes to study the intrinsic properties of monodomain $\mathrm{NiI_2}$ without the complex domain dynamics from magnetoelectric cooling protocols [45] that one encounters in hexagonal/triangular lattice systems. Thus, in addition to electric and magnetic fields, uniaxial strain can be added to the suite of external fields towards the realization of functional devices in this class of multiferroics.

Beyond these possible extensions, there remain significant unresolved questions in both FeSe and the IBSCs more broadly. In particular, it will be critical to perform tunable strain experiments, complementary to those we showed in Chapter 9, with a technique more sensitive to the spin degrees of freedom, such as RIXS [80]. RIXS measurements of the spin excitation anisotropy have been reported at fixed strain conditions in FeSe [96]. However, a tunable uniaxial strain would establish the relationship of this spin excitation anisotropy to the structural and orbital degrees of freedom, particularly above T_s where a strain-induced nematic order parameter is observed and distinct strain-induced Fermi surface anisotropy is observed compared to the ordered state below T_s [108]. This is critical because the observation of anisotropy alone without correlating to the other degrees of freedom makes the interpretation of the current RIXS experiment difficult.

Meanwhile, the role of spin fluctuations in FeSe for nematicity, in particular their development across the nematic transition and lattice-coupling below T_S, are still not completely resolved. Our transport measurements suggest that the spin excitation anisotropy could have a significant development with strain beyond the detwinning point within the nematic phase, which could be directly monitored by such measurements. For FeSe, it would also be crucial to extend measurements of both the spin fluctuations and the orbital anisotropy to below the superconducting transition in order to fully elucidate their respective roles in the pairing mechanism.

It would also be insightful to perform similar measurements in spin nematic systems, such as $\mathrm{Ba(Fe_{1-x}Co_x)_2As_2}$. Orbital ordering has been reported in the iron pnictides [332], however these measurements are also under fixed strain conditions. Thus, the details of the coupling between this orbital order and structure/long-range magnetism are unresolved experimentally, and would be important to establish any qualitative distinctions with the magnetically disordered nematic phase of FeSe. These more detailed measurements as a function of continuously tunable uniaxial strain would provide a more complete picture to establish the distinct phenomenology of orbital and spin-driven nematicity, if any.

Finally, materials tuned close to the nematic quantum critical point (QCP) such as $\mathrm{FeSe}_{1-x}\mathrm{S}_x$ [102], in the absence of magnetism, also pose an interesting region of the phase diagram. In these systems, one can study the interaction of orbital fluctuations with superconductivity in the absence of a developed nematic phase. This may resolve the nature of the distinct superconducting gaps on opposite sides of the orbital nematic QCP in the S-doped systems [295], and could determine whether orbital nematic fluctuations play any role in the pairing mechanism. Overall, these measurements would establish the role of the orbital degrees of freedom and their interplay with spin fluctuations in determining the leading electronic instabilities [84, 104, 107, 300], including superconductivity, in the IBSCs.

References

1. Cao, Y. *et al.* Unconventional superconductivity in magic-angle graphene superlattices. *Nature* **556,** 43–50 (2018).
2. Cao, Y. *et al.* Correlated insulator behaviour at half-filling in magic-angle graphene superlattices. *Nature* **556,** 80–84 (2018).
3. Regan, E. C. *et al.* Mott and generalized Wigner crystal states in WSe_2/WS_2 moiré superlattices. *Nature* **579,** 359–363 (2020).
4. Xu, Y. *et al.* Correlated insulating states at fractional fillings of moiré superlattices. *Nature* **587,** 214–218 (2020).
5. Tang, Y. *et al.* Simulation of Hubbard model physics in WSe_2/WS_2 moiré superlattices. *Nature* **579,** 353–358 (2020).
6. Huang, B. *et al.* Layer-dependent ferromagnetism in a van der Waals crystal down to the monolayer limit. *Nature* **546,** 270–273 (2017).
7. Gong, C. *et al.* Discovery of intrinsic ferromagnetism in two-dimensional van der Waals crystals. *Nature* **546,** 265–269 (2017).
8. Sharpe, A. L. *et al.* Emergent ferromagnetism near three-quarters filling in twisted bilayer graphene. *Science* **365,** 605–608 (2019).
9. Wang, X. *et al.* Light-induced ferromagnetism in moiré superlattices. *Nature* **604,** 468–473 (2022).
10. Ciorciaro, L. *et al.* Kinetic magnetism in triangular moiré materials. *Nature* **623,** 509–513 (2023).
11. Cai, J. *et al.* Signatures of fractional quantum anomalous Hall states in twisted $MoTe_2$. *Nature* **622,** 63–68 (2023).
12. McGuire, M. A. Crystal and magnetic structures in layered, transition metal dihalides and trihalides. *Crystals* **7,** 121 (2017).
13. Mak, K. F., Shan, J. & Ralph, D. C. Probing and controlling magnetic states in 2D layered magnetic materials. *Nature Reviews Physics* **1,** 646–661 (2019).
14. Burch, K. S., Mandrus, D. & Park, J. G. Magnetism in two-dimensional van der Waals materials. *Nature* **563,** 47–52 (2018).

15. Khomskii, D. I. *Transition metal compounds* (Cambridge University Press, 2014).

16. Mermin, N. D. & Wagner, H. Absence of ferromagnetism or antiferromagnetism in one- or two-dimensional isotropic Heisenberg models. *Physical Review Letters* **17,** 1133–1136 (1966).

17. Jiang, S., Li, L., Wang, Z., Mak, K. F. & Shan, J. Controlling magnetism in 2D CrI_3 by electrostatic doping. *Nature Nanotechnology* **13,** 549–553 (2018).

18. McGuire, M. A., Dixit, H., Cooper, V. R. & Sales, B. C. Coupling of crystal structure and magnetism in the layered, ferromagnetic insulator CrI_3. *Chemistry of Materials* **27,** 612–620 (2015).

19. Chen, W. *et al.* Direct observation of van der Waals stacking–dependent interlayer magnetism. *Science* **366,** 983–987 (2019).

20. Li, T. *et al.* Pressure-controlled interlayer magnetism in atomically thin CrI_3. *Nature Materials* **18,** 1303–1308 (2019).

21. Huang, B. *et al.* Electrical control of 2D magnetism in bilayer CrI_3. *Nature Nanotechnology* **13,** 544–548 (2018).

22. Sun, Z. *et al.* Giant nonreciprocal second-harmonic generation from antiferromagnetic bilayer CrI_3. *Nature* **572,** 497–501 (2019).

23. Fei, Z. *et al.* Two-dimensional itinerant ferromagnetism in atomically thin Fe_3GeTe_2. *Nature Materials* **17,** 778–782 (2018).

24. Lee, J. U. *et al.* Ising-Type Magnetic Ordering in Atomically Thin $FePS_3$. *Nano Letters* **16,** 7433–7438 (2016).

25. Kim, K. *et al.* Suppression of magnetic ordering in XXZ-type antiferromagnetic monolayer $NiPS_3$. *Nature Communications* **10,** 345 (2019).

26. Jungwirth, T., Marti, X., Wadley, P. & Wunderlich, J. Antiferromagnetic spintronics. *Nature Nanotechnology* **11,** 231–241 (2016).

27. Wang, Z. *et al.* Very large tunneling magnetoresistance in layered magnetic semiconductor CrI_3. *Nature Communications* **9,** 2516 (2018).

28. Kim, H. H. *et al.* Evolution of interlayer and intralayer magnetism in three atomically thin chromium trihalides. *Proceedings of the National Academy of Sciences of the United States of America* **166,** 11131–11136 (2019).

29. Klein, D. R. *et al.* Probing magnetism in 2D van der Waals crystalline insulators via electron tunneling. *Science* **360,** 1218–1222 (2018).

30. Zhu, R. *et al.* Exchange Bias in van der Waals $CrCl_3/Fe_3GeTe_2$ Heterostructures. *Nano Letters* **20,** 5030–5035 (2020).

31. Song, T. *et al.* Direct visualization of magnetic domains and moiré magnetism in twisted 2D magnets. *Science* **374,** 1140–1144 (2021).

32. Xie, H. *et al.* Evidence of non-collinear spin texture in magnetic moiré superlattices. *Nature Physics* **19,** 1150–1155 (2023).

33. Tokura, Y., Seki, S. & Nagaosa, N. Multiferroics of spin origin. *Reports on Progress in Physics* **77** (2014).

34. Fiebig, M., Lottermoser, T., Meier, D. & Trassin, M. The evolution of multiferroics. *Nature Reviews Materials* **1** (2016).

35. Catalan, G. & Scott, J. F. Physics and applications of bismuth ferrite. *Advanced Materials* **21,** 2463–2485 (2009).

36. Kimura, T. *et al.* Magnetic control of ferroelectric polarization. *Nature* **426,** 55–58 (2003).

37. Song, Q. *et al.* Evidence for a single-layer van der Waals multiferroic. *Nature* **602,** 601–605 (2022).

38. Tokunaga, Y. *et al.* Multiferroicity in $NiBr_2$ with long-wavelength cycloidal spin structure on a triangular lattice. *Physical Review B* **84,** 060406 (2011).

39. Katsura, H., Nagaosa, N. & Balatsky, A. V. Spin current and magnetoelectric effect in noncollinear magnets. *Physical Review Letters* **95,** 057205 (2005).

40. Xiang, H. J., Kan, E. J., Zhang, Y., Whangbo, M. H. & Gong, X. G. General theory for the ferroelectric polarization induced by spin-spiral order. *Physical Review Letters* **107,** 157202 (2011).

41. Rastelli, E., Tassi, A. & Reatto, L. Non-simple magnetic order for simple Hamiltonians. *Physica B+C* **97,** 1–24 (1979).

42. Kuindersma, S. R., Sanchez, J. P. & Haas, C. Magnetic and structural investigations on NiI_2 and CoI_2. *Physica* **111B,** 231–248 (1981).

43. Day, P., Dinsdale, A., Krausz, E. R. & Robbins, D. J. Optical and neutron diffraction study of the magnetic phase diagram of $NiBr_2$. *Journal of Physics C: Solid State Physics* **9,** 2481–2490 (1976).

44. Kurumaji, T. *et al.* Magnetic-field induced competition of two multiferroic orders in a triangular-lattice helimagnet MnI_2. *Physical Review Letters* **106,** 167206 (2011).

45. Kurumaji, T. *et al.* Magnetoelectric responses induced by domain rearrangement and spin structural change in triangular-lattice helimagnets NiI_2 and CoI_2. *Physical Review B* **87,** 014429 (2013).

46. Botana, A. S. & Norman, M. R. Electronic structure and magnetism of transition metal dihalides: Bulk to monolayer. *Physical Review Materials* **3,** 044001 (2019).

47. Amoroso, D., Barone, P. & Picozzi, S. Spontaneous skyrmionic lattice from anisotropic symmetric exchange in a Ni-halide monolayer. *Nature Communications* **11,** 5784 (2020).

48. Seyler, K. L. *et al.* Ligand-field helical luminescence in a 2D ferromagnetic insulator. *Nature Physics* **14,** 277–281 (2018).

49. Klein, J. *et al.* The Bulk van der Waals Layered Magnet CrSBr is a Quasi-1D Material. *ACS Nano* **17,** 5316–5328 (2023).

50. Knox, R. S. *Introduction to exciton physics* (Springer US, 1983).

51. Wang, G. *et al.* Colloquium: Excitons in atomically thin transition metal dichalcogenides. *Reviews of Modern Physics* **90,** 021001 (2018).

52. Splendiani, A. *et al.* Emerging photoluminescence in monolayer MoS_2. *Nano Letters* **10,** 1271–1275 (2010).

53. Mak, K. F., Lee, C., Hone, J., Shan, J. & Heinz, T. F. Atomically thin MoS_2: A new direct-gap semiconductor. *Physical Review Letters* **105,** 136805 (2010).

54. He, K. *et al.* Tightly bound excitons in monolayer WSe_2. *Physical Review Letters* **113,** 026803 (2014).

55. Huang, D., Choi, J., Shih, C. K. & Li, X. Excitons in semiconductor moiré superlattices. *Nature Nanotechnology* **17,** 227–238 (2022).

56. Kang, S. *et al.* Coherent many-body exciton in van der Waals antiferromagnet $NiPS_3$. *Nature* **583,** 785–789 (2020).

57. Wu, M., Li, Z., Cao, T. & Louie, S. G. Physical origin of giant excitonic and magneto-optical responses in two-dimensional ferromagnetic insulators. *Nature Communications* **10,** 2371 (2019).

58. Wilson, N. P. *et al.* Interlayer electronic coupling on demand in a 2D magnetic semiconductor. *Nature Materials* **20,** 1657–1662 (2021).

59. Zhang, P. *et al.* All-optical switching of magnetization in atomically thin CrI_3. *Nature Materials* **21,** 1373–1378 (2022).

60. Ballhausen, C. J. *Introduction to Ligand Field Theory* (McGraw-Hill, 1962).

61. Kitzmann, W. R., Moll, J. & Heinze, K. Spin-flip luminescence. *Photochemical and Photobiological Sciences* **21,** 1309–1331 (2022).

62. Lohr, L. Spin-forbidden electronic excitations in transition metal complexes. *Coordination Chemistry Reviews* **8,** 241–259 (1972).

63. Dillon, J. F., Kamimura, H. & Remeika, J. P. Magneto-optical properties of ferromagnetic chromium trihalides. *Journal of Physics and Chemistry of Solids* **27,** 1531–1549 (1966).

64. Zhang, Z. *et al.* Direct Photoluminescence Probing of Ferromagnetism in Monolayer Two-Dimensional $CrBr_3$. *Nano Letters* **19,** 3138–3142 (2019).

65. Son, S. *et al.* Multiferroic-Enabled Magnetic-Excitons in 2D Quantum-Entangled Van der Waals Antiferromagnet NiI_2. *Advanced Materials* **34,** 2109144 (2022).

66. Wang, X. *et al.* Spin-induced linear polarization of photoluminescence in antiferromagnetic van der Waals crystals. *Nature Materials* **20,** 964–970 (2021).

67. Kim, J. H. *et al.* Terahertz evidence of electromagnon excitations in the multiferroic van der Waals insulator $\mathrm{NiI_2}$. *Physical Review B* **108,** 064414 (2023).

68. Jana, D. *et al.* Magnon gap excitations and spin-entangled optical transition in van der Waals antiferromagnet $\mathrm{NiPS_3}$. *arXiv,* 2306.07660 (2023).

69. Ergeçen, E. *et al.* Magnetically brightened dark electron-phonon bound states in a van der Waals antiferromagnet. *Nature Communications* **13,** 98 (2022).

70. Hwangbo, K. *et al.* Highly anisotropic excitons and multiple phonon bound states in a van der Waals antiferromagnetic insulator. *Nature Nanotechnology* **16,** 655–660 (2021).

71. Belvin, C. A. *et al.* Exciton-driven antiferromagnetic metal in a correlated van der Waals insulator. *Nature Communications* **12,** 4837 (2021).

72. Afanasiev, D. *et al.* Controlling the anisotropy of a van der Waals antiferromagnet with light. *Science Advances* **7,** eabf3096 (2021).

73. Lee, P. A., Nagaosa, N. & Wen, X. G. Doping a Mott insulator: Physics of high-temperature superconductivity. *Reviews of Modern Physics* **78,** 17–85 (2006).

74. Comin, R. & Damascelli, A. Resonant X-Ray Scattering Studies of Charge Order in Cuprates. *Annual Review of Condensed Matter Physics* **7,** 369–405 (2016).

75. Kamihara, Y., Watanabe, T., Hirano, M. & Hosono, H. Iron-Based Layered Superconductor $\mathrm{La[O_{1-x}F_x]FeAs}$ (x = 0.05-0.12) with $T_c = 26$ K. *Journal of the American Chemical Society* **130,** 3296–3297 (2008).

76. Rotter, M., Tegel, M. & Johrendt, D. Superconductivity at 38 K in the Iron Arsenide $\mathrm{Ba_{1-x}K_xFe_2As_2}$. *Physical Review Letters* **101,** 107006 (2008).

77. Chen, X., Dai, P., Feng, D., Xiang, T. & Zhang, F. C. Iron-based high transition temperature superconductors. *National Science Review* **1,** 371–395 (2014).

78. Si, Q., Yu, R. & Abrahams, E. High-temperature superconductivity in iron pnictides and chalcogenides. *Nature Reviews Materials* **1,** 16017 (2016).

79. Farrar, L. S. *et al.* Suppression of superconductivity and enhanced critical field anisotropy in thin flakes of FeSe. *npj Quantum Materials* **5,** 29 (2020).

80. Pelliciari, J. *et al.* Reciprocity between local moments and collective magnetic excitations in the phase diagram of $\mathrm{BaFe_2(As_{1-x}P_x)_2}$. *Communications Physics* **2,** 139 (2019).

81. Canfield, P. C. & Bud'ko, S. L. FeAs-Based Superconductivity: A Case Study of the Effects of Transition Metal Doping on $\mathrm{BaFe_2As_2}$. *Annual Review of Condensed Matter Physics* **1,** 27–50 (2010).

82. Chu, J.-H. *et al.* In-plane resistivity anisotropy in an underdoped iron arsenide superconductor. *Science* **329,** 824–826 (2010).

83. Kuo, H.-H., Chu, J.-H., Palmstrom, J. C., Kivelson, S. A. & Fisher, I. R. Ubiquitous signatures of nematic quantum criticality in optimally doped Fe-based superconductors. *Science* **352,** 985–962 (2016).

84. Fernandes, R. M., Chubukov, A. V. & Schmalian, J. What drives nematic order in iron-based superconductors? *Nature Physics* **10,** 97–104 (2014).

85. Nandi, S. *et al.* Anomalous suppression of the orthorhombic lattice distortion in superconducting $Ba(Fe_{1-x}Co_x)_2As_2$ single crystals. *Physical Review Letters* **104,** 057006 (2010).

86. Pratt, D. K. *et al.* Coexistence of competing antiferromagnetic and superconducting phases in the underdoped $Ba(Fe_{0.953}Co_{0.047})_2As_2$ compound using X-ray and neutron scattering techniques. *Physical Review Letters* **103,** 087001 (2009).

87. Pal, A. *et al.* Optical anisotropy in optimally doped iron-based superconductor. *npj Quantum Materials* **4,** 3 (2019).

88. Gallais, Y. & Paul, I. Charge nematicity and electronic Raman scattering in iron-based superconductors. *Comptes Rendus Physique* **17,** 113–139 (2016).

89. Yi, M. *et al.* Symmetry-breaking orbital anisotropy observed for detwinned $Ba(Fe_{1-x}Co_x)_2As_2$ above the spin density wave transition. *Proceedings of the National Academy of Sciences of the United States of America* **108,** 6878–6883 (2011).

90. Ewings, R. A. *et al.* High-energy spin excitations in $BaFe_2As_2$ observed by inelastic neutron scattering. *Physical Review B* **78,** 220501 (2008).

91. Kitagawa, K., Katayama, N., Ohgushi, K., Yoshida, M. & Takigawa, M. Commensurate itinerant antiferromagnetism in $BaFe_2As_2$: ^{75}As-NMR studies on a self-flux grown single crystal. *Journal of the Physical Society of Japan* **77,** 1–6 (2008).

92. Tanatar, M. A. *et al.* Direct imaging of the structural domains in the iron pnictides AFe_2As_2 (A=Ca,Sr,Ba). *Physical Review B* **79,** 180508 (2009).

93. Tanatar, M. A. *et al.* Origin of the Resistivity Anisotropy in the Nematic Phase of FeSe. *Physical Review Letters* **117,** 127001 (2016).

94. Böhmer, A. E. & Kreisel, A. Nematicity, magnetism and superconductivity in FeSe. *Journal of Physics Condensed Matter* **30,** 023001 (2018).

95. Watson, M. D. *et al.* Emergence of the nematic electronic state in FeSe. *Physical Review B* **91,** 155106 (2015).

96. Lu, X. *et al.* Spin-excitation anisotropy in the nematic state of detwinned FeSe. *Nature Physics* **18,** 806–812 (2022).

97. Wang, Q. *et al.* Strong interplay between stripe spin fluctuations, nematicity and superconductivity in FeSe. *Nature Materials* **15,** 159–163 (2016).

98. Chen, T. *et al.* Anisotropic spin fluctuations in detwinned FeSe. *Nature Materials* **18,** 709–716 (2019).

99. Baek, S. H. *et al.* Orbital-driven nematicity in FeSe. *Nature Materials* **14,** 210–214 (2015).

100. Hsu, F. C. *et al.* Superconductivity in the PbO-type structure α-FeSe. *Proceedings of the National Academy of Sciences of the United States of America* **105,** 14262–14264 (2008).

101. Böhmer, A. E. *et al.* Lack of coupling between superconductivity and orthorhombic distortion in stoichiometric single-crystalline FeSe. *Physical Review B* **87,** 180505 (2013).

102. Hosoi, S. *et al.* Nematic quantum critical point without magnetism in $\mathrm{FeSe}_{1-x}\mathrm{S}_x$ superconductors. *Proceedings of the National Academy of Sciences of the United States of America* **113,** 8139–8143 (2016).

103. Sun, J. P. *et al.* High-T_c Superconductivity in FeSe at High Pressure: Dominant Hole Carriers and Enhanced Spin Fluctuations. *Physical Review Letters* **118,** 147004 (2017).

104. Yi, M. *et al.* Nematic Energy Scale and the Missing Electron Pocket in FeSe. *Physical Review X* **9,** 041049 (2019).

105. Rhodes, L. C., Watson, M. D., Haghighirad, A. A., Evtushinsky, D. V. & Kim, T. K. Revealing the single electron pocket of FeSe in a single orthorhombic domain. *Physical Review B* **101,** 235128 (2020).

106. Pfau, H. *et al.* Momentum Dependence of the Nematic Order Parameter in Iron-Based Superconductors. *Physical Review Letters* **123,** 066402 (2019).

107. Fanfarillo, L. *et al.* Orbital-dependent Fermi surface shrinking as a fingerprint of nematicity in FeSe. *Physical Review B* **94,** 155138 (2016).

108. Cai, C. *et al.* Momentum-resolved measurement of electronic nematic susceptibility in the $\mathrm{FeSe}_{0.9}\mathrm{S}_{0.1}$ superconductor. *Physical Review B* **101,** 180501 (2020).

109. Cowan, R. D. *The Theory of Atomic Structure and Spectra* (University of California Press, 1981).

110. De Groot, F. & Kotani, A. *Core level spectroscopy of solids* (CRC Press, 2008).

111. Zaanen, J., Sawatzky, G. A. & Allen, J. W. Band gaps and electronic structure of transition-metal compounds. *Physical Review Letters* **55,** 418–421 (1985).

112. Dresselhaus, M. S., Dresselhaus, G. & Jorio, A. *Group Theory: Application to the Physics of Condensed Matter* (Springer Berlin Heidelberg, 2007).

113. Haverkort, M. W., Zwierzycki, M. & Andersen, O. K. Multiplet ligand-field theory using Wannier orbitals. *Physical Review B* **85,** 165113 (2012).

114. Liechtenstein, A. I., Anisimov, V. I. & Zaanen, J. Density-functional theory and strong interactions: Orbital ordering in Mott-Hubbard insulators. *Physical Review B* **52,** R5467–R5470 (1995).

115. Van der Marel, D. & Sawatzky, G. A. Electron-electron interaction and localization in d and f transition mettals. *Physical Review B* **37,** 674–684 (1988).

116. Anderson, P. W. Antiferromagnetism. Theory of Superexchange. *Physical Review* **79,** 350–355 (1950).

117. Anderson, P. W. New approach to the theory of superexchange interactions. *Physical Review* **115,** 2–13 (1959).

118. Goodenough, J. B. & Loeb, A. L. Theory of ionic ordering, crystal distortion, and magnetic exchange due to covalent forces in spinels. *Physical Review* **98,** 391–408 (1955).

119. Kanamori, J. Superexchange interaction and symmetry properties of electron orbitals. *Journal of Physics and Chemistry of Solids* **10,** 87–98 (1959).

120. Takubo, K. *et al.* Unusual Superexchange Pathways in an NiS_2 Triangular Lattice with Negative Charge-Transfer Energy. *Physical Review Letters* **99,** 037203 (2007).

121. Wang, R. P. *et al.* Excitonic dispersion of the intermediate spin state in $LaCoO_3$ revealed by resonant inelastic x-ray scattering. *Physical Review B* **98,** 035149 (2018).

122. Kim, J. *et al.* Excitonic quasiparticles in a spin-orbit Mott insulator. *Nature Communications* **5,** 4453 (2014).

123. Schlappa, J. *et al.* Spin-orbital separation in the quasi-one-dimensional Mott insulator Sr_2CuO_3. *Nature* **485,** 82–85 (2012).

124. Lindgard, P. A., Birgeneau, R. J., Guggenheim, H. J. & Als-Nielsen, J. Spin-wave dispersion and sublattice magnetization in $NiCl_2$. *Journal of Physics C: Solid State Physics* **8,** 1059–1069 (1975).

125. Riedl, K. *et al.* Microscopic origin of magnetism in monolayer $3d$ transition metal dihalides. *Physical Review B* **106,** 035156 (2022).

126. Kapeghian, J. *et al.* Effects of Pressure on the Electronic and Magnetic Properties of Bulk NiI_2. *Physical Review B* **109,** 014403 (2024).

127. Day, P. *et al.* Inelastic neutron scattering study of magnetic excitations in the helimagnetic and antiferromagnetic phases of $NiBr_2$. *Solid State Communications* **51,** 627–630 (1984).

128. Regnault, L. P., Rossat-Mignod, J., Adam, A., Billerey, D. & Terrier, C. Inelastic neutron scattering investigation of the magnetic excitations in the helimagnetic state of $NiBr_2$. *Journal de Physique Paris* **43,** 1283–1290 (1982).

129. Sødequist, J. & Olsen, T. Type II multiferroic order in two-dimensional transition metal halides from first principles spin-spiral calculations. *2D Materials* **10** (2023).

130. Jackeli, G. & Khaliullin, G. Mott insulators in the strong spin-orbit coupling Limit: From Heisenberg to a Quantum Compass and Kitaev Models. *Physical Review Letters* **102,** 017205 (2009).

131. Li, X. *et al.* Realistic Spin Model for Multiferroic NiI_2. *Physical Review Letters* **131,** 036701 (2023).

132. Mostovoy, M. Ferroelectricity in spiral magnets. *Physical Review Letters* **96,** 067601 (2006).

133. Sergienko, I. A. & Dagotto, E. Role of the Dzyaloshinskii-Moriya interaction in multiferroic perovskites. *Physical Review B* **73,** 094434 (2006).

134. Yamasaki, Y. *et al.* Electric control of spin helicity in a magnetic ferroelectric. *Physical Review Letters* **98,** 147204 (2007).

135. Arima, T. H. *et al.* Spin-lattice coupling in ferroelectric spiral magnets: Comparison between the cases of $(Tb,Dy)MnO_3$ and $CoCr_2O_4$. *Journal of the Physical Society of Japan* **76,** 3–6 (2007).

136. Arima, T. H. Ferroelectricity induced by proper-screw type magnetic order. *Journal of the Physical Society of Japan* **76,** 3–6 (2007).

137. Jia, C., Onoda, S., Nagaosa, N. & Han, J. H. Bond electronic polarization induced by spin. *Physical Review B* **74,** 224444 (2006).

138. Kaplan, T. A. & Mahanti, S. D. Canted-spin-caused electric dipoles: A local symmetry theory. *Physical Review B* **83,** 174432 (2011).

139. Jia, C., Onoda, S., Nagaosa, N. & Han, J. H. Microscopic theory of spin-polarization coupling in multiferroic transition metal oxides. *Physical Review B* **76,** 144424 (2007).

140. Tanaka, Y. *et al.* Incommensurate orbital modulation behind ferroelectricity in $CuFeO_2$. *Physical Review Letters* **109,** 127205 (2012).

141. Fumega, A. O. & Lado, J. L. Microscopic origin of multiferroic order in monolayer NiI_2. *2D Materials* **9,** 025010 (2022).

142. Wu, D. W., Yuan, Y. B., Liu, S., Long, M. Q. & Wang, Y. P. First-principles study of spin-orbital coupling induced ferroelectricity in $NiBr_2$. *Physical Review B* **108,** 054429 (2023).

143. Amini, M. *et al.* Atomic-scale visualization of multiferroicity in monolayer NiI_2. *Advanced Materials* **36,** 2311342 (2024).

144. Sakurai, J. J. *Advanced Quantum Mechanics* (Addison-Wesley Publishing Company, 1967).

145. Di Matteo, S. Resonant x-ray diffraction: Multipole interpretation. *Journal of Physics D: Applied Physics* **45,** 163001 (2012).

146. Van Veenendaal, M. *Theory of Inelastic Scattering and Absorption of X-rays* (Cambridge University Press, 2015).

147. Rehr, J. J. & Albers, R. C. Theoretical approaches to x-ray absorption fine structure. *Reviews of Modern Physics* **72,** 621–654 (2000).

148. Frati, F., Hunault, M. O. & De Groot, F. M. Oxygen K-edge X-ray Absorption Spectra. *Chemical Reviews* **120,** 4056–4110 (2020).

149. Grunes, L. A. Study of the K edges of $3d$ transition metals in pure and oxide form by x-ray-absorption spectroscopy. *Physical Review B* **27,** 2111–2131 (1983).

150. Yamamoto, T. Assignment of pre-edge peaks in K-edge x-ray absorption spectra of 3d transition metal compounds: electric dipole or quadrupole? *X-Ray Spectrometry* **37,** 572–584 (2008).

151. Brouder, C. Angular dependence of X-ray absorption spectra. *Journal of Physics: Condensed Matter* **2,** 701–738 (1990).

152. Carra, P., Thole, B. T., Altarelli, M. & Wang, X. X-ray circular dichroism and local magnetic fields. *Physical Review Letters* **70,** 694–697 (1993).

153. Thole, B. T., Carra, P., Sette, F. & Van Der Laan, G. X-ray circular dichroism as a probe of orbital magnetization. *Physical Review Letters* **68,** 1943–1946 (1992).

154. Zaanen, J., Westra, C. & Sawatzky, G. A. Determination of the electronic structure of transition-metal compounds: $2p$ x-ray photoemission spectroscopy of nickel dihalides. *Physical Review B* **33,** 8060 (1986).

155. Van der Laan, G., Zaanen, J., Sawatzky, G. A., Karnatak, R. & Esteva, J. M. Comparison of x-ray absorption with x-ray photoemission of nickel dihalides and NiO. *Physical Review B* **33,** 4253–4263 (1986).

156. Ament, L. J., Van Veenendaal, M., Devereaux, T. P., Hill, J. P. & Van Den Brink, J. Resonant inelastic x-ray scattering studies of elementary excitations. *Reviews of Modern Physics* **83,** 705–767 (2011).

157. Murakami, Y. *et al.* Resonant X-Ray Scattering from Orbital Ordering in $LaMnO_3$. *Physical Review Letters* **81,** 582–585 (1998).

158. Wilkins, S. B., Hatton, P. D., Roper, M. D., Prabhakaran, D. & Boothroyd, A. T. Soft X-Ray Resonant Magnetic Diffraction. *Physical Review Letters* **90,** 187201 (2003).

159. Fink, J., Schierle, E., Weschke, E. & Geck, J. Resonant elastic soft x-ray scattering. *Reports on Progress in Physics* **76** (2013).

160. Hannon, J. P., Trammell, G. T., Blume, M. & Gibbs, D. X-ray resonance exchange scattering. *Physical Review Letters* **61,** 1245–1248 (1988).

161. Dvorak, J., Jarrige, I., Bisogni, V., Coburn, S. & Leonhardt, W. Towards 10 meV resolution: The design of an ultrahigh resolution soft X-ray RIXS spectrometer. *Review of Scientific Instruments* **87,** 115109 (2016).

162. Sato, K. Measurement of magneto-optical kerr effect using piezo-birefringent modulator. *Japanese Journal of Applied Physics* **20,** 2403–2409 (1981).

163. Kapitulnik, A., Dodge, J. S. & Fejer, M. M. High-resolution magneto-optic measurements with a Sagnac interferometer (invited). *Journal of Applied Physics* **75,** 6872–6877 (1994).

164. Ferre, J. & Gehring, G. A. Linear optical birefringence of magnetic crystals. *Reports on Progress in Physics* **47,** 513–611 (1984).

165. Zhang, Q. *et al.* Observation of Giant Optical Linear Dichroism in a Zigzag Antiferromagnet $FePS_3$. *Nano Letters* **21,** 6938–6945 (2021).

166. Jorio, A., Dresselhaus, M. S., Saito, R. & Dresselhaus, G. *Raman Spectroscopy in Graphene Related Systems* (Wiley, 2011).

167. Loudon, R. The Raman effect in crystals. *Advances in Physics* **13,** 423–482 (1964).

168. McClain, W. M. Excited state symmetry assignment through polarized two-photon absorption studies of fluids. *The Journal of Chemical Physics* **55,** 2789–2796 (1971).

169. Fleury, P. A. & Loudon, R. Scattering of Light by One- and Two-Magnon Excitations. *Physical Review* **166,** 514 (1968).

170. Cenker, J. *et al.* Direct observation of two-dimensional magnons in atomically thin CrI_3. *Nature Physics* **17,** 20–25 (2021).

171. Lyu, B. *et al.* Probing the Ferromagnetism and Spin Wave Gap in VI_3 by Helicity-Resolved Raman Spectroscopy. *Nano Letters* **20,** 6024–6031 (2020).

172. McCreary, A. *et al.* Quasi-two-dimensional magnon identification in antiferromagnetic $FePS_3$ via magneto-Raman spectroscopy. *Physical Review B* **101,** 064416 (2020).

173. Loudon, R. Time-reversal Symmetry in Light-scattering Theory. *Journal of Raman Spectroscopy* **7,** 10–14 (1978).

174. Wettling, W., Cottam, M. G. & Sandercock, J. R. The relation between one-magnon light scattering and the complex magneto-optic effects in YIG. *Journal of Physics C: Solid State Physics* **8,** 211–228 (1975).

175. Matsukura, F., Tokura, Y. & Ohno, H. Control of magnetism by electric fields. *Nature Nanotechnology* **10,** 209–220 (2015).

176. Pimenov, A. *et al.* Possible evidence for electromagnons in multiferroic manganites. *Nature Physics* **2,** 97–100 (2006).

177. Rovillain, P. *et al.* Magnetoelectric excitations in multiferroic $TbMnO_3$ by Raman scattering. *Physical Review B* **81,** 054428 (2010).

178. Kibayashi, S., Takahashi, Y., Seki, S. & Tokura, Y. Magnetochiral dichroism resonant with electromagnons in a helimagnet. *Nature Communications* **5,** 4583 (2014).

179. Khomskii, D. Classifying multiferroics: mechanisms and effects. *Physics* **2** (2009).

180. Spaldin, N. A. & Ramesh, R. Advances in magnetoelectric multiferroics. *Nature Materials* **18,** 203–212 (2019).

181. Astrov, D. N. The magnetoelectric effect in antiferromagnetics. *Sov. Phys. – JETP* **11,** 708 (1960).

182. Rado, G. T. & Folen, V. J. Observation of the Magnetically Induced Magnetoelectric Effect and Evidence for Antiferromagnetic Domains. *Physical Review Letters* **7,** 310–311 (1961).

183. Newnham, R. E., Kramer, J. J., Schulze, W. A. & Cross, L. E. Magnetoferroelectricity in Cr_2BeO_4. *Journal of Applied Physics* **49,** 6088–6091 (1978).

184. Lai, Y. *et al.* Two-dimensional ferromagnetism and driven ferroelectricity in van der Waals $CuCrP_2S_6$. *Nanoscale* **11,** 5163–5170 (2019).

185. Pollini, I., Thomas, J. & Lenselink, A. Optical properties of layered transition-metal iodides. *Physical Review B* **30,** 2140–2148 (1984).

186. Ju, H. *et al.* Possible Persistence of Multiferroic Order down to Bilayer Limit of van der Waals Material NiI_2. *Nano Letters* **21,** 5126–5132 (2021).

187. Kurumaji, T. Spiral spin structures and skyrmions in multiferroics. *Physical Sciences Reviews* **5** (2020).

188. Friedt, J. M., Sanchez, J. P. & Shenoy, G. K. Electronic and magnetic properties of metal diiodides MI_2 (M=V, Cr, Mn, Fe, Co, Ni, and Cd) from ^{129}I Mössbauer spectroscopy. *The Journal of Chemical Physics* **65,** 5093–5102 (1976).

189. Liu, H. *et al.* Vapor Deposition of Magnetic Van der Waals NiI_2 Crystals. *ACS Nano* **14,** 10544–10551 (2020).

190. Kuindersma, S. R., Boudewijn, P. R. & Haas, C. Near infrared *d*-*d* transitions of NiI_2, CdI_2:Ni^{2+}, and CoI_2. *Phys. Stat. Sol. (b)* **108,** 187–194 (1981).

191. Xiao, J. *et al.* Intrinsic two-dimensional ferroelectricity with dipole locking. *Physical Review Letters* **120,** 227601 (2018).

192. Jin, W. *et al.* Raman fingerprint of two terahertz spin wave branches in a two-dimensional honeycomb Ising ferromagnet. *Nature Communications* **9,** 5122 (2018).

193. Deng, Y. *et al.* Gate-tunable room-temperature ferromagnetism in two-dimensional Fe_3GeTe_2. *Nature* **563,** 94–99 (2018).

194. Sivadas, N., Okamoto, S., Xu, X., Fennie, C. J. & Xiao, D. Stacking-Dependent Magnetism in Bilayer CrI_3. *Nano Letters* **18,** 7658–7664 (2018).

195. Akram, M. *et al.* Moiré skyrmions and chiral magnetic phases in twisted CrX_3 (X = I, Br, and Cl) bilayers. *Nano Letters* **21,** 6633–6639 (2021).

196. Nguyen, T. P. T., Yamauchi, K., Oguchi, T., Amoroso, D. & Picozzi, S. Electric-field tuning of the magnetic properties of bilayer VI_3: A first-principles study. *Physical Review B* **104,** 014414 (2021).

197. Prayitno, T. B. Controlling phase transition in monolayer metal diiodides XI_2 (X: Fe, Co, and Ni) by carrier doping. *Journal of Physics: Condensed Matter* **33,** 335803 (2021).

198. Narayan, A., Cano, A., Balatsky, A. V. & Spaldin, N. A. Multiferroic quantum criticality. *Nature Materials* **18,** 223–228 (2019).

199. Kresse, G. & Furthmüller, J. Efficient iterative schemes for ab initio total-energy calculations using a plane-wave basis set. *Physical Review B* **54,** 11169–11186 (1996).

200. Kresse, G. & Joubert, D. From ultrasoft pseudopotentials to the projector augmented-wave method. *Physical Review B* **59,** 1758–1775 (1999).

201. Blaha, P. *et al.* WIEN2k: An APW+lo program for calculating the properties of solids. *Journal of Chemical Physics* **152,** 074101 (2020).

202. Perdew, J. P., Burke, K. & Ernzerhof, M. Generalized Gradient Approximation Made Simple. *Physical Review Letters* **77,** 3865–3868 (1996).

203. Rohrbach, A., Hafner, J. & Kresse, G. Electronic correlation effects in transition-metal sulfides. *Journal of Physics: Condensed Matter* **15,** 979–996 (2003).

204. Perdew, J. P. *et al.* Restoring the density-gradient expansion for exchange in solids and surfaces. *Physical Review Letters* **100,** 136406 (2008).

205. Becke, A. D. On the large-gradient behavior of the density functional exchange energy. *Journal of Chemical Physics* **85,** 7184–7187 (1986).

206. Pimenov, A. *et al.* Magnetic and magnetoelectric excitations in $TbMnO_3$. *Physical Review Letters* **102,** 107203 (2009).

207. Klein, D. R. *et al.* Enhancement of interlayer exchange in an ultrathin two-dimensional magnet. *Nature Physics* **15,** 1255–1260 (2019).

208. Larson, D. T. & Kaxiras, E. Raman spectrum of CrI_3: An ab initio study. *Physical Review B* **98,** 085406 (2018).

209. Jiang, Y. *et al.* Dilemma in optical identification of single-layer multiferroics. *Nature* **619,** E40–E43 (2023).

210. Song, Q. *et al.* Reply to: Dilemma in optical identification of single-layer multiferroics. *Nature* **619,** E44–E46 (2023).

211. Fiebig, M., Fröhlich, D., Krichevtsov, B. B. & Pisarev, R. V. Second harmonic generation and magnetic-dipole-electric-dipole interference in antiferromagnetic Cr_2O_3. *Physical Review Letters* **73,** 2127–2130 (1994).

212. Zhang, D., Schoenherr, P., Sharma, P. & Seidel, J. Ferroelectric order in van der Waals layered materials. *Nature Reviews Materials* **8,** 25–40 (2023).

213. Lebedev, D. *et al.* Electrical Interrogation of Thickness-Dependent Multiferroic Phase Transitions in the 2D Antiferromagnetic Semiconductor NiI_2. *Advanced Functional Materials* **33,** 2212568 (2023).

214. Occhialini, C. A. *et al.* Signatures of pressure-enhanced helimagnetic order in van der Waals multiferroic NiI_2. *arXiv,* 2306.11720 (2023).

215. Bikaljević, D. *et al.* Noncollinear Magnetic Order in Two-Dimensional $NiBr_2$ Films Grown on Au(111). *ACS Nano* **15,** 14985–14995 (2021).

216. Zhang, J. S. *et al.* Giant pressure-enhancement of multiferroicity in $CuBr_2$. *Physical Review Research* **2,** 013144 (2020).

217. Soler-Delgado, D. *et al.* Probing Magnetism in Exfoliated VI_3 Layers with Magnetotransport. *Nano Letters* **22,** 6149–6155 (2022).

218. Guan, Z. *et al.* Recent Progress in Two-Dimensional Ferroelectric Materials. *Advanced Electronic Materials* **6,** 1–30 (2020).

219. Fabrykiewicz, P., Przeniosło, R. & Sosnowska, I. Crystal symmetry for incommensurate helical and cycloidal modulations. *Acta crystallographica. Section A, Foundations and advances* **77,** 160–172 (2021).

220. Song, T. *et al.* Switching 2D magnetic states via pressure tuning of layer stacking. *Nature Materials* **18,** 1298–1302 (2019).

221. Valenta, J. *et al.* Pressure-induced large increase of Curie temperature of the van der Waals ferromagnet VI_3. *Physical Review B* **103,** 054424 (2021).

222. Yankowitz, M. *et al.* Dynamic band-structure tuning of graphene moiré superlattices with pressure. *Nature* **557,** 404 (2018).

223. Harms, N. C. *et al.* Symmetry progression and possible polar metallicity in $NiPS_3$ under pressure. *npj 2D Materials and Applications* **6,** 40 (2022).

224. Terada, N. *et al.* Room-Temperature Type-II Multiferroic Phase Induced by Pressure in Cupric Oxide. *Physical Review Letters* **129,** 217601 (2022).

225. Martins, L. G. P. *et al.* High-pressure studies of atomically thin van der Waals materials. *Applied Physics Reviews* **10,** 011313 (2023).

226. Zong, A. *et al.* Spin-mediated shear oscillators in a van der Waals antiferromagnet. *Nature* **620,** 988–993 (2023).

227. Zhou, F. *et al.* Dynamical criticality of spin-shear coupling in van der Waals antiferromagnets. *Nature Communications* **13,** 6598 (2022).

228. Adam, A. *et al.* Hydrostatic Pressure effect on the commensurate-incommensurate phase transition of $NiBr_2$. *Physics Letters* **84,** 24–27 (1981).

229. Tateiwa, N. & Haga, Y. Evaluations of pressure-transmitting media for cryogenic experiments with diamond anvil cell. *Review of Scientific Instruments* **80,** 123901 (2009).

230. Feng, Y., Jaramillo, R., Wang, J., Ren, Y. & Rosenbaum, T. Invited article: High-pressure techniques for condensed matter physics at low temperature. *Review of Scientific Instruments* **81,** 041301 (2010).

231. Adam, A. *et al.* Neutron diffraction study of the commensurate and incommensurate magnetic structures of $NiBr_2$. *Solid State Communications* **35,** 1–5 (1980).

232. Achkar, A. J. *et al.* Bulk sensitive x-ray absorption spectroscopy free of self-absorption effects. *Physical Review B* **83,** 081106 (2011).

233. Kim, K. T. *et al.* Origin of circular dichroism in resonant elastic X-ray scattering from magnetic and polar chiral structures. *Physical Review B* **106,** 035116 (2022).

234. Schüßler-Langeheine, C. *et al.* Resonant magnetic X-ray scattering from ultrathin Ho-metal films down to a few atomic layers. *Journal of Electron Spectroscopy and Related Phenomena* **114-116,** 953–957 (2001).

235. Van der Laan, G. Studying spintronics materials with soft X-ray resonant scattering. *Current Opinion in Solid State and Materials Science* **10,** 120–127 (2006).

236. Gordon, E. E., Derakhshan, S., Thompson, C. M. & Whangbo, M. H. Spin-Density Wave as a Superposition of Two Magnetic States of Opposite Chirality and Its Implications. *Inorganic Chemistry* **57,** 9782–9785 (2018).

237. Kenzelmann, M. *et al.* Magnetic inversion symmetry breaking and ferroelectricity in $TbMnO_3$. *Physical Review Letters* **95,** 087206 (2005).

238. Wilkins, S. B. *et al.* Nature of the magnetic order and origin of induced ferroelectricity in $TbMnO_3$. *Physical Review Letters* **103,** 207602 (2009).

239. Villarreal, R. *et al.* Magnetic Phase Diagram of CuO via High-Resolution Ultrasonic Velocity Measurements. *Physical Review Letters* **109,** 167206 (2012).

240. Wang, Z. *et al.* Magnetoelectric effect and phase transitions in CuO in external magnetic fields. *Nature Communications* **7,** 10295 (2016).

241. Terada, N. *et al.* Spiral-spin-driven ferroelectricity in a multiferroic delafossite $AgFeO_2$. *Physical Review Letters* **109,** 097203 (2012).

242. Occhialini, C. A. *et al.* Nature of excitons and their ligand-mediated delocalization in nickel dihalide charge-transfer insulators. *arXiv,* 2404.10818 (2024).

243. Agranovich, V. M. & Toshich, B. S. Collective properties of Frenkel excitons. *Sov. Phys. JETP* **26,** 104–112 (1968).

244. Kim, D. S. *et al.* Anisotropic Excitons Reveal Local Spin Chain Directions in a van der Waals Antiferromagnet. *Advanced Materials* **35,** 2206585 (2023).

245. Kozielski, M., Pollini, I. & Spinolo, G. Electronic absorption spectra of Ni^{2+} in $NiCl_2$ and $NiBr_2$. (Phonon and magnon sidebands). *Journal of Physics C: Solid State Physics* **5,** 1253–1264 (1972).

246. Robbins, D. J. & Day, P. Temperature variation of exciton-magnon absorption bands in metamagnetic transition-metal dihalides. *Journal of Physics C: Solid State Physics* **9,** 867–882 (1976).

247. Pollini, I., Spinolo, G. & Benedek, G. Vibrational structure of crystal-field spectra in layered 3*d*-metal dihalides. *Physical Review B* **22,** 6369–6390 (1980).

248. Giordano, P., Pollini, I., Reatto, L. & G, S. ^1E_g spin-forbidden transition in $NiBr_2$: temperature dependence. *Physical Review B* **17,** 257–262 (1978).

249. Benedek, G., Pollini, I., Piseri, L. & Tubino, R. Evidence of two-phonon vibronic progressions in layered 3*d*-metal dihalides. *Physical Review B* **20,** 4303–4307 (1979).

250. Zhang, F. C. & Rice, T. M. Effective Hamiltonian for the superconducting Cu oxides. *Physical Review B* **37,** 3759–3761 (1988).

251. Tjeng, L. H. *et al.* Spin-resolved photoemission on anti-ferromagnets: Direct observation of Zhang-Rice singlets in CuO. *Physical Review Letters* **78,** 1126–1129 (1997).

252. Banda, E. J. Optical absorption of $NiPS_3$ in the near-infrared, visible and near-ultraviolet regions. *Journal of Physics C: Solid State Physics* **19,** 7329–7335 (1986).

253. Rosseinsky, D. R. & Dorrity, I. A. Absorption Spectrum of Single Crystals of NiI_2 at 300-5 K. *Inorganic Chemistry* **17,** 1600–1603 (1978).

254. Sell, D. D., Greene, R. L. & White, R. M. Optical exciton-magnon absorption in MnF_2. *Physical Review* **158,** 489–510 (1967).

255. Freeman, S. Molecular-Orbital Theory of the Excited-State Exchange Interaction. *Physical Review B* **7,** 3960 (1967).

256. Freeman, S. & Hopfield, J. J. Exciton-magnon interaction in magnetic insulators. *Physical Review Letters* **21,** 910–913 (1968).

257. Nag, A. *et al.* Many-body physics of single and double spin-flip excitations in NiO. *Physical Review Letters* **124,** 067202 (2020).

258. Brik, M. G., Camardello, S. J., Srivastava, A. M., Avram, N. M. & Suchocki, A. Spin-Forbidden Transitions in the Spectra of Transition Metal Ions and Nephelauxetic Effect. *ECS Journal of Solid State Science and Technology* **5,** R3067–R3077 (2016).

259. Okada, K., Kotani, A. & Thole, B. T. Charge transfer satellites and multiplet splitting in X-ray photoemission spectra of late transition metal halides. *Journal of Electron Spectroscopy and Related Phenomena* **58,** 325–343 (1992).

260. De Groot, F. M., Arrio, M. A., Sainctavit, P., Cartier, C. & Chen, C. T. Fluorescence yield detection: Why it does not measure the X-ray absorption cross section. *Solid State Communications* **92,** 991–995 (1994).

261. Carboni, R., Giovannini, S., Antonioli, G. & Boscherini, F. Self-absorption correction strategy for fluorescence-yield soft x-ray near edge spectra. *Physica Scripta T* **T115,** 986–988 (2005).

262. Wang, R. P. *et al.* Saturation and self-absorption effects in the angle-dependent $2p3d$ resonant inelastic X-ray scattering spectra of Co^{3+}. *Journal of Synchrotron Radiation* **27,** 979–987 (2020).

263. De Groot, F. M. F., Fuggle, J. C., Thole, B. T. & Sawatzky, G. A. $L_{2,3}$ x-ray-absorption edges of d^0 compounds: K, Ca, Sc, and Ti in O_h symmetry. *Physical Review B* **41,** 928 (1990).

264. Ushakov, A. V., Streltsov, S. V. & Khomskii, D. I. Crystal field splitting in correlated systems with negative charge-transfer gap. *Journal of Physics Condensed Matter* **23,** 445601–445607 (2011).

265. Scaramucci, A., Ammann, J., Spaldin, N. A. & Ederer, C. Separating different contributions to the crystal-field parameters using Wannier functions. *Journal of Physics Condensed Matter* **27,** 175503 (2015).

266. De Groot, F. M. F., Kuiper, P. & Sawatzky, G. A. Local spin-flip spectral distribution obtained by resonant x-ray Raman scattering. *Physical Review B* **57,** 14584–14587 (1998).

267. Haverkort, M. W. *et al.* Bands, resonances, edge singularities and excitons in core level spectroscopy investigated within the dynamical mean-field theory. *EPL* **108,** 57004 (2014).

268. Lu, Y., Höppner, M., Gunnarsson, O. & Haverkort, M. W. Efficient real-frequency solver for dynamical mean-field theory. *Physical Review B* **90,** 085102 (2014).

269. Li, J. *et al.* Single- and Multimagnon Dynamics in Antiferromagnetic α-Fe_2O_3 Thin Films. *Physical Review X* **13,** 011012 (2023).

270. Elnaggar, H. *et al.* Magnetic excitations beyond the single- and double-magnons. *Nature Communications* **14,** 19–26 (2023).

271. Bisogni, V. *et al.* Ground-state oxygen holes and the metal-insulator transition in the negative charge-transfer rare-earth nickelates. *Nature Communications* **7,** 13017 (2016).

272. Wojnar, M. K., Laorenza, D. W., Schaller, R. D. & Freedman, D. E. Nickel(II) metal complexes as optically addressable qubit candidates. *Journal of the American Chemical Society* **142,** 14826–14830 (2020).

273. Bisogni, V. *et al.* Orbital control of effective dimensionality: From spin-orbital fractionalization to confinement in the anisotropic ladder system $\mathrm{CaCu_2O_3}$. *Physical Review Letters* **114,** 096402 (2015).

274. Martinelli, L. *et al.* Collective nature of orbital excitations in layered cuprates in the absence of apical oxygens. *arXiv,* 2304.02115 (2023).

275. Cudazzo, P., Sottile, F., Rubio, A. & Gatti, M. Exciton dispersion in molecular solids. *Journal of Physics Condensed Matter* **27,** 113204 (2015).

276. Gombar, S., Mali, P., Pantić, M., Pavkov-Hrvojević, M. & Radošević, S. Dynamics of Frenkel excitons in pentacene. *Materials* **11,** 2219 (2018).

277. Nag, A. *et al.* Quadrupolar magnetic excitations in an isotropic spin-1 antiferromagnet. *Nature Communications* **13,** 2327 (2022).

278. Braicovich, L. *et al.* Dispersion of magnetic excitations in the cuprate $\mathrm{La_2CuO_4}$ and $\mathrm{CaCuO_2}$ compounds measured using resonant X-ray scattering. *Physical Review Letters* **102,** 167401 (2009).

279. Braicovich, L. *et al.* Magnetic excitations and phase separation in the underdoped $\mathrm{La}_{2-x}\mathrm{Sr}_x\mathrm{CuO}_4$ superconductor measured by resonant inelastic X-Ray scattering. *Physical Review Letters* **104,** 077002 (2010).

280. Lee, J. J. *et al.* Charge-orbital-lattice coupling effects in the *dd* excitation profile of one-dimensional cuprates. *Physical Review B* **89,** 041104(R) (2014).

281. Meltzer, R. S., Lowe, M. & McClure, D. S. Magnon sidebands in the optical absorption spectrum of $\mathrm{MnF_2}$. *Physical Review* **180,** 561–578 (1969).

282. Tanabe, Y. & Gondaira, K.-I. Line shape of spin wave sidebands. *J. Phys. Soc. Jap.* **25,** 1562–1575 (1968).

283. Abbamonte, P. *et al.* Dynamical reconstruction of the exciton in LiF with inelastic x-ray scattering. *Proceedings of the National Academy of Sciences* **105,** 12159–12163 (2008).

284. Cudazzo, P., Gatti, M., Rubio, A. & Sottile, F. Frenkel versus charge-transfer exciton dispersion in molecular crystals. *Physical Review B* **88,** 195152 (2013).

285. Schuster, R., Knupfer, M. & Berger, H. Exciton band structure of pentacene molecular solids: Breakdown of the Frenkel exciton model. *Physical Review Letters* **98,** 037402 (2007).

286. Yang, K. *et al.* Inelastic X-Ray Scattering Study of Exciton Properties in an Organic Molecular Crystal. *Physical Review Letters* **98,** 036404 (2007).

287. Pogrebna, A. *et al.* Spectral tunability of laser-induced spin dynamics in the ferromagnetic semiconductor $CdCr_2Se_4$. *Physical Review B* **98,** 214427 (2018).

288. Genkin, G. M., Nozdrin, Y. N., Tokman, I. D. & Shastin, V. N. Direct observation of photomagnetization of the ferromagnet $CdCr_2Se_4$ by circularly polarized light. *Journal of Experimental and Theoretical Physics Letters* **35,** 162–164 (1982).

289. Bae, Y. J. *et al.* Exciton-coupled coherent magnons in a 2D semiconductor. *Nature* **609,** 282–286 (2022).

290. Matthiesen, M. *et al.* Controlling Magnetism with Light in a Zero Orbital Angular Momentum Antiferromagnet. *Physical Review Letters* **130,** 076702 (2023).

291. Bayliss, S. L. *et al.* Optically addressable molecular spins for quantum information processing. *Science* **370,** 1309–1312 (2020).

292. Haverkort, M. W. Spin and orbital degrees of freedom in transition metal oxides and oxide thin films studied by soft x-ray absorption spectroscopy. *arXiv,* cond–mat/0505214 (2005).

293. Minola, M. *et al.* Collective nature of spin excitations in superconducting cuprates probed by resonant inelastic X-Ray scattering. *Physical Review Letters* **114,** 217003 (2015).

294. Occhialini, C. A. *et al.* Spontaneous orbital polarization in the nematic phase of FeSe. *Nature Materials* **22,** 985–991 (2023).

295. Liu, D. *et al.* Orbital Origin of Extremely Anisotropic Superconducting Gap in Nematic Phase of FeSe Superconductor. *Physical Review X* **8,** 031033 (2018).

296. Chen, X., Maiti, S., Fernandes, R. M. & Hirschfeld, P. J. Nematicity and superconductivity: Competition versus cooperation. *Physical Review B* **102,** 184512 (2020).

297. Wilkins, S. B. *et al.* Direct observation of orbital ordering in $La_{0.5}Sr_{1.5}MnO_4$ using soft x-ray diffraction. *Physical Review Letters* **91,** 167205 (2003).

298. Willers, T. *et al.* Correlation between ground state and orbital anisotropy in heavy fermion materials. *Proceedings of the National Academy of Sciences of the United States of America* **112,** 2384–2388 (2015).

299. Rosenberg, E. W., Chu, J. H., Ruff, J. P., Hristov, A. T. & Fisher, I. R. Divergence of the quadrupole-strain susceptibility of the electronic nematic system $YbRu_2Ge_2$. *Proceedings of the National Academy of Sciences of the United States of America* **116,** 7232–7237 (2019).

300. Li, J. *et al.* Spin-Orbital-Intertwined Nematic State in FeSe. *Physical Review X* **10,** 011034 (2020).

301. Shimojima, T. *et al.* Lifting of xz/yz orbital degeneracy at the structural transition in detwinned FeSe. *Physical Review B* **90,** 121111 (2014).

302. Massat, P. *et al.* Charge-induced nematicity in FeSe. *Proceedings of the National Academy of Sciences of the United States of America* **113,** 9177–9181 (2016).

303. Bartlett, J. M. *et al.* Relationship between Transport Anisotropy and Nematicity in FeSe. *Physical Review X* **11,** 021038 (2021).

304. Ghini, M. *et al.* Strain tuning of nematicity and superconductivity in single crystals of FeSe. *Physical Review B* **103,** 205139 (2021).

305. Chinotti, M., Pal, A., Degiorgi, L., Böhmer, A. E. & Canfield, P. C. Ingredients for the electronic nematic phase in FeSe revealed by its anisotropic optical response. *Physical Review B* **98,** 094506 (2018).

306. Schütt, M., Schmalian, J. & Fernandes, R. M. Origin of DC and AC conductivity anisotropy in iron-based superconductors: Scattering rate versus spectral weight effects. *Physical Review B* **94,** 075111 (2016).

307. Baek, S. H. *et al.* Separate tuning of nematicity and spin fluctuations to unravel the origin of superconductivity in FeSe. *npj Quantum Materials* **5,** 8 (2020).

308. Huh, S. S. *et al.* Absence of Y-pocket in 1-Fe Brillouin zone and reversed orbital occupation imbalance in FeSe. *Communications Physics* **3,** 52 (2020).

309. Fernandes, R. M., Böhmer, A. E., Meingast, C. & Schmalian, J. Scaling between magnetic and lattice fluctuations in iron pnictide superconductors. *Physical Review Letters* **111,** 137001 (2013).

310. Park, J. *et al.* Rigid platform for applying large tunable strains to mechanically delicate samples. *Review of Scientific Instruments* **91,** 083902 (2020).

311. Lebert, B. W., Balédent, V., Toulemonde, P., Ablett, J. M. & Rueff, J. P. Emergent high-spin state above 7 GPa in superconducting FeSe. *Physical Review B* **97,** 180503 (2018).

312. Joseph, B. *et al.* A study of the electronic structure of $\mathrm{FeSe}_{1-x}\mathrm{Te}_x$ chalcogenides by Fe and Se K-edge x-ray absorption near edge structure measurements. *Journal of Physics Condensed Matter* **22,** 485702 (2010).

313. Simonelli, L. *et al.* Electronic properties of $\mathrm{FeSe}_{1-x}\mathrm{Te}_x$ probed by x-ray emission and absorption spectroscopy. *Journal of Physics Condensed Matter* **24,** 415501 (2012).

314. Modrow, H., Bucher, S., Rehr, J. J. & Ankudinov, A. L. Calculation and interpretation of K-shell x-ray absorption near-edge structure of transition metal oxides. *Physical Review B* **67,** 035123 (2003).

315. De Figueiredo, A. G. *et al.* Orbital localization and the role of the Fe and As $4p$ orbitals in $\mathrm{BaFe_2As_2}$ probed by XANES. *Physical Review B* **105,** 045130 (2022).

316. Chen, J. M. *et al.* Electronic structure and characteristics of Fe 3d valence states of $Fe_{1.01}Se$ superconductors under pressure probed by x-ray absorption spectroscopy and resonant x-ray emission spectroscopy. *Journal of Chemical Physics* **137,** 244702 (2012).

317. Lee, C. C., Yin, W. G. & Ku, W. Ferro-Orbital order and strong magnetic anisotropy in the parent compounds of iron-pnictide superconductors. *Physical Review Letters* **103,** 267001 (2009).

318. Sanchez, J. J. *et al.* The transport–structural correspondence across the nematic phase transition probed by elasto X-ray diffraction. *Nature Materials* **20,** 1519–1524 (2021).

319. Chen, C. C. *et al.* Orbital order and spontaneous orthorhombicity in iron pnictides. *Physical Review B* **82,** 100504 (2010).

320. Koch, R. J. *et al.* Room temperature local nematicity in FeSe superconductor. *Physical Review B* **100,** 020501 (2019).

321. Ishida, K. *et al.* Pure nematic quantum critical point accompanied by a superconducting dome. *Proceedings of the National Academy of Sciences* **119,** e2110501119 (2022).

322. Onari, S. & Kontani, H. In-plane anisotropy of transport coefficients in electronic nematic states: Universal origin of nematicity in Fe-based superconductors. *Physical Review B* **96,** 094527 (2017).

323. Fernandes, R. M., Abrahams, E. & Schmalian, J. Anisotropic in-plane resistivity in the nematic phase of the iron pnictides. *Physical Review Letters* **107,** 217002 (2011).

324. He, M. *et al.* Evidence for short-range magnetic order in the nematic phase of FeSe from anisotropic in-plane magnetostriction and susceptibility measurements. *Physical Review B* **97,** 104107 (2018).

325. Udina, M., Grilli, M., Benfatto, L. & Chubukov, A. V. Raman Response in the Nematic Phase of FeSe. *Physical Review Letters* **124,** 197602 (2020).

326. Wang, Q. *et al.* Magnetic ground state of FeSe. *Nature Communications* **7,** 12182 (2016).

327. Sun, J., Matsuura, K. & Ye et al., G. Dome-shaped magnetic order competing with high-temperature superconductivity at high pressures in FeSe. *Nature Communications* **7,** 12146 (2016).

328. Hanaguri, T. *et al.* Two distinct superconducting pairing states divided by the nematic end point in $FeSe_{1-x}S_x$. *Science Advances* **4,** eaar6419 (2018).

329. Bunău, O. & Joly, Y. Self-consistent aspects of x-ray absorption calculations. *Journal of Physics Condensed Matter* **21,** 345501 (2009).

330. Lafuerza, S. *et al.* Evidence of Mott physics in iron pnictides from x-ray spectroscopy. *Physical Review B* **96,** 045133 (2017).

331. Yang, W. L. *et al.* Evidence for weak electronic correlations in iron pnictides. *Physical Review B* **80,** 014508 (2009).

332. Kim, Y. K. *et al.* Existence of orbital order and its fluctuation in superconducting $Ba(Fe_{1-x}Co_x)_2As_2$ single crystals revealed by x-ray absorption spectroscopy. *Physical Review Letters* **111,** 217001 (2013).

333. Pelliciari, J. *et al.* Fluctuating magnetism of Co- And Cu-doped NaFeAs. *Applied Physics Letters* **118,** 112604 (2021).

334. Lee, S. H. *et al.* Coupling of spin and orbital excitations in the iron-based superconductor $FeSe_{0.5}Te_{0.5}$. *Physical Review B* **81,** 220502 (2010).

335. Hu, L. *et al.* Observation of a magnetic phase transition in monolayer $NiPS_3$. *Physical Review B* **107,** L220407 (2023).

336. Nakatsuji, S. *et al.* Spin disorder on a triangular lattice. *Science* **309,** 1697–1700 (2005).

337. He, W., Kong, L., Zhao, W. & Yu, P. Atomically Thin 2D van der Waals Magnetic Materials: Fabrications, Structure, Magnetic Properties and Applications. *Coatings* **12,** 122 (2022).

338. Stock, C. *et al.* Neutron-scattering measurement of incommensurate short-range order in single crystals of the $S = 1$ triangular antiferromagnet $NiGa_2S_4$. *Physical Review Letters* **105,** 037402 (2010).

339. Zhou, B. *et al.* Possible structural transformation and enhanced magnetic fluctuations in exfoliated α-$RuCl_3$. **128,** 291–295 (2019).

340. Moore, M. W., Day, P., Wilkinson, C. & Ziebeck, K. R. The effect of iodide doping on the incommensurate helical magnetic structure of $NiBr_2$. *Solid State Communications* **53,** 1009–1013 (1985).

341. Blase, X., Duchemin, I., Jacquemin, D. & Loos, P. F. The Bethe-Salpeter Equation Formalism: From Physics to Chemistry. *Journal of Physical Chemistry Letters* **11,** 7371–7382 (2020).

342. Wu, M., Li, Z. & Louie, S. G. Optical and magneto-optical properties of ferromagnetic monolayer $CrBr_3$: A first-principles *GW* and *GW* plus Bethe-Salpeter equation study. *Physical Review Materials* **6,** 014008 (2022).

343. Qian, T. X., Zhou, J., Cai, T. Y. & Ju, S. Anisotropic electron-hole excitation and large linear dichroism in the two-dimensional ferromagnet CrSBr with in-plane magnetization. *Physical Review Research* **5,** 033143 (2023).

344. Monino, E. & Loos, P. F. Spin-Conserved and Spin-Flip Optical Excitations from the Bethe-Salpeter Equation Formalism. *Journal of Chemical Theory and Computation* **17,** 2852–2867 (2021).

345. Acharya, S. *et al.* A theory for colors of strongly correlated electronic systems. *Nature Communications* **14,** 5565 (2023).